Computational Analysis of Heat and Mass Transfer for Stenosed Curved Arterial Blood Flow with Nanofluid and Variable Viscosity

THESIS

Submitted in partial fulfilment of the requirements for the degree of

DOCTOR OF PHILOSOPHY

by

CHANDAN KUMAWAT

Under the Supervision of

PROF. BHUPENDRA KUMAR SHARMA

BITS Pilani
Pilani | Dubai | Goa | Hyderabad | Mumbai

BIRLA INSTITUTE OF TECHNOLOGY AND SCIENCE, PILANI

2023

Dedicated to My Parents

Mr. Satya Narayan Kumawat

and

Smt. Manju Devi

BIRLA INSTITUTE OF TECHNOLOGY & SCIENCE, PILANI

CERTIFICATE

This is to certify that the thesis titled **"Computational Analysis of Heat and Mass Transfer for Stenosed Curved Arterial Blood Flow with Nanofluid and Variable Viscosity"** submitted by **Mr. Chandan Kumawat**, ID No. **2018PHXF0421P** for the award of Ph.D. of the institute embodies original work done by him under my supervision.

Signature of the Supervisor
Name: **DR. BHUPENDRA KUMAR SHARMA**
Designation: **Professor**

Date:

Acknowledgements

Thank god Almighty for the abundant grace showering on me and providing me strength and hope throughout the journey of my life. Thesis is the combined effort of all those who inspire and guide, who participate, who boost your morale and of those who support when you stumble. I find this is a felicitous opportunity to express our heartfelt thanks and gratitude to all those involved in the Ph.D work .

Words do not suffice to express our profound indebtedness and deep sense of gratitude to our respected, revered Professor Bhupendra Kumar Sharma for his support and encouragement during the tenure of my Ph.D. work. He always motivated me to learn new techniques and knowledge which really helped me in my Ph.D. work. Under his supervision I improved my presentation skills as well as content writing skills, His personal generosity helped to enjoy moments at this prestigious Institute BITS, Pilani. I am also highly indebted for providing timely guidance and meticulous supervision and inculcating the culture of doing research.

I wish to express our gratitude towards my DAC committee members Prof. Ashish Tiwari and Dr. Sangita Yadav. Their valuable comments and suggestions during this tenure have significantly impact on quality of my thesis work. Whenever I contacted them, they were very humble, kind and patiently listen to doubt and clarify it despite of their busy schedule.

I owe a debt of gratitude to HODs of Mathematics department Prof. Devendra Kumar for providing me the necessary facilities for this piece of work. I also gratefully acknowledge the faculty members of Department of Mathematics, BITS Pilani for paying their interest and genuine interest during my end semester seminars and non teaching staff of mathematics department for their help. I extend my thanks to SRCD and AGSRD for their helpful support.

I sincerely acknowledge the financial support provided by UGC- CSIR New Delhi, during the tenure of my doctoral research work.

I would like to extend my heartfelt appreciation and gratitude to my parents, Smt. Manju Devi and Mr. Satya Narayan Kumawat, for their unwavering support, love, and encouragement throughout my academic journey. Their sacrifices, guidance, and belief in my abilities have been instrumental in my achievements. From the very beginning, my parents instilled in me the value of education and the importance of hard work. My parents have not only supported me emotionally but have also made countless sacrifices to ensure I had the resources I needed to excel in my academic pursuits. Their selflessness and dedication to my

well-being have been a constant source of inspiration.

I would like to express my deepest gratitude and appreciation to my loving wife Shalini. Throughout this long and challenging journey of completing this thesis, she has been my unwavering source of support, understanding, and encouragement. Her patience, love, and belief in me have been my constant inspiration. Her sacrifices and unwavering faith in my abilities have made it possible for me to pursue my academic goals. I am profoundly grateful for her willingness to listen to my ideas, provide constructive feedback, and help me maintain a healthy work-life balance. Her presence in my life has made every day more meaningful and enjoyable. I am truly blessed to have her by my side.

I would like to extend my heartfelt thanks to all my afternoon tea and card club friends Dr. Sandeep, Dr. Barkha, Dr. Komal, Dr. Sugandha, Dr. Satyendra, Pallav, Komal, Meghna, Shilpa, Sarita, and Praveen for being with me in this long journey. I am also thankful to my hostel squad Dr. Deepak, Dr. Sajan, Himanshu, Amit, Sanjeev, Gourav, Ankit, Satpal for the late-night intellectual sessions that turned into gossip fests to the countless teas runs that fueled our intellectual endeavors, you all made this journey memorable and fun. Thanks for the laughter, the memes, links sharing and the endless support. I would also thank my juniors Rishu, Umesh, Anup and Richa for their research related queries that enhanced my subject knowledge. In last I am thankful to Dr. Kapil and Riya for their support in my every ups and down moments. Due to all of these friends, I cherished each and every moments during my entire stay at BITS Pilani.

Place: BITS Pilani
Date: October 2023

Chandan Kumawat
(Department of Mathematics)

Abstract

This thesis presents a computational investigation of blood phenomena with heat and mass transport for the stenosed curved artery under the external applied magnetic field and heat source. The two-phase flow nature of blood flow for the different types of stenosis shapes is also part of this thesis work. The blood's variable viscosity (hematocrit and temperature dependent) nature and nanoparticle properties are also included to make this thesis more realistic. The thesis contains eight chapters, and chapter wise summary is as follows:

A brief introduction of biomechanics, cardiovascular system and physical parameters, as well as gaps in existing research, is provided in the first chapter.

The second chapter examines the effects of thermal radiation and magnetic field on the two-phase blood flow through a stenosed curved artery. The flow viscosity for both core and plasma region are considered variable. The blood flow viscosity of the core region is assumed hematocrit dependent, while plasma region viscosity is temperature-dependent. The energy equations for both regions are solved using the perturbation method, while the momentum equation is solved numerically using the second-order finite difference method. Variations in flow physical phenomena such as flow rate, wall shear stress and frictional impedance for the different values of a magnetic field, arterial curvature and thermal radiation have been discussed graphically.

In the third chapter, numerical analysis of heat and mass transfer for the two-phase blood flow through curved artery under the presence of a magnetic field and chemical reaction has been done. The temperature-dependent viscosity for the core region blood flow is considered, while plasma region flow viscosity is assumed constant. To make this study more realistic, permeable wall condition instead of no-slip condition at the arterial wall for flow velocity has been considered. The effect of various physical parameters such as magnetic field (M), viscosity variation parameter (λ_1), Darcy number (Da), heat source (H), chemical reaction parameter (ξ) etc., are displayed graphically on the flow velocity, temperature, concentration, wall shear stress (WSS) and frictional resistance profiles.

The fourth chapter provides the entropy generation analysis for MHD two-phase curved arterial blood flow under the elliptic shape stenosis condition. The temperature-dependent viscosity for the core region blood flow is considered, while plasma region flow viscosity is assumed constant. This work has also considered the effects of Joule heating, heat source, viscous dissipation and chemical reactions. The coupled system of non-dimensional governing equations is solved numerically using the second-order finite difference method. Blood flow pattern contours have been plotted for various values of the magnetic field, arterial curvature, heat source, and viscosity variation parameter in order to understand the flow

behaviour.

In chapter 5, the computational study of entropy generation and heat transport for non-Newtonian blood flow through a stenosed curved artery under the consequences of the Hall effect and thermal radiation has been performed. The power-law fluid properties for core region blood flow is considered, while plasma region flow adopted the Newtonian fluid properties. Stone's strongly implicit scheme is used to solve a set of highly non-linear coupled partial differential equations. The influence of various parameters such as Hall parameter (m_a), Brinkman number (Br), flow behaviour index (q), Radiation parameter (N), magnetic field (M), arterial curvature etc., have been discussed graphically.

The study of electrokinetic energy conversion and entropy optimization power-law fluid through overlapped stenosed curved artery with the chemical reaction and Joule effect has been performed in chapter 6. The thermal properties of gold nanoparticles are added to the blood properties. The effects of gold nanoparticles' volume fraction and their different diameter size are also included in this chapter. The significance of various physical parameters such as nanoparticle volume fraction (m), their size (dp), magnetic field intensity (M), inverse Debye length ($\bar{\kappa}$), flow behaviour index (Sc), heat source (H) and chemical reaction parameter (ξ) on the blood flow velocity, temperature, concentration, EKEC efficiency, wall shear stress, nusselt number and entropy generation have been explained graphically.

In chapter 7, the analysis of two-phase MHD blood flow through overlapped stenosed curved artery with induced magnetic field and viscous dissipation has been done. The power-law fluid properties for core region blood flow is considered, while plasma region flow adopted the Newtonian fluid properties. The thermal properties of iron oxide (Fe_3O_4) nanoparticles are added to the blood properties. The influence of various parameters, such as Fe_3O_4 nanoparticle volume fraction (m), Brinkman number (Br), flow behaviour index (q), Heat Source (H), magnetic field (M), arterial curvature (ε) and magnetic Reynold number (Rm) etc., have been discussed graphically.

At the end of the whole work, we have summarized the main outcomes of the thesis along with the future scope of this thesis in the chapter 8.

Contents

List of Figures

List of Tables

List of Symbols

$'$	Represents non-dimensional quantities
^{nf}	Nanofluid
r'	Radial direction
z'	Axial direction
t'	Time
$R_1'(z',t')$	Radius of time-dependent stenosis in core region
$R(z',t')$	Radius of time-dependent stenosis in plasma region
R_0	Radius of the blood vessel without stenosis
L	Length of the blood vessel
d'	Location of stenosis
b	radius of curvature of curved artery
u_c', v_c', w_c'	velocities of core region in r', θ', z' directions, respectively
u_p', v_p', w_p'	velocities of plasma region in r', θ', z' directions, respectively
P_c', P_p'	Pressures in core and plasma region, respectively
T_c', T_p'	Temperature in core and plasma region, respectively
C_c', C_p'	Concentration in core and plasma region, respectively
Gr	Thermal Grashof number
Gm	Solute Grashof number
M	Magnetic field
N	Thermal radiation parameter
H	Heat source
h_m	Hematocrit level
K_c, K_p	Thermal conductivity in core and plasma region, respectively
$\bar{C}_c, \bar{C}_p$	Specific heat in core and plasma region, respectively
Re	Reynold number
Ec	Eckert number
Pr	Prandtl number
Br	Brinkman number

k_0	Thermal conductivity ratio
D_c, D_p	Mass diffusivity in core and plasma region, respectively
Sc	Schmidt number
Da	Darcy number (Permeability parameter)
Q	Volumetric flow rate
Nu	Nusselt number
E'_c, E'_p	Entropy generation in core and plasma region, respectively
$\bar{J}$	Electric current density
m_a	Hall parameter
$\bar{E}$	Electric field
e	Electron charge
K	Flow consistency
q	Flow behaviour index
m	Nanoparticle volume fraction
db, dp	Fluid and nanoparticle diameter, respectively
$\vec{B}_i$	Induced magnetic field
Rm	Magnetic Reynold number

Greeks letters

θ'	Angular direction
δ^*	Maximum height of stenosis
$\Omega(t')$	Time-varying parameter
β	ration of central core radius to normal artery radius
ω	Angular frequency of the forced oscillation
μ_c, μ_p	Viscosity in core and plasma region, respectively
ρ_c, ρ_p	Density in core and plasma region, respectively
γ_T, γ_c^*	Coefficient of thermal and solute expansion, respectively
ε	Arterial curvature
ξ	Chemical reaction parameter
λ	Frictional resistance (impedance)
τ_w	Wall shear stress
ρ_0	Density ratio
μ_0	Viscosity ratio
σ	Electrical conductivity of fluid
Ψ	Total electric potential
ψ_i, ψ_a	Induced and streaming potential
ρ_{el}	Net electric charge density

Ξ	Uniform dielectric constant
κ	Electro-kinetic width (inverse Debye length)
$\bar{\chi}$	EKEC efficiency
μ_e	Magnetic permeability

Physical Parameters

Values of parameters		
Parameters	Values	Resources
Magnetic field strenght (M)	0.1-6.0	[1, 2, 3]
Plasma viscosity (μ_p)	1.10-1.30 mPa	[4]
Viscosity ratio (μ_0)	0.5-1	[5, 6]
Radiation parameter (N)	0-15	[7]
Thermal conductivity ratio (k_0)	0.4-0.8	[6, 8]
Density ratio (ρ_0)	1.05	[9, 10]
Thermal Grashof number (Gr)	0.1-17	[11, 12]
Steady pressure gradient (P_0)	1-10	[13, 14, 15]
Curvature parameter (ε)	0-0.4	[16]
Hematocrit parameter (h_m)	0-1	[17]
Schmidth Number (Sc)	0.5-1.5	[13]
Heat source (H)	0-9	[18, 19, 20]
Chemical reaction parameter (ξ)	0.5-2	[13, 21]
Solute Grashof number (Gc)	1-6	[13, 12]
Brinkman number (Br)	0.1-3	[22, 23]
Hall parameter (m_a)	0-1	[24]
Flow behaviour index (q)	0.7-1.25	[25, 26]
Inverse Debye length ($\bar{\kappa}$)	1-10	[27, 28]
Magnetic Reynold number (Rm)	1-5	[29]

Table 1: Range of values of existing parameters with their resources

Chapter 1

Introduction

Biofluid mechanics is the study of fluid dynamics in biological systems, including the movement of fluids within the body and the interaction of fluids with biological tissues. This field of study is crucial to understanding the functioning of the human body, as well as the design of medical devices and treatments. It involves the application of principles of fluid mechanics to understand the behaviour of fluids in living organisms. Bio-mechanics has a wide range of applications in various fields, such as medicine, biology, and engineering. One of the essential applications of biofluid mechanics is in understanding the blood flow in the human body. Blood is a complex fluid that exhibits many flow behaviours, such as laminar, turbulent, and transitional. The study of blood flow in the human body is crucial in understanding various medical conditions such as cardiovascular diseases, stenosis, stroke, and aneurysms. By understanding the flow patterns of blood in the human body, doctors can identify areas of blockages and treat them accordingly. Another application of biofluid mechanics is in the study of respiratory mechanics. The air we breathe in is fluid, and breathing involves the flow of air through the respiratory system. Various fluid mechanics principles govern the flow of air in the respiratory system, and understanding these principles is essential in diagnosing and treating respiratory diseases such as asthma and chronic obstructive pulmonary disease (COPD).

One important tool used in the study of biofluid mechanics is computational fluid dynamics (CFD). CFD involves using mathematical models and computer simulations to study fluid flow. This approach allows researchers to investigate the behaviour of fluids in complex systems, such as the human body, and to test the effectiveness of different medical treatments and devices. Another important tool used in biofluid mechanics is medical imaging. Medical imaging techniques, such as MRI and CT scans allow researchers to visualize the internal structures of the body and to study the movement of fluids within these structures. This information can be used to develop more accurate models of fluid flow and to guide the design of medical treatments and devices.

Bio-fluid mechanics also plays a vital role in various fields, such as sports medicine, orthopaedics, and physical therapy. By understanding the mechanics of biological systems, researchers and doctors can develop new techniques and treatments to improve the quality of life of patients.

1.1 Cardiovascular System

The cardiovascular system is a complex network of organs, vessels, and tissues that work together to transport blood and nutrients throughout the body. The main work of the cardiovascular system under the pumping action is to provide highly oxygenated blood to the body's tissues and organs and then transport the oxygen-depleted blood for re-oxygenation to the lungs. This system is very important for keeping homeostasis and giving all of the body's cells the nutrients they need to work.

The heart is the central organ of the cardiovascular system. It is a muscular pump that is responsible for generating the force required to circulate blood throughout the body. The heart has four chambers, including the right atrium, right ventricle, left atrium, and left ventricle. The right atrium receives deoxygenated blood from the body and pumps it into the right ventricle. The right ventricle then pumps the blood to the lungs, where it is re-oxygenated. The oxygen-rich blood then returns to the left atrium, which pumps it into the left ventricle. The left ventricle is the most muscular chamber of the heart and is responsible for pumping the oxygen-rich blood throughout the body.

Blood is the primary fluid of the cardiovascular system that transports nutrients, proteins, hormones, and waste products throughout the body. Blood comprises four components: plasma, red blood cells (RBC), white blood cells (WBC), and platelets. Plasma contains the major volume (approximately 55%) of human blood. The major part of plasma is water (92 %), and the rest is protein, ions, electrolytes, hormones, blood cells, etc. The second main component of blood is RBC, which contains approximately 45 % of the blood volume, and RBC provides oxygen to the tissues and organs from the lungs. The ratio of red blood cells in the blood is known as hematocrit, and its quantity plays a vital role in blood viscosity. White blood cells are part of the body's immune system and help fight infections and diseases. Platelets are small cell fragments that are responsible for blood clotting.

The complete blood vessel network of the cardiovascular system is closed, and this vessel network is divided into three parts: arteries, veins, and capillaries. Arteries are the strongest and more elastic among all blood vessels. The primary function of arteries, except pulmonary arteries, is to transport oxygenated blood from the heart to the rest of the body's tissues and organs. Since the arteries are strong and flexible, it contribute to the stabilization

of blood pressure during the heart's pumping process. Conversely, veins carry deoxygenated blood back to the heart from the body's tissues and organs. The walls of veins are thinner than those of arteries, and they have valves that prevent blood from flowing backward. Capillaries are small, thin-walled vessels that connect arteries and veins. They are responsible for the exchange of nutrients, gases, and waste products between the blood and the body's tissues.

1.2 Blood Rheology

Blood rheology is the study of the flow properties of blood. It is an essential aspect of cardiovascular physiology and is crucial in maintaining adequate blood flow through the body's circulatory system. The main factors affecting blood rheology are blood viscosity, hematocrit level, shear stress, vessel diameter, etc. Therefore, blood nature according to vessel diameter, shear stress, and strain is expressed as follows:

1.2.1 Newtonain Fluid

In the continuum mechanics, a fluid is said to be Newtonian fluid if its flow relationship between shear stress and strain rate is linear. In other words, it can be said that if a fluid follows Newton's law of viscosity then it is called a Newtonian fluid.

$$\tau = \mu\left(\frac{\partial u}{\partial y}\right), \tag{1.1}$$

where τ is shear stress, μ is viscosity coefficient and $\frac{\partial u}{\partial y}$ is the strain rate (velocity gradient). The fluid shows Newtonian nature if τ becomes constant.
In the blood perspective, blood shows the Newtonian fluid properties if it flows through a larger diameter ($> 1mm$) blood vessels at the high shear rates ($\approx 100/sec$).
All the gases and most of the liquids such as water, mineral oil, alcohol, skim milk etc. are some of the classical examples of Newtonian fluid which used in humans everyday life.

1.2.2 Non-Newtonian fluid

Blood exhibits a non-Newtonian fluidic nature if it flows into smaller diametric blood vessels with low shear stress. A fluid is said to be a non-Newtonian fluid if it does not follow Newton's law of viscosity. In other words, it can be said that the viscosity constant is not constant. Some of the non-Newtonian fluid models used for blood are listed below-

1.2.2.1 Power-law fluid

The power-law fluid model is a time-independent fluid model to describe the non-linear relationship between shear stress and velocity gradient. The mathematical expression for power-law fluid is written as [25]-

$$\tau = K\left(\frac{\partial u}{\partial y}\right)^{q}, \tag{1.2}$$

or

$$\frac{\tau}{\frac{\partial u}{\partial y}} = K\left(\frac{\partial u}{\partial y}\right)^{q-1}.$$

Here K is flow consistency index and q represent the flow behavior index.

- If $q < 1$, fluid exhibit the pseudoplastic (shear thinning) fluidic nature, in which fluids apparent viscosity decreases with the increase in shear rate.
  Ketchup, blood, petroleum jelly, and lotions are the classical example of the pseudoplastic fluid.
- If $q = 1$, fluid becomes the Newtonian fluid.
- $q > 1$, fluid shows the Diltant (shear thickening) fluidic nature, in which fluids apparent viscosity rises at the higher stress rate. Mixture of cornstarch and water, concentrated clay suspension are the some diltant fluid examples.

1.2.2.2 Casson fluid

A shear thinning fluid model is developed by Casson [30], in which they assumed that fluid have infinite viscosity at zero shear rate, yield stress below which no flow occurs and a zero viscosity at an infinite rate of shear. The mathematical expression is defined as:

$$\begin{cases} \tau^{\frac{1}{2}} = \tau_y^{\frac{1}{2}} + \left[\mu\left(-\frac{\partial u}{\partial y}\right)\right]^{\frac{1}{2}}, & \text{if} \quad \tau > \tau_y, \\ \frac{\partial u}{\partial y} = 0, & \text{if} \quad \tau \leq \tau_y, \end{cases} \tag{1.3}$$

where, τ_y represents the yield-stress.

1.3 Toroidal Co-ordinate system

The toroidal coordinate system is a three-dimensional orthogonal coordinate system that is particularly useful in describing phenomena that exhibit toroidal symmetry. This coordinate

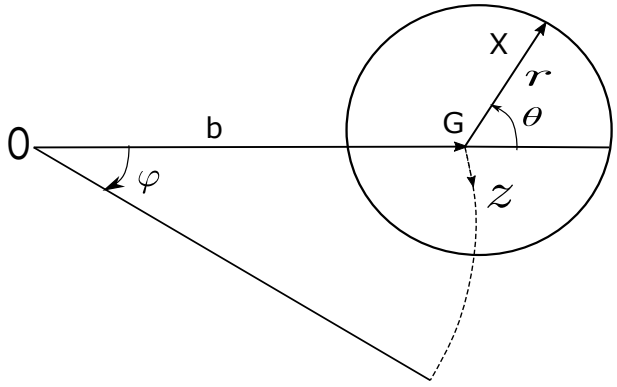

Figure 1.1: The coordinate system used for the flow in a curved tube.

system is often used in plasma physics, electromagnetics, and fluid dynamics.

Let (r,θ,z) be the toroidal system's coordinates, which are employed to investigate the flow behaviour in the figure (1.1). In given figure, G represents the center of tube cross section making an poloidal angle φ with the fixed axial plane and X as arbitrary point with polar coordinates (r,θ) . The radius of curved tube and axial coordinate are given through relation $OG = b$ and $z = b\varphi$ respectively. Where b is the radius of curvature of curved artery. The z-axis represents the axial direction, and r is taken along the radial direction.
The transformation of toroidal coordinate system into rectangular coordinate is follows as-
$x_1 = (b + r\cos\theta)\cos\varphi, \quad y_1 = (b + r\cos\theta)\cos\varphi, \quad z_1 = r\sin\theta.$

1.4 Governing Equations of Fluid dynamics

The fluid flow follows the laws of conservation of mass, momentum, energy and mass flux.

1.4.1 Conservation of Mass or Equation of Continuity

The law of conservation of mass is a fundamental principle stating that the total amount of mass in a closed system remains constant over time. This principle is mathematically expressed through the equation of continuity, which states that any increase in mass within a closed surface must be balanced by the amount of mass entering the surface minus the amount exiting it. The mathematical form of this law in vector notation is written as-

$$\frac{\partial \rho}{\partial t} + \nabla \cdot (\rho \vec{V}), \tag{1.4}$$

where, ρ denotes the fluid density, $\vec{V} = (u,v,w)$ is the velocity vector and ∇ is the vector differential operator.

1.4.2 Conservation of Momentum

Momentum is defined as the mass of an object multiplied by its velocity. The movement of fluids is directed by the Navier-Stokes equations of motion, which are derived from the fundamental principle of the second law of motion. This principle asserts that the momentum change rate in volume V is equal to the sum of body forces. The mathematical form of momentum equation in vector notation is written as-

$$\rho\left(\frac{\partial\vec{V}}{\partial t}+(\vec{V}\cdot\nabla)\vec{V}\right)=-\nabla p+\mu\nabla^2\vec{V}+\rho F, \tag{1.5}$$

where, ∇p is pressure gradient, F is the external force and ∇^2 is Laplacian operator.

1.4.3 Conservation of Energy

Energy conservation is a fundamental principle in physics that states that the total amount of energy in a closed system remains constant over time. In mechanical way, the law of conservation of energy states that the fluid's energy increasing rate in volume V is equal to the negative of the outward flux of the energy, plus the energy generated due to work done by the body and the surface forces, thermal conduction and heat sources such as chemical reaction, Joule heating, etc., if present. This means that energy can neither be created nor destroyed, but it can be transformed from one form to another. This principle has many applications in physics and engineering, including designing machines and engines and studying heat transfer and thermodynamics. By understanding and applying the principle of energy conservation, we can develop more efficient and sustainable technologies and help protect the environment for future generations. The mathematical formulation of law of energy conservation is written as-

$$\rho\bar{C}_p\left(\frac{\partial\vec{T}}{\partial t}+(\vec{V}\cdot\nabla)\vec{T}\right)=K_c\nabla^2T+\frac{\partial Q}{\partial t}, \tag{1.6}$$

where, T is the fluid temperature, $\bar{C}_p$ is the specific heat at constant volume, K_c is the fluid's thermal conductivity and Q is the external heating source or sink.

1.4.4 Conservation of Concentration species

When dealing with the conservation of mass or continuity in a fluid of varying density, it's important to consider that the fluid could potentially be a mixture of multiple fluids. To uphold the principle of mass conservation, it's necessary to apply this principle to each individual component within the mixture. It's also important to note that mass transfer refers to the overall movement of mass from one location to another. The mathematical

formulation of law of concentration conservation is written as-

$$\left(\frac{\partial \vec{C}}{\partial t} + (\vec{V} \cdot \nabla)\vec{C}\right) = Dp\nabla^2 C + Rc, \tag{1.7}$$

where $\vec{C}$ is the concentration of components in the mixture, Dp is the molecular diffusivity and Rc is the chemical reaction parameter.

1.5 Dimensionless parameters

Dimensionless parameters are numerical quantities that express the relationships between different physical variables in a system. A parameter is said to be a dimensionless parameter, if it does not have any dimension, it is just a quantity. Dimensionless parameters are typically ratios of physical quantities that have the same dimensions, and they are often used to characterize the behaviour of systems that are governed by similar physical principles. These parameters are important in many areas of physics, biology, finance and engineering, as they allow us to analyze the behaviour of complex systems without the need for detailed knowledge of all the individual components. We will briefly discuss about some of dimensionless parameter here-

1.5.1 Reynold Number (Re)

The Reynold number has much powerful significance in the field of mechanics. The Reynold number is used to describe the behaviour of fluids in motion, whether it is laminar or turbulent. In biology, the Reynold number is used to describe the swimming behaviour of microorganisms. Reynold number is also used to predict the transition state of fluid from laminar to turbulent. The Reynold number is defined as the ratio of inertial forces to viscous forces in a fluid, and it is used to predict the onset of turbulence in fluid flow. Mathematically, Reynold number is represented as-

$$Re = \frac{\text{inertial force}}{\text{viscous force}} = \frac{\rho v d}{\mu}, \tag{1.8}$$

where, v is fluid velocity, d characteristic linear dimension.

1.5.2 Schmidt Number (Sc)

Schmidt number is used to distinguish the dominance between momentum and mass diffusion. Schmidt number is the ratio of momentum diffusivity with mass diffusivity. It was

named after German engineer Ernst Heinrich Wilhelm Schmidt and it used in the concentration equation. The formula of Schmidt number is-

$$Sc = \frac{\text{viscous diffusion rate}}{\text{mass diffusion rate}} = \frac{\nu}{Dp} = \frac{\mu}{\rho Dp}, \tag{1.9}$$

where Dp is mass diffusivity and ν is kinematic viscosity.

1.5.3 Brinkman number (Br)

Brinkman number (Br) estimation is a critical phenomenon in bio-fluid mechanics because, with the help of this, figuring out how much heat is conducted from the artery becomes very easy. Brinkaman number is the ratio between heat produced by viscous dissipation and heat transported by molecular conduction. It is defined as-

$$Br = \frac{\mu v^2}{K_c(T_w - T_0)}, \tag{1.10}$$

where K_c is the fluid thermal conductivity, T_w is the wall temperature and T_0 is the bulk temperature.

1.5.4 Grashof number

In the fluid-mechanics, Grashof number is a dimensionless number which is used to describe the ratio between buoyancy force to viscous force. The estimation of a Grashof number is made when natural convection situation for a fluid flow is assumed.

Thermal Grashof number (Gr)

Thermal Grashof number is used when free convection is caused by a change in the density of a fluid due to a temperature gradient, and given by

$$Gr = \frac{g\gamma_T L^3(T_w - T_0)}{\nu^3}, \tag{1.11}$$

Solute Grashof number (Gm)

Solute Grashof number is used when free convection is caused by a change in the density of a fluid due to a concentration gradient, and given by

$$Gm = \frac{g\gamma_c^* L^3(C_w - C_0)}{\nu^3}, \tag{1.12}$$

where, g is gravitational acceleration, γ_T and γ_c^* is coefficient of thermal and solute expansions, respectively. C_w is the concentration at wall.

1.5.5 Nusselt number (Heat transfer coefficient)

A Nusselt number is a dimensionless number that represents the ratio of convective to conductive heat transfer across a surface. The Nusselt number is an important parameter in bio-fluid mechanics because it determines the rate of heat transfer between the fluid and a solid surface. In many biological systems, such as blood vessels or lungs, the transfer of heat is critical for maintaining proper function. For example, in the lungs, the transfer of heat is necessary to warm and humidify incoming air, which helps prevent damage to the delicate lung tissue. It is formulated as-

$$Nu = \frac{\text{Convective heat transfer}}{\text{Conductive heat transfer}} = \frac{h}{K_c/L} = \frac{hL}{K_c}, \tag{1.13}$$

where, h convective heat transfer coefficient.

1.5.6 Sherwood number (Mass transfer coefficient)

The Sherwood number is defined as the ratio of the mass transfer coefficient to the diffusion coefficient, multiplied by a characteristic length scale. The Sherwood number is a dimensionless parameter used to describe the mass transfer between a fluid and a solid surface. It is an important parameter in bio-fluid mechanics, as it can be used to study the transport of nutrients and other substances across biological membranes.It is formulated as-

$$Sh = \frac{\text{Convective mass transfer rate}}{\text{Diffusion rate}} = \frac{h}{Dp/L} = \frac{hL}{Dp}, \tag{1.14}$$

where h is convective mass transfer coefficient and Dp is mass diffusivity.

1.6 Pathological Conditions

1.6.1 Stenosis

In the cardiovascular system, stenosis is a medical situation that is related to the abnormal narrowing of a blood vessel or any other tubular structure in the body. The human body faces this situation due to the accumulation of plaque, scar tissue, or other debris inside the vessel wall that obstructs blood flow or other fluids through the affected area. Any area of the body might experience blood vessel constriction, although the heart, neck, and leg arteries are the most frequently affected. The symptoms of stenosis depend on the location and severity of the narrowing. If stenosis occurs in the heart's arteries, then it becomes the most serious and deadly situation for humans. Most of the time, chest pain, angina, and heart attacks happen

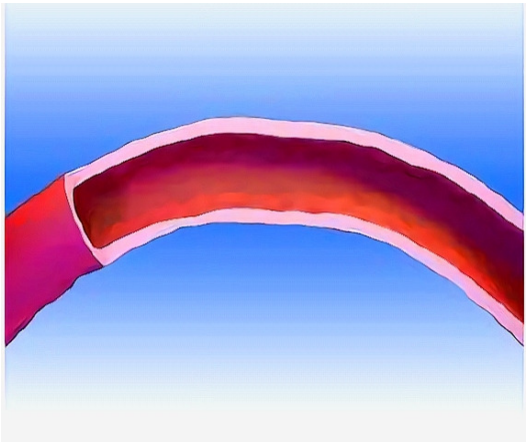

Figure 1.2: Healthy curved artery

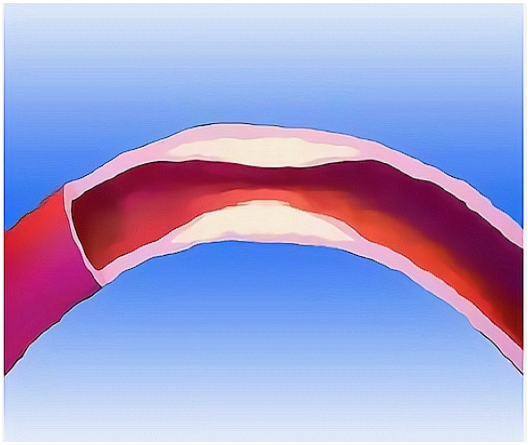

Figure 1.3: Stenosed curved artery

when stenosis builds up in the heart's arteries. If it occurs in the neck arteries, it can cause dizziness, headaches, and stroke-like symptoms. Stenosis in the legs can make you hurt or cramp when you move around. This is called claudication.
Stenosis can be diagnosed through a variety of tests, including physical examination, imaging studies, and blood tests. Physical examination can reveal signs of reduced blood flow, such as weak or absent pulses in the affected area. Imaging studies, such as ultrasound, MRI, or CT scans, can provide detailed pictures of the narrowed area, allowing doctors to determine the severity and location of the stenosis. Blood tests can also help to diagnose stenosis by measuring the levels of certain enzymes and proteins that are associated with reduced blood flow. Treatment for stenosis depends on the severity of the condition and the location of the narrowing. In some cases, lifestyle changes such as diet and exercise can help to reduce the buildup of plaque in the arteries and prevent further narrowing. Medications such as aspirin, beta-blockers, or cholesterol-lowering drugs may also be prescribed to reduce the risk of heart attacks and other complications. In more severe cases, surgical procedures such as angioplasty or stent placement may be necessary to open up the narrowed area and restore blood flow. The figure 1.2-1.3, differentiate the real healthy and stenosed curved artery.

Young [31, 32] developed a mathematical model to observe the effect of time-dependent stenosis on the blood flow through the tube and suggested that stenosis is the reason for the major problem in the cardiovascular system. An analytical study of blood flow through the stenosed curved artery using a toroidal coordinate system is completed by [33]. They used the perturbation technique to the observed combined effect of curvature and stenosis on the flow velocity. Further, this study is carried forward by [34] to deliberate the application of catheter in the stenosed curved tube. He used the numerical technique and reported that the pressure gradient and frictional resistance rise for high curvature.

1.6.2 Variable viscosity of Blood flow

In the human circulatory system, blood flow can be affected by pressure, blood viscosity and flow velocity. The flowing ability of blood in vessels is mainly measured by its viscosity and how fast it flows in vessels. The viscosity of blood is determined by the concentration of red blood cells, plasma proteins, temperature and other cellular components in the blood. When blood viscosity is high, it can increase the risk of cardiovascular disease and other health complications. Therefore considering constant blood viscosity in any investigation does not predict the actual behaviour of blood flow.

The blood viscosity is significant affected by red bolood cells (RBC) due to presence of hemoglobin protein in it. The hemoglobin have ability to bind oxygen. As RBCs travel through blood vessels, they can become stacked together, forming structures called rouleaux. The effect of RBC on the blood viscosity is computed in terms of hematocrit level and its mathematically form is defined as [17]-

$$\mu(r) = \mu_0(1+\beta_1 h(r)), \tag{1.15}$$

where

$$h(r) = h_m\left[1-\left(\frac{r}{R_0}\right)^{m_1}\right],$$

Here h_m represent the maximum hematocrit level at arterial center, m_1 is the parameter that determine exact shape of velocity profile, β_1 is constant. R_0 is the radius of the artery.

Blood viscosity is also influenced by the flow temperature, and blood viscosity tends to decrease as temperature increases, which can make it easier for blood to flow through blood vessels. There are so many linear and non-linear temperature-dependent viscosity models that have been taken to analyse blood flow behaviour. Some viscosity models are defined as-

Linear temperature-dependent viscosity model [35]-

$$\mu(T) = \mu_0\left[1+\lambda_1\left(\frac{T-T_0}{T_w-T_0}\right)\right], \tag{1.16}$$

Exponential temperature-dependent viscosity model [36]-

$$\mu(T) = \mu_0 \exp\left[\lambda_1\left(\frac{1}{2}-\frac{T-T_0}{T_w-T_0}\right)\right], \tag{1.17}$$

where T, T_w are fluid and arterial wall temperature, λ_1 is the variable viscosity parameter.

Plasma proteins, such as fibrinogen and albumin, also play a role in blood viscosity. Fibrinogen is a protein that helps blood clot, and it can increase blood viscosity when it is

present in high concentrations. Albumin is a protein that helps maintain fluid balance in the body, and it can decrease blood viscosity when it is present in high concentrations.

1.6.3 Magnetic field effect

In the last few decades, the study of the magnetic field effect in biological fluids has attracted the attention of researchers as the human body experience different intensities of the magnetic field in their day-to-day life. The magnetic field has been utilized to manipulate and control the motion and behaviour of biofluids such as blood and other fluids within the human body. The presence of a high concentration quantity of haemoglobin in red blood cells (RBC), intercellular protein and cell membrane allows the blood flow to function like a bio-magnetic fluid. The magnetic field has so many applications in the medical field, and it is used in various medical treatments and therapies.

The magnetic field plays an essential role in targeting drug delivery. In this treatment, magnetic nanoparticles are used as a drug and injected into blood; therefore, these nanoparticles can reach the disease area. This approach has proved to be very effective in treating diseases such as cancer and other chronic conditions. Magnetic resonance imaging (MRI) is also the best example that uses the magnetic field concept. The MRI is a non-invasive diagnostic technique that is used to identify the actual position of diseases. The use of MRI has established itself as a crucial tool for the diagnosis and management of multiple medical disorders. Also, magnetic fields are used in tissue engineering to manipulate and control the behaviour of cells and 3D printing of cells and tissue.

Firstly, Issacci et al. [37], numerically discussed the induced magnetic field concept in the curved pipe by considering a toroidal coordinate system. They found the solution in the power series form for both low and intermediate Hartmaan numbers and explained that with enhancing magnetic field intensity, the fluid compression improves near the tube wall in velocity contours. The magnetic field effect on the 90° horizontal bend vessel is analyzed numerically by Akar et al.[38]. They reported that wall shear stress and static pressure were significantly enhanced near the vessel wall in the magnetic field's presence and also found that deoxygenated blood is more influenced than that of oxygenated blood.

1.6.4 Hall effect

The Hall effect is a physical phenomenon in which an electrical current flowing through a conductor is influenced by an external magnetic field. This effect is named after Edwin Hall, who first observed it in 1879. In biofluids, the Hall effect can have important applications, particularly in the measurement of blood flow. If an external magnetic field is applied to a

charged conductor in the perpendicular direction, then this conductor generates an electric field in the normal direction to the applied magnetic field and current. This generated electric field is called the Hall voltage.

In biofluids, the Hall effect can be used to measure blood flow velocity. This is done using a technique called magnetic resonance imaging (MRI). In MRI, a strong magnetic field is applied to the body, causing the hydrogen atoms in the body's tissues to align themselves in a particular direction. When a radio wave is applied to the body, the hydrogen atoms absorb the energy and then emit it back as a radio signal. By measuring the radio signal, a detailed image of the body's tissues can be obtained. To measure blood flow using MRI, a contrast agent is injected into the bloodstream. This contrast agent contains tiny iron particles that become magnetized when they enter the magnetic field. As the blood flows through the body, magnetized particles are carried along with it. By measuring the Hall voltage generated by the movement of the magnetized particles, the velocity and direction of the blood flow can be determined.

The use of the Hall effect in blood flow measurement has important applications in medicine. For example, it can be used to diagnose cardiovascular diseases such as atherosclerosis, which is characterized by a buildup of plaque in the arteries that can restrict blood flow. By measuring blood flow in the affected area, doctors can determine the severity of the disease and develop appropriate treatment strategies. Datta et al.[39] examined the impact of the Hall effect on flat plate flow in the presence of an oscillating magnetic field. According to this study, enhancing the Hall parameter results in a rise in the oscillation in the shear stress profile, whereas the resonance frequency of the boundary layer declines. Szwast and Pitatkiewicz [40] performed experimental research to determine the Hall effect on blood electrolytic properties. The outcome of this research states that Hall current is independent of electrolytic concentration, but its current measurement can be utilized to develop sensors. These sensors can predict the flow velocity and its behaviour during the blood pump.

1.6.5 Heat Source

Heat sources can significantly impact biofluids, which are fluids found within living organisms, such as blood or lymph. These heat sources can include external factors, such as environmental temperature, or internal factors, such as metabolic processes within the body. The effect of heat sources on biofluids can be seen through changes in their physical and chemical properties. One of the most significant changes that occur is an increase in temperature. Heat sources can raise the temperature of biofluids, which can impact their viscosity, density, and thermal conductivity.

When biofluids are exposed to heat sources, their viscosity decreases, making them more

fluid and easier to flow. This decrease in viscosity can have important implications for blood flow, as it can impact the ability of the blood to circulate efficiently through the body. The effect of heat sources on biofluids can also be seen at the molecular level. When biofluids are heated, the molecules within them become more energetic, leading to increased molecular motion. This can impact the chemical reactions that occur within biofluids, leading to changes in their composition and properties. In this regrad, Kot and Elmaboud [41] performed a numerical study to demonstrate the effect of the heat source in the vertical annulus pipe and state that the heat transfer rate at the wall significantly rises with the positive addition in the value of the heat source. In this study, they also adopted the cylindrical shape catheter and suggested that maintaining the catheter radius ratio is important for both flow velocity and temperature.

1.6.6 Thermal Radiation

Thermal radiation is the transmission of heat energy via electromagnetic waves from one source to another. In the medical field, thermal radiation has various applications, including therapeutic and diagnostic purposes. Thermal radiation is used in the treatment of certain types of cancer. One method of treatment is known as hyperthermia, which involves heating the tumor tissue to temperatures between 40 and 45 degrees Celsius. The heat causes the cancer cells to become more sensitive to radiation and chemotherapy, making these treatments more effective. Hyperthermia is often used in combination with other treatments for cancer and stenosis.

Another application of thermal radiation in the medical field is in the use of infrared imaging. Infrared imaging is a non-invasive diagnostic tool that uses thermal radiation to detect and measure changes in temperature in different parts of the body. This technology is particularly useful in identifying areas of inflammation or infection that may not be visible on the surface of the skin. Infrared imaging is commonly used in the diagnosis of musculoskeletal injuries, such as sprains and strains, and is also used to monitor the progression of conditions such as arthritis. Mishra et al.[42] performed a numerical study on the arterial blood flow to analyze the impact of electromagnetic hyperthermia treatment on cancer cells. In this study, they used the finite difference approach to solve the governing equation. Further, this study carries forward by [43] for the stretching permeable capillaries to numerically visualize the effect of radiation parameter. This study shows that the thickness of the thermal boundary layer grows with the value of the radiation parameter.

1.6.7 Two-phase Blood flow

The characteristics of blood flow are multifaceted. One fundamental aspect is the volume of erythrocytes or hematocrit level. Extensive in vivo and in vitro analyses have revealed a range of rheological properties associated with blood flow, which include:

- **Fåhræus effect -** This effect describes the hematocrit level in the vessel and states that RBC concentration becomes low as the diameter of the blood vessel decreases. Moreover, it can be said that blood vessel with less than 500 μm diameter has fewer red blood cell volume concentration than the other blood components.

- **Fåhræus Lindvuist effect -** This effect is commented on the flow viscosity when blood flows into a smaller-sized vessel. According to this effect, blood flow viscosity and hematocrit level decrease with the decay in blood vessel diameter.

Haynes [44] presents a theory on blood viscosity in a small-diameter blood vessel and provides information about blood's two-phase nature. This study explained that the red blood cells are aggregated towards the arterial centre and found a cell-free zone near the arterial wall, known as the plasma region. To investigate the significant impact of peripheral layer viscosity on the blood velocity passes through the stenosed artery, Shukla et al. [45] developed a two-layer mathematical model. In this study, they consider blood as a Newtonian fluid in both (core and plasma) region and pointed out that resistance and wall shear stress of the flow diminishes as plasma viscosity decreases.

1.6.8 Entropy Generation

Entropy generation is a fundamental concept in thermodynamics that describes the amount of energy that is wasted or lost during a thermodynamic process. In an isolated system, fluid friction, molecular vibration, heat and mass flux, joule heating and thermal radiation are the leading cause of irreversibility. Bio-fluid dynamics involves the study of the movement of fluids in biological systems. This includes the flow of blood in the circulatory system, the flow of air in the respiratory system, and the movement of other bodily fluids such as lymph and interstitial fluid. In order to understand the efficiency of these systems, it is important to consider the amount of entropy that is generated during fluid flow.

In the atherosclerosis deposition condition, entropy analysis is very important to quantify the inefficiency of blood flow. By measuring the amount of entropy generated during blood flow through a diseased artery, researchers can gain insight into the efficiency of the circulatory system and develop strategies for improving blood flow in patients with

atherosclerosis. Entropy generation analysis is also important in gases exchange process between body and environment. This entropy estimation provides respiratory system situation by knowing efficiency of this gases exchange process. Bejan [46] developed a new method (finite-size device and finite-time processes) to minimize the entropy generation. He applied this approach to thermal optimization in various thermal engineering fields, including storage systems, solar power plants, refrigerators, fossil power plants, and so on. Rashidi et al. [47] numerically investigated the entropy generation of Magnetohydrodynamics (MHD) peristaltic flow through porous media. Ranjit et al.[48] addressed the entropy generation in the electroosmotic flow through the microfluidic channel subject to Joule heating. Mathematically expression for entropy generation is written as below-

$$E^{gen} = \underbrace{\frac{K_c(\nabla T)^2}{T_w^2}}_{\text{Thermal irreversibility}} + \underbrace{\frac{\mu}{T_w}F}_{\text{Fluid friction irrversibility}} + \underbrace{\frac{\sigma B^2}{T_w}v^2}_{\text{Joule heating irrversibility}} + \underbrace{\frac{Dp(\nabla C)^2}{C_w}}_{\text{solute irrversibility}}, \tag{1.18}$$

where, B is magnetic field, F is the viscous dissipation, T_w and C_w are the temperature and concentration of fluid at the wall.

1.6.9 Nanofluid

Nanotechnology refers to studying materials and devices at the nanometer scale, typically between 1 and 100 nanometers. It is a rapidly growing field with many potential applications, including in the medical field. Wilczewska et al. [49] state that due to their small dimension size, nanoparticles reflect their unique biological property to penetrate the tissue and cell membranes, which helps in the direct interaction of nanoparticles with the proteins and smaller cells.

The most common use of nanoparticles in the medical field is targeted drug delivery. With traditional drug delivery methods, medications are delivered to the body through pills, injections, or intravenous drips. This can lead to the medication being distributed throughout the body, potentially causing side effects and reducing the effectiveness of the treatment. With nanotechnology, medications can be designed to be delivered directly to the target cells or tissues, improving efficacy and reducing the risk of side effects. Nanotechnology-based imaging techniques, such as quantum dots or magnetic nanoparticles, can provide higher resolution and sensitivity, allowing for earlier detection of diseases.

The mostly nanoparticles are hyper-thermal than the blood, therefore when nanoparticles added into blood, it increases the blood thermal properties. Also, nanoparticles increase the temperature of base fluid when they are mixed with it. The mathematical formulation of

nanofluid thermal properties are written as [50]-

$$\begin{cases} \mu^{nf} = \frac{\mu^b}{(1-m)^{2.5}}, \\ \frac{K_c^{nf}}{K_c^b} = \frac{K_c^p+(m-1)K_c^b-(m-1)m(K_c^b-K_c^p)}{K_c^p+(m-1)K_c^b+m(K_c^b-K_c^p)}, \\ \frac{\rho^{nf}}{\rho^b} = (1-m)+m\left(\frac{\rho^p}{\rho^b}\right), \\ \frac{\sigma^{nf}}{\sigma^b} = \frac{\sigma^p+(m-1)\sigma^b-(m-1)m(\sigma^b-\sigma^p)}{\sigma^p+(m-1)\sigma^b+m(\sigma^b-\sigma^p)}, \\ \frac{Dp^{nf}}{Dp^b} = \frac{1-m}{1+m/2}. \end{cases} \tag{1.19}$$

where m is the nanoparticle volume fraction into base fluid.
$\mu^{nf}, K_c^{nf}, \rho^{nf}, \sigma^{nf}, Dp^{nf}$ are the nanofluid's viscosity, thermal conductivity, density, electrical conductivity and molecular diffusivity, respectively.
where $\mu^b, K_c^b, \rho^b, \sigma^b, Dp^b$ are the base fluid (blood) viscosity, thermal conductivity, density, electrical conductivity and molecular diffusivity, respectively.
where K_c^p, ρ^p, σ^p are the nanoparticles thermal conductivity, density, and electrical conductivity, respectively.
Some of the author's also studied the nanoparticle size effect on the flow. The mathematical formulation of these model is given by [51]-

$$\frac{K_c^{nf}}{K_c^b} = 1+4.4Re_p^{0.4}Pr^{0.66}\left(\frac{T_b}{T_{fr}}\right)^{10}\left(\frac{K_c^p}{K_c^b}\right)^{.03}m^{0.66}, \tag{1.20}$$

$$\frac{\mu^{nf}}{\mu^b} = \frac{1}{1-34.87\left(\frac{dp}{db}\right)^{-0.3}m^{1.03}}, \tag{1.21}$$

where,

$$Re_p = \frac{2\rho^b\bar{k}_bT_b}{\pi(\mu^b)^2d_p},$$

$$db = 0.1\frac{6M_a}{N_a\pi\rho^b}.$$

T_b, db denotes the blood temperature and blood cells diameter, respectively.
Re_p is the particle Reynold number, T_{fr} blood freezing temperature, dp is nanoparticle diameter.
$\bar{k}_b$ is Boltzmann constant (1.38064×10^{-23})
M_a is molecular weight of base fluid (Blood)
N is Avogadro number

1.7 Methodology

The fluid flow through curved arteries follows the law of conservation of mass, momentum, energy and concentration. The governing equations of blood flow through curved arteries are the system of coupled linear or non-linear partial differential equations (PDEs). Since the system of these governing equations in curved arteries are so complicated and finding its analytical solution is not possible in every fluidic condition. Therefore, the solution of these coupled PDE systems is obtained using semi-analytical and numerical approaches. In this thesis, we mostly used numerical schemes instead of the semi-analytical (perturbation) method because governing equations in the toroidal coordinate system are highly complicated. Therefore, sometimes perturbation technique is difficult and time-consuming to find governing equation solutions under assuming some flow conditions. A brief introduction of the used solution method is given below-

1.7.1 Perturbation Theory

Perturbation technique is a mathematical tool used to solve problems in which an analytical solution is difficult or impossible to obtain. It involves introducing a small parameter into a system of equations, which allows for an approximate solution to be obtained through a series expansion. To apply the perturbation technique to quantum mechanics, a small parameter is introduced into the system of equations. This parameter represents a small deviation from the idealized behavior of the particles, such as a small change in the potential energy or the shape of the particle. By expanding the solution in a power series in this parameter, an approximate solution can be obtained. This technique is used in many fields of science and engineering, including physics, chemistry, and biology. In the perspective of flow through curved arteries by considering toroidal coordinate system, the perturbation technique about $\varepsilon\cos\theta$ in power series is written as follow [16]-

$$v(r,\theta,z) = v_0(r,z) + \varepsilon\cos\theta v_1(r,z) + (\varepsilon\cos\theta)^2 v_2(r,z) + ..., \tag{1.22}$$

where v_0, v_1, v_2 are the zeroth, first and second order solution of velocity, respectively. ε is the arterial curvature parameter and r, θ and z are the toroidal system's coordinate, which represents the radial, angular and axial directions, respectively.

1.7.2 Finite difference method

The finite difference method (FDM) is very oldest and simplest numerical technique for solving differential equations. It involves approximating the derivative of a function using

finite differences. The concept of finite differences is based on the idea that the derivative of a function can be approximated by the slope of a tangent line. Due to easy in use, finite difference method is commonly used in various fields, including engineering, physics, and economics. The spatial domain and time interval (if applicable) are finitely discritized into grid/nodal points. Distance between each grid points are called step size. The total number of grid points are varies with the step size and length of spatial domain. The approimation of derivatives are performed using Taylor's series expansion. The Taylor series expansion of $v_{i+1,j}$, where $v_{i,j}$ known at (i,j) point is written as follows-

$$v_{i+1,j} = v_{i,j} + \left(\frac{\partial v}{\partial x}\right)_{i,j} \Delta x + \left(\frac{\partial^2 v}{\partial x^2}\right)_{i,j} \frac{(\Delta x)^2}{2!} + \left(\frac{\partial^3 v}{\partial x^3}\right)_{i,j} \frac{(\Delta x)^3}{3!} + \cdots, \tag{1.23}$$

where, Δx is the step-size in x-direction.
From above equation 1.23, the first derivative at (i,j) can be obtained as-

$$\left(\frac{\partial v}{\partial x}\right)_{i,j} = \frac{v_{i+1,j} - v_{i,j}}{\Delta x} - \left(\frac{\partial^2 v}{\partial x^2}\right)_{i,j} \frac{(\Delta x)^2}{2!} - \left(\frac{\partial^3 v}{\partial x^3}\right)_{i,j} \frac{(\Delta x)^3}{3!} - \cdots, \tag{1.24}$$

and

$$\left(\frac{\partial v}{\partial x}\right)_{i,j} \approx \frac{v_{i+1,j} - v_{i,j}}{\Delta x}, \tag{1.25}$$

Equation 1.25 is called first-order accurate with Taylor series, and remaining terms in 1.24 are the truncation error.
The first-order derivative also can be written in following form:

$$\left(\frac{\partial v}{\partial x}\right)_{i,j} = \begin{cases} \frac{v_{i+1,j} - v_{i,j}}{\Delta x} + O(\Delta x) & \text{Forward Difference} \\ \frac{v_{i,j} - v_{i-1,j}}{\Delta x} + O(\Delta x) & \text{Backward Difference} \\ \frac{v_{i+1,j} - v_{i-1,j}}{2\Delta x} + O(\Delta x)^2 & \text{Central Difference,} \end{cases} \tag{1.26}$$

The second-order derivative $\left(\frac{\partial^2 v}{\partial x^2}\right)_{i,j}$ also can be approximated using Taylor series expansion and it is written as-

$$\left(\frac{\partial^2 v}{\partial x^2}\right)_{i,j} = \frac{v_{i+1,j} - 2v_{i,j} + v_{i-1,j}}{(\Delta x)^2} + O(\Delta x)^2. \tag{1.27}$$

Equation 1.27 is the second-order accurate with Taylor series. In the similar manner, higher order derivative can be obtained using Taylor series expansion.
In order to use FDM method, the derivative terms in differential equation can be appromiated in the difference form and generate the system of algebraic equations. If the system of these

algebraic equations are linear, then they formed a matrix and can be solved using iterative techniques such as LU-decomposition, Guass Jacobi and Guass Seidel etc. If the system of algebraic equations are non-linear, then solution of these equations can be find using root-finding technique such as Newton -Raphson method.

1.7.3 Stones Strongly Implicit Technique

Stone's strongly implicit technique is used for multidimensional PDE, and this technique was proposed by Stone [52] in 1968. This implicit scheme is used for solving banded systems arising due to the discretization process of multidimensional PDE. Let us understand the Stones scheme by a example of 2D PDE.

$$\frac{\partial^2 v}{\partial x^2} + \frac{\partial^2 v}{\partial y^2} = -A, \tag{1.28}$$

Now, discretized above equation by central difference formula

$$\frac{v_{i+1,j} - 2v_{i,j} + v_{i-1,j}}{(\Delta x)^2} + \frac{v_{i,j+1} - 2v_{i,j} + v_{i,j-1}}{(\Delta y)^2} = -A_{i,j}, \tag{1.29}$$

where Δx and Δy is the step size in x and y directions respectively. L_1 and L_2 are the total number of grid points in x and y directions, respectively. Here $\Delta x = \frac{X}{(L_1-1)}$ and $\Delta y = \frac{Y}{L_2-1}$. A unique global nodal index k will be assigned for every mesh point.

$$k = (j-1) * L_1 + i,$$

Further equation 1.29 will be re-frame using nodal point k

$$\frac{v_{k+1} - 2v_k + v_{k-1}}{(\Delta x)^2} + \frac{v_{k+L_1} - 2v_k + v_{k-L_1}}{(\Delta y)^2} = -A_k. \tag{1.30}$$

After assigning nodal point to every mesh point, it form a system of algebraic equation and then system will be solved using LU-Decomposition method.

1.8 Gaps in Existing Research

As per the literature mentioned earlier and many more research articles, it is well known that plaque deposition (stenosis) is a major reason for cardiovascular diseases (CVD) such as heart attack, angina or stroke. These cardiovascular diseases sometimes become more serious, and the patient leaves their life. Therefore, in this thesis work, we developed some

mathematical models for curved arterial flow to analyse blood flow rheology under some physical parameters presence assumptions flow such as magnetic field, thermal radiation, nanoparticle, Joule heating, Hall parameter, and heat source etc. It is observed that the following aspects of blood flow have not been studied earlier:

1. Less attention has been given on blood flow through stenosed curved artery with variable viscosity.
2. Two-phase model for blood flow through the curved artery with stenosis has not been covered so much.
3. Two-phase model for blood flow through curved artery with varying viscosity (Hematocrit & Temperature dependent) has not been covered yet.
4. Two-phase model for blood flow through curved artery with Nano-particle has been ignored in most of the studies.
5. In most of the studies, only heat transport covered and less attention has been given on mass transport.
6. In most of the studies for curved artery only different types of nano-particles has been considered but the effect of the size of nano-particles has not been covered.

1.9 Thesis Organization

In thesis, we proposed and analyzed the dynamics of blood flow in diseased curved arteries with the help of mathematical modeling. In the thesis effect of physical various parameters such as magnetic field, thermal radiation, heat source, viscosity variation aspects, Hall effect, nanoparticles etc., has been investigated step by step. The obtained results of this thesis is widely useful in the cleaning healing of various diseases such as cancer, stenosis and blood flow prediction. Following this introductory part, the thesis is organized as follows:
Chapter 1 includes the brief introduction of bio-fluid mechanics and physical parameter. This chapter also includes the gap in existing research and used methodology description. In **Chapter 2**, we developed the mathematical MHD blood flow model in a two-phase stenosed curved artery with heat transfer using a toroidal coordinate system. The blood viscosity for both core and plasma regions is considered variable. In the core region, hematocrit-dependent while temperature-dependent viscosity for the plasma region has been considered. In **Chapter 3**, we extended the work and the effects of both heat and mass transfer on blood flow have been extended with permeable arterial wall condition. In this chapter,

core region viscosity is temperature-dependent, while plasma region viscosity is constant. **Chapter 4** discussed the entropy generation concept for the two-phase blood flow under Joule heating, viscous dissipation and external heat source effects. **Chapter 5** is extended the previous work by considering non-Newtonian fluid (Power-law fluid) properties for the core-region flow. The effects of thermal radiation and Hall parameter have been considered for heat transfer and blood entropy generation. In **Chapter 6**, we studied electrokinetic energy conversion and entropy generation analysis for blood flow with gold nanoparticle properties. The effect of nanoparticle size is also observed in the heat and mass transfer phenomena. In **Chapter 7**, entropy generation analysis for two-phase power-law blood flow through a curved overlapping stenosed artery with an induced magnetic field has been analyzed. The effect of iron oxide nanoparticles on heat transport under the presence of a cylindrical shape catheter is also studied. Finally, the main outcomes and future scope of the thesis are summarized in **Chapter 8**.

Chapter 2

Mathematical analysis of two-phase blood flow through a stenosed curved artery with hematocrit and temperature-dependent viscosity [1]

2.1 Introduction

The investigation of fluid flow through curved tubes is a motivating topic for researchers and has broad applications in industrial, chemical engineering and medical science. In the bio-medical field, assuming an artery as curved is a realistic situation rather than considering it circular. The prediction of fluid behaviour in the curved tubes is challenging due to the curvature, which generates centrifugal and pressure forces. To observe the flow etiquette in the curved tubes, Dean [53, 54] developed a mathematical model by assuming the pipe's curvature is small. Further, this study has been extended by Berger et al.[55] for the unsteady flow in curved pipes. In this work, they observed the nature of flow velocity for both Newtonian and non-Newtonian fluids.

In the human circulatory system, blood flow can be affected by pressure, blood viscosity, and flow velocity. Also, in the lubricating fluid system, fluid viscosity is influenced by heat generation due to inner friction, and thus considering constant viscosity is not appropriate. Firstly, variation in blood viscosity under normothermic and hypothermic conditions was examined by Rand et al. [56]. In this, they analyzed the relation between blood viscosity and hematocrit for different temperatures. Snyder et al.[57] did an experimental study to observed the influence of temperature and hematocrit on blood viscosity. For this study, they select a lizard because lizard have the efficiency to encounter temperature fluctuation. Further, under various conditions, some researchers [58, 59] extended this study and reported that blood viscosity shows the enhancing profile with increment in hematocrit and reflects

[1] A considerable part of this chapter is published in *Physica Scripta*, 96(12), 125277, 2021.

the reverse effect with temperature. The experimental work done by Cinar et al. [60] depicted the importance of temperature and hyperglycemia on blood pressure and viscosity. They found that the temperature highly influences plasma viscosity in comparison to core region viscosity. The experimental study to determine the combined effect of hematocrit, volume expander, and temperature on the blood viscosity under the hypothermic condition for cardiac operations was accomplished by Eckmann et al.[61]. Mekheimer and Elmaboud [62] presented a mathematical model of variable viscosity, and thermal conductivity for peristaltic flow passes through the vertical asymmetric channel. Tanveer et al.[63] discussed the variable viscosity effect on the Sisko fluid flow through curved channels. All the above works are done only for the single-phase blood flow. Ponalagusamy [64] performed a numerical investigation for describing the combined effect of a radially varying magnetic field and viscosity for the two-phase blood flow in the tapered stenosed artery. To determine the effect of variable viscosity (Hematocrit-dependent) on the two-phase pulsatile blood flow through the stenosed circular artery, Tripathi and Sharma [65, 66] developed a mathematical model.

The study of the magnetic field is quite crucial in biological fluids. Blood is highly influenced by the magnetic field due to presence of haemoglobin in it, which reflects the electrical conducting nature of blood. A mathematical study to analyze the impact of the applied magnetic field on the biological system was performed by Rao et al. [67]. They reported that biological system is strongly affected by the magnetic field. There are various applications of the uniform/non-uniform magnetic field in the biological field, such as magnetic targeting drug delivery [68, 69], for the cell separation by using magnetic devices [70], adjust the blood flow during surgery, cancer therapy and to control gastro-intestinal disorder etc. [71]. Haik et al. [72] observed that the blood flow rate can be slow down to 30 % by imposing a strong magnetic field of strength 10T. The mathematical research of two-phase blood flow through the stenosed artery in the presence of a magnetic field with various viscosity conditions (hematocrit and temperature-dependent) discussed by [17, 13]. They reported that flow velocity reduced with the enhancement in the magnetic field strength, which plays a significant role in magnetic therapy. Due to widely applications of magneto nanoparticles in blood flow, such as nanomedicine, MRI, drug delivery, downstream process etc., Bhatti [73, 74] performed a mathematical study to demonstrate the impact of nanoparticles under the peristaltic arterial wall condition.

In the cardiovascular system, at various arterial system locations, segmental narrowing (stenosis) occurs due to deposition of fatty substances, abnormal intra-vascular growth, and malfunction of the arteries. Young [31, 32] developed a mathematical model to observe the effect of time-dependent stenosis on the blood flow through the tube and suggested that

stenosis is the reason for the major problem in the cardiovascular system. An analytical study of blood flow through the stenosed curved artery using a toroidal coordinate system is completed by [33]. They used the perturbation technique to the observed combined effect of curvature and stenosis on the flow velocity. Further, this study is carried forward by [34] to deliberate the application of catheter in the stenosed curved tube. He used the numerical technique and reported that the pressure gradient and frictional resistance rise for high curvature. Gijsen et al. [75] described the significance of unsteady non-Newtonian blood flow on the blood velocity passes through the 90° curved artery. A theoretical analysis to demonstrate the influence of metallic nanoparticle on blood flow passes through a stenosed curved artery is completed by Nadeem [76]. Numerical study of pulsatile blood flow through a stenotic curved artery for the realistic boundary condition [77] and for both dynamic and static model was done by [78]. Further, this study carried ahead by Shahzadi et al.[79, 80] for the constrict the curved artery by assuming circular and ballon shape catheter. They also considered nanoparticle as a drug agent and observed the flow phenomena and heat transfer profile in this work.

In the current scenario, due to rising toxic materials and pollution in our surroundings, human beings are suffering from various types of serious diseases such as cancer, tumours, etc., and researchers are trying to wipe out these with the help of experimental and mathematical findings. Firstly, Mori and Nakayama [81, 82] discussed the forced convective heat transfer in the curved pipe for both the laminar and turbulent region and state that heat transfer increases with the enhancement in both Prandtl and Dean number. Patanakar et al.[83] developed the numerical approach to predict the heat transfer of a fully developed flow in helically coiled pipes. A study to predict the behaviour of heat transfer in a curved pipe by assuming the toroidal coordinate system was done by [84] and the impact of nano-particle diameter was analyzed by [85]. Further, Ramanamurthy et al. [86] and Sultan et al. [18] discussed the heat and mass transfer for both Newtonian and non-Newtonian unsteady blood flow model. In this investigation, they adopt a mathematical model of a curved artery with combined stenosis and aneurysm.

An experimental study to determine the flow velocity for steady and pulsatile blood flow in the glass tube was held by Bugliarello et al. [87, 88]. They find that when blood flows through the narrow vessels, there exists a cell-free layer near the wall known as the plasma layer. To investigate the significant impact of peripheral layer viscosity on the blood velocity passes through the stenosed artery, Shukla et al. [45] developed a two-layer mathematical model. In this study, they consider blood as a Newtonian fluid in both (core and plasma) region and pointed out that resistance and wall shear stress of the flow diminishes as plasma

viscosity decreases. Further, he carried forward this study by considering blood as non-Newtonian in both region [89]. Many researchers [9, 6, 90] developed the two-phase blood flow model for the circular stenosed artery by assuming both the nature of blood (Newtonian and non-Newtonian) in the core region to figure out the impact of plasma layer thickness, viscosity and stenosis height on the flow velocity, resistance and flow rate.

All the above-cited computational and experimental works signify the heat and mass transport phenomena for the single/two-phase blood flow model. As per the author's best knowledge, two-phase blood flow for stenosed curved artery (assuming toroidal coordinate system) with variable viscosity has not been studied in details earlier. Therefore, we performed a mathematical study to discuss the flow and heat transfer phenomena for the two-phase blood flow through a stenosed curved artery. By taking motivation from the literature survey, this mathematical study also considered the variable viscosity in core and plasma regions. The hematocrit dependent viscosity is considered in the core region. The temperature dependent viscosity of blood flow in the plasma region is considered in the mathematical model, which is a more realistic situation in an investigation of blood flow according to [60]. To make our research more realistic for the complex cardiovascular system, a patient-specific stenosed artery geometry and the heat transfer profile is also considered in the present study. A series solution approach [76] is employed to obtain analytic expressions of energy profile. A second-order finite difference scheme [91] is adopted to simplify the governing equation under the assumption of fully-developed flow and mild stenosis.The effect of the various parameter such as Magnetic field, Grashoff number, radiation, stenosis height, λ_1 etc., on the flow velocity, temperature, flow rate and flow resistance depicted graphically. Clinical researchers and biologists can adopt the present mathematical study to lower the risk of lipid deposition, predict cardiovascular disease risk and current state by understanding the symptomatic spectrum, and then diagnose patients based on risk.

2.2 Problem formulation

An incompressible viscous unsteady flow through a stenosed curved artery of length L is considered as shown in Figure (2.1). A two-phase approach is applied to predict more realistic behaviour of blood flow. Let (r,θ,z) be the toroidal system's coordinates, which are employed to investigate the flow behaviour in the geometry mentioned earlier . The z-axis represents the curved artery's axis, and r taken along the radial direction. The blood flow velocity is $V = (u(r,\theta,z), v(r,\theta,z), w(r,\theta,z))$

A uniform magnetic field B is applied perpendicular to the blood flow (axial direction z). In this investigation, the magnetic Reynold number is considered very small ($<<<1$) so

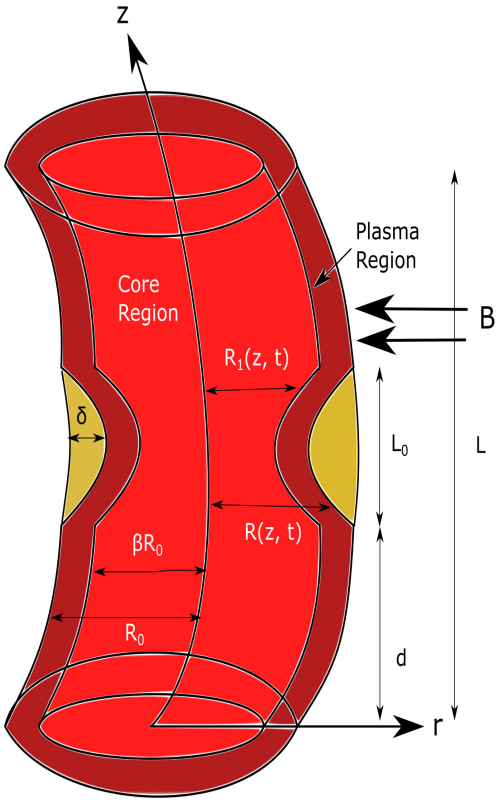

Figure 2.1: Geometry of two-phase stenosed curved artery

that the induced magnetic field can be ignored, also the electric field is taken to be zero. The fully developed flow condition for the blood is considered in this study, which indicates that flow velocity and temperature profile will not be changed along the flow direction (z-axis). The viscosity of both core and plasma regions have been considered variable. In the core region, hematocrit-dependent and for plasma region, temperature-dependent viscosity have been considered.

2.2.1 Geometry of the problem

Time-dependent stenosis is considered for both core and plasma wall and represented by $R_1(z,t)$ and $R(z,t)$, respectively. Mathematically expressions of time-dependent elliptic shape stenoses for the blood flow are as follows [92]:
Geometry of the stenosis in plasma region-

$$R(z,t) = \begin{cases} \left[R_0 - \delta \sin\left(\pi\left(\frac{z-d}{L_0}\right)\right)\right]\Omega(t) & \text{for} \quad d \le z \le d + L_0 \\ R_0\Omega(t), & \text{otherwise,} \end{cases} \tag{2.1}$$

Geometry of stenosis in the core region-

$$R_1(z,t) = \begin{cases} \left[\beta R_0 - \delta \sin\left(\pi(\frac{z-d}{L_0})\right)\right]\Omega(t) & \text{for} \quad d \le z \le d+L_0 \\ \beta R_0 \Omega(t), & \text{otherwise,} \end{cases} \tag{2.2}$$

The time-varying parameter $\Omega(t)$ is expressed as

$$\Omega(t) = 1 - \eta(\cos(\omega t) - 1)e^{-\eta\omega t}. \tag{2.3}$$

where L_0 is the length of stenosis, R_0 radius of normal artery, δ is the maximum height of stenosis, d is the location of stenosis, β is ratio of central core radius to normal artery radius, L is the length of artery, η is constant, ω are the angular frequency of the forced oscillation.

2.2.2 Variable viscosity model

The viscosity of blood in the core-region is considered as hematocrit dependent, and a mathematical expression is given by [17]:

$$\mu_c(r) = \mu_c(1 + \beta_1 h(r)), \tag{2.4}$$

where

$$h(r) = h_m\left[\left(\frac{R_1}{R_0}\right)^{m_1} - \left(\frac{r}{R_0}\right)^{m_1}\right],$$

where h_m represent the hematocrit and β_1 is constant.
Mathematical model of temperature-dependent viscosity for the plasma region is-

$$\mu_p(T) = \mu_p\left[1 + \lambda_1\left(\frac{T_p - T_0}{T_w - T_0}\right)\right]. \tag{2.5}$$

2.2.3 Governing equations

The governing equations for the curved tube for both core and plasma are deliberated as follows [16]
Continuity Equation :

$$\frac{b}{D}\frac{\partial w}{\partial z} + \frac{\partial u}{\partial r} + \frac{1}{r}\frac{\partial v}{\partial \theta} + \frac{u}{r} + \frac{u\cos\theta - v\sin\theta}{D} = 0, \tag{2.6}$$

Here b denotes the radius of curvature and $D = b + r\cos\theta$.
For the Core region i.e. $0 < r < R_1(z,t)$

Momentum equations-
r-direction:

$$\rho_c\left(\frac{\partial u_c}{\partial t}+\frac{bw_c}{D}\frac{\partial u_c}{\partial z}+u_c\frac{\partial u_c}{\partial r}+\frac{v_c}{r}\frac{\partial u_c}{\partial \theta}-\frac{v_c^2}{r}-\frac{w_c^2\cos\theta}{D}\right)=-\frac{\partial P_c}{\partial r}+\mu_c(r)\left(\frac{b^2}{D^2}\frac{\partial^2 u_c}{\partial z^2}\right.$$
$$+\frac{\partial^2 u_c}{\partial r^2}+\frac{1}{r}\frac{\partial u_c}{\partial r}-\frac{u_c}{r^2}+\frac{1}{r^2}\frac{\partial^2 u_c}{\partial \theta^2}-\frac{2}{r^2}\frac{\partial v_c}{\partial \theta}+\frac{1}{D}\left[\cos\theta\frac{\partial u_c}{\partial r}-\frac{\sin\theta}{r}\frac{\partial u_c}{\partial \theta}+\frac{v_c\sin\theta}{r}\right]$$
$$\left.+\frac{2b\sin\theta}{D^2}\frac{\partial w_c}{\partial z}-\frac{\cos\theta}{D^2}[u_c\cos\theta-v_c\sin\theta]\right)+\left[\frac{4}{3}\frac{\partial u_c}{\partial r}-\frac{2}{3}\left(\frac{b}{D}\frac{\partial w_c}{\partial z}+\frac{u_c\cos\theta-v_c\sin\theta}{D}\right.\right.$$
$$\left.\left.+\frac{1}{r}\frac{\partial v_c}{\partial \theta}+\frac{u_c}{r}\right)\right]\frac{\partial \mu_c(r)}{\partial r}, \tag{2.7}$$

θ- direction :

$$\rho_c\left(\frac{\partial v_c}{\partial t}+\frac{w_c b}{D}\frac{\partial v_c}{\partial z}+u_c\frac{\partial v_c}{\partial r}+\frac{v_c}{r}\frac{\partial v_c}{\partial \theta}+\frac{u_c v_c}{r}+\frac{w_c^2\sin\theta}{D}\right)=-\frac{1}{r}\frac{\partial P_c}{\partial \theta}+\mu_c(r)\left(\frac{b^2}{D^2}\frac{\partial^2 v_c}{\partial z^2}\right.$$
$$+\frac{\partial^2 v_c}{\partial r^2}+\frac{1}{r}\frac{\partial v_c}{\partial r}-\frac{v_c}{r^2}+\frac{1}{r^2}\frac{\partial^2 v_c}{\partial \theta^2}+\frac{2}{r^2}\frac{\partial u_c}{\partial \theta}+\frac{1}{D}\left[\cos\theta\frac{\partial v_c}{\partial r}-\frac{\sin\theta}{r}\frac{\partial v_c}{\partial \theta}-\frac{u_c\sin\theta}{r}\right]+$$
$$\left.\frac{2b\sin\theta}{D^2}\frac{\partial w_c}{\partial z}+\frac{\sin\theta}{D^2}[u_c\cos\theta-v_c\sin\theta]\right)+\left[\frac{\partial v_c}{\partial r}-\frac{v_c}{r}+\frac{1}{r}\frac{\partial u_c}{\partial \theta}\right]\frac{\partial \mu_c(r)}{\partial r}, \tag{2.8}$$

z- direction :

$$\rho_c\left(\frac{\partial w_c}{\partial t}+\frac{w_c b}{D}\frac{\partial w_c}{\partial z}+u_c\frac{\partial w_c}{\partial r}+\frac{v_c}{r}\frac{\partial w_c}{\partial \theta}+\frac{w_c(u_c\cos\theta-v_c\sin\theta)}{D}\right)=-\frac{b}{D}\frac{\partial P_c}{\partial z}+\mu_c(r)\left(\frac{\partial^2 w_c}{\partial r^2}\right.$$
$$+\frac{1}{r}\frac{\partial w_c}{\partial r}+\frac{b^2}{D^2}\frac{\partial^2 w_c}{\partial z^2}+\frac{1}{r^2}\frac{\partial^2 w_c}{\partial \theta^2}-\frac{w_c}{D^2}+\frac{1}{D}\left[\cos\theta\frac{\partial w_c}{\partial r}-\frac{\sin\theta}{r}\frac{\partial w_c}{\partial \theta}\right]+\frac{2b}{D^2}\left[\cos\theta\frac{\partial u_c}{\partial z}\right.$$
$$\left.\left.-\sin\theta\frac{\partial v_c}{\partial z}\right]\right)+\left[\frac{b}{D}\frac{\partial u_c}{\partial z}+\frac{\partial w_c}{\partial r}-\frac{w_c\cos\theta}{D}\right]\frac{\partial \mu_c(r)}{\partial r}-\sigma B^2 w_c+g\rho_c\gamma_T(T_c-T_0), \tag{2.9}$$

Energy equation :

$$\rho_c\bar{C}_c\left(\frac{\partial T_c}{\partial t}+u_c\frac{\partial T_c}{\partial r}+\frac{v_c}{r}\frac{\partial T_c}{\partial \theta}+\frac{w_c b}{D}\frac{\partial T_c}{\partial z}\right)=K_c\left(\frac{\partial^2 T_c}{\partial r^2}+\frac{1}{r}\frac{\partial T_c}{\partial r}+\frac{b^2}{D^2}\frac{\partial^2 T_c}{\partial z^2}+\frac{\cos\theta}{D}\frac{\partial T_c}{\partial r}\right.$$
$$\left.-\frac{\sin\theta}{rD}\frac{\partial T_c}{\partial \theta}+\frac{1}{r^2}\frac{\partial^2 T_c}{\partial \theta^2}\right)-\frac{\partial q_c}{\partial r}, \tag{2.10}$$

where u_c, v_c, w_c are the dimensional core region velocity component in r, θ, z directions, respectively. $\mu_c, T_c, \rho_c, K_c, q_c, B$ are the dimensional viscosity, temperature, density, thermal conductivity, radiation parameter and uniform magnetic field in the core region, respectively.
Plasma region i.e. $R_1(z,t) < r < R(z,t)$
Momentum equations-

r-direction :

$$\rho_p\left(\frac{\partial u_p}{\partial t}+\frac{bw_p}{D}\frac{\partial u_p}{\partial z}+u_p\frac{\partial u_p}{\partial r}+\frac{v_p}{r}\frac{\partial u_p}{\partial \theta}-\frac{v_p^2}{r}-\frac{w_p^2\cos\theta}{D}\right)=-\frac{\partial P_p}{\partial r}+\mu_p(T)\left(\frac{b^2}{D^2}\frac{\partial^2 u_p}{\partial z^2}\right.$$
$$+\frac{\partial^2 u_p}{\partial r^2}+\frac{1}{r}\frac{\partial u_p}{\partial r}-\frac{u_p}{r^2}+\frac{1}{r^2}\frac{\partial^2 u_p}{\partial \theta^2}-\frac{2}{r^2}\frac{\partial v_p}{\partial \theta}+\frac{1}{D}\left[\cos\theta\frac{\partial u_p}{\partial r}-\frac{\sin\theta}{r}\frac{\partial u_p}{\partial \theta}+\frac{v_p\sin\theta}{r}\right]$$
$$\left.+\frac{2b\sin\theta}{D^2}\frac{\partial w_p}{\partial z}-\frac{\cos\theta}{D^2}[u_p\cos\theta-v_p\sin\theta]\right)+\left[\frac{4}{3}\frac{\partial u_p}{\partial r}-\frac{2}{3}\left(\frac{b}{D}\frac{\partial w_p}{\partial z}+\frac{u_p\cos\theta-v_p\sin\theta}{D}\right.\right.$$
$$\left.\left.+\frac{1}{r}\frac{\partial v_p}{\partial \theta}+\frac{u_p}{r}\right)\right]\frac{\partial \mu_p(T)}{\partial r}+\left(\frac{1}{r}\frac{\partial v_p}{\partial r}-\frac{v_p}{r^2}+\frac{1}{r^2}\frac{\partial u_p}{\partial \theta}\right)\frac{\partial \mu_p(T)}{\partial \theta}+\left(\frac{b^2}{D^2}\frac{\partial u_p}{\partial z}+\frac{b}{D}\frac{\partial w_p}{\partial r}\right.$$
$$\left.-\frac{bw_p\cos\theta}{D^2}\right)\frac{\partial \mu_p(T)}{\partial z}, \tag{2.11}$$

θ- direction :

$$\rho_p\left(\frac{\partial v_p}{\partial t}+\frac{w_p b}{D}\frac{\partial v_p}{\partial z}+u_p\frac{\partial v_p}{\partial r}+\frac{v_p}{r}\frac{\partial v_p}{\partial \theta}+\frac{u_p v_p}{r}+\frac{w_p^2\sin\theta}{D}\right)=-\frac{1}{r}\frac{\partial P_p}{\partial \theta}+\mu_p(T)\left(\frac{b^2}{D^2}\frac{\partial^2 v_p}{\partial z^2}\right.$$
$$+\frac{\partial^2 v_p}{\partial r^2}+\frac{1}{r}\frac{\partial v_p}{\partial r}-\frac{v_p}{r^2}+\frac{1}{r^2}\frac{\partial^2 v_p}{\partial \theta^2}+\frac{2}{r^2}\frac{\partial u_p}{\partial \theta}+\frac{1}{D}\left[\cos\theta\frac{\partial v_p}{\partial r}-\frac{\sin\theta}{r}\frac{\partial v_p}{\partial \theta}-\frac{u_p\sin\theta}{r}\right]$$
$$\left.+\frac{2b\sin\theta}{D^2}\frac{\partial w_p}{\partial z}+\frac{\sin\theta}{D^2}[u_p\cos\theta-v_p\sin\theta]\right)+\left(\frac{\partial v_p}{\partial r}-\frac{v_p}{r}+\frac{1}{r}\frac{\partial u_p}{\partial \theta}\right)\frac{\partial \mu_p(T)}{\partial r}+\left[\frac{4}{3}\left(\frac{1}{r^2}\frac{\partial v_p}{\partial \theta}\right.\right.$$
$$\left.\left.+\frac{u_p}{r^2}\right)-\frac{2}{3}\left(\frac{1}{r}\frac{b}{D}\frac{\partial w_p}{\partial z}+\frac{1}{r}\frac{u_p\cos\theta-v_p\sin\theta}{D}+\frac{1}{r}\frac{\partial u_p}{\partial r}\right)\right]\frac{\partial \mu_p(T)}{\partial \theta}+\frac{b}{D}\left(\frac{1}{r}\frac{\partial w_p}{\partial \theta}+\frac{w_p\sin\theta}{b+r\cos\theta}\right.$$
$$\left.+\frac{b}{D}\frac{\partial v_p}{\partial z}\right)\frac{\partial \mu_p(T)}{\partial z}, \tag{2.12}$$

z- direction :

$$\rho_p\left(\frac{\partial w_p}{\partial t}+\frac{w_p b}{D}\frac{\partial w_p}{\partial z}+u_p\frac{\partial w_p}{\partial r}+\frac{v_p}{r}\frac{\partial w_p}{\partial \theta}+\frac{w_p(u_p\cos\theta-v_p\sin\theta)}{D}\right)=-\frac{b}{D}\frac{\partial P_p}{\partial z}+\mu_p(T)$$
$$\left(\frac{\partial^2 w_p}{\partial r^2}+\frac{1}{r}\frac{\partial w_p}{\partial r}+\frac{b^2}{D^2}\frac{\partial^2 w_p}{\partial z^2}+\frac{1}{r^2}\frac{\partial^2 w_p}{\partial \theta^2}-\frac{w_p}{D^2}+\frac{1}{D}\left[\cos\theta\frac{\partial w_p}{\partial r}-\frac{\sin\theta}{r}\frac{\partial w_p}{\partial \theta}\right]+\frac{2b}{D^2}\right.$$
$$\left.\left[\cos\theta\frac{\partial u_p}{\partial z}-\sin\theta\frac{\partial v_p}{\partial z}\right]\right)+\left(\frac{b}{D}\frac{\partial u_p}{\partial z}+\frac{\partial w_p}{\partial r}-\frac{w_p\cos\theta}{D}\right)\frac{\partial \mu_p(T)}{\partial r}+\left(\frac{1}{r^2}\frac{\partial w_p}{\partial \theta}+\frac{w_p\sin\theta}{rD}\right.$$
$$\left.+\frac{b}{rD}\frac{\partial v_p}{\partial z}\right)\frac{\partial \mu_p(T)}{\partial \theta}+\frac{b}{b+r\cos\theta}\left[\frac{4}{3}\left(\frac{b}{D}\frac{\partial w_p}{\partial z}+\frac{u_p\cos\theta-v_p\sin\theta}{D}\right)-\frac{2}{3}\left(\frac{\partial u_p}{\partial r}+\frac{1}{r}\frac{\partial v_p}{\partial \theta}\right.\right.$$
$$\left.\left.+\frac{u_p}{r}\right)\right]\frac{\partial \mu_p(T)}{\partial z}-\sigma B^2 w_p+g\rho_p\gamma_T(T_p-T_0), \tag{2.13}$$

Energy equation :

$$\rho_p \bar{C}_p \left(\frac{\partial T_p}{\partial t} + u_p \frac{\partial T_p}{\partial r} + \frac{v_p}{r} \frac{\partial T_p}{\partial \theta} + \frac{w_p b}{D} \frac{\partial T_p}{\partial z} \right) = K_p \left(\frac{\partial^2 T_p}{\partial r^2} + \frac{1}{r} \frac{\partial T_p}{\partial r} + \frac{b^2}{D^2} \frac{\partial^2 T_p}{\partial z^2} + \frac{\cos\theta}{D} \frac{\partial T_p}{\partial r} - \frac{\sin\theta}{rD} \frac{\partial T_p}{\partial \theta} + \frac{1}{r^2} \frac{\partial^2 T_p}{\partial \theta^2} \right) - \frac{\partial q_p}{\partial r}, \tag{2.14}$$

where u_p, v_p, w_p are the dimensional core region velocity component in r, θ, z directions, respectively.

$\mu_p, T_p, \rho_p, K_p, q_p, B$ are the dimensional viscosity, temperature, density, thermal conductivity, radiation parameter and uniform magnetic field in the plasma region, respectively.

The appropriate boundary conditions for the two-phase blood flow model under consideration are as follows:

$$\begin{cases} \frac{\partial w_c}{\partial r} = 0, & \frac{\partial T_c}{\partial r} = 0 & \text{at} \quad r = 0, \\ w_c = w_p, & T_c = T_p, & \text{at} \quad r = R_1(z,t), \\ \tau_c = \tau_p, & \frac{\partial T_c}{\partial r} = \frac{\partial T_p}{\partial r}, & \text{at} \quad r = R_1(z,t), \\ w_p = 0, & T_p = T_w, & \text{at} \quad r = R(z,t). \end{cases} \tag{2.15}$$

where T_w represents the wall temperature.

Here

$$\frac{\partial w_c}{\partial r} = 0, \quad \frac{\partial T_c}{\partial r} = 0, \qquad \text{at} \quad r = 0,$$

represent the velocity and temperature condition on the axis.

$$w_c = w_p, \quad \tau_c = \tau_p, \qquad \text{at} \quad r = R_1(z,t),$$

describe the continuity condition of velocity and shear stress at the core-plasma interface.

$$T_c = T_p, \quad \frac{\partial T_c}{\partial r} = \frac{\partial T_p}{\partial r}, \qquad \text{at} \quad r = R_1(z,t),$$

represent the continuity of flow temperature at the core-plasma interface.

$$w_p = 0, \quad T_p = 1, \qquad \text{at} \quad r = R(z,t).$$

describe the no-slip condition for velocity and isothermal condition for the flow temperature at the arterial wall.

2.2.4 Non-dimensional and mild stenosis simplification

To convert above governing equations in dimensionless form, introducing the following non-dimensional parameters, which are described through the table 2.1 :

Table 2.1: Non-dimensional parameter

$r = R_0 r'$	$z = L_0 z'$	$\theta = \theta'$	$\omega = \frac{u_0}{L_0}\omega'$	$L = L_0 L'$
$d = L_0 d'$	$\rho_0 = \frac{\rho_p}{\rho_c}$	$R = R_0 R'$	$R_1 = R_0 R_1'$	$u_c = \frac{\delta u_0}{L_0} u_c'$
$v_c = \frac{\delta u_0}{L_0} v_c'$	$w_c = u_0 w_c'$	$u_p = \frac{\delta u_0}{L_0} u_p'$	$v_p = \frac{\delta u_0}{L_0} v_p'$	$w_p = u_0 w_p'$
$P_c = \frac{u_0 L_0 \mu_p}{R_0^2} P_c'$	$P_p = \frac{u_0 L_0 \mu_p}{R_0^2} P_p'$	$\alpha = \frac{R_0}{L_0}$	$T_c' = \frac{T_c - T_0}{T_w - T_0}$	$T_p' = \frac{T_p - T_0}{T_w - T_0}$
$\delta^* = \frac{\delta}{R_0}$	$\mu_0 = \frac{\mu_p}{\mu_c}$	$Gr = \frac{g\rho_p \gamma_T R_0^2 (T_w - T_0)}{u_0 \mu_p}$	$\varepsilon = \frac{R_0}{b}$	$k_0 = \frac{K_p}{K_c}$
$\tau_c = \frac{\tau_c' u_0 \mu_p}{R_0^2}$	$\tau_p = \frac{\tau_p' u_0 \mu_p}{R_0^2}$	$M = \frac{\sigma B^2 R_0^2}{\mu_p}$	$N = \frac{4R_0^2 \alpha_p^2}{K_p}$	$\alpha_0 = \frac{\alpha_p^2}{\alpha_c^2}$

The dimensionless form of the stenoses geometry for both core and plasma regions are given as follows:

$$R'(z',t') = \begin{cases} \left[1 - \delta^* \sin\left(\pi(z' - d')\right)\right]\Omega(t') & \text{for} \quad d' \le z' \le d' + 1 \\ \Omega(t'), & \text{otherwise,} \end{cases} \tag{2.16}$$

$$R_1'(z',t') = \begin{cases} \left[\beta - \delta^* \sin\left(\pi(z' - d')\right)\right]\Omega(t') & \text{for} \quad d' \le z' \le d' + 1 \\ \beta\Omega(t'), & \text{otherwise.} \end{cases} \tag{2.17}$$

With the help of above mentioned non-dimensional parameters and considering the condition of fully developed flow, low Reynold number ($Re << 1$), mild stenosis ($\delta^* << 1$) with $O(1) = \alpha = \frac{R_0}{L_0}$, the governing equations of both core and plasma region will be converted as follows:

Core region

$$\frac{\partial P_c'}{\partial r'} = 0, \tag{2.18}$$

$$\frac{\partial P_c'}{\partial \theta'} = 0, \tag{2.19}$$

$$\frac{1}{\bar{D}}\frac{\partial P'_c}{\partial z'} = \frac{1+\beta_1 h_m(R_1'^{m_1} - r'^{m_1})}{\mu_0}\left(\frac{\partial^2 w'_c}{\partial r'^2} + \frac{1}{r'}\frac{\partial w'_c}{\partial r'} + \frac{1}{r'^2}\frac{\partial^2 w'_c}{\partial \theta'^2} - \frac{\varepsilon^2 w'_c}{\bar{D}^2} + \frac{\varepsilon}{\bar{D}}\left[\cos\theta'\frac{\partial w'_c}{\partial r'} - \frac{\sin\theta'}{r'}\frac{\partial w'_c}{\partial \theta'}\right]\right) - \frac{m_1\beta_1 h_m r'^{m_1-1}}{\mu_0}\left[\frac{\partial w'_c}{\partial r'} - \frac{\varepsilon w'_c\cos\theta'}{\bar{D}}\right] - Mw'_c + \frac{GrT'_c}{\rho_0}, \tag{2.20}$$

$$\frac{\partial^2 T'_c}{\partial r'^2} + \frac{1}{r'}\frac{\partial T'_c}{\partial r'} + \frac{\varepsilon\cos\theta'}{\bar{D}}\frac{\partial T'_c}{\partial r'} - \frac{\varepsilon\sin\theta'}{r'\bar{D}}\frac{\partial T'_c}{\partial \theta'} + \frac{1}{r'^2}\frac{\partial^2 T'_c}{\partial \theta'^2} - \frac{k_0}{\alpha_0}NT'_c = 0. \tag{2.21}$$

where $\bar{D} = 1 + \varepsilon r'\cos\theta'$,

Plasma region

$$\frac{\partial P'_p}{\partial r'} = 0, \tag{2.22}$$

$$\frac{\partial P'_p}{\partial \theta'} = 0, \tag{2.23}$$

$$\frac{1}{\bar{D}}\frac{\partial P'_p}{\partial z'} = (1+\lambda_1 T'_p)\left(\frac{\partial^2 w'_p}{\partial r'^2} + \frac{1}{r'}\frac{\partial w'_p}{\partial r'} + \frac{1}{r'^2}\frac{\partial^2 w'_p}{\partial \theta'^2} - \frac{\varepsilon^2 w'_p}{\bar{D}^2} + \frac{\varepsilon}{\bar{D}}\left[\cos\theta'\frac{\partial w'_p}{\partial r'} - \frac{\sin\theta'}{r'}\frac{\partial w'_p}{\partial \theta'}\right]\right) + \lambda_1\left(\frac{\partial w'_p}{\partial r'} - \frac{\varepsilon w'_p\cos\theta'}{\bar{D}}\right)\frac{\partial T'_p}{\partial r'} + \lambda_1\left(\frac{1}{r'^2}\frac{\partial w'_p}{\partial \theta'} + \frac{\varepsilon w'_p\sin\theta'}{r'\bar{D}}\right)\frac{\partial T'_p}{\partial \theta'} - Mw'_p + GrT'_p, \tag{2.24}$$

$$\frac{\partial^2 T'_p}{\partial r'^2} + \frac{1}{r'}\frac{\partial T'_p}{\partial r'} + \frac{\varepsilon\cos\theta'}{\bar{D}}\frac{\partial T'_p}{\partial r'} - \frac{\varepsilon\sin\theta'}{r'\bar{D}}\frac{\partial T'_p}{\partial \theta'} + \frac{1}{r'^2}\frac{\partial^2 T'_p}{\partial \theta'^2} - NT'_p = 0. \tag{2.25}$$

Here $'$ represents the non-dimensional quantities.

Non-dimensional boundary conditions for both core and plasma region are given as:

$$\begin{cases} \frac{\partial w'_c}{\partial r'} = 0, \quad \frac{\partial T'_c}{\partial r'} = 0, & \text{at} \quad r' = 0, \\ w'_c = w'_p, \quad T'_c = T'_p, & \text{at} \quad r' = R'_1(z',t'), \\ \tau'_c = \tau'_p, \quad \frac{\partial T'_c}{\partial r'} = \frac{\partial T'_p}{\partial r'}, & \text{at} \quad r' = R'_1(z',t'), \\ w'_p = 0, \quad T'_p = 1, & \text{at} \quad r' = R'(z',t'). \end{cases} \tag{2.26}$$

2.3 Procedure of solution

2.3.1 Temperature profile solution

Using perturbation technique [79, 80], the solution of temperature profile in both core and plasma region can be assumed as-

$$T'_c(r',\theta',z') = T'_{c0}(r',z') + \varepsilon\cos\theta' T'_{c1}(r',z') + (\varepsilon\cos\theta')^2 T'_{c2}(r',z') + \cdots, \tag{2.27}$$

$$T'_p(r',\theta',z') = T'_{p0}(r',z') + \varepsilon\cos\theta' T'_{p1}(r',z') + (\varepsilon\cos\theta')^2 T'_{p2}(r',z') + \cdots. \tag{2.28}$$

Zeroth order solution

$$\frac{\partial^2 T'_{c0}}{\partial r'^2} + \frac{1}{r'}\frac{\partial T'_{c0}}{\partial r'} - \frac{k_0}{\alpha_0} N T'_{c0} = 0, \tag{2.29}$$

$$\frac{\partial^2 T'_{p0}}{\partial r'^2} + \frac{1}{r'}\frac{\partial T'_{p0}}{\partial r'} - N T'_{p0} = 0, \tag{2.30}$$

Boundary conditions for the zeroth order solutions are-

$$\begin{cases} \frac{\partial T'_{c0}}{\partial r'} = 0, & \text{at} \quad r' = 0, \\ \frac{\partial T'_{c0}}{\partial r'} = \frac{\partial T'_{p0}}{\partial r'}, \quad T'_{c0} = T'_{p0}, & \text{at} \quad r' = R'_1(z',t'), \\ T'_{p0} = 1, & \text{at} \quad r' = R'(z',t'), \end{cases} \tag{2.31}$$

The solution of zeroth order temperature equations in both core and plasma region are-

$$T'_{c0} = C_1\, I_0\left(\sqrt{N_1} r\right) + C_2\, K_0\left(\sqrt{N_1} r\right), \tag{2.32}$$

$$T'_{p0} = C_3\, I_0\left(\sqrt{N} r\right) + C_4\, K_0\left(\sqrt{N} r\right), \tag{2.33}$$

First order solution

$$\frac{\partial^2 T'_{c1}}{\partial r'^2} + \frac{1}{r'}\frac{\partial T'_{c1}}{\partial r'} - \frac{T'_{c1}}{r'^2} + r'\frac{\partial^2 T'_{c0}}{\partial r'^2} + 2\frac{\partial T'_{c0}}{\partial r'} - \frac{k_0}{\alpha_0} N(r' T'_{c0} + T'_{c1}) = 0, \tag{2.34}$$

$$\frac{\partial^2 T'_{p1}}{\partial r'^2} + \frac{1}{r'}\frac{\partial T'_{p1}}{\partial r'} - \frac{T'_{p1}}{r'^2} + r'\frac{\partial^2 T'_{p0}}{\partial r'^2} + 2\frac{\partial T'_{p0}}{\partial r'} - N(r' T'_{p0} + T'_{p1}) = 0, \tag{2.35}$$

Boundary conditions for the first order solutions are-

$$\begin{cases} \frac{\partial T'_{c1}}{\partial r'} = 0, & \text{at} \quad r' = 0, \\ \frac{\partial T'_{c1}}{\partial r'} = \frac{\partial T'_{p1}}{\partial r'}, \quad T'_{c1} = T'_{p1}, & \text{at} \quad r' = R'_1(z',t'), \\ T'_{p1} = 0, & \text{at} \quad r' = R'(z',t'), \end{cases} \tag{2.36}$$

The solution of first order temperature equations in both core and plasma region are-

$$T'_{c1} = C_5\, I_1\left(\sqrt{N_1}r'\right) + C_6\, K_1\left(\sqrt{N_1}r'\right) - \frac{C_1\sqrt{N_1}}{4\sqrt{\pi}} I_1\left(\sqrt{N_1}r'\right) G^{2,2}_{2,4}\left(\sqrt{N_1}r', \frac{1}{2}\middle| \begin{matrix} 1, \frac{3}{2} \\ 1,2,0,0 \end{matrix}\right) +$$
$$C_1\,\sqrt{N_1}K_1\left(\sqrt{N_1}r'\right)\left[\frac{N_1 r'^2}{2} I_1^2\left(\sqrt{N_1}r'\right) - \frac{N_1 r'^2}{2} I_0^2\left(\sqrt{N_1}r'\right) + \sqrt{N_1}r' I_0\left(\sqrt{N_1}r'\right) I_1\left(\sqrt{N_1}r'\right)\right], \tag{2.37}$$

$$T'_{p1} = C_7\, I_1\left(\sqrt{N}r'\right) + C_8\, K_1\left(\sqrt{N}r'\right) - \frac{\sqrt{N}}{4\sqrt{\pi}}\left(C_3 I_1\left(\sqrt{N}r'\right) + C_4 K_1\left(\sqrt{N}r'\right)\right)$$
$$G^{2,2}_{2,4}\left(\sqrt{N}r', \frac{1}{2}\middle| \begin{matrix} 1, \frac{3}{2} \\ 1,2,0,0 \end{matrix}\right)$$
$$+ C_4\,\sqrt{N}\, I_1\left(\sqrt{N}r'\right)\left[\frac{Nr'^2}{2} K_1^2\left(\sqrt{N}r'\right) - \frac{Nr'^2}{2} K_0^2\left(\sqrt{N}r'\right) + \sqrt{N}r' K_0\left(\sqrt{N}r'\right) K_1\left(\sqrt{N}r'\right)\right]$$
$$+ C_3\,\sqrt{N}\, K_1\left(\sqrt{N}r'\right)\left[\frac{Nr'^2}{2} I_1^2\left(\sqrt{N}r'\right) - \frac{Nr'^2}{2} I_0^2\left(\sqrt{N}r'\right) + \sqrt{N}r' I_0\left(\sqrt{N}r'\right) I_1\left(\sqrt{N}r'\right)\right]. \tag{2.38}$$

where $I_0,\ I_1$ are the modified Bessel functions of first kind. $K_0,\ K_1$ are the modified Bessel functions of second kind, and $N_1 = \frac{k_0 N}{\alpha_0}$.
The constants C_1 to C_8 are evaluated through MATLAB software and not mentioned due to sake of brevity.

2.3.2 Velocity profile solution

Pressure gradient in both regions are constant so it can be written as

$$\frac{\partial P'_c}{\partial z'} = \frac{\partial P'_p}{\partial z'} = P_0, \tag{2.39}$$

Boundary conditions for velocity profile for both core and plasma regions are-

$$\begin{cases} \frac{\partial w'_c}{\partial r'} = 0, & & \text{at} \quad r' = 0, \\ w'_c = w'_p, & \tau'_c = \tau'_p, & \text{at} \quad r' = R'_1(z',t'), \\ w'_p = 0, & & \text{at} \quad r' = R'(z',t'), \\ \frac{\partial w'_c}{\partial \theta'} = 0, & & \text{at} \quad \theta' = 0 \quad \text{and} \quad \theta' = \pi, \\ \frac{\partial w'_p}{\partial \theta'} = 0, & & \text{at} \quad \theta' = 0 \quad \text{and} \quad \theta' = \pi. \end{cases} \tag{2.40}$$

To obtain the solution of equations (2.20) and (2.24), the finite difference method is employed, which was described by the [91].

Central difference formula is used to state spatial derivative for which a semi- annular region $[0 \quad R(z',t')] \times [0 \quad \pi]$ divided into the uniform grid. The spatial derivatives are described as-

$$\frac{\partial w'_f}{\partial r'} = \frac{(w'_f)_{i+1,j} - (w'_f)_{i-1,j}}{2\Delta r}, \tag{2.41}$$

$$\frac{\partial w'_f}{\partial \theta'} = \frac{(w'_f)_{i,j+1} - (w'_f)_{i,j-1}}{2\Delta \theta}, \tag{2.42}$$

$$\frac{\partial^2 w'_f}{\partial r'^2} = \frac{(w'_f)_{i+1,j} - 2(w'_f)_{i,j} + (w'_f)_{i-1,j}}{(\Delta r)^2}, \tag{2.43}$$

where $f = c$, if $0 < r' < R'_1(z',t')$ and $f = p$, if $R'_1(z',t') < r' < R'(z',t')$.

Δr and $\Delta\theta$ denotes the step-size in the r' and θ' directions, respectively. In the present study step size is considered uniform. If the L_1 and L_2 denotes the number of sub-intervals, in which the interval $[0 \quad R(z',t')] \times [0 \quad \pi]$ are divided by using uniform grids, then $\Delta r'$ and $\Delta\theta'$ represent mathematically as-

$\Delta r = \frac{R'(z',t')}{L_1}$ and $\Delta\theta = \frac{\pi}{L_2}$.

The grid points $(r'_i, \ \theta'_j)$ are represent as-

$$r'_i = (i-1)\Delta r', \qquad i = 1,2,3\ldots,L_1+1,$$

$$\theta'_j = (j-1)\Delta\theta', \qquad j = 1,2,3\ldots,L_2+1.$$

The velocity equations are discretized with the help of equations (2.41-2.43). These discretized equations are converted into algebraic equations by varying i from 1 to L_1+1 and j from 1 to L_2+1. The algebraic equations form a tridiagonal block matrix and which are solved by using Gauss- Seidel iterative approach in MATLAB. The tolerance of error is considered 10^{-6} at every iteration.

After determining the velocity and temperature profile for the both region, we have obtained the flow rate, wall shear stress numerically by adopting finite difference method.

The Volumetric flow rate Q, in non-dimensional form is described as-

$$Q = \int_0^{R'(z',t')} \int_0^{\pi} r'w'dr'd\theta',$$

$$Q = \int_0^{R'_1(z',t')} \int_0^{\pi} r'w'_c(r',\theta',z')dr'd\theta' + \int_{R'_1(z',t')}^{R'(z',t')} \int_0^{\pi} r'w'_p(r',\theta',z')dr'd\theta', \tag{2.44}$$

The frictional resistance in λ is defined as-

$$\lambda = \frac{\int_0^L (-\frac{\partial p'}{\partial z'}) dz'}{Q}, \tag{2.45}$$

where L is the length of the curved artery.
Dimensional form of the wall shear for curved artery is written as-

$$\tau_w = -\mu_p(T) \left[\frac{\partial w'_p}{\partial r'} \right]_{r'=R'(z',t')},$$

Non-dimensional form of wall shear stress reduces:

$$\tau_w = -\mu_p(1+\lambda_1 T'_p) \left[\frac{\partial w'_p}{\partial r'} \right]_{r'=R'(z',t')}. \tag{2.46}$$

2.4 Results and Discussion

The main aim of the present study is to understand the nature of two-fluid flow through a stenosed curved artery with variable viscosity in both core and plasma region. Hematocrit dependent viscosity is considered in the core region and temperature dependent viscosity is considered in the plasma region. The thickness of the plasma region is assumed the 15% of the whole blood region, according to artery diameter and hematocrit level [88]. The non-dimensional energy equations for both regions have been solved using perturbation technique, while velocity, WSS, impedance equations are numerically computed by using finite difference method (FDM). For the FDM technique, flow region are discretized uniformly in the both radial (r') and angular direction (θ') with $\Delta r = \Delta\theta' = 0.001$. The tolerance of error is considered 10^{-6} in the whole numerical process. Default values of the parameters which were used for pictorially analyze the importance of the model are listed below in the table (1). In the all figures of velocity and temperature profiles, the continuous and dotted lines symbolized the core and plasma region, respectively.

The validation of our study with the published work of Ayub et al.[80] is compared graphically through the Figure (2.2). In the process of present study validation the effect of magnetic field is neglected and blood assumed as a single-phase fluid, and impact of catheter and nanofluids ignored in the analysis of [80]. The perturbation technique was used by [80] to simplify the governing equations. Therefore in this comparison, perturbation technique has been used for [80] work and finite difference method for the present analysis. It observed that there is a good agreement between our study and [80].

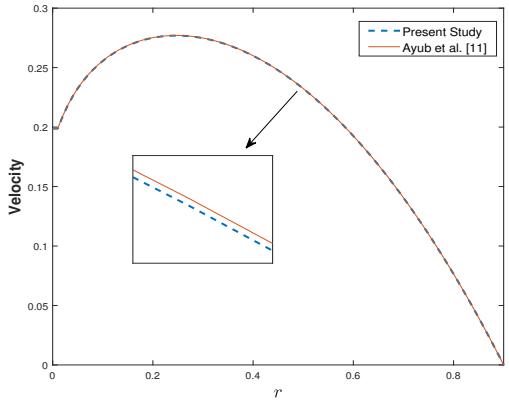

Figure 2.2: Comparison of present study with published work

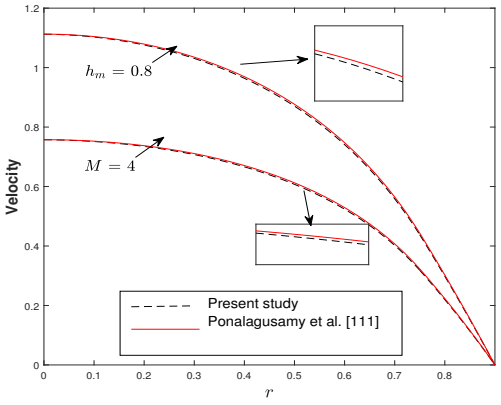

Figure 2.3: Comparison of present study for h_m and M with published work

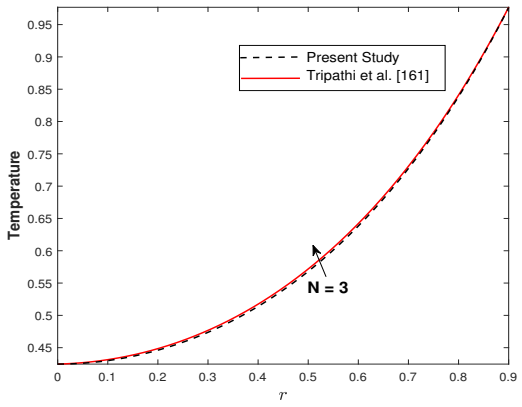

Figure 2.4: Comparison of present study for N with published work

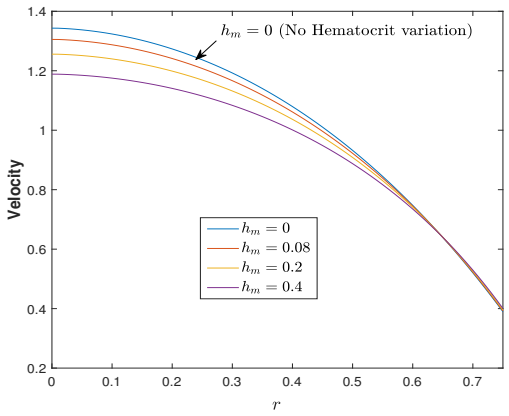

Figure 2.5: Variation in Core-region Velocity with h_m

Validation of the two-phase blood flow model of the present study is made with the published work of Pongalagusamy et al. [17] and Tripathi et al. [65] and depicted graphically through the Figures (2.3-2.4). This validation has been performed under some limitations such as low Reynold number ($Re << 1$), straight artery ($\varepsilon = 0$). The validation for hematocrit parameter (h_m) and Magnetic field (M) has been depicted in Figure (2.3), and the present study is in fair agreement with the published research of [17]. For this validation, the energy equation has been neglected in our study. The validation of the energy equation with the help of the Radiation parameter (N) has been presented via Figure (2.4), and this study reveals a good agreement with the published work of Tripathi et al. [65]. This validation is performed under the condition of a straight artery ($\varepsilon = 0$) and $Re << 1$.

The distribution of the core region velocity with the radial direction for different values of hematocrit parameter (h_m) is depicted in the Figure (2.5). In this study, both cases

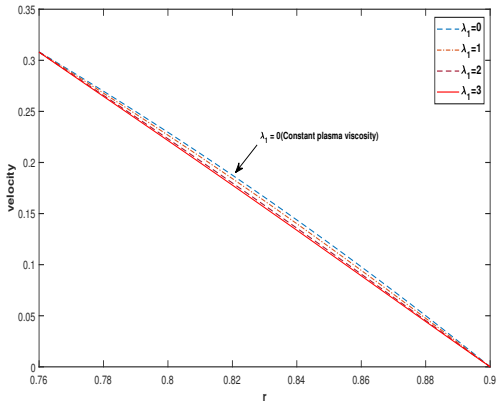

Figure 2.6: Variation in Plasma-region Velocity with λ_1

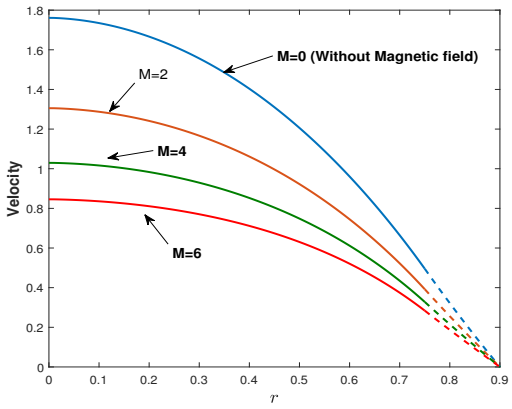

Figure 2.7: Variation of Velocity with different values of Magnetic field strength (M)

of constant viscosity ($h_m = 0$) and hematocrit dependent viscosity ($h_m \neq 0$) is considered. From the Figure (2.5), it can be observed that h_m directly affect the blood viscosity. It is widely accepted that as the hematocrit level rises, the dominance of red blood cells in the blood increases, causing the blood to thicken. As a result, blood viscosity enhances with the increment in the value of h_m, resulting in reduced fluid velocity in the core region. When a person is at rest and their heart rate is low, this decreased flow can raise the risk of tissue infarction. This figure also reveals that blood flow velocity is high if constant viscosity is considered in the modeling, while velocity in the core region, diminishes with the increment in the hematocrit parameter value (h_m). In contrast, the flow reaches near the interface of both layer, velocity shows reverse effects, and velocity increases slightly with a hike in the value of h_m.

The temperature has a significant impact on the viscosity of the flow. As a result, the current study has used a temperature-dependent viscosity model for the plasma region to better understand the temperature impact. The impact of temperature-dependent viscosity in the plasma region velocity is presented in Figure (2.6). Plasma viscosity depends on the λ_1, and temperature dominance decreases in plasma viscosity with the positive add in the value of λ_1. Therefore, with the rise in λ_1, plasma viscosity increases, resulting in retards of the blood flow, which is in fair agreement with experimental study of [60], that blood viscosity increases as temperature dominance in the blood flow decreases. A slight decay in plasma velocity with the rise in values of λ_1 can be noticed in the Figure (2.6). The present mathematical study revealed that the plasma viscosity of a curved artery rises with a drop in the flow temperature, as a result, blood velocity in plasma region decreases.

A comparative study to demonstrate the influence of magnetic field M on blood velocity in the radial direction is presented through the Figure (2.7). It is noted that blood is highly

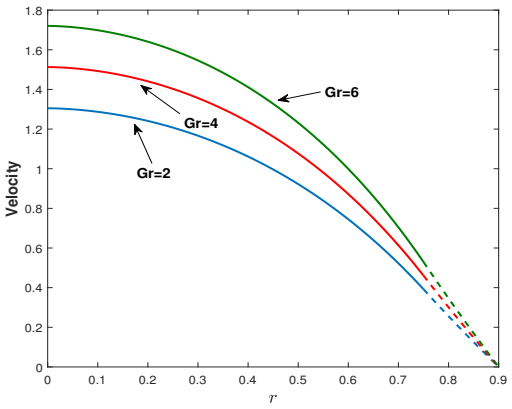

Figure 2.8: Variation of Velocity for Grashof number (Gr)

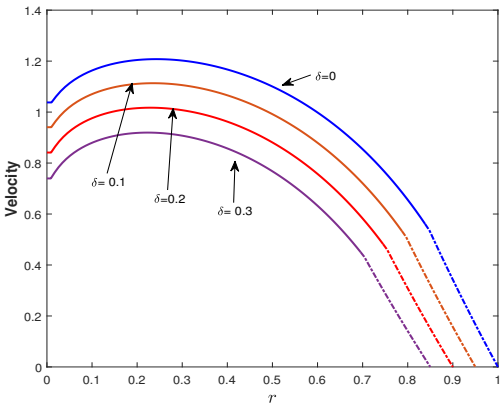

Figure 2.9: Variation in Velocity with maximum stenosis height parameter (δ)

affected by the magnetic field due to the presence of hemoglobin and magnetic iron oxide particles in it. Blood exhibits a strong electromotive field when it flows under the applied magnetic field. After applying the magnetic field, blood viscosity rises due to the generation of the Lorentz force, which reduced the flow velocity. From the Figure (2.7), it is concluded that decay in the blood velocity is observed with rise in the strength of magnetic field. It is perceived that with a hike in M from 0 to 2, depletion in velocity profile is high, in comparison with a hike in M from 2 to 4, so it can be concluded that the reduction rate of velocity profile decays with the enhancement in the magnetic field strength. The influence of thermal Grashof number (Gr) on blood velocity for a stenosed curved artery is deliberated in the Figure (2.8). A positive increment in the value of Gr, leads to the amplify in flow velocity which happen due to the dominance of buoyancy force over the viscous force.

Figure (2.9) illustrates the effect of maximum stenosis height (δ) of curved artery over the flow velocity. Effects of both cases of stenosis situation (with and without stenosis) are observed. When $\delta = 0$, it signifies that there is no stenosis in the artery and the value of non-dimensional radius becomes 1, as depth of the stenosis increase, then R reduces. From the figure, it is noted that, a slightly rise in the values of δ, leads to the diminishes in the flow velocity. It is also analyzed that velocity rises slowly in the radial direction from $r = 0$ to $r \approx 0.20$ due to shifting of maximum velocity towards the outer wall of artery after that it starts decreasing rapidly (non-linearly) and approaches to 0.

Figures (2.10-2.11) have been designed to analyze the impact of maximum stenosis height parameter (δ) and curvature parameter (ε) on the wall shear stress profile (τ_w), in the stenotic region of the curved artery. Range of the stenotic region is taken from z=0.75 to z=1.75. From both figures, a downfall in the τ_w profile can be observed in stenotic region from z=0.75 to 1.25, while a reverse effect in the magnitude of WSS observed in rest of

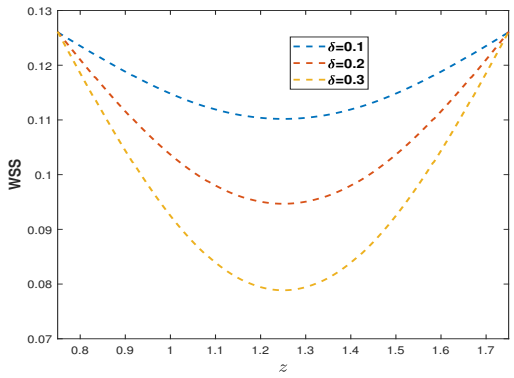

Figure 2.10: Variation in WSS with δ

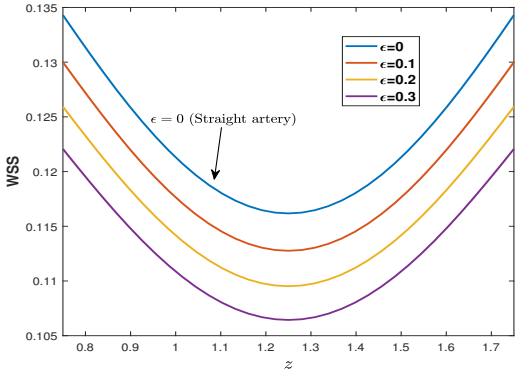

Figure 2.11: Variation in WSS with Curvature parameter (ε)

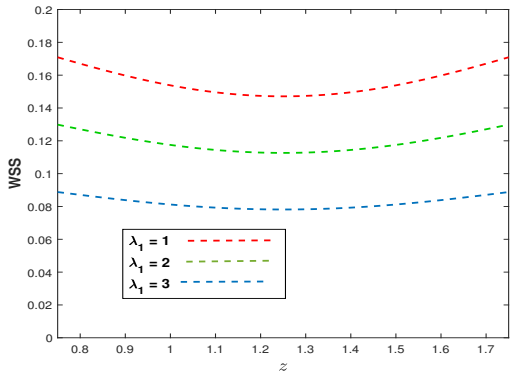

Figure 2.12: Variation in WSS with Plasma viscosity variation parameter (λ_1)

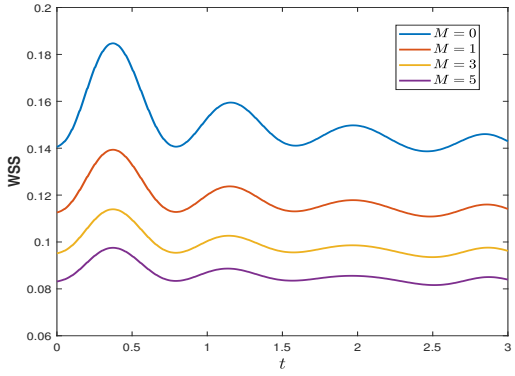

Figure 2.13: Variation in WSS for different values of M with time (t)

stenotic region. Figure (2.10) revels that, there is a inverse relation between WSS and maximum stenosis height (δ), i.e. a rising in δ leads to the decay in the WSS, and these finding have the significantly agreement with the observations of Mekheimer and Kot [16]. Curvature of the artery plays a significant role in the shear stress profile near the outer wall of artery, so that both curvature ($\varepsilon \neq 0$) and non-curvature ($\varepsilon = 0$) effects are considered. From the Figure (2.11), it is observed that the wall shear stress remain high in the straight artery ($\varepsilon = 0$), in comparison with the curved artery ($\varepsilon \neq 0$). It is also found that the high curvature leads to the diminishes in the τ_w , which reveals the similarity with the observations of [79]. From the above observations, it may be concluded that as arterial curvature increases, there is a greater risk of plaque (lipid) deposition in the flow due to a decrease in wall shear stress. This study also reveals the good agreement with the published experimental works [93] which suggest that the development of stenosis in the blood flow is responsible for decreasing the wall shear stress profile.

As per the previous study, plasma viscosity is influenced by the temperature, so temper-

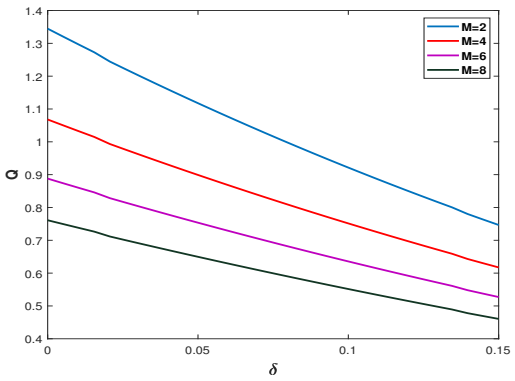

Figure 2.14: Variation in flow rate Q with M

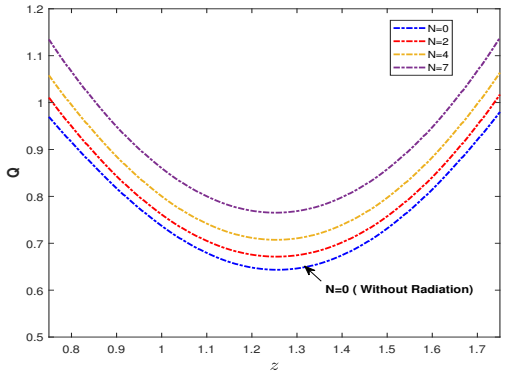

Figure 2.15: Variation in flow rate for radiation parameter N in the stenotic region

ature have significant role in the study of the wall shear stress. To demonstrate the effect of temperature (in terms of λ_1) on the τ_w in stenotic region is picturized graphically through the Figure (2.12). As concluded above, with the improvement in the value in λ_1, temperature dominance reduces in the blood flow, resulting in blood viscosity in the plasma region rising significantly. Therefore, with the positive add in λ_1, flow velocity slows down; due to this reason, friction in flow decays at the arterial wall. As a result, the magnitude of wall shear stress decreases with the enhancement in the value of λ_1. It is also observed that variation in the WSS profile for the whole stenotic region decreases with an increase in λ_1. The high WSS is responsible for endothelial damage and pathological response is suggested by Fry [94], so these type of damaging diseases, can be resolved by the reducing in the plasma viscosity (with increment in the λ_1), at the clinical surgery.

Figure (2.13) described the variation in wall shear stress profile with time (t) and observed an oscillation in the profile of WSS. The oscillatory profile of WSS shows the decaying nature with the increment in the time. The significance of magnetic field on the τ_w with the variation in time is observed in this figure, and noted that amplitude of the τ_w decreases with rising in M. In the absence of a magnetic field, flow exhibits significantly more shear stress in comparison with presence of the magnetic field i.e strong magnetic field strength leads to the decay in the τ_w with the marching in time.

Deviation in the flow rate profile (Q) with maximum stenosis height (δ) for the different values of magnetic field strength M is depicted in Figure (2.14). It is observed that, for a fixed numeric value of δ, a reduction in profile of flow rate can be seen with the rise in the value of M, due to generation of Lorentz force which retards the flow. It is also find that blood flow rate is higher for non-stenotic artery in comparison with the stenosed artery. The diminution rate of flow rate is high for low magnetic field strenght and it becomes low with enhancement in M.

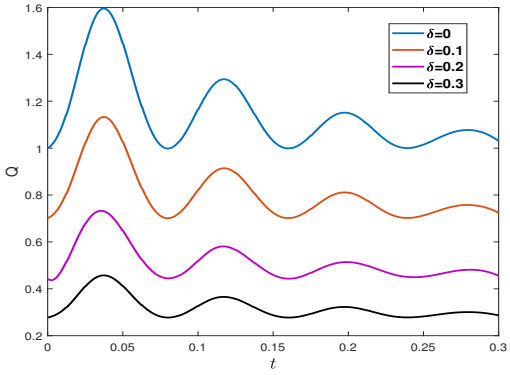

Figure 2.16: Variation of Q for stenotis height δ with time

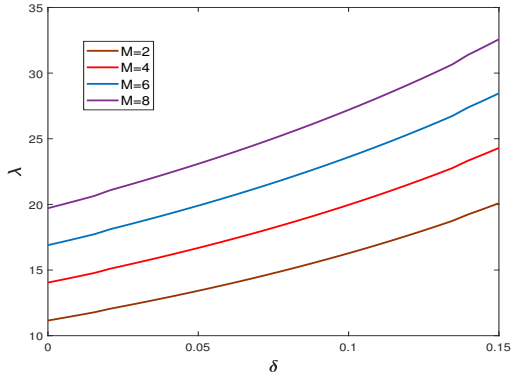

Figure 2.17: Variation of flow impedance λ with δ for magnetic field M

Figure (2.15) replicates the relation between flow rate and stenotic region of curved artery for the different values of radiation parameter (N), and perceived that rate of blood flow shows a decline nature as z increases from z=0.75 to 1.25 (due to increase in stenosis height), while opposite behavior is observed in the rest of stenotic region in axial direction. It is also noted that with increment in N, flow rate enhances. The oscillating behavior of flow rate along with time for various values of maximum stenosis height (δ) is analyzed graphically through the Figure 2.16 and it is clear that oscillation behaviour of flow rate decreases as time t increases. It is noticed that an enhancing in δ leads to decaying in Q, and amplitude of the oscillation shows the same effect with δ.

Figures (2.17) and (2.18) demonstrate the relation between frictional resistance λ and maximum stenosis height δ for the various numeric values of magnetic field and the length of the curved artery L. A growth (almost linearly) in the frictional resistance can be observed with an increase in stenosis depth and also concluded that friction friction is becomes lesser in the case of without stenosis ($\delta = 0$). An increment in the magnetic field strength leads to increase in flow resistance due to the generation of Lorentz force in the perpendicular to flow direction. The resistance of flow is highly influenced by the length of the curved artery and in this study it is detected that with an increase in length of artery, flow resistance becomes higher, this signify that frictional resistance is experienced higher in the large arteries that than for the small arteries.

The behavior of λ in the axial direction (stenotic region) for the different values of radiation parameter N is presented in the Figure (2.19) and pointed that, firstly flow resistance increase rapidly in the axial direction from z=.75 to 1.25 (stenosis height increases),after that it decrease in the rest of the stenosis region. The blood flow experienced maximum frictional resistance at z=1.25 (throat of stenosis). This figure shows that the implication of radiation parameter generates the heat in the blood flow; therefore, blood flow gets smoother.

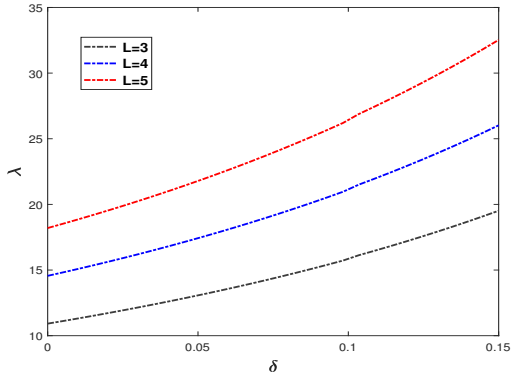

Figure 2.18: Variation of flow impedance with λ for artery length

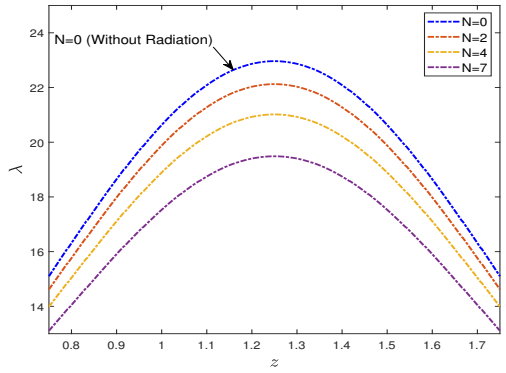

Figure 2.19: Variation of flow impedance in stenosis region$z$ for N

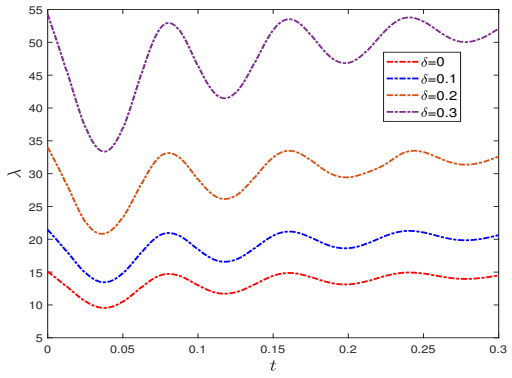

Figure 2.20: Variation of flow impedance with time t for δ

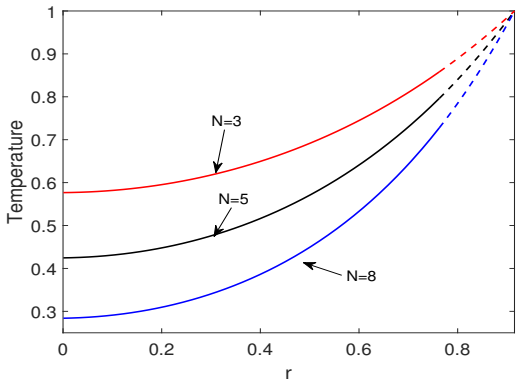

Figure 2.21: Variation of temperature profile for radiation parameter N

As a result, blood flow resistance diminishes significantly with the apply strong radiation in flow. It has also been worth noting that for the different values of N, the difference in the flow resistance becomes higher at the throat of stenosis than for the rest stenotic region. Figure (2.20) is developed to analyzed the variation in frictional resistance (λ) with time (t) for the different values of maximum stenosis height δ. The resistance exhibits an oscillation profile with t and these oscillation decays as t increases. It is also pointed out that resistance increases with the growth of stenosis height and amplitude of oscillation becomes higher with slightly rise in δ, which is in good agreement with the finding of [16].

The variation in the non-temperature profile in the radial direction for the different values of thermal radiation parameter (N) can be analyzed by Figure (2.21). The figure exhibits a non-linear growth of blood temperature in both core and plasma region with radial direction and attains maximum value near the arterial wall. A significant downfall in the temperature profile found with enhancement in radiation parameter. This happens because

thermal conductivity shows the reverse effect with radiation parameter, signifying that maximum heat is radiated away from the system. The outcome of our study shows a significant agreement with the previous findings [95, 6].

Blood flow trapping through a curved artery is an exciting phenomenon to understand flow nature. Figures (2.22-2.24) described the flow behaviour for the curved artery in the presence of mild stenosis for the different parameters such as M, N, ε. The streamlines show a smoothness in the flow due to steady flow and constant pressure gradient. The flow trapping configuration for different values of magnetic field is discussed in Figure (2.22), and a hinder in the maximum velocity region found with the enhancement in the magnetic field strength due to the occurrence of Lorentz force. The Figure (2.23) reveals the enhancement in the region for maximum velocity with the increase in radiation parameter from $N = 4$ to 6. The curvature of artery plays an important role in blood flow, and influence of curvature can be viewed through the Figure (2.24). From the above figure it is perceived that with the rise in the curvature from $\varepsilon = 0.2$ to 0.4, a downfall in the flow is observed, also it is concluded that curvature of artery retards the flow.

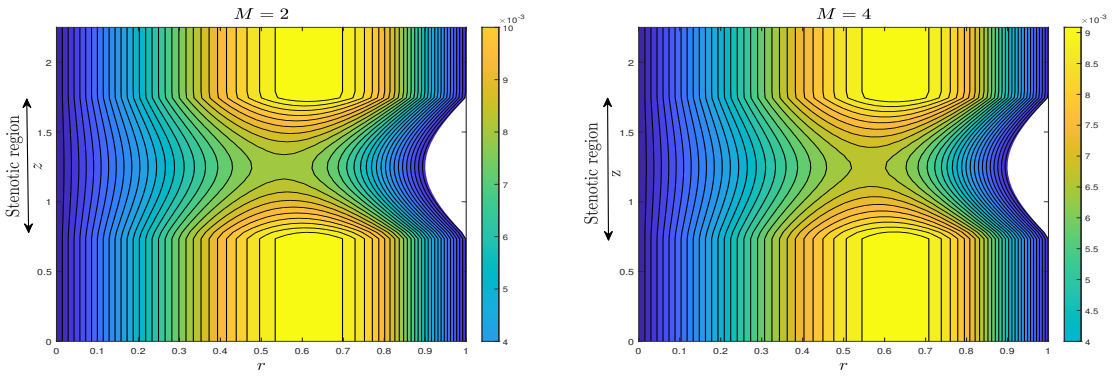

(a) (b)

Figure 2.22: Blood flow pattern for different values of Heat source, (a) $M = 2$, (b) $M = 4$.

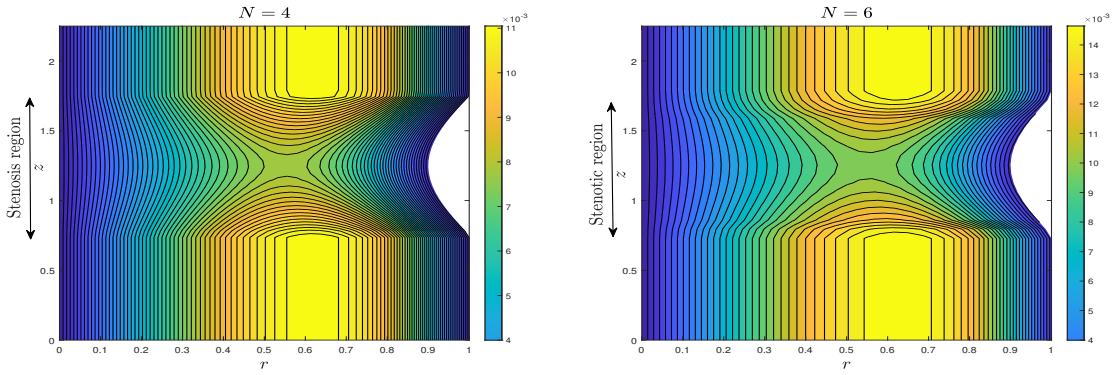

(a) (b)

Figure 2.23: Blood flow pattern for different values of radiation parameter, (a) $N = 4$, (b) $N = 6$.

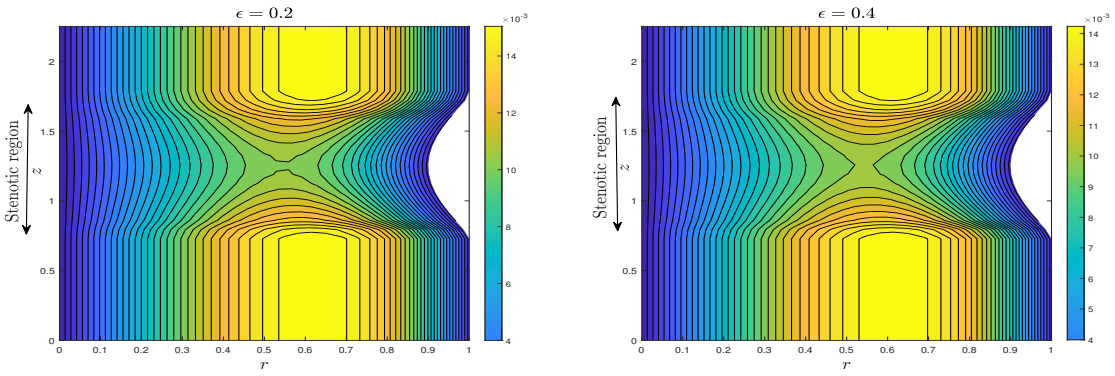

(a) (b)

Figure 2.24: Blood flow pattern for different values of curvature, (a) $\varepsilon = 0.2$, (b) $\varepsilon = 0.4$.

2.5 Conclusion

Mathematical investigation of a two-phase model for MHD blood flow through a stenosed curved artery with varying viscosity in both zones (core and plasma) has been presented in this study. A patient-specific artery geometry in the presence of stenosis (plaque) has been considered. Hematocrit-dependent viscosity is considered in the core region, whereas plasma region's viscosity is supposed to be temperature-dependent. The energy equation is solved using perturbation technique, while a second-order finite difference method is applied for momentum equation with the tolerance of 10^{-6} in iteration process. The graphical results demonstrate the influence of various physical parameters such as M, h_m, λ_1, δ, ε, N on the

blood velocity, flow rate, WSS, impedance and temperature profiles. Clinical researchers and biologists can adopt the current mathematical analysis of two-phase blood flow through a curved artery to lower the risk of atherosclerosis formation or assess the flow behaviour profile such as velocity, temperature, wall shear stress, and so on. They can also use this study to predict current status and fear of cardiovascular disease and then diagnose patients accordingly risk and situation. The major finding of the present study are listed below-

- Plasma viscosity is influenced by temperature, therefore positive rise in λ_1 leads to rise in wall shear stress whereas blood flow in plasma region shows reverse effects with λ_1 .
- Significant growth in fear of deposition of plaque (lipid) appears with the rise in arterial curvature, which happen due to a reduction in the wall shear stress profile.
- The use of external radiation parameter (N) in hyperthermia and laser therapies can reduce the deposition of plaque and clot at a time of healing process, which happens due to hike in flow temperature with increase in N.
- The flow velocity and WSS show the downfall in their own profiles with the increment in the magnetic field strength, whereas the frictional resistance profile increases.
- The flow velocity is higher for the uniform or less height of stenosis in the artery.
- The growth in stenosis height leads to the flow impedance, whereas flow rate shows the reverse effect.

Chapter 3

Hemodynamical analysis of MHD two phase blood flow through a curved permeable artery having variable viscosity with heat and mass transfer [1]

3.1 Introduction

Thermal therapies such as hyperthermia, laser treatment, and cryosurgery are all based on heat transfer techniques that are used to cure serious diseases, including cancer, clotting, destroying aberrant tissues, cardiovascular problems and so on. Therefore, in the computational study of blood flow, the researchers include the thermal properties in their mathematical modelling. Elmaboud et al. [41] performed a numerical study to demonstrate the effect of the heat source in the vertical annulus pipe and state that the heat transfer rate at the wall significantly rises with the positive addition in the value of the heat source. In this study, they also adopted the cylindrical shape catheter and suggested that maintaining the catheter radius ratio is important for both flow velocity and temperature. An experimental and computational study to prevent peritoneal metastasis cancer has been performed by Gorji et al. [96, 97, 98]. These studies adopted the pressurized intraperitoneal aerosol chemotherapy (PIPAC) and ePIPAC techniques to cure cancer. The aerosol formation has been determined experimentally using laser diffraction, while the aerosol distribution pattern is distinguished numerically in the "COMSOL"software. The influence of heat source and entropy generation in the peristaltic blood flow has been described by Ali et al. [99]. This study also signifies the importance of Cu-Ag nano-particles in the drug delivery process.

According to the authorized research, it found that endothelial walls have permeable nature in a realistic situation with ultramicroscopic pores, which used in the filtration. Deposition of cholesterol, fatty acid, dilated and damaged arterial wall is responsible for increased

[1] A considerable part of this chapter is published in *Biomechanics and Modelling in Mechanobiology*, 21(3), 797-825, 2022.

permeability. Firstly, Beaver et al. [100] did an experimental study and observed that Darcy law might not necessarily satisfy the governing equations at the wall. They also developed the mathematical model for the boundary condition at the permeable wall. Further, this study is carried forward by [101], in which they analyzed the laminar flow in a rectangular duct by considering one wall is permeable and the rest impermeable. An analytical investigation of pulsatile blood flow through a stenotic artery has performed by Chakravarti et al.[102]. This study considers vessel wall as the composition of two-layer such as media and adventitia layer. Mishra et al.[103] presented a mathematical model to inspect the impact of permeable wall on the wall shear stress and flow rate profile. Srivastav et al. [104] assumed blood as two-fluid (core and plasma region fluid) and developed a mathematical model of the two-fluid blood flow model to calculate the frictional impedance of the flow. According to this study, the arterial wall's permeability aids in the operation of the sick artery. Khahshan et al.[105] recently present theoretical research on blood (Casson fluid) filtration between two permeable membranes. Furthermore, Ellahi et al.[106, 107] developed various blood flow models to figure out the role of permeable wall under the condition of tapered/ uniform stenosed artery, nanofluid and magnetic field.

All the above-published experimental and numerical research signifies the momentum and heat transfer phenomena for single/ two-phase blood flow model, and flow passes through the stenotic circular/ curved artery. As per author's best knowledge, the effect of heat and mass transfer for two-phase blood flow for the stenosed permeable curved artery (assuming toroidal coordinate system) with variable viscosity has not been studied earlier. Our study considered mass transfer as a decisive part of the investigation to emphasize the role of mass movement from one place to another in the two-phase blood flow model. Therefore, we performed a numerical study to explain the heat and mass transfer phenomena for the two-phase blood flow through permeable curved artery. By motivated from above literature, a temperature-dependent viscosity in the core region has been considered. In the present study, mathematical analysis of temperature-dependent viscosity, magnetic field, heat source, wall permeability and chemical reaction on the two-phase blood flow through the stenotic curved artery is depicted. A second-order finite difference scheme [91] is adopted to simplify the non-dimensional velocity, temperature, and concentration equations for both core and plasma region under the consideration of mild stenosis and fully developed flow condition. Clinical researchers and biologists can adopt the present mathematical study to lower the risk of lipid deposition, to predict the risk of cardiovascular disease and current stateof disease by understanding the symptomatic spectrum, and then diagnose patients based on risk.

3.2 Problem formulation

An unsteady, viscous, laminar and incompressible blood flow through a stenosed curved artery of finite length L is considered in this study as shown in figure 3.1. The arterial wall is considered of permeable nature. As per the suggestion of published work [87, 88], a two-phase blood flow approach has been considered for the more realistic situation. Let (r,θ,z) be the toroidal system's coordinates, which are employed to investigate the flow behaviour in the geometry mentioned earlier. The z-axis represents the curved artery's axis, and r is taken along the radial direction. The direction of blood flow is along the z-direction. The blood flow velocity is $V = (u(r,\theta,z), v(r,\theta,z), w(r,\theta,z))$.

A uniform magnetic field B is applied perpendicular to the blood flow (axial direction z). In this investigation, the magnetic Reynold number is considered very small ($Re <<< 1$) so that the induced magnetic field can be ignored, also the electric field is taken to be zero. The fully developed flow condition for the blood flow is considered in this study, which indicates that flow velocity and temperature profile will not be changed along the flow direction (z-axis). In the core region, temperature-dependent viscosity is taken while plasma region viscosity is assumed as constant.

3.2.1 Geometry of the stenosis

Time dependent stenosis is considered for both core and plasma wall and represented by $R_1(z,t)$ and $R(z,t)$, respectively. Mathematically expressions of elliptic shape stenoses are as follows [92]:
Geometry of the stenosis in plasma region is considered as:

$$R(z,t) = \begin{cases} \left[R_0 - \delta \sin\left(\pi(\frac{z-d}{L_0})\right)\right]\Omega(t) & \text{for} \quad d \le z \le d+L_0, \\ R_0\Omega(t) & \text{otherwise.} \end{cases} \tag{3.1}$$

Geometry of stenosis in the core region is considered as:

$$R_1(z,t) = \begin{cases} \left[\beta R_0 - \delta \sin\left(\pi(\frac{z-d}{L_0})\right)\right]\Omega(t) & \text{for} \quad d \le z \le d+L_0, \\ \beta R_0\Omega(t) & \text{otherwise.} \end{cases} \tag{3.2}$$

The time-varying parameter $\Omega(t)$ is expressed as

$$\Omega(t) = 1 - \eta(\cos(\omega t) - 1)e^{-\eta\omega t}. \tag{3.3}$$

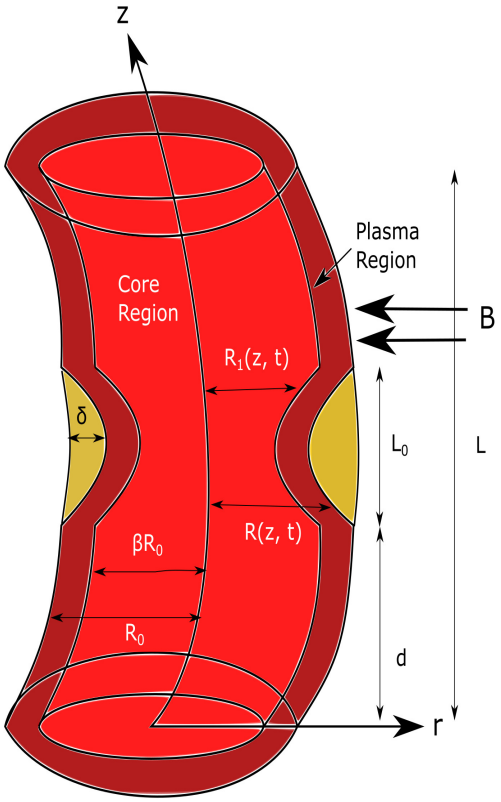

Figure 3.1: Geometry of two-phase stenosed curved artery

where L_0 is the length of stenosis
R_0 radius of normal artery, δ is the maximum height of stenosis, d is the location of stenosis, β is ratio of central core radius to normal artery radius, L is the length of artery, η is constant, ω are the angular frequency of the forced oscillation.

3.2.2 Variable viscosity model

The blood viscosity for the core-region is considered as temperature dependent, and mathematical form is given by [36]

$$\mu_c(T) = \mu_p \exp\left[\lambda_1\left(\frac{1}{2} - \frac{T_c - T_0}{T_w - T_0}\right)\right]. \tag{3.4}$$

3.2.3 Governing equations

The governing equations for curved tube for both core and plasma regions are deliberated as follows [16, 108]

Continuity Equation :

$$\frac{b}{D}\frac{\partial w}{\partial z}+\frac{\partial u}{\partial r}+\frac{1}{r}\frac{\partial v}{\partial \theta}+\frac{u}{r}+\frac{u\cos\theta-v\sin\theta}{D}=0, \tag{3.5}$$

where, b denotes the radius of curvature.

$$D=b+r\cos\theta,$$

For the Core region i.e. $0<r<R_1(z,t)$
Momentum equations-
r-direction:

$$\rho_c\left(\frac{\partial u_c}{\partial t}+\frac{bw_c}{D}\frac{\partial u_c}{\partial z}+u_c\frac{\partial u_c}{\partial r}+\frac{v_c}{r}\frac{\partial u_c}{\partial \theta}-\frac{v_c^2}{r}-\frac{w_c^2\cos\theta}{D}\right)=-\frac{\partial P_c}{\partial r}+\mu_c(T)\left(\frac{\partial^2 u_c}{\partial r^2}+\frac{1}{r}\frac{\partial u_c}{\partial r}\right.$$
$$\left.-\frac{u_c}{r^2}+\frac{b^2}{D^2}\frac{\partial^2 u_c}{\partial z^2}+\frac{1}{r^2}\frac{\partial^2 u_c}{\partial \theta^2}-\frac{2}{r^2}\frac{\partial v_c}{\partial \theta}+\frac{1}{D}\left[\cos\theta\frac{\partial u_c}{\partial r}-\frac{\sin\theta}{r}\frac{\partial u_c}{\partial \theta}+\frac{v_c\sin\theta}{r}\right]+\frac{2b\sin\theta}{D^2}\frac{\partial w_c}{\partial z}\right.$$
$$\left.-\frac{\cos\theta}{D^2}[u_c\cos\theta-v_c\sin\theta]\right)+\left[\frac{4}{3}\frac{\partial u_c}{\partial r}-\frac{2}{3}\left(\frac{b}{D}\frac{\partial w_c}{\partial z}+\frac{1}{r}\frac{\partial v_c}{\partial \theta}+\frac{u_c\cos\theta-v_c\sin\theta}{D}+\frac{u_c}{r}\right)\right]$$
$$\frac{\partial \mu_c(T)}{\partial r}+\left(\frac{1}{r}\frac{\partial v_c}{\partial r}-\frac{v_c}{r^2}+\frac{1}{r^2}\frac{\partial u_c}{\partial \theta}\right)\frac{\partial \mu_c(T)}{\partial \theta}+\left(\frac{b^2}{D^2}\frac{\partial u_c}{\partial z}+\frac{b}{D}\frac{\partial w_c}{\partial r}-\frac{bw_c\cos\theta}{D^2}\right)\frac{\partial \mu_c(T)}{\partial z}, \tag{3.6}$$

θ- direction :

$$\rho_c\left(\frac{\partial v_c}{\partial t}+\frac{w_c b}{D}\frac{\partial v_c}{\partial z}+u_c\frac{\partial v_c}{\partial r}+\frac{v_c}{r}\frac{\partial v_c}{\partial \theta}+\frac{u_c v_c}{r}+\frac{w_c^2\sin\theta}{D}\right)=-\frac{1}{r}\frac{\partial P_c}{\partial \theta}+\mu_c(T)\left(\frac{\partial^2 v_c}{\partial r^2}+\frac{1}{r}\frac{\partial v_c}{\partial r}\right.$$
$$\left.-\frac{v_c}{r^2}+\frac{b^2}{D^2}\frac{\partial^2 v_c}{\partial z^2}+\frac{1}{r^2}\frac{\partial^2 v_c}{\partial \theta^2}+\frac{2}{r^2}\frac{\partial u_c}{\partial \theta}+\frac{1}{D}\left[\cos\theta\frac{\partial v_c}{\partial r}-\frac{\sin\theta}{r}\frac{\partial v_c}{\partial \theta}-\frac{u_c\sin\theta}{r}\right]+\frac{2b\sin\theta}{D^2}\frac{\partial w_c}{\partial z}\right.$$
$$\left.+\frac{\sin\theta}{D^2}[u_c\cos\theta-v_c\sin\theta]\right)+\left(\frac{\partial v_c}{\partial r}-\frac{v_c}{r}+\frac{1}{r}\frac{\partial u_c}{\partial \theta}\right)\frac{\partial \mu_c(T)}{\partial r}+\left[\frac{4}{3}\left(\frac{1}{r^2}\frac{\partial v_c}{\partial \theta}+\frac{u_c}{r^2}\right)\right.$$
$$\left.-\frac{2}{3}\left(\frac{1}{r}\frac{b}{D}\frac{\partial w_c}{\partial z}+\frac{1}{r}\frac{u_c\cos\theta-v_c\sin\theta}{D}+\frac{1}{r}\frac{\partial u_c}{\partial r}\right)\right]\frac{\partial \mu_c(T)}{\partial \theta}+\frac{b}{D}\left(\frac{1}{r}\frac{\partial w_c}{\partial \theta}+\frac{w_c\sin\theta}{D}\right.$$
$$\left.+\frac{b}{D}\frac{\partial v_c}{\partial z}\right)\frac{\partial \mu_c(T)}{\partial z}, \tag{3.7}$$

z- direction :

$$\rho_c\left(\frac{\partial w_c}{\partial t}+\frac{w_c b}{D}\frac{\partial w_c}{\partial z}+u_c\frac{\partial w_c}{\partial r}+\frac{v_c}{r}\frac{\partial w_c}{\partial \theta}+\frac{w_c(u_c\cos\theta-v_c\sin\theta)}{D}\right)=-\frac{b}{D}\frac{\partial P_c}{\partial z}+\mu_c(T)\left(\frac{\partial^2 w_c}{\partial r^2}\right.$$
$$+\frac{b^2}{D^2}\frac{\partial^2 w_c}{\partial z^2}+\frac{1}{r}\frac{\partial w_c}{\partial r}+\frac{1}{r^2}\frac{\partial^2 w_c}{\partial \theta^2}-\frac{w_c}{D^2}+\frac{1}{D}\left[\cos\theta\frac{\partial w_c}{\partial r}-\frac{\sin\theta}{r}\frac{\partial w_c}{\partial \theta}\right]+\frac{2b}{D^2}\left[\cos\theta\frac{\partial u_c}{\partial z}\right.$$
$$\left.\left.-\sin\theta\frac{\partial v_c}{\partial z}\right]\right)+\left(\frac{b}{D}\frac{\partial u_c}{\partial z}+\frac{\partial w_c}{\partial r}-\frac{w_c\cos\theta}{D}\right)\frac{\partial \mu_c(T)}{\partial r}+\left(\frac{1}{r^2}\frac{\partial w_c}{\partial \theta}+\frac{w_c\sin\theta}{rD}+\frac{b}{rD}\frac{\partial v_c}{\partial z}\right)$$
$$\frac{\partial \mu_c(T)}{\partial \theta}+\frac{b}{D}\left[\frac{4}{3}\left(\frac{b}{D}\frac{\partial w_c}{\partial z}+\frac{u_c\cos\theta-v_c\sin\theta}{D}\right)-\frac{2}{3}\left(\frac{\partial u_c}{\partial r}+\frac{1}{r}\frac{\partial v_c}{\partial \theta}+\frac{u_c}{r}\right)\right]\frac{\partial \mu_c(T)}{\partial z}-\sigma B^2 w_c$$
$$+g\rho_c\gamma_T(T_c-T_0)+g\rho_c\gamma_c^*(C_c-C_0) \tag{3.8}$$

, Energy equation :

$$\rho_c\bar{C}_c\left(\frac{\partial T_c}{\partial t}+u_c\frac{\partial T_c}{\partial r}+\frac{v_c}{r}\frac{\partial T_c}{\partial \theta}+\frac{w_c b}{D}\frac{\partial T_c}{\partial z}\right)=K_c\left(\frac{\partial^2 T_c}{\partial r^2}+\frac{1}{r}\frac{\partial T_c}{\partial r}+\frac{b^2}{D^2}\frac{\partial^2 T_c}{\partial z^2}+\frac{\cos\theta}{D}\frac{\partial T_c}{\partial r}\right.$$
$$\left.-\frac{\sin\theta}{rD}\frac{\partial T_c}{\partial \theta}+\frac{1}{r^2}\frac{\partial^2 T_c}{\partial \theta^2}\right)+Q_c, \tag{3.9}$$

Concentration equation :

$$\left(\frac{\partial C_c}{\partial t}+u_c\frac{\partial C_c}{\partial r}+\frac{v_c}{r}\frac{\partial C_c}{\partial \theta}+\frac{w_c b}{D}\frac{\partial C_c}{\partial z}\right)=D_c\left(\frac{\partial^2 C_c}{\partial r^2}+\frac{1}{r}\frac{\partial C_c}{\partial r}+\frac{b^2}{D^2}\frac{\partial^2 C_c}{\partial z^2}+\frac{\cos\theta}{D}\frac{\partial C_c}{\partial r}\right.$$
$$\left.-\frac{\sin\theta}{rD}\frac{\partial C_c}{\partial \theta}+\frac{1}{r^2}\frac{\partial^2 C_c}{\partial \theta^2}\right)-R_c(C_c-C_0). \tag{3.10}$$

Where, u_c, v_c, w_c are the dimensional core region velocity component in r, θ, z directions, respectively.

$\mu_c, T_c, C_c, \rho_c, K_c, B, D_c, R_c$ are the dimensional viscosity, temperature,concentration density, thermal conductivity, uniform magnetic field, mass diffusivity and dimensional chemical reaction parameter in the core region, respectively.

Plasma region i.e. $R_1(z,t) < r < R(z,t)$

Momentum equations-

r-direction :

$$\rho_p\left(\frac{\partial u_p}{\partial t}+\frac{bw_p}{D}\frac{\partial u_p}{\partial z}+u_p\frac{\partial u_p}{\partial r}+\frac{v_p}{r}\frac{\partial u_p}{\partial \theta}-\frac{v_p^2}{r}-\frac{w_p^2\cos\theta}{D}\right)=-\frac{\partial P_p}{\partial r}+\mu_p\left(\frac{\partial^2 u_p}{\partial r^2}+\frac{1}{r}\frac{\partial u_p}{\partial r}\right.$$
$$-\frac{2}{r^2}\frac{\partial v_p}{\partial \theta}+\frac{b^2}{D^2}\frac{\partial^2 u_p}{\partial z^2}-\frac{u_p}{r^2}+\frac{1}{r^2}\frac{\partial^2 u_p}{\partial \theta^2}+\frac{1}{D}\left[\cos\theta\frac{\partial u_p}{\partial r}-\frac{\sin\theta}{r}\frac{\partial u_p}{\partial \theta}+\frac{v_p\sin\theta}{r}\right]$$
$$\left.+\frac{2b\sin\theta}{D^2}\frac{\partial w_p}{\partial z}-\frac{\cos\theta}{D^2}[u_p\cos\theta-v_p\sin\theta]\right), \tag{3.11}$$

θ- direction :

$$\rho_p\left(\frac{\partial v_p}{\partial t}+\frac{w_p b}{D}\frac{\partial v_p}{\partial z}+u_p\frac{\partial v_p}{\partial r}+\frac{v_p}{r}\frac{\partial v_p}{\partial \theta}+\frac{u_p v_p}{r}+\frac{w_p^2\sin\theta}{D}\right)=-\frac{1}{r}\frac{\partial P_p}{\partial \theta}+\mu_p\left(\frac{\partial^2 v_p}{\partial r^2}\right.$$
$$+\frac{1}{r}\frac{\partial v_p}{\partial r}+\frac{2}{r^2}\frac{\partial u_p}{\partial \theta}+\frac{b^2}{D^2}\frac{\partial^2 v_p}{\partial z^2}-\frac{v_p}{r^2}+\frac{1}{r^2}\frac{\partial^2 v_p}{\partial \theta^2}+\frac{1}{D}\left[\cos\theta\frac{\partial v_p}{\partial r}-\frac{\sin\theta}{r}\frac{\partial v_p}{\partial \theta}-\frac{u_p\sin\theta}{r}\right]$$
$$\left.+\frac{2b\sin\theta}{D^2}\frac{\partial w_p}{\partial z}+\frac{\sin\theta}{D^2}[u_p\cos\theta-v_p\sin\theta]\right), \tag{3.12}$$

z- direction :

$$\rho_p\left(\frac{\partial w_p}{\partial t}+\frac{w_p b}{D}\frac{\partial w_p}{\partial z}+u_p\frac{\partial w_p}{\partial r}+\frac{v_p}{r}\frac{\partial w_p}{\partial \theta}+\frac{w_p(u_p\cos\theta-v_p\sin\theta)}{D}\right)=-\frac{b}{D}\frac{\partial P_p}{\partial z}+\mu_p$$
$$\left(\frac{\partial^2 w_p}{\partial r^2}+\frac{b^2}{D^2}\frac{\partial^2 w_p}{\partial z^2}+\frac{1}{r^2}\frac{\partial^2 w_p}{\partial \theta^2}+\frac{1}{r}\frac{\partial w_p}{\partial r}-\frac{w_p}{D^2}+\frac{1}{D}\left[\cos\theta\frac{\partial w_p}{\partial r}-\frac{\sin\theta}{r}\frac{\partial w_p}{\partial \theta}\right]\right.$$
$$\left.+\frac{2b}{D^2}\left[\cos\theta\frac{\partial u_p}{\partial z}-\sin\theta\frac{\partial v_p}{\partial z}\right]\right)-\sigma B^2 w_p+g\rho_p\gamma_T(T_p-T_0)+g\rho_p\gamma_c^*(C_p-C_0), \tag{3.13}$$

Energy equation :

$$\rho_p\bar{C}_p\left(\frac{\partial T_p}{\partial t}+u_p\frac{\partial T_p}{\partial r}+\frac{v_p}{r}\frac{\partial T_p}{\partial \theta}+\frac{w_p b}{D}\frac{\partial T_p}{\partial z}\right)=K_p\left(\frac{\partial^2 T_p}{\partial r^2}+\frac{1}{r}\frac{\partial T_p}{\partial r}+\frac{b^2}{D^2}\frac{\partial^2 T_p}{\partial z^2}+\frac{\cos\theta}{D}\frac{\partial T_p}{\partial r}\right.$$
$$\left.-\frac{\sin\theta}{rD}\frac{\partial T_p}{\partial \theta}+\frac{1}{r^2}\frac{\partial^2 T_p}{\partial \theta^2}\right)+Q_p, \tag{3.14}$$

Concentration equation :

$$\left(\frac{\partial C_p}{\partial t}+u_p\frac{\partial C_p}{\partial r}+\frac{v_p}{r}\frac{\partial C_p}{\partial \theta}+\frac{w_p b}{D}\frac{\partial C_p}{\partial z}\right)=D_p\left(\frac{\partial^2 C_p}{\partial r^2}+\frac{1}{r}\frac{\partial C_p}{\partial r}+\frac{b^2}{D^2}\frac{\partial^2 C_p}{\partial z^2}+\frac{\cos\theta}{D}\frac{\partial C_p}{\partial r}\right.$$
$$\left.-\frac{\sin\theta}{rD}\frac{\partial C_p}{\partial \theta}+\frac{1}{r^2}\frac{\partial^2 C_p}{\partial \theta^2}\right)-R_p(C_p-C_0). \tag{3.15}$$

Where, u_p, v_p, w_p are the dimensional plasma region velocity component in r, θ, z directions, respectively.

$\mu_p, T_p, C_p, \rho_p, K_p, B, D_p, R_p$ are the dimensional viscosity, temperature, concentration, density, thermal conductivity, uniform magnetic field, mass diffusivity and dimensional chemical reaction parameter in the plasma region, respectively.

3.2.4 Non-dimensional and mild stenosis simplification:

To reduce above dimensional governing equations into dimensionless equations for both regions, we will introduce non-dimensional parameters which are listed in table 3.1-

Table 3.1: Non-dimensional parameter

$r = R_0 r'$	$z = L_0 z'$	$\theta = \theta'$	$\omega = \frac{u_0}{L_0}\omega'$	$L = L_0 L'$
$d = L_0 d'$	$t = \frac{L_0}{u_0} t'$	$R = R_0 R'$	$R_1 = R_0 R_1'$	$u_c = \frac{\delta u_0}{L_0} u_c'$
$v_c = \frac{\delta u_0}{L_0} v_c'$	$w_c = u_0 w_c'$,	$u_p = \frac{\delta u_0}{L_0} u_p'$	$v_p = \frac{\delta u_0}{L_0} v_p'$	$w_p = u_0 w_p'$
$P_c = \frac{u_0 L_0 \mu_p}{R_0^2} P_c'$	$P_p = \frac{u_0 L_0 \mu_p}{R_0^2} P_p'$	$\alpha = \frac{R_0}{L_0}$	$\theta_c = \frac{T_c - T_0}{T_w - T_0}$,	$\theta_p = \frac{T_p - T_0}{T_w - T_0}$
$\delta^* = \frac{\delta}{R_0}$	$Q_0 = \frac{Q_p}{Q_c}$	$\phi_c = \frac{C_c - C_0}{C_w - C_0}$	$\phi_p = \frac{C_p - C_0}{C_w - C_0}$	$\rho_0 = \frac{\rho_p}{\rho_c}$
$Re = \frac{\rho_p R_0 u_0}{\mu_p}$	$Gr = \frac{g\rho_p \gamma_T R_0^2 (T_w - T_0)}{u_0 \mu_p}$	$\varepsilon = \frac{R_0}{b}$	$k_0 = \frac{K_p}{K_c}$	$\tau_c = \frac{\tau_c' u_0 \mu_p}{R_0^2}$
$\tau_p = \frac{\tau_p' u_0 \mu_p}{R_0^2}$	$M = \frac{\sigma B^2 R_0^2}{\mu_p}$	$Gm = \frac{g\rho_p \gamma_c^* R_0^2 (C_w - C_0)}{u_0 \mu_p}$	$\xi = \frac{R_p \rho_p R_0^2}{\mu_p}$	$\xi_0 = \frac{R_p}{R_c}$
$s_0 = \frac{\bar{C}_p}{\bar{C}_c}$	$Sc = \frac{\mu_p}{\rho_p D_p}$	$D_0 = \frac{D_p}{D_c}$	$K_0 = \frac{K_p}{K_c}$	$H = \frac{Q_p R_0^2}{(T_w - T_0) K_p}$

The dimensionless form of the stenoses geometry for both core and plasma regions are given as follows:

$$R'(z',t') = \begin{cases} \left[1 - \delta^* \sin\left(\pi(z' - d')\right)\right]\Omega(t') & \text{for} \quad d' \le z' \le d' + 1, \\ \Omega(t') & \text{otherwise}, \end{cases} \tag{3.16}$$

$$R_1'(z',t') = \begin{cases} \left[\beta - \delta^* \sin\left(\pi(z' - d')\right)\right]\Omega(t') & \text{for} \quad d' \le z' \le d' + 1, \\ \beta\Omega(t') & \text{otherwise}. \end{cases} \tag{3.17}$$

With the help of above mentioned non-dimensional parameters and considering the assumed condition of fully developed flow, low Reynold number ($Re <<< 1$), mild stenosis ($\delta^* << 1$) with $O(1) = \alpha = \frac{R_0}{L_0}$, the governing equations of both core and plasma region are converted into more simpler form as follows:

Core region

$$\frac{\partial P_c'}{\partial r'} = 0, \tag{3.18}$$

$$\frac{\partial P_c'}{\partial \theta'} = 0, \tag{3.19}$$

$$\frac{1}{\bar{D}}\frac{\partial P_c'}{\partial z'} = \exp(\lambda_1[1/2 - T_c'])\left(\frac{\partial^2 w_c'}{\partial r'^2} + \frac{1}{r'}\frac{\partial w_c'}{\partial r'} - \frac{\varepsilon^2 w_c'}{\bar{D}^2} + \frac{\varepsilon}{\bar{D}}\left[\cos\theta'\frac{\partial w_c'}{\partial r'} - \frac{\sin\theta'}{r'}\frac{\partial w_c'}{\partial \theta'}\right] + \frac{1}{r'^2}\frac{\partial^2 w_c'}{\partial \theta'^2}\right) - \lambda_1 \exp(\lambda_1[1/2 - T_c'])\left(\frac{\partial w_c'}{\partial r'} - \frac{\varepsilon w_c' \cos\theta'}{\bar{D}}\right)\frac{\partial T_c'}{\partial r'} - \lambda_1 \exp(\lambda_1[1/2 - \theta_c])\left(\frac{1}{r'^2}\frac{\partial w_c'}{\partial \theta'} + \frac{\varepsilon w_c' \sin\theta'}{r'\bar{D}}\right)\frac{\partial \theta_c}{\partial \theta'} - Mw_c' + \frac{GrT_c' + GmC_c'}{\rho_0}, \tag{3.20}$$

$$\frac{\partial^2 T_c'}{\partial r'^2} + \frac{1}{r'}\frac{\partial T_c'}{\partial r'} + \frac{\varepsilon\cos\theta'}{\bar{D}}\frac{\partial T_c'}{\partial r'} - \frac{\varepsilon\sin\theta'}{r'\bar{D}}\frac{\partial T_c'}{\partial \theta'} + \frac{1}{r'^2}\frac{\partial^2 T_c'}{\partial \theta'^2} + \frac{k_0}{Q_0}H = 0, \tag{3.21}$$

$$\frac{1}{D_0 Sc}\left(\frac{\partial^2 C_c'}{\partial r'^2} + \frac{1}{r'}\frac{\partial C_c'}{\partial r'} + \frac{\varepsilon\cos\theta'}{\bar{D}}\frac{\partial C_c'}{\partial r'} - \frac{\varepsilon\sin\theta'}{r'\bar{D}}\frac{\partial C_c'}{\partial \theta'} + \frac{1}{r'^2}\frac{\partial^2 C_c'}{\partial \theta'^2}\right) - \frac{\xi}{\xi_0}C_c' = 0, \tag{3.22}$$

where

$$\bar{D} = 1 + \varepsilon r'\cos\theta',$$

Plasma region

$$\frac{\partial P_p'}{\partial r'} = 0, \tag{3.23}$$

$$\frac{\partial P_p'}{\partial \theta'} = 0, \tag{3.24}$$

$$\frac{1}{\bar{D}}\frac{\partial P_p'}{\partial z'} = \left(\frac{\partial^2 w_p'}{\partial r'^2} + \frac{1}{r'}\frac{\partial w_p'}{\partial r'} + \frac{1}{r'^2}\frac{\partial^2 w_p'}{\partial \theta'^2} - \frac{\varepsilon^2 w_p'}{\bar{D}^2} + \frac{\varepsilon}{\bar{D}}\left[\cos\theta'\frac{\partial w_p'}{\partial r'} - \frac{\sin\theta'}{r'}\frac{\partial w_p'}{\partial \theta'}\right]\right) - Mw_p' + GrT_p' + GmC_p', \tag{3.25}$$

$$\frac{\partial^2 T_p'}{\partial r'^2} + \frac{1}{r'}\frac{\partial T_p'}{\partial r'} + \frac{\varepsilon\cos\theta'}{\bar{D}}\frac{\partial T_p'}{\partial r'} - \frac{\varepsilon\sin\theta'}{r'\bar{D}}\frac{\partial T_p'}{\partial \theta'} + \frac{1}{r'^2}\frac{\partial^2 T_p'}{\partial \theta'^2} + H = 0, \tag{3.26}$$

$$\frac{1}{Sc}\left(\frac{\partial^2 C_p'}{\partial r'^2} + \frac{1}{r'}\frac{\partial C_p'}{\partial r'} + \frac{\varepsilon\cos\theta'}{\bar{D}}\frac{\partial C_p'}{\partial r'} - \frac{\varepsilon\sin\theta'}{r'\bar{D}}\frac{\partial C_p'}{\partial \theta'} + \frac{1}{r'^2}\frac{\partial^2 C_p'}{\partial \theta'^2}\right) - \xi C_p' = 0, \tag{3.27}$$

Non-dimensional boundary conditions for both core and plasma region are given as-

$$\begin{cases} \frac{\partial w_c'}{\partial r'}=0, & \frac{\partial T_c'}{\partial r'}=0, & \frac{\partial C_c'}{\partial r'}=0, & \text{at} \quad r'=0, \\ w_c'=w_p', & T_c'=T_p', & C_c'=C_p', & \text{at} \quad r'=R_1'(z',t'), \\ \tau_c'=\tau_p', & \frac{\partial T_c'}{\partial r'}=\frac{\partial T_p'}{\partial r'}, & \frac{\partial C_c'}{\partial r'}=\frac{\partial C_p'}{\partial r'}, & \text{at} \quad r'=R_1'(z',t'), \\ w_p'=w_b, & \frac{\partial w_p'}{\partial r'}=\frac{\zeta}{\sqrt{Da}}(w_b-w_{porous}), & & \text{at} \quad r'=R'(z',t') \\ T_p'=1, & C_p'=1, & & \text{at} \quad r'=R'(z',t'), \\ \frac{\partial w_c'}{\partial \theta'}=0, & \frac{\partial T_c'}{\partial \theta'}=0, & \frac{\partial C_c'}{\partial \theta'}=0 & \text{at} \quad \theta'=0 \quad \text{and} \quad \theta'=\pi, \\ \frac{\partial w_p'}{\partial \theta'}=0, & \frac{\partial T_p'}{\partial \theta'}=0, & \frac{\partial C_p'}{\partial \theta'}=0, & \text{at} \quad \theta'=0 \quad \text{and} \quad \theta'=\pi. \end{cases} \tag{3.28}$$

Where $w_{porous}=-\left(\frac{Da}{\mu_p}\right)\frac{\partial P_p'}{\partial z'}$.

3.3 Procedure of solution

With the help of boundary conditions, a numerical solution of non-dimensional governing equations 3.20-3.27 is obtained by using finite difference scheme [91].
Central difference formula is used to state spatial derivative for which a semi- annular region $[0 \quad R(z',t')]\times[0 \quad \pi]$ divided into the uniform grid. The spatial derivatives are described as-

$$\begin{cases} \frac{\partial A_f}{\partial r'}=\frac{(A_f)_{i+1,j}-(A_f)_{i-1,j}}{2\Delta r}, \\ \\ \frac{\partial A_f}{\partial \theta'}=\frac{(A_f)_{i,j+1}-(A_f)_{i,j-1}}{2\Delta \theta}, \\ \\ \frac{\partial^2 A_f}{\partial r'^2}=\frac{(A_f)_{i+1,j}-2(A_f)_{i,j}+(A_f)_{i-1,j}}{(\Delta r)^2}, \\ \\ \frac{\partial^2 A_f}{\partial \theta'^2}=\frac{(A_f)_{i,j+1}-2(A_f)_{i,j}+(A_f)_{i,j-1}}{(\Delta \theta)^2}. \end{cases} \tag{3.29}$$

where $f=c$ if $0<r'<R_1'(z',t')$ and $f=p$ if $R_1'(z',t')<r'<R'(z',t')$.
"A" refers the velocity (w'), temperature (T') and concentration (C'), respectively.
Δr and $\Delta\theta$ denotes the step-size in the r' and θ' directions, respectively. In the present study step size is considered uniform. If the L_1 and L_2 denotes the number of sub-intervals, in which the interval $[0 \quad R(z',t')]\times[0 \quad \pi]$ are divided by using uniform grids, then $\Delta r'$ and $\Delta\theta'$ represent mathematically as-

$\Delta r = \frac{R'(z',t')}{L_1}$ and $\Delta\theta = \frac{\pi}{L_2}$.
The grid points $(r'_i,\ \theta'_j)$ are represent as-

$$r'_i = (i-1)\Delta r', \qquad i = 1,2,3\cdots,L_1+1$$

$$\theta'_j = (j-1)\Delta\theta', \qquad j = 1,2,3\cdots,L_2+1$$

Pressure gradient in both regions are constant so it can be written as-

$$\frac{\partial P'_c}{\partial z'} = \frac{\partial P'_p}{\partial z'} = P_0. \tag{3.30}$$

The velocity and temperature equations are discretized with the help of equation (3.29). These discretized equations are converted into algebraic equations by varying i from 1 to L_1+1 and j from 1 to L_2+1. The algebraic equations form a tridiagonal block matrix and which are solved by using Gauss- Seidel iterative approach in MATLAB. The tolerance of error is considered 10^{-6} at every iteration.
The boundary conditions are also into the form of derivative for both r' and θ' directions, respectively. Therefore these conditions have been discretized according to the equation 3.29. After that these discretized boundary conditions form the system of equations and will be solved using the Gauss-Seidel method.
After determining the velocity and temperature profile for the both region, we have obtained the flow rate, wall shear stress numerically by adopting finite difference method. The solution steps is given in the figure 3.2.
The Volumetric flow rate Q, frictional resistance λ and the wall shear stress τ_w are defined as-

$$Q = \int_0^{R'(z',t')}\int_0^{\pi} r'w'dr'd\theta',$$

$$Q = \int_0^{R'_1(z',t')}\int_0^{\pi} r'w'_c(r',\theta',z')dr'd\theta' + \int_{R'_1(z',t')}^{R'(z',t')}\int_0^{\pi} r'w'_p(r',\theta',z')dr'd\theta', \tag{3.31}$$

$$\lambda = \frac{\int_0^L(-\frac{\partial p'}{\partial z'})dz'}{Q}, \tag{3.32}$$

$$\tau_w = -\left[\frac{\partial w'_p}{\partial r'}\right]_{r'=R'(z',t')}, \tag{3.33}$$

The heat and mass transfer coefficients across the upper wall (upper wall) of the stenosed artery respectively are calculated as-

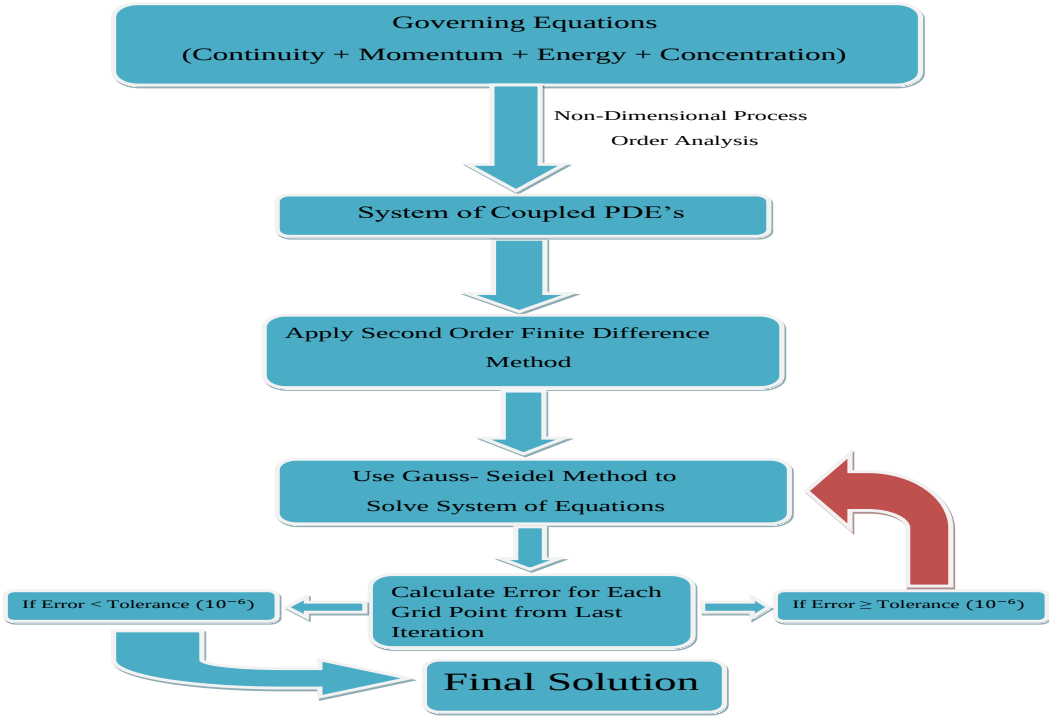

Figure 3.2: Methodology flow chart

The non-dimensional form of Nusselt number is defined as-

$$Nu = -\left[\frac{\partial T'_p}{\partial r'}\right]_{r'=R'(z',t')}, \tag{3.34}$$

The non-dimensional form of Sherwood number is defined as-

$$Sh = -\left[\frac{\partial C'_p}{\partial r'}\right]_{r'=R'(z',t')}. \tag{3.35}$$

3.4 Results and Discussion

A mathematical study has been proposed to analyze the impact of variable viscosity and permeability on the two-phase blood flow that passes through a curved artery in the presence of the magnetic field with heat and mass transfer. The impact of various physical parameters like temperature-dependent viscosity (λ_1), permeable wall (Da), magnetic field (M) on the blood velocity, heat source (H) on temperature and chemical reaction (ξ) on the concentration profile analyzed. This study considered the viscosity of core region as

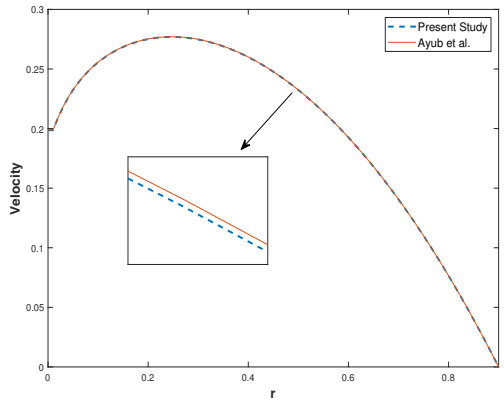

Figure 3.3: Comparison of present study with published work

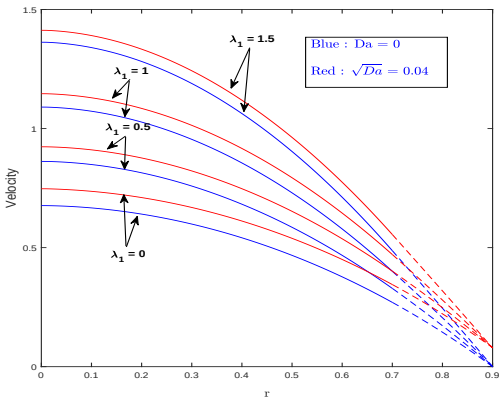

Figure 3.4: Variation in velocity with λ_1

temperature-dependent while, plasma region's viscosity as a constant. The thickness of the plasma viscosity is assumed 20%, according to artery diameter and hematocrit level [88]. The non-dimensional governing equations have been solved by using the second-order finite difference method (FDM). The flow region has been discretized uniformly in the radial (r') and angular direction (θ') with $\Delta r = \Delta\theta = 0.001$, respectively. The tolerance of error is considered 10^{-6} in the whole numerical process. MATLAB codes for FDM are developed to compute the velocity, temperature, concentration, WSS, frictional resistance for the various physical parameters. Default values of the parameters which were used for pictorially analyzed the importance of the model are listed below in the table 1. In all the figures of velocity, temperature, and concentration profiles, the continuous and dashed lines symbolized the core and plasma region, respectively.

The validation of the present study with the published work of Ayub et al.[80] has been picturized graphically through the figure 3.3. For comparison, the effect of the magnetic field, permeable wall, variable viscosity and two-phase nature of blood neglected in the present work, and the impact of nanofluids and catheter have been ignored in the observation of [80]. The perturbation technique was used by [80] to simplify the governing equations. Therefore in this comparison, perturbation technique has used for [80] work and finite difference method for the present study. It is observed that there is a good agreement between our study and published work [80], which replicates the validation of the present study.

The effect of temperature-dependent viscosity on the blood flow velocity in the radial direction is picturized graphically in the figure 3.4. Both constant ($\lambda_1 = 0$) and temperature-dependent ($\lambda_1 \neq 0$) viscosity scenarios are studied in this work. It is observed that the nature of blood viscosity is directly impacted by temperature, as shown in figure 3.4. According to the findings, it can be noted that with the positive add in the value of λ_1, aggregation of

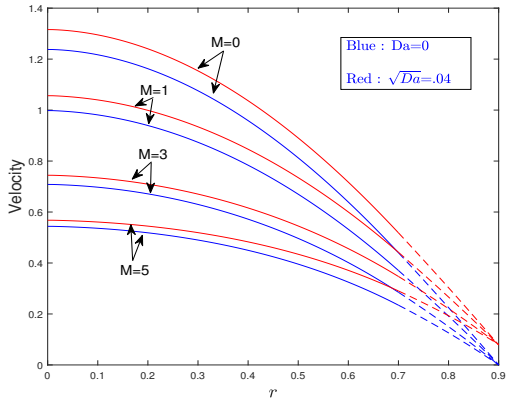

Figure 3.5: Variation in velocity with M

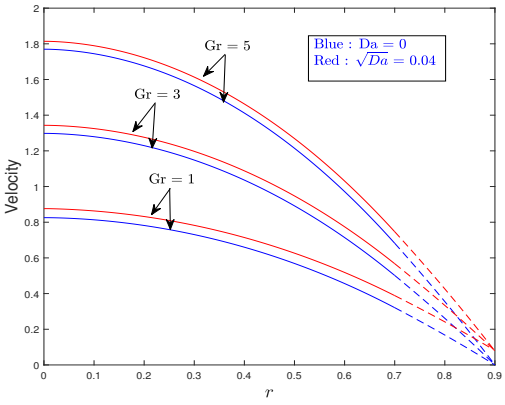

Figure 3.6: Variation in velocity with Gr

RBC's decreases due to dominance of temperature which becomes higher in the blood flow; therefore, viscosity of core region decays. As a result, the increase in the value of λ_1 reveals a significant improvement in the blood velocity profile, which are in the good agreement with the previous experimental published work [57]. As we apply the variable viscosity (temperature-dependent) in the core region, it directly affects the core region's flow velocity and indirectly reflects the change in the plasma region velocity due to continuity of wall interface condition. The effect of wall permeability can also be seen in the figure 3.4. It has been found that blood velocity is higher when the wall is permeable in comparison with impermeable wall. It has also been seen that the velocity difference between permeable and impermeable walls reduces as the λ_1 increases.

A comparative study to demonstrate the influence of magnetic field M on the blood flow velocity for both types of walls (permeable and impermeable) is illustrated in the figure 3.5. It is noted that blood is highly affected by the magnetic field due to the presence of hemoglobin and magnetic iron oxide particle in it. When blood flows through a magnetic field that is applied externally, it produces a strong electromotive field. When a magnetic field is introduced into the flow, a force known as Lorentz force arises in the perpendicular direction of flow, slowing down the flow due to improvement in the blood viscosity. Therefore, a rise in the magnetic field strength is responsible for the decay in the blood velocity. It has also been observed that blood velocity is higher for the permeable artery wall under a magnetic field than the impermeable artery wall. Figure 3.5 clearly indicates that when the magnetic field improves, the velocity variation between permeable and impermeable walls reduces due to an increase in the Lorentz force's dominance in the flow.

Figures 3.6-3.7 depicted the impact of thermal Grashof (Gr) and solute Grashof number (Gm) on the blood flow velocity for both permeable and impermeable walls situations respectively. From both figures, it can be analyzed that flow velocity increases with the rise

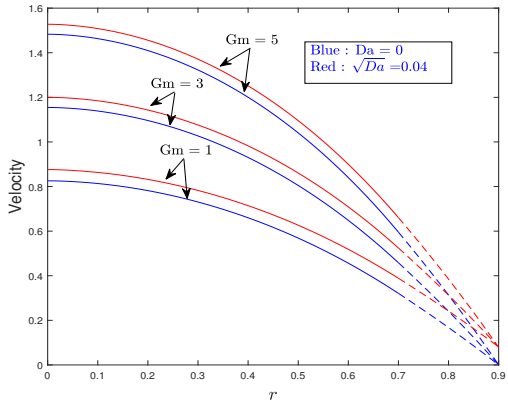

Figure 3.7: Variation in velocity with *Gm*

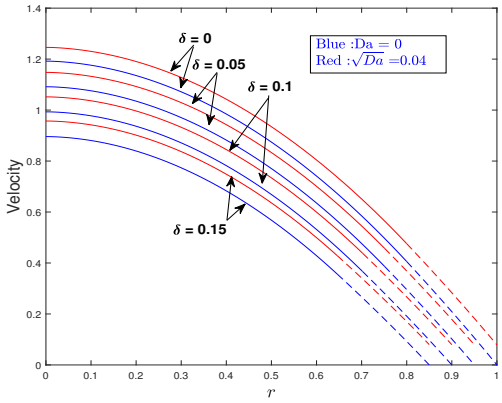

Figure 3.8: Variation in velocity with δ

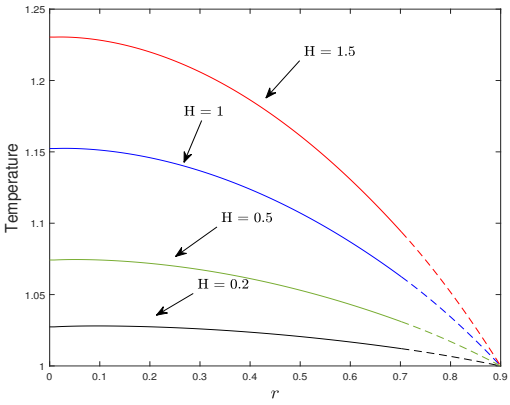

Figure 3.9: Variation in temperature with *H*

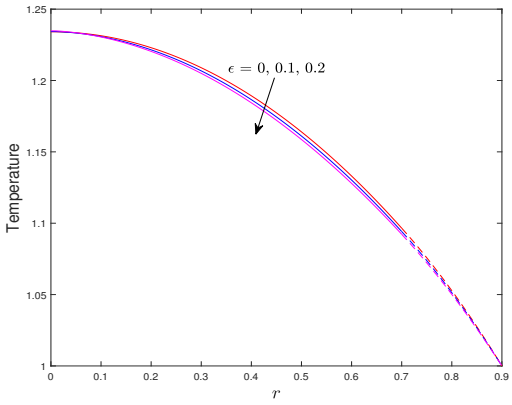

Figure 3.10: Variation in temperature with ε

in the value of *Gr* and *Gm*, respectively. This is happening due to the dominance of thermal and solute buoyancy force over the viscous force in the flow. It has also been observed that variation in the velocity profile is higher in the center of the artery. As flow approaches the artery wall, this variation becomes exceedingly sluggish due to the increase in the viscous force near the wall.

Figure 3.8 illustrates the effect of maximum stenosis height (δ) of the curved artery over the flow velocity under both situations of the artery wall (permeable and impermeable). The velocity variation of both stenotic and uniform arteries has been investigated in this work. When $\delta = 0$, it signifies that there is no stenosis in the artery (uniform) and the value of non-dimensional radius becomes 1, and $\delta \neq 0$ represents the stenosis in the artery. The figure shows that a modest increase in the value of δ results in a decrease in flow velocity.

Figure 3.9 exhibits the impact of the heat source parameter (H) on the temperature profile in both the core and plasma regions. As external heat applies to the body, the tissues

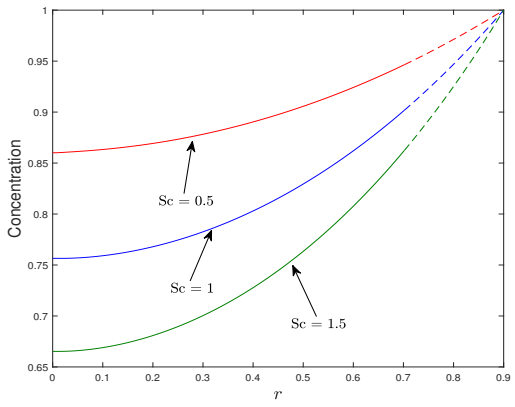

Figure 3.11: Variation in concentration with Sc

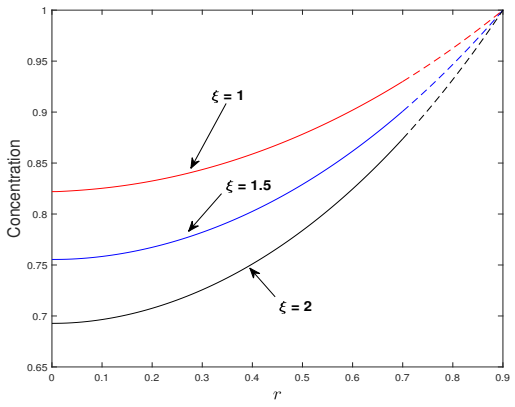

Figure 3.12: Variation in concentration with ξ

absorb this heat. Therefore, fluid generates more heat into the flow process, which significantly boosts the blood temperature. As a result, increases in the heat source parameter cause a rise in the flow temperature in both regions. An increment in blood temperature due to the external heat, it is widely used in thermo-therapy to kill cancer and tumor cells. The effect of the arterial curvature parameter (ε) on the non-dimensional blood temperature profile is shown in figure 3.10. In this study, the uniform artery (circular artery) is represented by $\varepsilon = 0$, whereas the curved nature of the artery is represented by $\varepsilon \neq 0$. From the above figure, a modest downfall in the blood temperature profile has been obtained with the rise in curvature parameter. As a result, the production of frictional heating is lower when blood flows through a curved artery, whereas it generates more heat when it passes through a straight artery (circular), as seen in the figure.

A numerical study to illustrate the influence of the Schmidt number (Sc) and chemical reaction parameter (ξ) on the concentration profile for both core and plasma has been presented through the figures 3.11-3.12. From both figures, it is noted that as blood flow proceeds towards the artery wall from the center of an artery, the concentration profile increases. It also concluded that, with the increases in the Schmidt number and chemical reaction parameter value, a decay in the concentration profile occurs. This occurs as a result of a decrease in molecular diffusivity at larger values of both Sc and ξ, resulting in a fall in species concentration in the flow. Figure 3.13 replicates the deviation in concentration (mass) transport profile of blood flow for the varying values of arterial curvature in both the core and plasma regions. A comparison has also been made between the straight ($\varepsilon = 0$) and curved ($\varepsilon \neq 0$) arteries. From the figure 3.13 it can be noticed that with the rise in arterial curvature, transportation of mass increases in both core and plasma regions. Therefore, mass transport is higher when blood flows through curved arteries than straight arteries.

The significance of magnetic field (M) and maximum stenosis depth (δ) on the wall

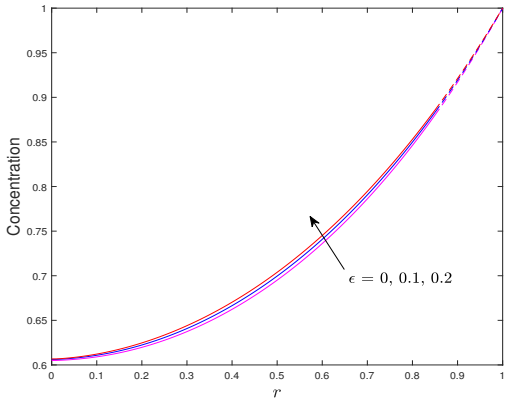

Figure 3.13: Variation in concentration with ε

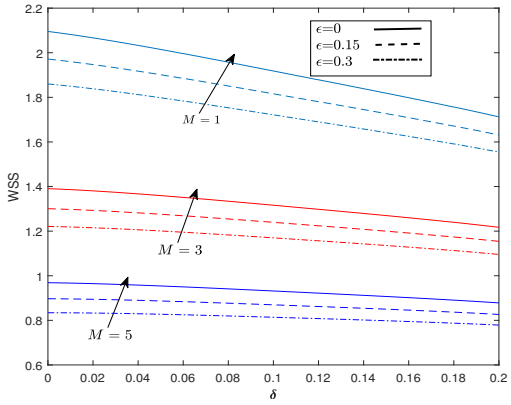

Figure 3.14: Variation in WSS with ε and M

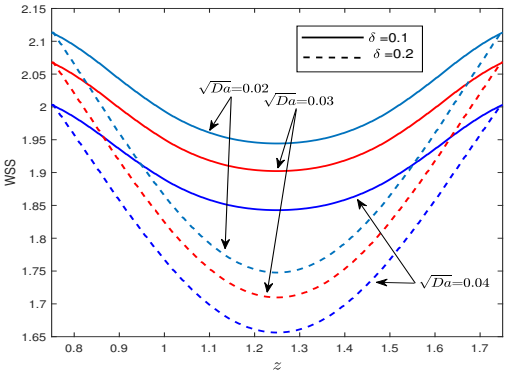

Figure 3.15: Variation in WSS with δ and Da

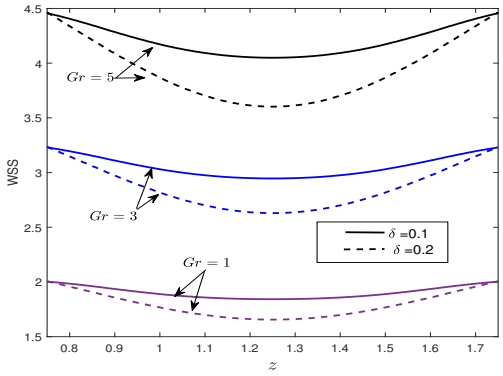

Figure 3.16: Variation in WSS with δ and Gr

shear stress profile for both curved ($\varepsilon \neq 0$) and straight ($\varepsilon = 0$) arteries have been elaborated in Figure 3.14. The WSS profile has been found on decaying linearly with stenosis depth. A growth in magnetic field strength indicates the drop in the WSS profile for both curved or straight arteries and also noted that as with the increase in δ, the decrement rate of WSS profile reduced with M. This study also reveals that straight arteries ($\varepsilon = 0$) experience higher wall shear stress than curved arteries. Therefore as ε grows up from 0, WSS reflects the downfall in their profile. This study also reveals the good agreement with the published experimental works [93, 109] which suggest that the development of stenosis in the blood flow is responsible for decreasing the wall shear stress profile.

The effect of permeability parameter (Da) and thermal Grashof number (Gr) on the wall shear stress in the stenotic zone for the various stenosis circumstances are portrayed graphically through the figures 3.15-3.16, respectively. Due to an increase in stenosis height, the WSS profile for the stenotic region diminishes from $z = 0.75$ to $z = 1.25$; then, the magnitude of WSS rises for the rest of the stenotic area. A rise in permeability parameter (Da)

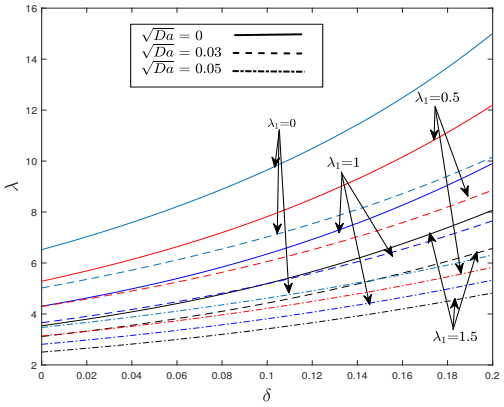

Figure 3.17: Variation in frictional resistance with λ_1 and Da

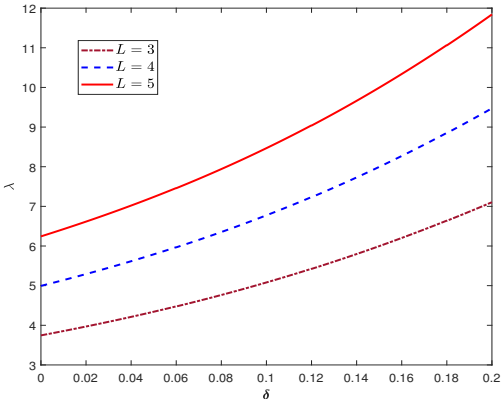

Figure 3.18: Variation in frictional resistance with artery length L

leads to the decay in the WSS profile, whereas the reverse effect is observed with the thermal Grashof number. This study also revealed that variation in the WSS profile for the two fixed stenosis heights increases with the rise in thermal Grashof number.

The distribution of frictional resistance (λ) experienced by the streaming blood flow for the various values of viscosity variation parameter (λ_1) and artery length (L), with stenosis depth (δ) have depicted by figures 3.17-3.18, respectively. With the increase in stenosis depth, a non-linear growth in frictional resistance has been observed, with this growth being slower in the domain $0 < \delta < 1$ than in the rest of the stenosis height region. According to figure 3.17, an enhancement in the value of λ_1 causes a drop in core region viscosity due to increased temperature dominance in the viscosity. Therefore, a rise λ_1 value reflects the decay in flow resistance for permeable and impermeable wall situations. This study also suggest that flow frictional resistance is high for the impermeable artery walls ($Da = 0$) than the permeable arterial walls. This is happening due to increased flux for permeable walls. The resistance of the flow is highly affected by the length of the artery. Therefore a numerical study has been carried out to analyze the effect of artery length on the permeable curved artery and displayed in the figure 3.18. It is detected that frictional flow resistance enhances the larger arteries.

Figures 3.19-3.20 exhibit the deviation in frictional resistance of blood flow of the stenotic section of the curved artery for the varied values of heat source (H) and wall permeability condition (Da), respectively. Initially, frictional resistance increases rapidly in the axial direction from $z = 0.75$ to $z = 1.25$ due to increased stenosis height, then after it decays in the rest of the stenosis region. Blood flow experiences high frictional resistance at the throat of stenosis ($z = 1.25$). A comparative study has been conducted to examine the effect of heat source on permeable and impermeable wall situations and obtained that blood

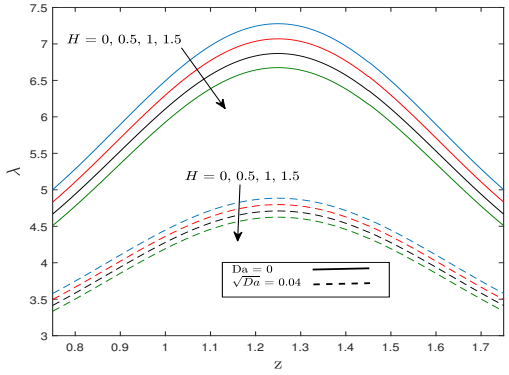

Figure 3.19: Variation in frictional resistance with H and Da

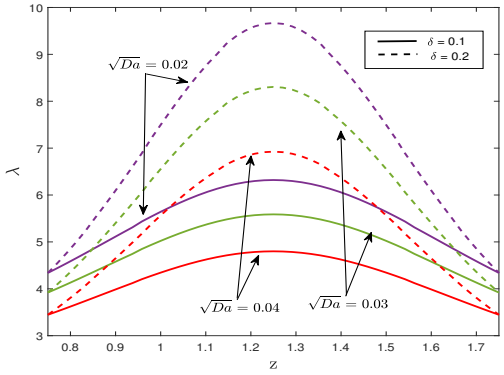

Figure 3.20: Variation in frictional resistance with δ and Da

flow encountered the high frictional resistance in an impermeable arterial wall condition than the permeable arterial wall. The present research also suggested that a high value of the heat source parameter is responsible for the decay in the flow resistance due to an increase in flow temperature with H. Figure 3.20 reveals the effect of permeability wall (Da) strength for different stenosis heights of the curved artery. A drop in the flow resistance with the increase in Da is observed, also noticed that variance in λ is lower for small stenosis than big stenosis height for all values of Da.

Figure 3.21 illustrates the variation in the heat transfer rate (Nusselt number) at the arterial wall in the whole stenotic zone for various heat source (H) values. This figure reveals that the heat transfer rate lowers with the increase in stenosis depth because the distance between blood flow and the outer arterial wall rises significantly. It's also important to note that the Nusselt number rises as the value of the external heat source in the flow increases. This occurs because fluid generates the heat energy in the frictional heating process in the flow, which directly impacts the heat transfer coefficient. Due to an increase in the heat transfer rate at the arterial wall with the positive add in heat source parameter (H), it is commonly used in thermotherapy to treat cancer and tumor cells.

The influence of the curvature parameter (ε) in the mass transfer coefficient (Sherwood number) with stenosis depth has been presented through the figure 3.22. This comparative study has studied the variance in mass transfer for both curved ($\varepsilon \neq 0$) and straight ($\varepsilon = 0$) arteries. This figure stated that at arterial wall transfer of mass is higher for the curved artery than the straight artery, resultant value mass transfer coefficient rises with the increase in value of curvature parameter (ε). Figure 3.23 displays the impact of the chemical reaction parameter (ξ) on the Sherwood number in the stenotic region. From the figure, it can be concluded that firstly values of Sherwood number decreases due to a rise in stenosis depth from $z = .75$ to $z = 1.25$, then it shows reverse effect in rest of stenotic region. It is

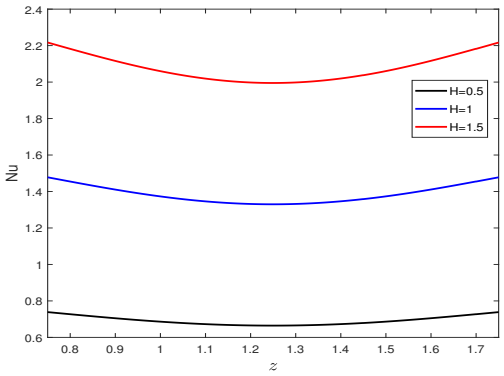

Figure 3.21: Variation in Nusselt number with H

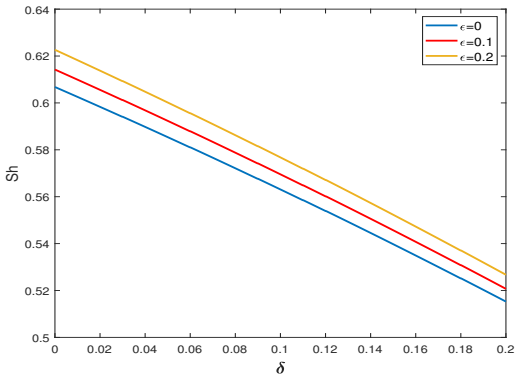

Figure 3.22: Variation in Sherwood number with curvature parameter ε

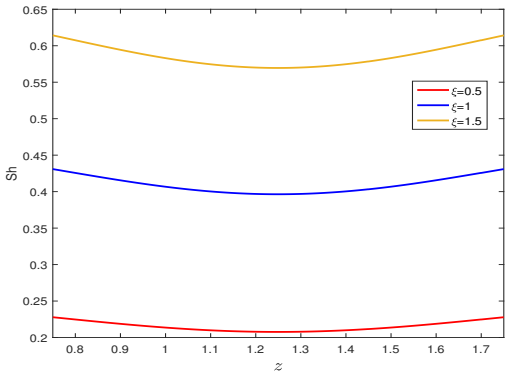

Figure 3.23: Variation in Sherwood number with chemical reaction parameter ξ

also observed that at arterial wall mass transfer coefficient enhances with increment in the values of chemical reaction parameter.

Blood flow trapping through a stenosed curved artery with a permeable wall is an exciting phenomenon to understand the flowing nature. The figures 3.24-3.26 exhibit the comparative discussion of blood trapping for various parameters magnetic field (M), viscosity variation parameter (λ_1) and heat source (H), respectively. The streamlines show a smoothness in the flow due to steady flow and constant pressure gradient. Figure 3.24 described the impact of the magnetic field on the blood flow in both radial and flow directions. The trapping configuration has revealed that an increase in magnetic field strength causes a restriction in the maximum velocity region due to the generation of Lorentz force, which slows the flow. The significance of temperature-dependent viscosity (in terms of λ_1) in flow trapping is visualized in figure 3.25. According to this figure, growth in value of λ_1 leads to a drop in core region viscosity. Therefore, the maximum velocity area increases with a rise in λ_1, especially in the stenotic region from $z = 0.75$ to $z = 1.75$. The fluid temperature has an important impact on the variation of blood flow patterns. Fluid temperature enhances by applying an external heat source to the blood flow. Therefore, a significant difference in the flow pattern through curved artery for both heat source conditions ($H = 0$, & $H \neq 0$) can be observed through the figure 3.26. It's also worth noting that when a heat source is applied to the arterial wall, the maximum velocity area increases in a stenotic region.

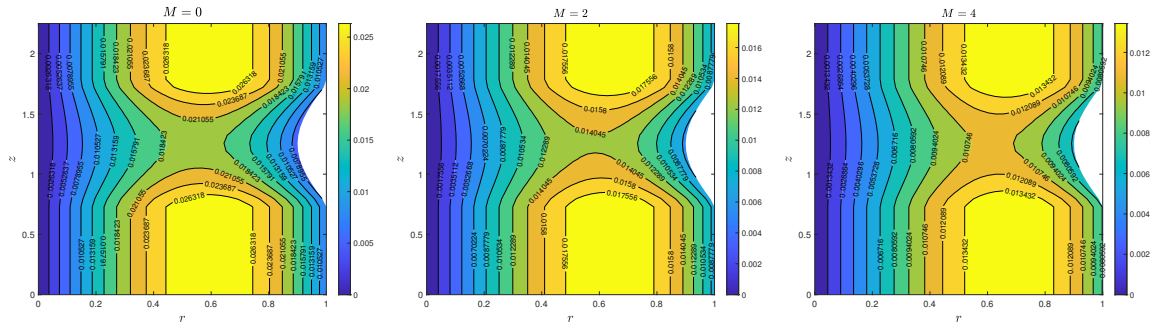

(a) (b) (c)

Figure 3.24: Blood flow pattern for different values of magnetic field, (a) $M = 0$, (b) $M = 2$, (c) $M = 4$.

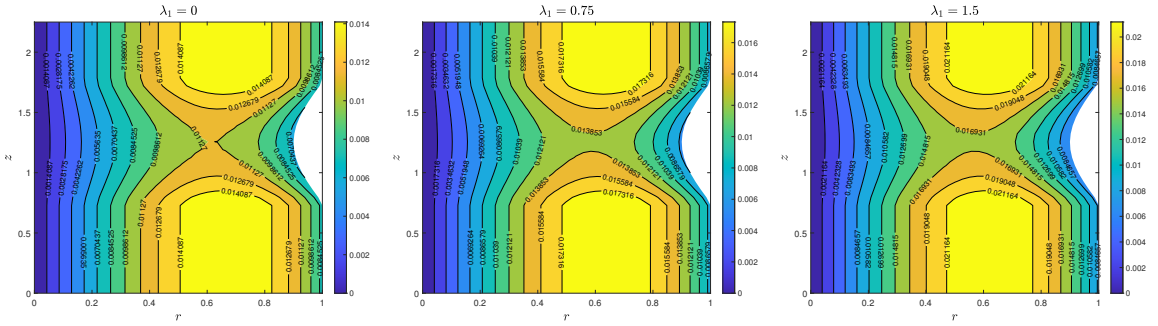

(a) (b) (c)

Figure 3.25: Blood flow pattern for different values of viscosity variation parameter, (a) $\lambda_1 = 0$, (b) $\lambda_1 = 0.75$, (c) $\lambda_1 = 1.5$.

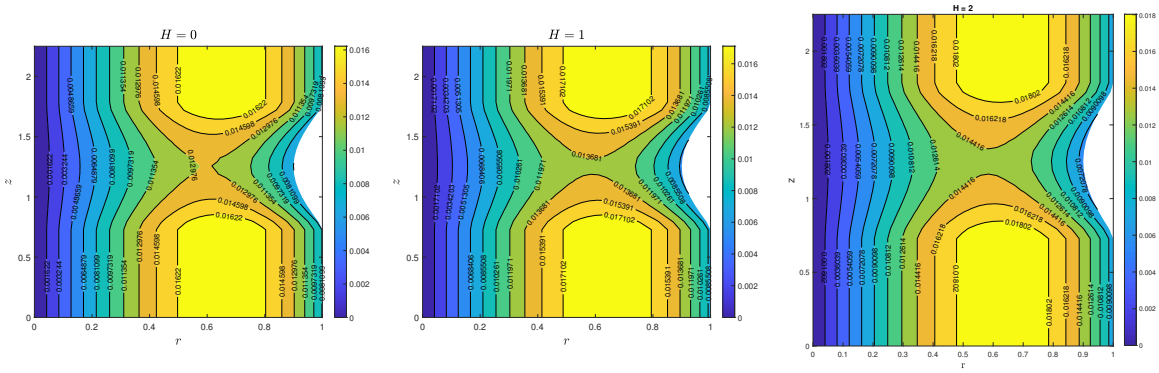

(a) (b) (c)

Figure 3.26: Blood flow pattern for different values of Heat source, (a) $H = 0$, (b) $H = 1$, (c) $H = 2$.

3.5 Conclusion

A numerical investigation of a two-phase model for blood flow through a stenosed permeable curved artery with variable viscosity of the core region (temperature-dependent) has been considered in this paper. A patients-specific artery in the presence of stenosis (plaque) has been considered. A comparative study for both permeable and impermeable walls is also addressed. The second-order finite difference method has been employed to solve non-dimensional governing equations in "MATLAB"software. For each iterative process, we have taken tolerance as 10^{-6}. The impact of various physical parameters such as M, λ_1,

Da, H, ξ, δ on the flow velocity, temperature, concentration, WSS and frictional resistance have been picturized graphically. Clinical researchers and biologist can adopt the current mathematical analysis of two-phase blood flow through a curved artery to lower the risk of atherosclerosis formation or assess the flow behaviour profile such as velocity, temperature, concentration, and so on. They can also use this study to predict current status and fear of cardiovascular disease, and then diagnose patients accordingly risk and situation. The major finding of the present study are listed below-

- It is observed that the blood viscosity is affected by the temperature so, a positive increment in the value of λ_1 causes decay in core viscosity.
- Significant growth in fear of deposition of plaque (lipid) appears with the rise in both arterial curvature and permeability wall condition, which happen due to a reduction in the wall shear stress profile.
- The use of external heat source parameter (H) in hyperthermia and laser therapies can reduce the deposition of plaque and clot at a time of healing process, which happens due to hike in flow temperature with increase in H.
- The temperature profile is higher for the straight arteries ($\varepsilon = 0$) compared to curved arteries ($\varepsilon \neq 0$), while blood concentration reflects the reverse effect with arterial curvature.
- Blood concentration decreases with growth in the chemical reaction parameter (ξ).
- The mass transfer at the wall rises for the curved arteries ($\varepsilon \neq 0$), while it reflects the reverse effects with increased chemical reaction parameter (ξ).

Chapter 4

Entropy generation for MHD two phase blood flow through a curved permeable artery having variable viscosity with heat and mass transfer[1]

4.1 Introduction

The fluid flow through a curved tube has a vital role in medical and engineering industries such as chemical reactors, heat exchangers, aerospace, angiography, cardiovascular flow etc. In medical field, computational simulation of blood flow in the cardiovascular and arterial systems has become increasingly important in determining the severity and current state of various diseases. These computational investigations are independent of risk and can be modified accordingly to disease conditions, so findings of these studies are utilized to improve existing clinical techniques and develop new alternative therapies. Therefore, it encourages biologists and researchers to examine the flow velocity, heat and mass transfer in both experimental and numerical ways. Escuer et al. [110] performed a numerical study to analyze the drug delivery phenomena in blood flow. In this study, the arterial wall is assumed a three-layer model. This study suggested that both arterial curvature and plaque (lipid) deposition play a major role in drug distribution and disease treatment. A numerical study to evaluate the effect of various stenosis sizes in the curved blood vessel under the realistic arterial boundary condition has been published by Bit et al. [77].

The minimization of entropy generation is a fascinating topic for engineers and scientists to reduce irreversibility by constructing an innovative thermal management system. In an isolated system, fluid friction, molecular vibration, heat and mass flux, joule heating and thermal radiation are the leading cause of irreversibility. The decrease in the entropy generation rate is essential to improve the efficiency of a closed isolate system, especially in

[1] A considerable part of this chapter is published in *International Communication in Heat and Mass Transfer*, 133, 105954, 2022.

energy storage systems, heat exchangers, power plants, etc. Bejan [46] developed a new method (finite-size device and finite-time processes) to minimize the entropy generation. He applied this approach to thermal optimization in various thermal engineering fields, including storage systems, solar power plants, refrigerators, fossil power plants, and so on. A mathematical investigation of entropy generation for blood flow in thermotherapy has been performed by Mekheimer et al.[23] . In this study, they considered gold or copper nanoparticles in the form of drug agents. Hasnain et al. [111] studied the two-phase fluid analysis for entropy generation in an inclined channel. This analysis took micropolar fluid at the upper plate and water-based nanofluid at the lower plate. Dutta et al. [112] conducted an experimental investigation in the respiration process to assess the impact of several parameters such as specific or relative humidity, temperature change, and breathing air friction on entropy generation. In this work, they suggested that entropy generation is higher for the air-breathing in comparison with the condition of friction effect with tract. Qasem et al. [113, 114, 115] created multiple mathematical flow models of flow across stretching surfaces and wavy channels to interpret the entropy generation.

All the above-published experimental and numerical work signifies the heat and mass transport phenomena for the single/two-phase blood flow model. As per the author's best knowledge, two-phase blood flow for stenosed curved artery (assuming toroidal coordinate system) has not been studied earlier. Therefore, this paper discusses heat and mass transport phenomena for two-phase blood flow through a stenosed curved artery with a permeable wall. This mathematical study observed the effect of various parameters such as temperature-dependent viscosity, magnetic field, heat source, joule heating, and chemical reaction on the two-phase blood flow through the curved artery. This work also discussed the entropy generation arising due to heat and mass flux, viscous dissipation, and joule heating in the flow. This study has also included a comparative study between permeable and impermeable wall conditions for flow velocity, wall shear stress, and impedance. A second-order finite difference scheme [91] is adopted to simplify the non-dimensional velocity, temperature, and concentration equations for both core and plasma region under the consideration of mild stenosis and fully developed flow condition. Clinical researchers and biologists can use the current mathematical research to lower the risk of lipid deposition and predict the risk of cardiovascular disease, and then diagnose patients based on risk.

4.2 Problem formulation

An unsteady, laminar and incompressible blood flow through a stenosed curved artery of finite length L having a permeable wall is investigated in this study. As per the suggestion of published work [87, 88], a two-phase blood flow approach has been considered for the more realistic situation. In the core region, temperature-dependent viscosity is taken while plasma region viscosity is assumed constant nature.

4.2.1 Geometry of the stenosis

Time dependent stenosis is considered for both core and plasma wall and represented by $R_1(z,t)$ and $R(z,t)$, respectively. The geometry of two-phase blood flow through stenosed curved artery is defined in the figure (4.1) Mathematically expressions of elliptic shape stenosis are as follows [92]:
Geometry of the stenosis in plasma region is considered as:

$$R(z,t) = \begin{cases} \left[R_0 - \delta \sin\left(\pi(\frac{z-d}{L_0})\right)\right]\Omega(t) & \text{for} \quad d \le z \le d+L_0, \\ R_0\Omega(t) & \text{otherwise.} \end{cases} \tag{4.1}$$

Geometry of stenosis in the core region is considered as:

$$R_1(z,t) = \begin{cases} \left[\beta R_0 - \delta \sin\left(\pi(\frac{z-d}{L_0})\right)\right]\Omega(t) & \text{for} \quad d \le z \le d+L_0, \\ \beta R_0\Omega(t) & \text{otherwise.} \end{cases} \tag{4.2}$$

The time-varying parameter $\Omega(t)$ is expressed as

$$\Omega(t) = 1 - \eta(\cos(\omega t) - 1)e^{-\eta\omega t}. \tag{4.3}$$

where L_0 is the length of stenosis
R_0 radius of normal artery, δ is the maximum height of stenosis, d is the location of stenosis, β is ratio of central core radius to normal artery radius, L is the length of artery, η is constant, ω are the angular frequency of the forced oscillation.

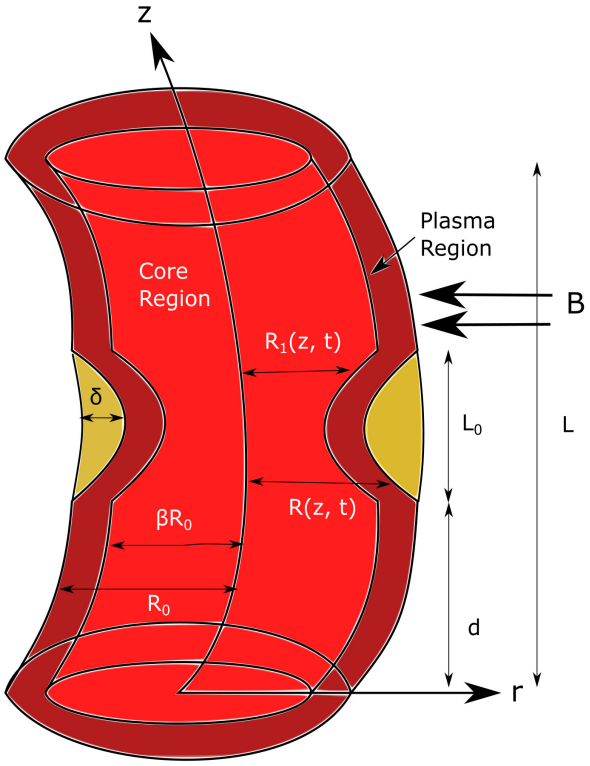

Figure 4.1: Geometry of two-phase stenosed curved artery

4.2.2 Variable viscosity model

The blood viscosity for the core-region is considered as temperature dependent, and mathematical form is given by [36]

$$\begin{cases} \mu_c(T) = \mu_0 \exp\left[\lambda_1\left(\frac{1}{2} - \frac{T_c - T_0}{T_w - T_0}\right)\right], & 0 < r < R_1(z,t) \quad \text{(Core-region)}, \\ \mu_p = \mu_0, & R_1(z,t) < r < R(z,t) \quad \text{(Plasma-region)}. \end{cases} \tag{4.4}$$

where μ_c and μ_p are the viscosity of core and plasma region respectively.
μ_0 represents the reference viscosity, which is constant.

4.2.3 Governing equations

The governing equations for curved tube for both core and plasma regions are deliberated as follows [16, 108]
Continuity Equation :

$$\frac{b}{D}\frac{\partial w}{\partial z} + \frac{\partial u}{\partial r} + \frac{1}{r}\frac{\partial v}{\partial \theta} + \frac{u}{r} + \frac{u\cos\theta - v\sin\theta}{D} = 0, \tag{4.5}$$

where, b denotes the radius of curvature.

$$D = b + r\cos\theta,$$

For the Core region i.e. $0 < r < R_1(z,t)$
Momentum equations-
r-direction:

$$\rho_c\left(\frac{\partial u_c}{\partial t}+\frac{bw_c}{D}\frac{\partial u_c}{\partial z}+u_c\frac{\partial u_c}{\partial r}+\frac{v_c}{r}\frac{\partial u_c}{\partial \theta}-\frac{v_c^2}{r}-\frac{w_c^2\cos\theta}{D}\right)=-\frac{\partial P_c}{\partial r}+\mu_c(T)\left(\frac{\partial^2 u_c}{\partial r^2}+\frac{1}{r}\frac{\partial u_c}{\partial r}\right.$$
$$-\frac{u_c}{r^2}+\frac{b^2}{D^2}\frac{\partial^2 u_c}{\partial z^2}+\frac{1}{r^2}\frac{\partial^2 u_c}{\partial \theta^2}-\frac{2}{r^2}\frac{\partial v_c}{\partial \theta}+\frac{1}{D}\left[\cos\theta\frac{\partial u_c}{\partial r}-\frac{\sin\theta}{r}\frac{\partial u_c}{\partial \theta}+\frac{v_c\sin\theta}{r}\right]+\frac{2b\sin\theta}{D^2}\frac{\partial w_c}{\partial z}$$
$$\left.-\frac{\cos\theta}{D^2}[u_c\cos\theta-v_c\sin\theta]\right)+\left[\frac{4}{3}\frac{\partial u_c}{\partial r}-\frac{2}{3}\left(\frac{b}{D}\frac{\partial w_c}{\partial z}+\frac{1}{r}\frac{\partial v_c}{\partial \theta}+\frac{u_c\cos\theta-v_c\sin\theta}{b+r\cos\theta}+\frac{u_c}{r}\right)\right]$$
$$\frac{\partial \mu_c(T)}{\partial r}+\left(\frac{1}{r}\frac{\partial v_c}{\partial r}-\frac{v_c}{r^2}+\frac{1}{r^2}\frac{\partial u_c}{\partial \theta}\right)\frac{\partial \mu_c(T)}{\partial \theta}+\left(\frac{b^2}{D^2}\frac{\partial u_c}{\partial z}+\frac{b}{D}\frac{\partial w_c}{\partial r}-\frac{bw_c\cos\theta}{D^2}\right)\frac{\partial \mu_c(T)}{\partial z}, \tag{4.6}$$

θ- direction :

$$\rho_c\left(\frac{\partial v_c}{\partial t}+\frac{w_c b}{D}\frac{\partial v_c}{\partial z}+u_c\frac{\partial v_c}{\partial r}+\frac{v_c}{r}\frac{\partial v_c}{\partial \theta}+\frac{u_c v_c}{r}+\frac{w_c^2\sin\theta}{D}\right)=-\frac{1}{r}\frac{\partial P_c}{\partial \theta}+\mu_c(T)\left(\frac{\partial^2 v_c}{\partial r^2}+\frac{1}{r}\frac{\partial v_c}{\partial r}\right.$$
$$-\frac{v_c}{r^2}+\frac{b^2}{D^2}\frac{\partial^2 v_c}{\partial z^2}+\frac{1}{r^2}\frac{\partial^2 v_c}{\partial \theta^2}+\frac{2}{r^2}\frac{\partial u_c}{\partial \theta}+\frac{1}{D}\left[\cos\theta\frac{\partial v_c}{\partial r}-\frac{\sin\theta}{r}\frac{\partial v_c}{\partial \theta}-\frac{u_c\sin\theta}{r}\right]+\frac{2b\sin\theta}{D^2}\frac{\partial w_c}{\partial z}$$
$$\left.+\frac{\sin\theta}{D^2}[u_c\cos\theta-v_c\sin\theta]\right)+\left(\frac{\partial v_c}{\partial r}-\frac{v_c}{r}+\frac{1}{r}\frac{\partial u_c}{\partial \theta}\right)\frac{\partial \mu_c(T)}{\partial r}+\left[\frac{4}{3}\left(\frac{1}{r^2}\frac{\partial v_c}{\partial \theta}+\frac{u_c}{r^2}\right)-\frac{2}{3}\left(\frac{1}{r}\frac{b}{D}\right.\right.$$
$$\left.\left.\frac{\partial w_c}{\partial z}+\frac{1}{r}\frac{u_c\cos\theta-v_c\sin\theta}{D}+\frac{1}{r}\frac{\partial u_c}{\partial r}\right)\right]\frac{\partial \mu_c(T)}{\partial \theta}+\frac{b}{D}\left(\frac{1}{r}\frac{\partial w_c}{\partial \theta}+\frac{w_c\sin\theta}{D}+\frac{b}{D}\frac{\partial v_c}{\partial z}\right)\frac{\partial \mu_c(T)}{\partial z}, \tag{4.7}$$

z- direction :

$$\rho_c\left(\frac{\partial w_c}{\partial t}+\frac{w_c b}{D}\frac{\partial w_c}{\partial z}+u_c\frac{\partial w_c}{\partial r}+\frac{v_c}{r}\frac{\partial w_c}{\partial \theta}+\frac{w_c(u_c\cos\theta-v_c\sin\theta)}{D}\right)=-\frac{b}{D}\frac{\partial P_c}{\partial z}+\mu_c(r)\left(\frac{\partial^2 w_c}{\partial r^2}\right.$$
$$+\frac{b^2}{D^2}\frac{\partial^2 w_c}{\partial z^2}+\frac{1}{r}\frac{\partial w_c}{\partial r}+\frac{1}{r^2}\frac{\partial^2 w_c}{\partial \theta^2}-\frac{w_c}{D^2}+\frac{1}{D}\left[\cos\theta\frac{\partial w_c}{\partial r}-\frac{\sin\theta}{r}\frac{\partial w_c}{\partial \theta}\right]+\frac{2b}{D^2}\left[\cos\theta\frac{\partial u_c}{\partial z}-\right.$$
$$\left.\left.\sin\theta\frac{\partial v_c}{\partial z}\right]\right)+\left(\frac{b}{D}\frac{\partial u_c}{\partial z}+\frac{\partial w_c}{\partial r}-\frac{w_c\cos\theta}{D}\right)\frac{\partial \mu_c(T)}{\partial r}+\left(\frac{1}{r^2}\frac{\partial w_c}{\partial \theta}+\frac{w_c\sin\theta}{rD}+\frac{b}{rD}\frac{\partial v_c}{\partial z}\right)$$
$$\frac{\partial \mu_c(T)}{\partial \theta}+\frac{b}{D}\left[\frac{4}{3}\left(\frac{b}{D}\frac{\partial w_c}{\partial z}+\frac{u_c\cos\theta-v_c\sin\theta}{D}\right)-\frac{2}{3}\left(\frac{\partial u_c}{\partial r}+\frac{1}{r}\frac{\partial v_c}{\partial \theta}+\frac{u_c}{r}\right)\right]\frac{\partial \mu_c(T)}{\partial z}-\sigma B^2 w_c$$
$$+g\rho_c\gamma_T(T_c-T_0)+g\rho_c\gamma_c^*(C_c-C_0), \tag{4.8}$$

Energy equation :

$$\rho_c \bar{C}_c \left(\frac{\partial T_c}{\partial t} + u_c \frac{\partial T_c}{\partial r} + \frac{v_c}{r} \frac{\partial T_c}{\partial \theta} + \frac{w_c b}{D} \frac{\partial T_c}{\partial z} \right) = K_c \left(\frac{\partial^2 T_c}{\partial r^2} + \frac{1}{r} \frac{\partial T_c}{\partial r} + \frac{b^2}{D^2} \frac{\partial^2 T_c}{\partial z^2} + \frac{\cos\theta}{D} \frac{\partial T_c}{\partial r} - \frac{\sin\theta}{rD} \frac{\partial T_c}{\partial \theta} + \frac{1}{r^2} \frac{\partial^2 T_c}{\partial \theta^2} \right) + Q_c - \sigma B^2 w_c^2 + F_c, \tag{4.9}$$

Concentration equation :

$$\left(\frac{\partial C_c}{\partial t} + u_c \frac{\partial C_c}{\partial r} + \frac{v_c}{r} \frac{\partial C_c}{\partial \theta} + \frac{w_c b}{D} \frac{\partial C_c}{\partial z} \right) = D_c \left(\frac{\partial^2 C_c}{\partial r^2} + \frac{1}{r} \frac{\partial C_c}{\partial r} + \frac{b^2}{D^2} \frac{\partial^2 C_c}{\partial z^2} + \frac{\cos\theta}{D} \frac{\partial C_c}{\partial r} - \frac{\sin\theta}{rD} \frac{\partial C_c}{\partial \theta} + \frac{1}{r^2} \frac{\partial^2 C_c}{\partial \theta^2} \right) - R_c (C_c - C_0), \tag{4.10}$$

where F_c represent the dimensional form of viscous dissipation in core region and written as-

$$F_c = 2\mu_c(T_c) \left[\left(\left(\frac{\partial u_c}{\partial r} \right)^2 + \left(\frac{1}{r} \frac{\partial v_c}{\partial \theta} + \frac{u_c}{r} \right)^2 + \left(\frac{b}{D} \frac{\partial w_c}{\partial z} + \frac{u_c \cos\theta - v_c \sin\theta}{D} \right)^2 \right) + \frac{1}{2} \left(\left(\frac{\partial v_c}{\partial r} - \frac{v_c}{r} + \frac{1}{r} \frac{\partial u_c}{\partial \theta} \right)^2 + \left(\frac{b}{D} \frac{\partial u_c}{\partial z} + \frac{\partial w_c}{\partial r} - \frac{w_c \cos\theta}{D} \right)^2 \right) + \left(\frac{1}{r} \frac{\partial w_c}{\partial \theta} + \frac{w_c \sin\theta}{D} + \frac{b}{D} \frac{\partial v_c}{\partial z} \right)^2 \right]. \tag{4.11}$$

Where, u_c, v_c, w_c are the dimensional core region velocity component in r, θ, z directions, respectively.

$\mu_c, T_c, C_c, \rho_c, K_c, B, D_c, R_c$ are the dimensional viscosity, temperature, concentration density, thermal conductivity, uniform magnetic field, mass diffusivity and dimensional chemical reaction parameter in the core region, respectively.

Plasma region i.e. $R_1(z,t) < r < R(z,t)$

Momentum equations-

r-direction :

$$\rho_p \left(\frac{\partial u_p}{\partial t} + \frac{b w_p}{D} \frac{\partial u_p}{\partial z} + u_p \frac{\partial u_p}{\partial r} + \frac{v_p}{r} \frac{\partial u_p}{\partial \theta} - \frac{v_p^2}{r} - \frac{w_p^2 \cos\theta}{D} \right) = -\frac{\partial P_p}{\partial r} + \mu_p \left(\frac{\partial^2 u_p}{\partial r^2} + \frac{1}{r} \frac{\partial u_p}{\partial r} - \frac{2}{r^2} \frac{\partial v_p}{\partial \theta} + \frac{b^2}{D^2} \frac{\partial^2 u_p}{\partial z^2} - \frac{u_p}{r^2} + \frac{1}{r^2} \frac{\partial^2 u_p}{\partial \theta^2} + \frac{1}{D} \left[\cos\theta \frac{\partial u_p}{\partial r} - \frac{\sin\theta}{r} \frac{\partial u_p}{\partial \theta} + \frac{v_p \sin\theta}{r} \right] + \frac{2b \sin\theta}{D^2} \frac{\partial w_p}{\partial z} - \frac{\cos\theta}{D^2} [u_p \cos\theta - v_p \sin\theta] \right), \tag{4.12}$$

θ- direction :

$$\rho_p\left(\frac{\partial v_p}{\partial t}+\frac{w_p b}{D}\frac{\partial v_p}{\partial z}+u_p\frac{\partial v_p}{\partial r}+\frac{v_p}{r}\frac{\partial v_p}{\partial \theta}+\frac{u_p v_p}{r}+\frac{w_p^2\sin\theta}{D}\right)=-\frac{1}{r}\frac{\partial P_p}{\partial \theta}+\mu_p\left(\frac{\partial^2 v_p}{\partial r^2}+\frac{1}{r}\frac{\partial v_p}{\partial r}\right.$$
$$+\frac{2}{r^2}\frac{\partial u_p}{\partial \theta}+\frac{b^2}{D^2}\frac{\partial^2 v_p}{\partial z^2}-\frac{v_p}{r^2}+\frac{1}{r^2}\frac{\partial^2 v_p}{\partial \theta^2}+\frac{1}{D}\left[\cos\theta\frac{\partial v_p}{\partial r}-\frac{\sin\theta}{r}\frac{\partial v_p}{\partial \theta}-\frac{u_p\sin\theta}{r}\right]+\frac{2b\sin\theta}{D^2}\frac{\partial w_p}{\partial z}$$
$$\left.+\frac{\sin\theta}{D^2}[u_p\cos\theta-v_p\sin\theta]\right), \tag{4.13}$$

z- direction :

$$\rho_p\left(\frac{\partial w_p}{\partial t}+\frac{w_p b}{D}\frac{\partial w_p}{\partial z}+u_p\frac{\partial w_p}{\partial r}+\frac{v_p}{r}\frac{\partial w_p}{\partial \theta}+\frac{w_p(u_p\cos\theta-v_p\sin\theta)}{D}\right)=-\frac{b}{D}\frac{\partial P_p}{\partial z}+\mu_p\left(\right.$$
$$-\frac{w_p}{D^2}+\frac{1}{r^2}\frac{\partial^2 w_p}{\partial \theta^2}+\frac{b^2}{D^2}\frac{\partial^2 w_p}{\partial z^2}+\frac{\partial^2 w_p}{\partial r^2}+\frac{1}{r}\frac{\partial w_p}{\partial r}+\frac{1}{D}\left[\cos\theta\frac{\partial w_p}{\partial r}-\frac{\sin\theta}{r}\frac{\partial w_p}{\partial \theta}\right]$$
$$\left.+\frac{2b}{D^2}\left[\cos\theta\frac{\partial u_p}{\partial z}-\sin\theta\frac{\partial v_p}{\partial z}\right]\right)-\sigma B^2 w_p+g\rho_p\gamma_T(T_p-T_0)+g\rho_p\gamma_c^*(C_p-C_0), \tag{4.14}$$

Energy equation :

$$\rho_p\bar{C}_p\left(\frac{\partial T_p}{\partial t}+u_p\frac{\partial T_p}{\partial r}+\frac{v_p}{r}\frac{\partial T_p}{\partial \theta}+\frac{w_p b}{D}\frac{\partial T_p}{\partial z}\right)=K_p\left(\frac{\partial^2 T_p}{\partial r^2}+\frac{1}{r}\frac{\partial T_p}{\partial r}+\frac{b^2}{D^2}\frac{\partial^2 T_p}{\partial z^2}+\frac{\cos\theta}{D}\frac{\partial T_p}{\partial r}\right.$$
$$\left.-\frac{\sin\theta}{rD}\frac{\partial T_p}{\partial \theta}+\frac{1}{r^2}\frac{\partial^2 T_p}{\partial \theta^2}\right)+Q_p-\sigma B^2 w_p+F_p, \tag{4.15}$$

Concentration equation :

$$\left(\frac{\partial C_p}{\partial t}+u_p\frac{\partial C_p}{\partial r}+\frac{v_p}{r}\frac{\partial C_p}{\partial \theta}+\frac{w_p b}{D}\frac{\partial C_p}{\partial z}\right)=D_p\left(\frac{\partial^2 C_p}{\partial r^2}+\frac{1}{r}\frac{\partial C_p}{\partial r}+\frac{b^2}{D^2}\frac{\partial^2 C_p}{\partial z^2}+\frac{\cos\theta}{D}\frac{\partial C_p}{\partial r}\right.$$
$$\left.-\frac{\sin\theta}{rD}\frac{\partial C_p}{\partial \theta}+\frac{1}{r^2}\frac{\partial^2 C_p}{\partial \theta^2}\right)-R_p(C_p-C_0), \tag{4.16}$$

where F_p represent the dimensional form of viscous dissipation in plasma region and written as-

$$F_p=2\mu_p\left[\left(\left(\frac{\partial u_p}{\partial r}\right)^2+\left(\frac{1}{r}\frac{\partial v_p}{\partial \theta}+\frac{u_p}{r}\right)^2+\left(\frac{b}{D}\frac{\partial w_p}{\partial z}+\frac{u_p\cos\theta-v_p\sin\theta}{D}\right)^2\right)+\frac{1}{2}\left(\left(\frac{\partial v_p}{\partial r}\right.\right.\right.$$
$$\left.\left.\left.-\frac{v_p}{r}+\frac{1}{r}\frac{\partial u_p}{\partial \theta}\right)^2+\left(\frac{b}{D}\frac{\partial u_p}{\partial z}+\frac{\partial w_p}{\partial r}-\frac{w_p\cos\theta}{D}\right)^2\right)+\left(\frac{1}{r}\frac{\partial w_p}{\partial \theta}+\frac{w_p\sin\theta}{D}+\frac{b}{D}\frac{\partial v_p}{\partial z}\right)^2\right]. \tag{4.17}$$

Where, u_p, v_p, w_p are the dimensional plasma region velocity component in r, θ, z directions, respectively.

$\mu_p, T_p, C_p, \rho_p, K_p, B, D_p, R_p$ are the dimensional viscosity, temperature, concentration, density, thermal conductivity, uniform magnetic field, mass diffusivity and dimensional chemical reaction parameter in the plasma region,respectively.

To reduce above dimensional governing equations into dimensionless equations for both regions, we will introduce non-dimensional parameters through the table 4.1 -

Table 4.1: Non-dimensional parameter

$r = R_0 r'$	$z = L_0 z'$	$\theta = \theta'$	$\omega = \frac{u_0}{L_0}\omega'$	$L = L_0 L'$
$d = L_0 d'$	$t = \frac{L_0}{u_0} t'$	$R = R_0 R'$	$R_1 = R_0 R_1'$	$u_c = \frac{\delta u_0}{L_0} u_c'$
$v_c = \frac{\delta u_0}{L_0} v_c'$	$w_c = u_0 w_c'$	$u_p = \frac{\delta u_0}{L_0} u_p'$	$v_p = \frac{\delta u_0}{L_0} v_p'$	$w_p = u_0 w_p'$
$P_c = \frac{u_0 L_0 \mu_0}{R_0^2} P_c'$	$P_p = \frac{u_0 L_0 \mu_0}{R_0^2} P_p'$	$\alpha = \frac{R_0}{L_0}$	$T_c' = \frac{T_c - T_0}{T_w - T_0}$	$T_p' = \frac{T_p - T_0}{T_w - T_0}$
$\delta^* = \frac{\delta}{R_0}$	$Q_0 = \frac{Q_p}{Q_c}$	$C_c' = \frac{C_c - C_0}{C_w - C_0}$	$C_p' = \frac{C_p - C_0}{C_w - C_0}$	$\rho_0 = \frac{\rho_p}{\rho_c}$
$Re = \frac{\rho_p R_0 u_0}{\mu_p}$	$Gr = \frac{g \rho_p \gamma_T R_0^2 (T_w - T_0)}{u_0 \mu_p}$	$\varepsilon = \frac{R_0}{b}$	$K_0 = \frac{K_p}{K_c}$	$\tau_c = \frac{\tau_c' u_0 \mu_0}{R_0^2}$
$\tau_p = \frac{\tau_p' u_0 \mu_p}{R_0^2}$	$M = \frac{\sigma B^2 R_0^2}{\mu_0}$	$Gm = \frac{g \rho_p \gamma_c^* R_0^2 (C_w - C_0)}{u_0 \mu_0}$	$\xi = \frac{R_p \rho_p R_0^2}{\mu_p}$	$\xi_0 = \frac{R_p}{R_c}$
$Sc = \frac{\mu_p}{\rho_p D_p}$	$D_0 = \frac{D_p}{D_c}$	$k_0 = \frac{K_p}{K_c}$	$H = \frac{Q_p R_0^2}{(T_w - T_0) K_p}$	$Re = \frac{\rho_p R_0 u_0}{\mu_0}$
$Ec = \frac{u_0^2}{\bar{C}_p (T_w - T_0)}$	$Pr = \frac{\bar{C}_p \mu_0}{K_p}$	$Br = EcPr$	$s_0 = \frac{\bar{C}_p}{\bar{C}_c}$	

Where T_w, C_w represents the temperature and concentration at the arterial wall,
b represents the radius of curvature of the curved artery.

The dimensionless form of the stenoses geometry for both core and plasma regions are given as follows:

$$R'(z',t') = \begin{cases} \left[1 - \delta^* \sin\left(\pi(z' - d')\right)\right]\Omega(t') & \text{for} \quad d' \le z' \le d' + 1, \\ \Omega(t') & \text{otherwise.} \end{cases} \tag{4.18}$$

$$R_1'(z',t') = \begin{cases} \left[\beta - \delta^* \sin\left(\pi(z' - d')\right)\right]\Omega(t') & \text{for} \quad d' \le z' \le d' + 1, \\ \beta\Omega(t') & \text{otherwise.} \end{cases} \tag{4.19}$$

With the help of above mentioned non-dimensional parameters and considering the assumed condition of fully developed flow, low Reynold number ($Re <<< 1$), mild stenosis ($\delta^* << 1$) with $O(1) = \alpha = \frac{R_0}{L_0}$, the governing equations of both core and plasma region are converted into more simpler form as follows:

Core region

$$\frac{\partial P_c'}{\partial r'} = 0 \tag{4.20}$$

$$\frac{\partial P_c'}{\partial \theta'} = 0, \tag{4.21}$$

$$\frac{1}{\bar{D}}\frac{\partial P_c'}{\partial z'} = exp(\lambda_1[1/2 - T_c'])\left(\frac{\partial^2 w_c'}{\partial r'^2} + \frac{1}{r'}\frac{\partial w_c'}{\partial r'} + \frac{1}{r'^2}\frac{\partial^2 w_c'}{\partial \theta'^2} - \frac{\varepsilon^2 w_c'}{\bar{D}^2} + \frac{\varepsilon}{\bar{D}}\left[\cos\theta'\frac{\partial w_c'}{\partial r'} - \frac{\sin\theta'}{r'}\right.\right.$$
$$\left.\left.\frac{\partial w_c'}{\partial \theta'}\right]\right) - \lambda_1 exp(\lambda_1[1/2 - T_c'])\left(\frac{\partial w_c'}{\partial r'} - \frac{\varepsilon w_c'\cos\theta'}{\bar{D}}\right)\frac{\partial T_c'}{\partial r'} - \lambda_1 exp(\lambda_1[1/2 - T_c'])\left(\frac{1}{r'^2}\frac{\partial w_c'}{\partial \theta'}\right.$$
$$\left. + \frac{\varepsilon w_c'\sin\theta'}{r'\bar{D}}\right)\frac{\partial T_c'}{\partial \theta'} - M w_c' + \frac{GrT_c' + GmC_c'}{\rho_0}, \tag{4.22}$$

$$\frac{\partial^2 T_c'}{\partial r'^2} + \frac{1}{r'}\frac{\partial T_c'}{\partial r'} + \frac{\varepsilon\cos\theta'}{\bar{D}}\frac{\partial T_c'}{\partial r'} - \frac{\varepsilon\sin\theta'}{r'\bar{D}}\frac{\partial T_c'}{\partial \theta'} + \frac{1}{r'^2}\frac{\partial^2 T_c'}{\partial \theta'^2} + \frac{k_0}{Q_0}H + Br\, k_0\left(M\, w_c'^2 + F_c'\right) = 0, \tag{4.23}$$

$$\frac{1}{D_0 Sc}\left(\frac{\partial^2 C_c'}{\partial r'^2} + \frac{1}{r'}\frac{\partial C_c'}{\partial r'} + \frac{\varepsilon\cos\theta'}{\bar{D}}\frac{\partial C_c'}{\partial r'} - \frac{\varepsilon\sin\theta'}{r'\bar{D}}\frac{\partial C_c'}{\partial \theta'} + \frac{1}{r'^2}\frac{\partial^2 C_c'}{\partial \theta'^2}\right) - \frac{\xi}{\xi_0}C_c' = 0, \tag{4.24}$$

where

$$\bar{D} = 1 + \varepsilon r'\cos\theta',$$

$$F_c' = 2exp(\lambda_1(1/2 - T_c'))\left[\left(\frac{\partial w_c'}{\partial r'} - \frac{\varepsilon w_c'\cos\theta'}{\bar{D}}\right)^2 + \left(\frac{1}{r'}\frac{\partial w_c'}{\partial \theta'} + \frac{\varepsilon w_c'\sin\theta'}{\bar{D}}\right)^2\right].$$

Plasma region

$$\frac{\partial P_p'}{\partial r'} = 0, \tag{4.25}$$

$$\frac{\partial P_p'}{\partial \theta'} = 0, \tag{4.26}$$

$$\frac{1}{\bar{D}}\frac{\partial P_p'}{\partial z'} = \left(\frac{\partial^2 w_p'}{\partial r'^2} + \frac{1}{r'}\frac{\partial w_p'}{\partial r'} + \frac{1}{r'^2}\frac{\partial^2 w_p'}{\partial \theta'^2} - \frac{\varepsilon^2 w_p'}{\bar{D}^2} + \frac{\varepsilon}{\bar{D}}\left[\cos\theta'\frac{\partial w_p'}{\partial r'} - \frac{\sin\theta'}{r'}\frac{\partial w_p'}{\partial \theta'}\right]\right) - M w_p'$$
$$+ GrT_p' + GmC_p', \tag{4.27}$$

$$\frac{\partial^2 T_p'}{\partial r'^2} + \frac{1}{r'}\frac{\partial T_p'}{\partial r'} + \frac{\varepsilon\cos\theta'}{\bar{D}}\frac{\partial T_p'}{\partial r'} - \frac{\varepsilon\sin\theta'}{r'\bar{D}}\frac{\partial T_p'}{\partial \theta'} + \frac{1}{r'^2}\frac{\partial^2 T_p'}{\partial \theta'^2} + H + MBrw_p^2 + BrF_p' = 0, \tag{4.28}$$

$$\frac{1}{Sc}\left(\frac{\partial^2 C_p'}{\partial r'^2} + \frac{1}{r'}\frac{\partial C_p'}{\partial r'} + \frac{\varepsilon\cos\theta'}{\bar{D}}\frac{\partial C_p'}{\partial r'} - \frac{\varepsilon\sin\theta'}{r'\bar{D}}\frac{\partial C_p'}{\partial \theta'} + \frac{1}{r'^2}\frac{\partial^2 C_p'}{\partial \theta'^2}\right) - \xi C_p' = 0, \tag{4.29}$$

where

$$F'_p = 2\left[\left(\frac{\partial w'_p}{\partial r'} - \frac{\varepsilon w'_p \cos\theta'}{\bar{D}}\right)^2 + \left(\frac{1}{r'}\frac{\partial w'_p}{\partial \theta'} + \frac{\varepsilon w'_p \sin\theta'}{\bar{D}}\right)^2\right].$$

Non-dimensional boundary conditions for both core and plasma region are given as-

$$\begin{cases} \frac{\partial w'_c}{\partial r'} = 0, & \frac{\partial T'_c}{\partial r'} = 0, & \frac{\partial C'_c}{\partial r'} = 0, & \text{at} \quad r' = 0, \\ w'_c = w'_p, & T'_c = T'_p, & C'_c = C'_p, & \text{at} \quad r' = R'_1(z',t'), \\ \tau'_c = \tau'_p, & \frac{\partial T'_c}{\partial r'} = \frac{\partial T'_p}{\partial r'}, & \frac{\partial C'_c}{\partial r'} = \frac{\partial C'_p}{\partial r'}, & \text{at} \quad r' = R'_1(z',t'), \\ w'_p = w_b, & \frac{\partial w'_p}{\partial r'} = \frac{\zeta}{\sqrt{Da}}(w_b - w_{porous}), & & \text{at} \quad r' = R'(z',t'), \\ T'_p = 1, & C'_p = 1, & & \text{at} \quad r' = R'(z',t'), \\ \frac{\partial w'_c}{\partial \theta'} = 0, & \frac{\partial T'_c}{\partial \theta'} = 0, & \frac{\partial C'_c}{\partial \theta'} = 0, & \text{at} \quad \theta' = 0 \quad \text{and} \quad \theta' = \pi, \\ \frac{\partial w'_p}{\partial \theta'} = 0, & \frac{\partial T'_p}{\partial \theta'} = 0, & \frac{\partial C'_p}{\partial \theta'} = 0, & \text{at} \quad \theta' = 0 \quad \text{and} \quad \theta' = \pi. \end{cases} \tag{4.30}$$

Where $w_{porous} = -\left(\frac{Da}{\mu_p}\right)\frac{\partial P'_p}{\partial z'}$.

4.3 Procedure of solution

With the help of boundary conditions, a numerical solution of non-dimensional governing equations 4.22-4.29 is obtained by using finite difference scheme [91].

Central difference formula is used to state spatial derivative for which a semi- annular region $[0 \quad R'(z',t')] \times [0 \quad \pi]$ divided into the uniform grid. The spatial derivatives are described as-

$$\begin{cases} \frac{\partial A_f}{\partial r'} = \frac{(A_f)_{i+1,j} - (A_f)_{i-1,j}}{2\Delta r}, \\ \frac{\partial A_f}{\partial \theta'} = \frac{(A_f)_{i,j+1} - (A_f)_{i,j-1}}{2\Delta \theta}, \\ \frac{\partial^2 A_f}{\partial r'^2} = \frac{(A_f)_{i+1,j} - 2(A_f)_{i,j} + (A_f)_{i-1,j}}{(\Delta r)^2}, \\ \frac{\partial^2 A_f}{\partial \theta'^2} = \frac{(A_f)_{i,j+1} - 2(A_f)_{i,j} + (A_f)_{i,j-1}}{(\Delta \theta)^2}. \end{cases} \tag{4.31}$$

where $f = c$ if $0 < r' < R'_1(z',t')$ and $f = p$ if $R'_1(z',t') < r' < R'(z',t')$.

"A" refers the velocity (w'), temperature (T') and concentration (C'), respectively.

Δr and $\Delta\theta$ denotes the step-size in the r' and θ' directions, respectively. In the present study

step size is considered uniform. If the L_1 and L_2 denotes the number of sub-intervals, in which the interval $[0 \quad R(z',t')] \times [0 \quad \pi]$ are divided by using uniform grids, then $\Delta r'$ and $\Delta\theta'$ represent mathematically as-
$\Delta r = \frac{R'(z',t')}{L_1}$ and $\Delta\theta = \frac{\pi}{L_2}$
The grid points $(r'_i, \ \theta'_j)$ are represent as-

$$r'_i = (i-1)\Delta r', \qquad i = 1,2,3\cdots,L_1+1$$

$$\theta'_j = (j-1)\Delta\theta', \qquad j = 1,2,3\cdots,L_2+1$$

The Pressure gradient in both core and plasma region are considered constant [90, 116, 14] so it can be written as-

$$\frac{\partial P'_c}{\partial z'} = \frac{\partial P'_p}{\partial z'} = P_0. \tag{4.32}$$

The velocity and temperature equations are discretized with the help of equation (4.31). These discretized equations are converted into algebraic equations by varying i from 1 to L_1+1 and j from 1 to L_2+1. The algebraic equations form a tridiagonal block matrix and which are solved by using Gauss- Seidel iterative approach in MATLAB. The tolerance of error is considered 10^{-6} at every iteration.
After determining the velocity and temperature profile for the both region, we have obtained the flow rate, wall shear stress numerically by adopting finite difference method.
The Volumetric flow rate Q, frictional resistance λ and the wall shear stress τ_w are defined as-

$$Q = \int_0^{R'(z',t')} \int_0^{\pi} r'w'dr'd\theta',$$

$$Q = \int_0^{R'_1(z',t')} \int_0^{\pi} r'w'_c(r',\theta',z')dr'd\theta' + \int_{R'_1(z',t')}^{R'(z',t')} \int_0^{\pi} r'w'_p(r',\theta',z')dr'd\theta', \tag{4.33}$$

$$\lambda = \frac{\int_0^L (-\frac{\partial p'}{\partial z'})dz'}{Q}, \tag{4.34}$$

$$\tau_w = -\left[\frac{\partial w'_p}{\partial r'}\right]_{r'=R'(z',t')}, \tag{4.35}$$

The heat and mass transfer coefficients across the upper wall (upper wall) of the stenosed artery respectively are calculated as-
The non-dimensional form of Nusselt number is defined as-

$$Nu = -\left[\frac{\partial T'_p}{\partial r'}\right]_{r'=R'(z',t')}, \tag{4.36}$$

The non-dimensional form of Sherwood number is defined as-

$$Sh = -\left[\frac{\partial C_p'}{\partial r'}\right]_{r'=R'(z',t')}. \tag{4.37}$$

The mathematical expression of stream function (ψ) for both core and plasma region are deliberated as follows [108, 16]:

$$\begin{cases} \frac{\partial \psi}{\partial r'} = r' w_c', & 0 \le r' \le R_1'(z',t') \quad \text{(Core region)}, \\ \frac{\partial \psi}{\partial r'} = r' w_p' & R_1'(z',t') \le r' \le R'(z',t') \quad \text{(Plasma region)}. \end{cases} \tag{4.38}$$

4.4 Entropy generation and irreversibilty

Adopting the second law of thermodynamics, the amount of disturbance in a system can be expressed quantitatively by means of a connotation called entropy. According to Bejan [46] and Mekheimer [23], general form of entropy generation is written as-

$$E^{gen} = \underbrace{\frac{k(\nabla T)^2}{T_w^2}}_{\text{Thermal irreversibility}} + \underbrace{\frac{\mu}{T_w} F}_{\text{Fluid friction irrversibility}} + \underbrace{\frac{\sigma B^2}{T_w} u^2}_{\text{Joule heating irrversibility}} + \underbrace{\frac{D_b(\nabla C)^2}{C_w}}_{\text{solute irrversibility}} \tag{4.39}$$

where k, F, D_b represents the thermal conductivity, viscous dissipation and mass diffusivity, respectively.

Dimensional form of entropy generation for core and plasma region are written as-

$$\begin{aligned} E_c^{gen} = & \underbrace{\frac{K_c}{T_w^2}\left[\left(\frac{\partial T_c}{\partial r}\right)^2 + \left(\frac{1}{r}\frac{\partial T_c}{\partial \theta}\right)^2 + \left(\frac{b}{D}\frac{\partial T_c}{\partial z}\right)^2\right]}_{\text{Thermal irreversibility}} + \underbrace{\frac{F_c}{T_w}}_{\text{Fluid friction irrversibility}} \\ & + \underbrace{\frac{\sigma B^2}{T_w} w_c^2}_{\text{Joule heating irrversibility}} + \underbrace{\frac{D_c}{C_w}\left[\left(\frac{\partial C_c}{\partial r}\right)^2 + \left(\frac{1}{r}\frac{\partial C_c}{\partial \theta}\right)^2 + \left(\frac{b}{D}\frac{\partial C_c}{\partial z}\right)^2\right]}_{\text{solute irrversibility}} \end{aligned} \tag{4.40}$$

$$\begin{aligned} E_p^{gen} = & \underbrace{\frac{K_p}{T_w^2}\left[\left(\frac{\partial T_p}{\partial r}\right)^2 + \left(\frac{1}{r}\frac{\partial T_p}{\partial \theta}\right)^2 + \left(\frac{b}{D}\frac{\partial T_p}{\partial z}\right)^2\right]}_{\text{Thermal irreversibility}} + \underbrace{\frac{F_p}{T_w}}_{\text{Fluid friction irrversibility}} \\ & + \underbrace{\frac{\sigma B^2}{T_w} w_p^2}_{\text{Joule heating irrversibility}} + \underbrace{\frac{D_p}{C_w}\left[\left(\frac{\partial C_p}{\partial r}\right)^2 + \left(\frac{1}{r}\frac{\partial C_p}{\partial \theta}\right)^2 + \left(\frac{b}{D}\frac{\partial C_p}{\partial z}\right)^2\right]}_{\text{solute irrversibility}} \end{aligned} \tag{4.41}$$

where E_c^{gen} and E_p^{gen} represents the dimensional form of entropy generation in core and plasma region, respectively. In both above equation 4.40-4.41 first and last term of left side represent the thermal and solute irreversibilty. Second and third term described the fluid friction and joule heating irreversibility importance in the entropy generation process. By using non-dimensional parameters and order analysis, non-dimensional form of entropy generation in core and plasma are written as-

$$E_c'^{gen} = \frac{E_c^{gen}}{E}$$

$$E_p'^{gen} = \frac{E_p^{gen}}{E}$$

$$E_c'^{gen} = \frac{1}{k_0}\left[\left(\frac{\partial T_c'}{\partial r'}\right)^2 + \left(\frac{1}{r'}\frac{\partial T_c'}{\partial \theta'}\right)^2\right] + \frac{Br}{A}F_c' + \frac{BrMw_c'^2}{A} + \frac{\Gamma\Lambda}{AD_0k_0}\left[\left(\frac{\partial C_c'}{\partial r'}\right)^2 + \left(\frac{1}{r'}\frac{\partial C_c'}{\partial \theta'}\right)^2\right] \tag{4.42}$$

$$E_p'^{gen} = \left[\left(\frac{\partial T_p'}{\partial r'}\right)^2 + \left(\frac{1}{r'}\frac{\partial T_p'}{\partial \theta'}\right)^2\right] + \frac{Br}{A}F_p' + \frac{BrMw_p'^2}{A} + \frac{\Gamma\Lambda}{A}\left[\left(\frac{\partial C_p'}{\partial r'}\right)^2 + \left(\frac{1}{r'}\frac{\partial C_p'}{\partial \theta'}\right)^2\right] \tag{4.43}$$

where $E = \frac{K_p(T_w-T_0)^2}{T_w^2R_0^2}$, $A = \frac{T_w-T_0}{T_0}$, $\Lambda = \frac{C_w-C_0}{C_0}$, $\Gamma = \frac{D_pT_w(C_w-C_0)}{K_p(T_w-T_0)}$

The dimensionless form of the Bejan number (Be) is-

$$Be = \frac{\text{Entropy generation due to heat and mass flux}}{\text{Total entropy}}$$

The dimensionless form of Bejan number for the core and plasma region are written as-

$$Be_c = \frac{\frac{1}{k_0}\left[\left(\frac{\partial T_c'}{\partial r'}\right)^2 + \left(\frac{1}{r'}\frac{\partial T_c'}{\partial \theta'}\right)^2\right] + \frac{\Gamma\Lambda}{AD_0k_0}\left[\left(\frac{\partial C_c'}{\partial r'}\right)^2 + \left(\frac{1}{r'}\frac{\partial C_c'}{\partial \theta'}\right)^2\right]}{E_c'^{gen}} \tag{4.44}$$

$$Be_p = \frac{\left[\left(\frac{\partial T_p'}{\partial r'}\right)^2 + \left(\frac{1}{r'}\frac{\partial T_p'}{\partial \theta'}\right)^2\right] + \frac{\Gamma\Lambda}{A}\left[\left(\frac{\partial C_p'}{\partial r'}\right)^2 + \left(\frac{1}{r'}\frac{\partial C_p'}{\partial \theta'}\right)^2\right]}{E_p'^{gen}} \tag{4.45}$$

where Be_c and Be_p represents the dimensionless form of Bejan number in core and plasma region, respectively.

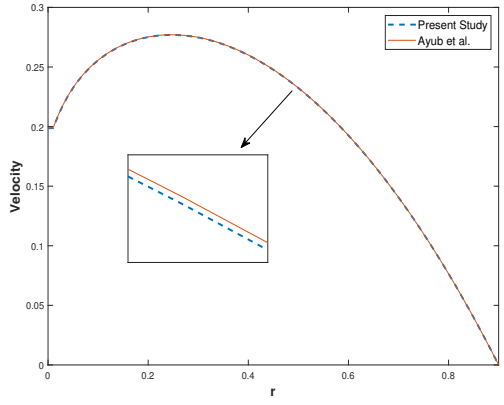

Figure 4.2: Comparison of present study with published work

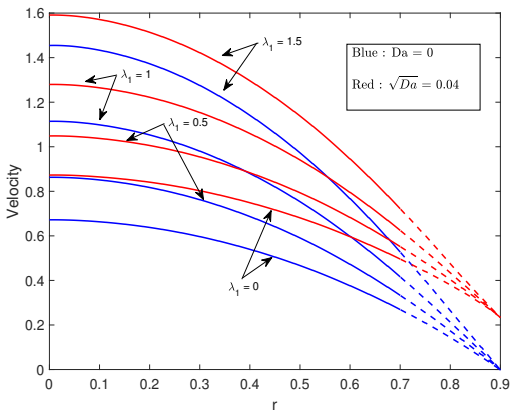

Figure 4.3: Variation in velocity with λ_1

4.5 Results and Discussion

A numerical study has been presented to investigate the impact of joule heating, temperature-dependent viscosity and arterial wall permeability condition on the two-phase blood flow through a stenosed curved artery with heat and mass transfer. This study also interprets the entropy generation curved artery flow, which arise due to thermal, solute, fluid friction and joule heating irreversibility in the two-phase blood flow. This research examined the numerical significance of several physical parameters, including temperature-dependent viscosity (λ_1), magnetic field (M), artery wall permeability (Da), heat source (H), joule heating, and chemical reaction parameter (ξ). This study considered the viscosity of core region as temperature-dependent while, plasma region's viscosity as a constant. The thickness of the plasma viscosity is assumed 20%, according to artery diameter and hematocrit level [88]. The non-dimensional governing equations have been solved by using the second-order finite difference method (FDM). The flow region has been discretized uniformly in the radial (r') and angular direction (θ') with $\Delta r = \Delta\theta = 0.001$, respectively. The tolerance of error is considered 10^{-6} in the whole numerical process. MATLAB codes for FDM are developed to compute the velocity, temperature, concentration, WSS, frictional resistance and entropy generation for the various physical parameters. Default values of the parameters which were used for pictorially analyzed the importance of the model are listed below in the table 1. In all the figures of velocity, temperature, and concentration profiles, the continuous and dashed lines symbolized the core and plasma region, respectively.

The validation of the present study with the published work of Ayub et al.[80] has been picturized graphically through the figure 4.2. For comparison, the effect of the magnetic field, permeable wall, variable viscosity and two-phase nature of blood neglected in

the present work, and the impact of nanofluids and catheter have been ignored in the observation of [80]. The perturbation technique was used by [80] to simplify the governing equations. Therefore in this comparison, perturbation technique has used for [80] work and finite difference method for the present study. It is observed that there is a good agreement between our study and published work [80], which replicates the validation of the present study.
The table 4.2 contains the default values of non-dimensional parameters which are used into the simulations.

Table 4.2: Default values of non-dimensional parameters

$\lambda_1 = 0.75$	$\varepsilon = 0.1$	$M = 2$	$Gr = 1$	$Gm = 1$	$\rho_0 = 1.05$	$P_0 = 2$
$k_0 = 0.6$	$Q_0 = 1$	$H = 1$	$Br = 0.3$	$D_0 = 1$	$Sc = 1$	$\xi = 1.5$
$\xi_0 = 1$	$\zeta = 0.1$	$\Lambda = 0.8$	$\Gamma = 0.5$	$A = 0.5$		

The influence of a temperature-dependent viscosity parameter (λ_1) on the blood flow that passes through the stenosed curved artery is graphically depicted in figure (4.3). In this comparative investigation, both viscosity conditions constant ($\lambda_1 = 0$) and variable ($\lambda_1 \neq 0$) have been considered into account. The figure (4.3) shows that blood viscosity is directly affected by temperature. As per the increase in the value of λ_1, core region viscosity diminishes due to dominance temperature inflow. It is also concluded that aggregation of RBC's can be lower with the increase in temperature, resultant risk of heart disease (heart attack and stroke) can be reduced due to an increase in blood viscosity, which is in line with earlier research [117]. As a result, the increase in the value of λ_1 reveals in a significant improvement in the blood velocity profile. As we apply the variable viscosity (temperature-dependent) in the core region, it directly affects the core region's flow velocity and indirectly reflects the change in the plasma region velocity due to continuity of wall interface condition. The effect of wall permeability can also be seen in the figure (4.3). It has been found that blood velocity is higher when the wall is permeable compared to the impermeable wall. It has also been seen that the velocity difference between permeable and impermeable walls rises as the λ_1 increases.

The blood is highly affected by the magnetic field, due to the presence of haemoglobin in the RBC, which contains iron oxide particles and is capable of binding oxygen molecules. The presence of oxygen has a significant impact on haemoglobin's molecular structural system. The RBC's shows paramagnetic nature with magnetic susceptibility $\approx 2.2 * 10^{-}5$. By taking motivation from the magnetic properties of blood, we mathematically described the significance of magnetic field on the two-phase blood flow via the figure (4.4). This study

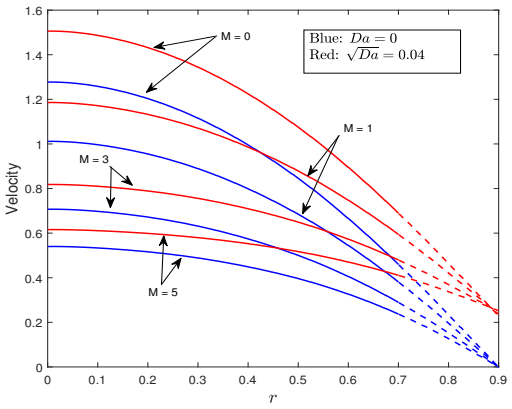

Figure 4.4: Variation in velocity with M

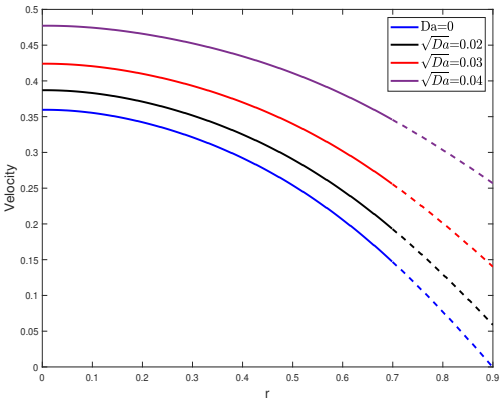

Figure 4.5: Variation in velocity with Da

states that when an external magnetic field is applied to the blood, it generates a strong electromotive field. In this study, a magnetic field is acting in the flow's normal direction, which produces a Lorentz force perpendicular to the flow direction, resultant it slowing down the flow speed. It has also been observed that blood velocity is higher for the permeable artery wall under a magnetic field than the impermeable artery wall. Figure (4.4) clearly indicates that when the magnetic field improves, the velocity variation between permeable and impermeable walls reduces due to an increase in the Lorentz force's dominance in the flow.

A comparative analysis of the velocity profile has been undertaken to demonstrate the importance of the artery permeable wall condition in blood flow, as shown in the figure (4.5). The figure shows that pores on the arterial wall increase with the positive add in the value of Da. Therefore, blood velocity enhances with the rise in arterial wall permeability. It can also be concluded that, in a realistic situation, the arterial wall is of permeable nature; hence blood flow velocity is always higher than the assuming impermeable wall condition. The figure also illustrates that when the value of Da rises, the velocity variation between centre and the artery wall diminishes.

The figure 4.6 presents the effect of the temperature-dependent viscosity parameter (λ_1) in the flow temperature for the permeable arterial wall. This study also reveals the comparison between constant and variable viscosity conditions. According to figure 4.6, as the value of λ_1 increases, viscous heating occurs in the flow owing to the rise in flow velocity, resulting in a surge in flow temperature. It's also worth noting that as λ_1 increases, so does the variation in flow temperature rises.

Figure 4.7-4.8, described the influence of Joule heating and Brinkman number on the blood flow temperature for both core and plasma region, respectively. The blood flow experiences an electromagnetic force due to the implication of joule heating. Therefore, flow

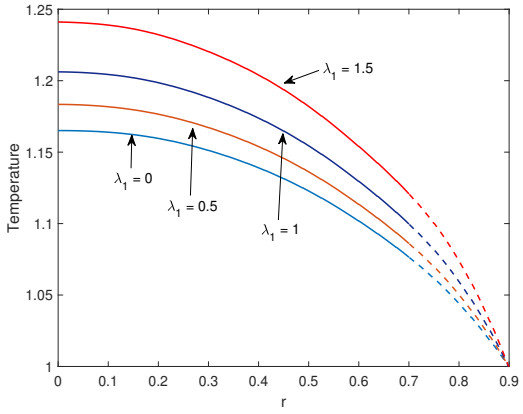

Figure 4.6: Variation in temperature with λ_1

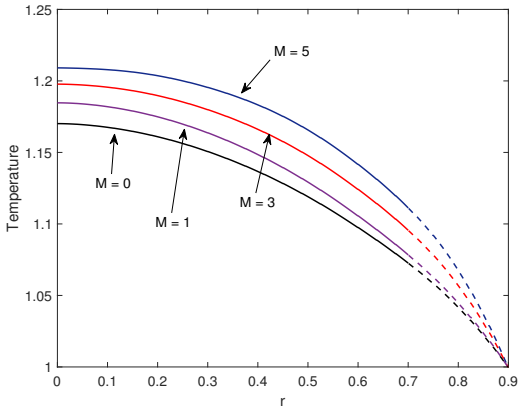

Figure 4.7: Variation in temperature with M

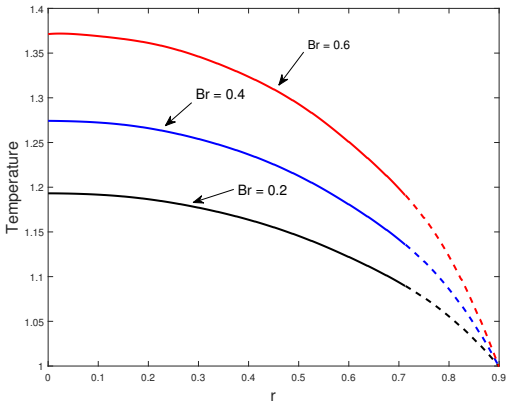

Figure 4.8: Variation in temperature with Br

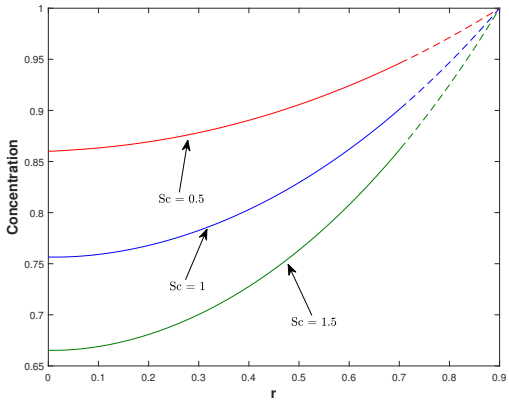

Figure 4.9: Variation in concentration with Sc

generates viscous heating, which leads to a hike in the flow temperature. The finding results are in fair agreement with the previously published work [118]. This result will be beneficial in magnetic and hyperthermic therapies to cure tumor/cancer cells due to the hike inflow temperature with the magnetic field. The Brinkman number is an important aspect of the fluid heat transfer process due to its heat conduction between viscous fluid and the wall. The ratio of viscous heat generation with external wall heating is known as the Brinkman number. Figure 4.8 graphically described the influence of Brinkman number on the blood flow for both core and plasma regions. It noticed that with the enhancement in the value of Br, significant growth in temperature profile is observed. This happens due to arise a downfall in the heat conduction which is generated by viscous dissipation in the flow with the positive increment in value of Br. As a result, flow temperature rises significantly. The current study's findings for Br are in good agreement with earlier research [119, 120].

A numerical study to illustrate the influence of the Schmidt number (Sc) and chemical reaction parameter (ξ) on the concentration profile for both core and plasma has been

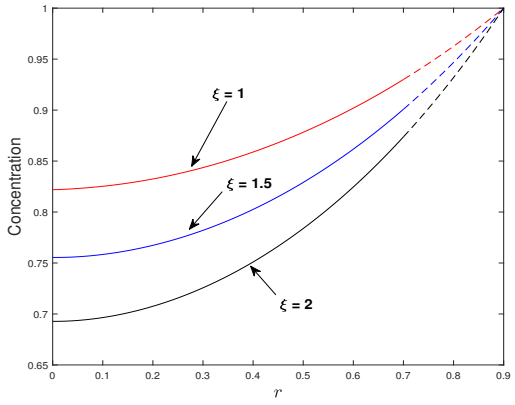

Figure 4.10: Variation in concentration with ξ

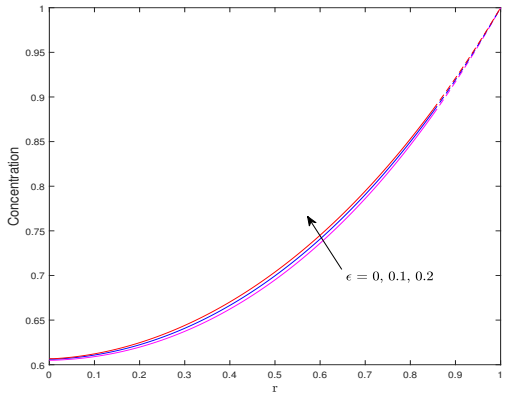

Figure 4.11: Variation in concentration with ε

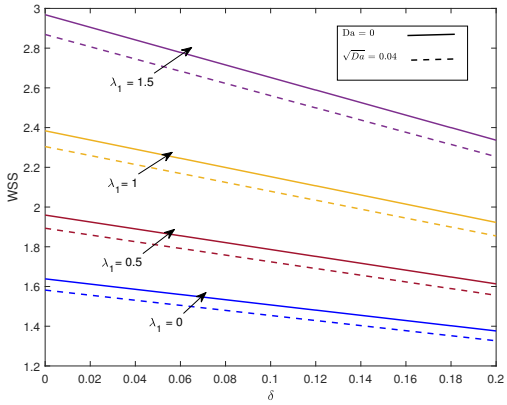

Figure 4.12: Variation in WSS with λ_1 and Da

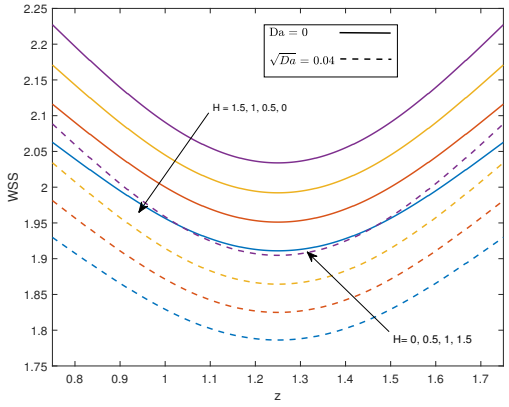

Figure 4.13: Variation in WSS with H and Da

presented through the figures 4.9-4.10. From both figures, it is noted that as blood flow proceeds towards the artery wall from the center of an artery, the concentration profile increases. It also concluded that, with the increases in the Schmidt number and chemical reaction parameter value, a decay in the concentration profile occurs. This occurs as a result of a decrease in molecular diffusivity at larger values of both Sc and ξ, resulting in a fall in species concentration in the flow. Figure 4.11 shows the variation in flow concentration profile for varying values of arterial curvature in both the core and plasma regions. This study compares the straight ($\varepsilon = 0$) and curved ($\varepsilon \neq 0$) arteries role on flow concentration. From figure 4.11, a modest improvement in concentration profile is recorded with the rise in artery curvature for both regions.

As per the literature survey, temperature has a significant role in studying wall shear stress (WSS). Figure 4.12 is displayed to elaborate the impact of temperature (in terms of λ_1) on the WSS for the stenosis depth (δ). In this study, WSS profile is investigated for both permeable ($Da \neq 0$) and impermeable walls ($Da = 0$). An increase in value of λ_1 causes a

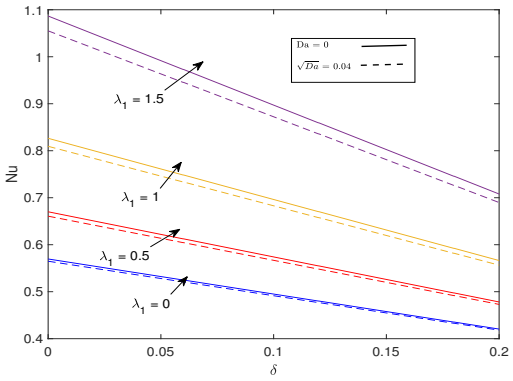

Figure 4.14: Variation in Nusselt number with λ_1 and Da

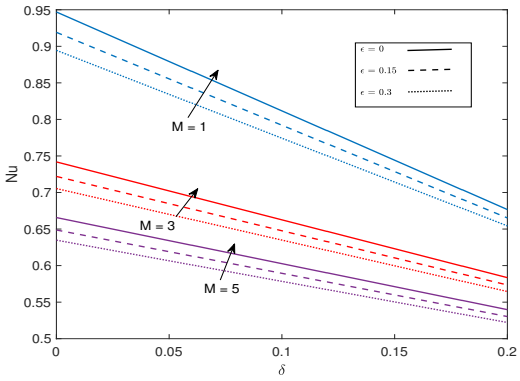

Figure 4.15: Variation in Nusselt number with M and curvature ε

gradually drop in the flow viscosity, resulting in a decay in the WSS profile, as seen in the figure. It is noticed that WSS is higher for the impermeable wall than a permeable wall. It also found that variation in decrement of WSS profile becomes higher when the arterial wall becomes more permeable. The high WSS is responsibe for endothelial damage and pathological response as suggested by Fry [94], so such type of damaging diseases, can be resolved by reducing in the viscosity (with increment in the λ_1).

The impact of heat source on the wall shear stress profile in the stenotic region of the curved artery is depicted in the figure 4.13. The effect of a heat source on permeable and impermeable walls is investigated in the present study, and the stenotic range is specified as $z = 0.75$ to $z = 1.75$. The WSS profile is higher for the impermeable wall ($Da = 0$) than the permeable wall, which shows good agreement with published work [121]. This study also suggested that an increase in the heat source leads to a hike in the arterial wall temperature, resultant wall shear stress profile curved artery increases in the stenotic region. As a result, using an external heat source in the flow during the clinical treatment process can lower the risk of atherosclerosis formation. This study will be helpful in the clinical healing process by reducing the fear of endothelial damage by applying external heat.

Figures 4.14-4.15 are developed to describe the effect of both temperature-dependent viscosity parameter (λ_1) and magnetic field on the heat transfer rate (Nusselt number) for the stenosis depth. The Nusselt number has also been compared between permeable and impermeable artery wall conditions from the figure 4.14. A linear decay in the heat transfer rate has been found with growth in stenosis height. Figure 4.14 described the dominance of temperature in the Nusselt number with the help of λ_1. The value of λ_1 has no direct impact on the Nusselt number because heat transfer rate is computed at the wall, but due to flow continuity condition at the fluid interface layer, it plays a vital role in the calculation of heat transfer rate. From the figure 4.14, it is concluded that at the arterial wall interface

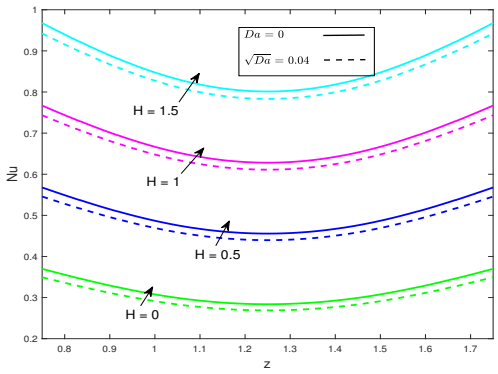

Figure 4.16: Variation in Nusselt number with H

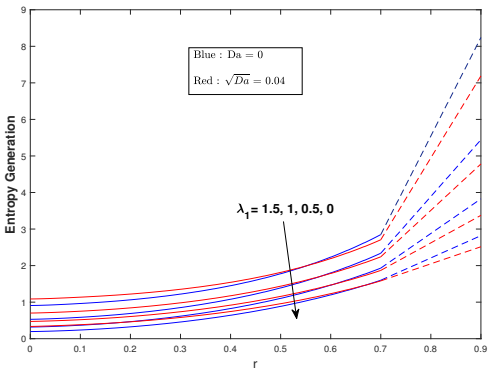

Figure 4.17: Variation in Entropy generation with viscosity variation parameter λ_1

magnitude of heat transfer rate increase with the positive increment in the value of λ_1, due to significant growth in frictional heating. As concluded above, with the increase in the value of λ_1 , blood flow gets smoother; hence, heat transfer at the wall increases. However, it is worth noting that the increase in the heat transfer is not proportional to the increase in the value of λ_1, instead, it grows drastically with a uniform increase in the value of λ_1. The effect of magnetic field (Joule heating) and arterial curvature on Nusselt number have been depicted in the figure 4.15. According to this study, when an external magnetic force is applied perpendicular to the blood flow, it slows the flow speed. Therefore, a reduction in viscous heating is observed; as a result, heat transfer at artery wall decays with enlargement in the magnetic field strength. This figure also shows that heat transfer is higher in the uniform artery ($\varepsilon = 0$) than the curved artery ($\varepsilon \neq 0$). It can also be stated that while blood flows freely (without stenosis/small stenosis), the heat transfer rate variance between curved and uniform arteries is greater, but as stenosis increases, the variation decreases.

The variation in the heat transfer coefficient (Nusselt number) in the stenotic region for the different values of heat source (H) has depicted by figure 4.16. This figure reveals that the heat transfer rate reduced due to the occurrence of stenosis in the blood flow. It's also important to note that the nusselt number rises as the value of the external heat source in the flow increases. This occurs because fluid generates the heat energy in the frictional heating process in the flow, which directly impacts the heat transfer coefficient. Figure 4.16 also found that the heat transfer rate is higher for the impermeable arterial wall condition than the permeable wall. As previously stated that in a realistic situation, arterial wall is permeable. As a result, it may be concluded that heat transfer at the artery wall is lower in actual life than estimated by the impermeable wall.

Figure 4.17 demonstrate the concept of entropy generation for the various values of viscosity variation parameter (λ_1) in the blood flow through the stenosed curved artery. It is

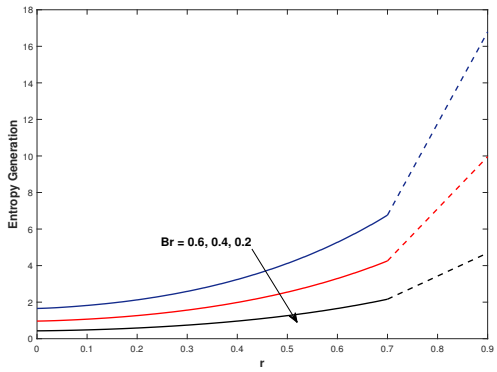

Figure 4.18: Variation in Entropy generation with Brinkman number Br

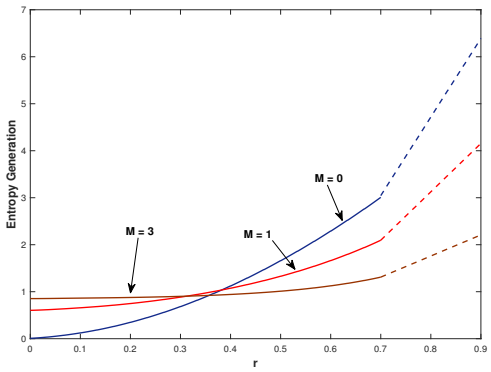

Figure 4.19: Variation in Entropy generation with M

widely acknowledged that an increase in entropy generation in any system indicates a drop in quality energy (i.e. exergy). A comparison study between permeable and impermeable artery wall conditions has also been detailed in figure 4.17. As concluded above, with the increase in the value of λ_1, flow generates more heat. Therefore flow feels more energy due to this heat generation. From the figure, it can be seen that flow converts most of the energy into work done in the center region of the artery, so less entropy generation is observed in the center region (core region). Due to less effect of permeable wall condition in the core region, entropy generation is slightly higher for the porous wall in the core region, but when flow approaches near the plasma region, a considerable reduction in entropy is observed for the permeable wall.

Figures 4.18-4.19 elucidates the effect of Brinkman number (Br) and Joule heating (M) on the entropy generation for the two-phase blood flow passes through a porous curved artery. From both figures, it can be stated that, due to higher heat transfer near the arterial wall, the flow generates more entropy near the wall. As a result of the presence of protein, nutrients, and significant heat transfer in the plasma region, it can also be determined that blood creates a large amount of energy in the plasma region, although the majority of this energy is not employed for work. The rise in viscous heating associate with a positive increment in the value of Brinkman number (Br) which contributes to the increase in entropy generation in blood flow. The finding results for Br are in good agreement with the previous findings of [22]. The effect of Joule heating in the production of entropy has been depicted via the figure 4.19. From the figure, it is found that with the applying joule heating, firstly, entropy generation increase in the core region but as flow reaches toward the arterial wall, it reflects the reverse effect.

The dominance of thermal and solute irreversibility in the total entropy generation is described with the help of Bejan number. The figure (4.20) elucidates the impact of joule

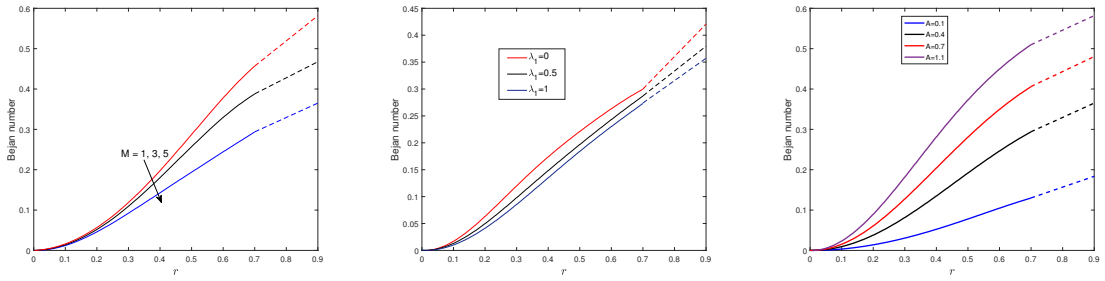

(a) (b) (c)

Figure 4.20: Variation in Bejan number for different values of , (a) magnetic field M, (b) Viscosity variation parameter λ_1, (c) A.

heating (M), viscosity variation parameter (λ_1) and temperature ratio parameter (A) on the Bejan number for the two-phase blood flow through the stenosed curved artery. The figure shows that entropy production due to heat and mass flux at the centre of the artery is less in comparison with viscous dissipation and joule heating. But as the flow approaches towards the arterial wall, blood flow generates more entropy due to thermal and solute irreversibility. From the figures (4.20a)-(4.20b), it can be concluded that viscous heating between fluid layers increases with the enhancement in the values of joule heating (M) and viscosity variation parameter (λ_1). As a result, entropy and disorderness rises in the blood flow due to the production of energy by viscous heating. Therefore, Bejan number decays with the increase in the value of (M) and (λ_1). Figure (4.20c) reflects that, for the larger value of temperature ratio parameter (A), the entropy production is higher than the fluid friction and joule heating; therefore, Bejan number increases with the positive add in the value of A.

Blood flow trapping through a stenosed curved artery with a permeable wall is an exciting phenomenon to understand the flowing nature. The figures 4.21-4.24 exhibit the comparative discussion of blood trapping for various parameters magnetic field (M), viscosity variation parameter (λ_1), heat source (H) and arterial curvature parameter (ε), respectively. The streamlines show a smoothness in the flow due to steady flow and constant pressure gradient. Figure 4.21 described the impact of the magnetic field on the blood flow in both radial and flow directions. The trapping configuration has revealed that an increase in magnetic field strength causes a restriction in the maximum velocity region due to the generation of Lorentz force, which slows the flow. The significance of temperature-dependent viscosity (in terms of λ_1) in flow trapping is visualised in figure 4.22. According to this figure, growth in value of λ_1 leads to a drop in core region viscosity. Therefore, the maximum velocity area increases with a rise in λ_1, specially in the stenotic region from $z = 0.75$ to $z = 1.75$. The fluid temperature has an important impact on the variation of blood flow patterns. Fluid

temperature enhances by applying an external heat source to the blood flow. Therefore, a significant difference in the flow pattern through curved artery for both heat source conditions ($H = 0$, & $H \neq 0$) can be observed through the figure 4.23. It's also worth noting that when a heat source is applied to the arterial wall, the maximum velocity area increases in a stenotic region. In this study, we are dealing with the curved artery, so blood flow configuration for the different values of curvature parameter (ε) has been depicted through the figure (4.24). A comparative study has been performed with the help of flow configuration to illustrate the difference between when blood passes through straight and curved arteries. The figure shows that, with the increase in arterial curvature, the maximum blood flow velocity area decreases. Therefore, it can be concluded that flow velocity is higher for the straight artery ($\varepsilon = 0$) than the curved arteries ($\varepsilon \neq 0$).

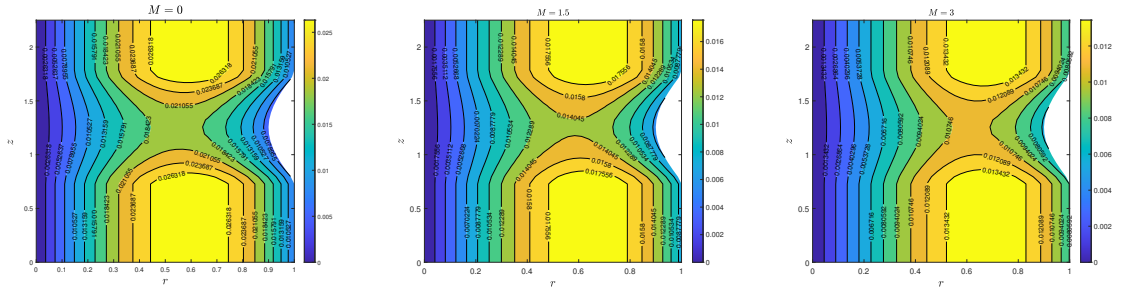

(a) (b) (c)

Figure 4.21: Blood flow pattern for different values of magnetic field, (a) $M = 0$, (b) $M = 1.5$, (c) $M = 3$.

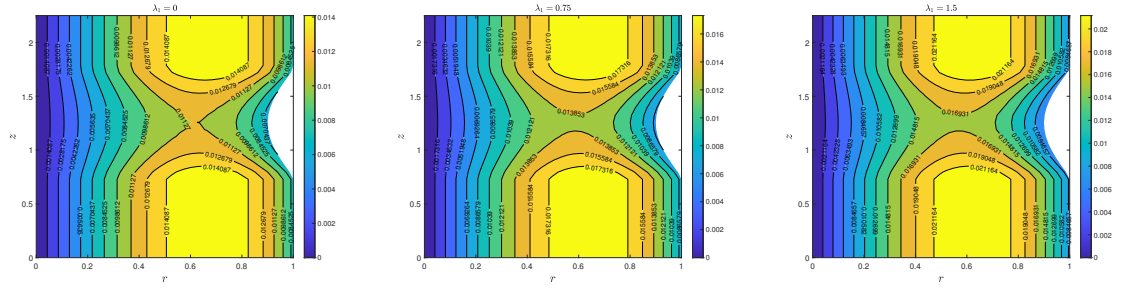

(a) (b) (c)

Figure 4.22: Blood flow pattern for different values of viscosity variation paramter, (a) $\lambda_1 = 0$, (b) $\lambda_1 = 0.75$, (c) $\lambda_1 = 1.5$.

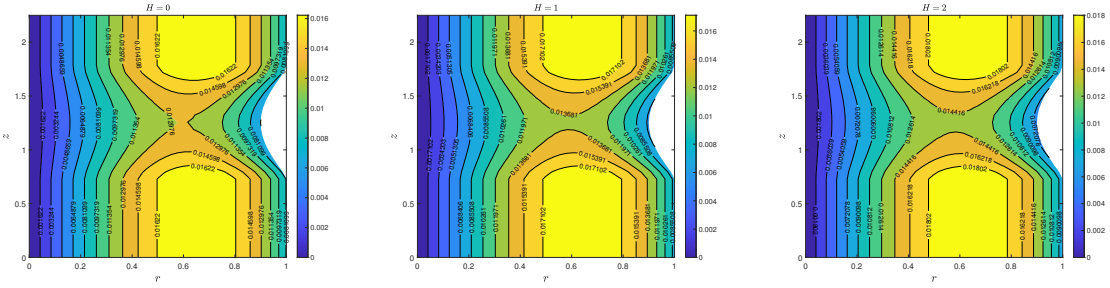

(a) (b) (c)

Figure 4.23: Blood flow pattern for different values of Heat source, (a) $H = 0$, (b) $H = 1$, (c) $H = 2$.

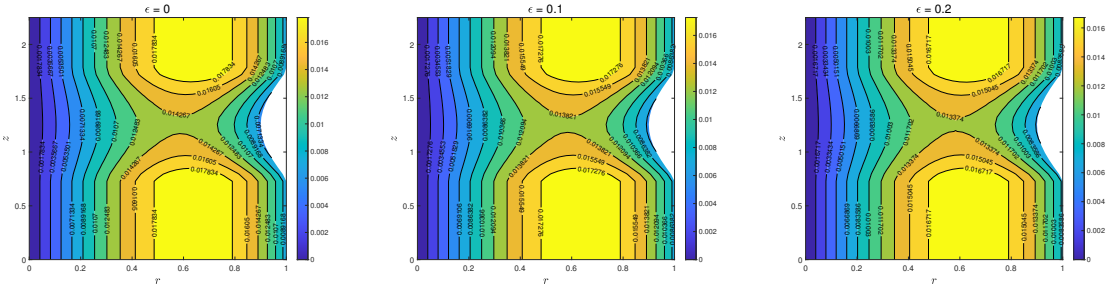

(a) (b) (c)

Figure 4.24: Blood flow pattern for different values of curvature, (a) $\varepsilon = 0$, (b) $\varepsilon = 0.1$, (c) $\varepsilon = 0.2$.

4.6 Conclusion

A numerical analysis of a two-phase blood flow model in the curved stenosed artery by assuming variable viscosity (temperature-dependent) in the core has been presented. A patient-specific artery geometry in the presence of stenosis (plaque) has been considered. The use of permeable arterial wall condition instead of the no-slip condition makes this study more realistic. The governing equations, including continuity, momentum, heat and mass transfer, are written in the toroidal coordinate system, which is solved by using the finite difference method for the appropriate boundary conditions in "MATLAB" software. The impact of various non-dimensional physical parameters such as M, λ_1, Da, Br, H, ξ, δ, on the flow velocity, temperature, concentration, WSS, frictional resistance, Nusselt number and Entropy generation have been presented graphically. Clinical researchers and biologists

can use the current mathematical research to lower the risk of lipid deposition and predict the risk of cardiovascular disease, and then diagnose patients based on risk. The significant finding of the current mathematical study are listed below-

- The positive add in the value of λ_1 causes a drop in core region viscosity; as a result, blood flow becomes smoother. Therefore both heat transfer rate and wall shear stress increase.
- Significant growth in fear of deposition of plaque (lipid) appears with the rise in both arterial curvature and permeability wall condition, which happen due to a reduction in the wall shear stress profile.
- With increasing external magnetic field strength, the magnitude of both wall shear stress and heat transport rate at the artery wall decreases.
- The use of an external heat source (H) in thermal therapies can reduce the growth of arteriosclerosis during the healing process and increase the heat transfer rate at the artery wall.
- Due to the presence of protein, nutrients, and significant heat transfer in the plasma region, blood produces a large amount of energy in the plasma region, although the majority of this energy is not employed for work.
- The entropy generation increases for the positive add in both λ_1 and Br.

Chapter 5

Numerical investigation of the entropy generation analysis for radiative MHD Power-law fluid flow of blood through a curved artery with Hall effect[1]

5.1 Introduction

Vascular diseases such as thrombosis, atherosclerosis and aneurysm are the most significant threats to human life. It frequently occurs when the cholesterol or liposomes get deposited at the artery's walls, eventually forming plaque. The narrowing of the artery restricts the flow of oxygen-rich blood. Identifying the vascular geometry and hemodynamic blood flow inside the artery is essential for preventing vascular disease progression. Arterial curvature is one of the geometrical factors associated with atherosclerosis. As a result, it is critical to conduct extensive research on hemodynamic factors such as curvature, blood flow, and mechanical conduct of the walls. Issaci et al.[37] examined the effect of low and intermediate Hartman numbers on the MHD flow in a curved pipe that can be applied to the first wall and fusion blanket of a nuclear reactor. They discovered that the velocity contour was circular and shifted toward the outer tube wall for low Hartman number, and for intermediate Hartman number, the velocity contour is distorted in an axisymmetric fashion. Nadeem and Ijaz [76] conducted a theoretical study of metallic nanoparticles through a curved stenosis artery with permeable wall. They discovered that the resistance impedance increases with stenosis height and decreases with nanoparticle volume fraction.

Abbasi et al. [122] developed a mathematical model to examine the Hall effect on the curve channel by considering the Carreau–Yasuda fluid. Their study revealed that the velocity profile is not symmetric about the center-line for the curved channel. The symmetric

[1] A considerable part of this chapter is published in *Waves in Random and Complex Media*

pattern gets disturbed, and the fluid velocity decreases if magnetic strength is increased. Akram et al. [123] investigated the effect of the Hall and ion slip parameters, as well as Electroosmotic Pumping, on the curved microchannel. They discovered that increasing the Joule heating parameter enhances the temperature profile since heat is generated due to the resistance it encounters from the electric current. The mathematical model of hemodynamic flow in a catheterized stenosed artery with thrombosis, susceptible to Hall and ion slip effects, was presented by Khanduri et al.[124]. Shehzad et al. [125] investigated Hall Currents, Joule and viscous dissipation effects on the MHD peristaltic flow over the curved channel. They discovered that increasing the magnetic field parameter due to the resistive Lorentz force reduces the flow rate inside the channel.

Mekheimer et al.[126] developed a mathematical model to study the influence of both magnetic field and the Hall effect on the blood flow velocity through a vertically symmetric stenosed artery. This study reveals that the wall shear stress profile reflects the opposite behaviour with the rise in the values of magnetic field and Hall parameter. Bhatti et al. [118] conducted a comparative study on peristaltic blood flow using Newtonian and non-Newtonian assumptions for the Joule and Hall effects as well as heat transfer. According to the study's findings, the Joule and Hall parameter exhibits the opposite behaviour for both the blood flow's velocity and temperature profile. A numerical observation to distinguish the impact of cilia length and the Hall effect on the flow through cylindrical tubes has been discussed by Farooq et al. [120], and they state that with the increase in cilia length, flow produces more entropy. Also, at the tube center, entropy production rises with the increase in Hall current and reflects the reverse effect near the tube wall.

The study of radiation's effect on blood flow is a crucial topic for researchers as it has many significant applications in biomedical engineering and thermal treatments. Radiation is mostly used to treat conditions such as cancer tumors, fibromyalgia, synovial bursa, muscle pain and stiffness etc. An analytic investigation of radiation heat transfer for the stenotic circular artery under the variable viscosity condition (hematocrit dependent) have been performed by Prakash et al. [127], and reported that increasing the thermal absorption parameter enhances the heat transfer rate at the arterial wall. A combined study of thermal radiation and nanoparticle (gold) on the heat transfer of blood flow have been completed by Eid et al. [128], and they reported that fluid temperature enhanced with the increase in nanoparticle volume in blood. In all the aforementioned studies on heat transfer, blood is assumed a single-phase fluid; therefore these work have been extended for the two-phase blood flow (core and plasma) by Sharma et al. [65, 13, 129], under both variable and constant condition of the core region viscosity and state the flow rate decreases with the increase in radiation parameter.

All the above computational and theoretical research work mentioned in the literature documented the flow and heat transport phenomena for the blood flow. To the best of the author's knowledge, no one has previously studied the estimation of entropy and flow behaviour for the power-law two-phase blood flow model in a stenosed curved artery under the influence of the Hall effect and magnetic field. Therefore, a mathematical model has been developed to investigate the entropy production and blood flow transport phenomena by adopting power-law fluid properties in a stenosed curved artery in the presence of the Hall effect and magnetic field intensity. To make this study more effective according to vascular diseases, a patient-specific elliptic shape stenosis model at the arterial wall has been considered. The present investigation considered the blood as non-Newtonian fluid (Power-law fluid) in the core region, while, showing the Newtonian fluid nature with constant viscosity in the plasma region. The effect of various parameters such as flow behaviour index (n), magnetic field, Hall parameter, radiation parameter and Brinkman number etc. have been illustrated with the help of graphs. Present investigation discussed the entropy generation concept, which occurs in the blood flow due to heat flux, viscous and Ohmic heating. A central difference scheme of second order [130] has been applied for the discretization of spatial derivatives, and Stone's strongly implicit method [131] is used for solving a system of non-linear equations. Clinical researchers and biologists can utilize finding of this computational investigation to predict endothelial cell damage and deposition of plaque in curved arteries with WSS profiles and can cure timely to reduce these severe situations. The use of radiation in thermal therapies will be helpful in the treatment of cancer cells, muscle pain and stiffness etc.

5.2 Problem formulation

An unsteady, incompressible flow of blood passing through a finite-length curved artery with elliptic shape stenosis is examined in this study. The two-phase blood flow assumption has been taken into account to make the study more feasible, as considered by [88, 132]. In the core region, blood is considered non-Newtonian (Power law fluid), while, in the plasma region, blood is considered Newtonian fluid with constant viscosity. In this investigation, blood flow through the curved artery, and the toroidal coordinate system (r, θ, z) have been employed to describe the arterial geometry. The z-axis represents the curved artery axis, and r is taken along the radial direction.

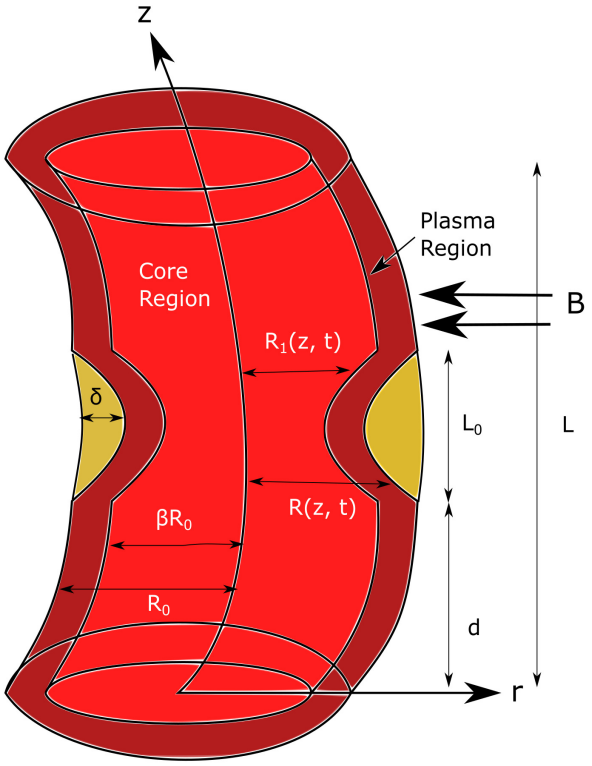

Figure 5.1: Graphical representation of curved artery

5.2.1 Mathematical formulation of stenosis

The elliptic shape stenosis condition has been assumed for both the core and plasma region. $R_1(z,t)$ and $R(z,t)$, represent the radius of the stenotic region for both the core and plasma region, respectively. Figure 5.1 present geometry of stenosed curved artery. Numerically formulation of overlapped diseases section (stenosis) for curved artery is written as preceding [133]:

Mathematical formulation of plasma region stenosis:

$$R(z,t) = \begin{cases} \left[R_0 - \delta \sin\left(\pi(\frac{z-d}{L_0})\right)\right]\Omega(t), & d \le z \le d+L_0, \\ R_0\Omega(t) & \text{Rest region.} \end{cases} \tag{5.1}$$

Mathematical formulation of core region stenosis:

$$R_1(z,t) = \begin{cases} \left[\beta R_0 - \delta \sin\left(\pi(\frac{z-d}{L_0})\right)\right]\Omega(t), & d \le z \le d+L_0, \\ \beta R_0\Omega(t) & \text{Rest region.} \end{cases} \tag{5.2}$$

$$\Omega(t) = 1 - \eta(\cos(\omega t) - 1)e^{-\eta\omega t}, \tag{5.3}$$

where L_0 & L represents the length of diseases section of artery, respectively. δ and d indicate the stenosis maximum height and location, respectively.
R_0 radius of healthy curved artery β expresses the ratio in the healthy artery section between core and complete artery radius. η is constant.

5.2.2 Magnetic field and Hall effect

A uniform magnetic field B is introduced along the θ direction and nature of tube is assumed electrically non-conducting. The (H_r, H_θ, H_z), represents the magnetic filed components in the r, θ, z directions, respectively.
The solenoidal relation represents is $\nabla.\vec{H} = 0$.
According to the Maxwell's electromagnetic field equations

$$\frac{\partial H_\theta}{\partial \theta} = 0. \tag{5.4}$$

The magnetic Reynold number used in the current computational investigation has been considered quite low. As a result, in comparison to the applied external magnetic field strength, the induced magnetic field effect is omitted in the current investigation.

$$H_r = H_z = 0 \quad \text{and} \quad H_\theta = B.$$

The equation of conservation of electric charge is written as-

$$\nabla.\vec{J} = 0,$$

where $\vec{J}$, represents the electric current density and components of its are (J_r, J_θ, J_z) , in the r, θ, z directions, respectively. The tube is non-conducting, therefore $J_\theta = 0$ everywhere in the flow.
In this study the effect of polarization effect also neglected, therefore $\vec{E} = 0$, is taken zero into whole calculation.
Taking the Hall effect into the consideration, the generalized Ohm's law is written as [24]-

$$\vec{J} + \frac{\omega_e \tau_e}{B}(\vec{J} \times \vec{H}) = \sigma\left(\vec{E} + \vec{V} \times \vec{B} + \frac{1}{e\eta_e}\nabla p_e\right), \tag{5.5}$$

where $\vec{V}$, ω_e, e, η_e, τ_e, p_e represent the velocity, electron frequency, electron charge, electron density, electron collision time and electron pressure, respectively.

With the use all above assumptions, the components of electron current density are-

$$\begin{cases} J_r = \frac{\sigma B}{1+m_a^2}(m_a u - w), \\ J_\theta = 0, \\ J_z = \frac{\sigma B}{1+m_a^2}(u + m_a w). \end{cases} \tag{5.6}$$

5.2.3 Governing equations

The Power-law fluid has been considered in the core region and stress component for the this fluid is written as follows [25]-

$$(\tau_c)_{ij} = -P_c I + K\mu_c \Omega_f (\phi_c)_{ij}, \tag{5.7}$$

where

$$\Omega_c = \left[(\phi_c)_{rr}^2 + (\phi_c)_{\theta\theta}^2 + (\phi_c)_{zz}^2 + 2\left((\phi_c)_{r\theta}^2 + (\phi_c)_{\theta z}^2 + (\phi_c)_{zr}^2 \right) \right]^{\frac{q-1}{2}}.$$

Plasma region blood adopt the Newtonian fluid properties, therefore stress component in this region is written as-

$$(\tau_p)_{ij} = -P_p I + \mu_p (\phi_p)_{ij}, \tag{5.8}$$

where, τ_c and τ_p represents the stress tensor for both core and plasma region, while, ϕ_c and ϕ_p, depicts the strain tensor profile in core and plasma region, respectively. K and q, represent the flow consistency and flow behaviour index, respectively. μ_c & μ_p, state the viscosity in core and plasma region.

The governing equations for curved artery can be written as follows [134, 80, 25]-

$$\frac{b}{D}\frac{\partial w}{\partial z} + \frac{\partial u}{\partial r} + \frac{1}{r}\frac{\partial v}{\partial \theta} + \frac{u}{r} + \frac{u\cos\theta - v\sin\theta}{D} = 0, \tag{5.9}$$

where, h denotes the radius of curvature.

$$D = b + r\cos\theta.$$

Core region ($0 < r < R_1(z,t)$),

Momentum equations

r-direction:

$$\rho_c\left(\frac{\partial u_c}{\partial t}+\frac{bw_c}{D}\frac{\partial u_c}{\partial z}+u_c\frac{\partial u_c}{\partial r}+\frac{v_c}{r}\frac{\partial u_c}{\partial \theta}-\frac{v_c^2}{r}-\frac{w_c^2\cos\theta}{D}\right)=\frac{b}{rD}\left(\frac{\partial}{\partial z}\left(r(\tau_c)_{rz}\right)-\frac{\cos\theta(\tau_c)_{zz}}{D}\right.$$
$$\left.+\frac{\partial}{\partial r}\left(\frac{Dr(\tau_c)_{rr}}{b}\right)+\frac{\partial}{\partial\theta}\left(\frac{D(\tau_c)_{r\theta}}{b}\right)\right)-\frac{(\tau_c)_{\theta\theta}}{r}-\frac{\sigma B^2}{1+m_a^2}(m_a u_c-w_c), \tag{5.10}$$

θ direction :

$$\rho_c\left(\frac{\partial v_c}{\partial t}+\frac{w_c b}{D}\frac{\partial v_c}{\partial z}+u_c\frac{\partial v_c}{\partial r}+\frac{v_c}{r}\frac{\partial v_c}{\partial\theta}+\frac{u_c v_c}{r}+\frac{w_c^2\sin\theta}{D}\right)=\frac{b}{rD}\left(\frac{\partial}{\partial z}\left(r(\tau_c)_{\theta z}\right)+\frac{\sin\theta(\tau_c)_{zz}}{D}\right.$$
$$\left.+\frac{\partial}{\partial r}\left(\frac{Dr(\tau_c)_{r\theta}}{b}\right)+\frac{\partial}{\partial\theta}\left(\frac{D(\tau_c)_{\theta\theta}}{b}\right)\right)+\frac{(\tau_c)_{r\theta}}{r}, \tag{5.11}$$

z direction :

$$\rho_c\left(\frac{\partial w_c}{\partial t}+\frac{u_c w_c\cos\theta}{D}+\frac{w_c b}{D}\frac{\partial w_c}{\partial z}+u_c\frac{\partial w_c}{\partial r}-\frac{v_c w_c\sin\theta}{D}+\frac{v_c}{r}\frac{\partial w_c}{\partial\theta}\right)=\frac{b}{rD}\left(\frac{\partial}{\partial z}\left(r(\tau_c)_{zz}\right)\right.$$
$$\left.+\frac{\partial}{\partial r}\left(\frac{Dr(\tau_c)_{rz}}{b}\right)+\frac{\partial}{\partial\theta}\left(\frac{D(\tau_c)_{\theta z}}{b}\right)\right)+\frac{\cos\theta\ (\tau_c)_{rz}}{D}-\frac{\sin\theta(\tau_c)_{z\theta}}{D}-\frac{\sigma B^2(u_c+m_a w_c)}{1+m_a^2}$$
$$+g\rho_c\gamma_T(T_c-T_0), \tag{5.12}$$

Energy equation :

$$\rho_c\bar{C}_c\left(\frac{\partial T_c}{\partial t}+u_c\frac{\partial T_c}{\partial r}+\frac{v_c}{r}\frac{\partial T_c}{\partial\theta}+\frac{w_c b}{D}\frac{\partial T_c}{\partial z}\right)=K_c\left(\frac{\partial^2 T_c}{\partial r^2}+\frac{1}{r}\frac{\partial T_c}{\partial r}+\frac{b^2}{D^2}\frac{\partial^2 T_c}{\partial z^2}+\frac{\cos\theta}{D}\frac{\partial T_c}{\partial r}\right.$$
$$\left.-\frac{\sin\theta}{rD}\frac{\partial T_c}{\partial\theta}+\frac{1}{r^2}\frac{\partial^2 T_c}{\partial\theta^2}\right)+\frac{\partial q_c}{\partial r}-\frac{m_a}{1+m_a^2}\sigma B^2 w_c^2+F_c, \tag{5.13}$$

Here, F_c denotes the viscous dissipation and its mathematical expression for blood flow of core region is given in equation 5.14-

$$F_c=2^{\frac{q-1}{2}}\mu_c K\left[(\phi_c)_{rr}^2+(\phi_c)_{\theta\theta}^2+(\phi_c)_{zz}^2+2\left((\phi_c)_{r\theta}^2+(\phi_c)_{\theta z}^2+(\phi_c)_{zr}^2\right)\right]^q. \tag{5.14}$$

Where, u_c, v_c, w_c represents the dimensional form of velocity components for core region in r,θ,z directions, respectively. Here, T_c, q_c, m_a, B indicates the blood flow temperature, applied thermal radiation, Hall parameter and uniform magnetic field which applied perpendicular to z-direction in their dimensional form for the core region blood flow.

Plasma region i.e. $R_1(z,t)<r<R(z,t)$

Momentum equations-

r-direction:

$$\rho_p\left(\frac{\partial u_p}{\partial t}+\frac{bw_p}{D}\frac{\partial u_p}{\partial z}+u_p\frac{\partial u_p}{\partial r}+\frac{v_p}{r}\frac{\partial u_p}{\partial \theta}-\frac{v_p^2}{r}-\frac{w_p^2\cos\theta}{D}\right)=\frac{b}{rD}\left(\frac{\partial}{\partial z}\left(r(\tau_p)_{rz}\right)-\frac{\cos\theta(\tau_p)_{zz}}{D}\right.$$
$$\left.+\frac{\partial}{\partial r}\left(\frac{Dr(\tau_p)_{rr}}{b}\right)+\frac{\partial}{\partial \theta}\left(\frac{D(\tau_p)_{r\theta}}{b}\right)\right)-\frac{(\tau_p)_{\theta\theta}}{r}-\frac{\sigma B^2}{1+m_a^2}(m_a u_p-w_p), \tag{5.15}$$

θ direction :

$$\rho_p\left(\frac{\partial v_p}{\partial t}+\frac{w_p b}{D}\frac{\partial v_p}{\partial z}+u_p\frac{\partial v_p}{\partial r}+\frac{v_p}{r}\frac{\partial v_p}{\partial \theta}+\frac{u_p v_p}{r}+\frac{w_p^2\sin\theta}{D}\right)=\frac{b}{rD}\left(\frac{\partial}{\partial z}\left(r(\tau_p)_{\theta z}\right)+\frac{\sin\theta(\tau_p)_{zz}}{D}\right.$$
$$\left.+\frac{\partial}{\partial r}\left(\frac{Dr(\tau_p)_{r\theta}}{b}\right)+\frac{\partial}{\partial \theta}\left(\frac{D(\tau_p)_{\theta\theta}}{b}\right)\right)+\frac{(\tau_p)_{r\theta}}{r}, \tag{5.16}$$

z direction :

$$\rho_p\left(\frac{\partial w_p}{\partial t}+\frac{u_p w_p\cos\theta}{D}+\frac{w_p b}{D}\frac{\partial w_p}{\partial z}+u_p\frac{\partial w_p}{\partial r}-\frac{v_p w_p\sin\theta}{D}+\frac{v_p}{r}\frac{\partial w_p}{\partial \theta}\right)=\frac{b}{rD}\left(\frac{\partial}{\partial z}\left(r(\tau_p)_{zz}\right)\right.$$
$$\left.+\frac{\partial}{\partial r}\left(\frac{Dr(\tau_p)_{rz}}{b}\right)+\frac{\partial}{\partial \theta}\left(\frac{D(\tau_p)_{\theta z}}{b}\right)\right)+\frac{\cos\theta\ (\tau_p)_{rz}}{D}-\frac{\sin\theta(\tau_p)_{z\theta}}{D}-\frac{\sigma B^2(u_p+m_a w_p)}{1+m_a^2}$$
$$+g\rho_p\gamma_T(T_p-T_0), \tag{5.17}$$

Energy equation :

$$\rho_p\bar{C}_p\left(\frac{\partial T_p}{\partial t}+u_p\frac{\partial T_p}{\partial r}+\frac{v_p}{r}\frac{\partial T_p}{\partial \theta}+\frac{w_p b}{D}\frac{\partial T_p}{\partial z}\right)=K_p\left(\frac{\partial^2 T_p}{\partial r^2}+\frac{1}{r}\frac{\partial T_p}{\partial r}+\frac{b^2}{D^2}\frac{\partial^2 T_p}{\partial z^2}+\frac{\cos\theta}{D}\frac{\partial T_p}{\partial r}\right.$$
$$\left.-\frac{\sin\theta}{rD}\frac{\partial T_p}{\partial \theta}+\frac{1}{r^2}\frac{\partial^2 T_p}{\partial \theta^2}\right)+\frac{\partial q_p}{\partial r}-\frac{m_a}{1+m_a^2}\sigma B^2 w_p^2+F_p, \tag{5.18}$$

Here, F_p denotes the viscous dissipation and its mathematical expression for blood flow of plasma region is given in equation 5.19-

$$F_p=2\mu_p\left[(\phi_p)_{rr}^2+(\phi_p)_{\theta\theta}^2+(\phi_p)_{zz}^2+2\left((\phi_p)_{r\theta}^2+(\phi_p)_{\theta z}^2+(\phi_p)_{zr}^2\right)\right]. \tag{5.19}$$

Where, u_p, v_p, w_p represents the dimensional form of velocity components for plasma region in r, θ, z directions, respectively. T_p, q_p, B, m_a demonstrate the dimensional form of plasma region temperature and radiation, uniform magnetic field and Hall parameter, respectively. The above-mentioned dimensional form of governing and stenosis geometry equations will be transformed into the non-dimensional form using the following non-dimensional parameters mentioned in the table 5.1. The dimensionless form of stenosis is considered as [134].

Table 5.1: Dimensionless parameter

$r = R_0 r'$	$z = L_0 z'$	$\theta = \theta'$	$\omega = \frac{u_0}{L_0}\omega'$	$L = L_0 L'$
$d = L_0 d'$	$t = \frac{L_0}{u_0} t'$	$R = R_0 R'$	$R_1 = R_0 R_1'$	$u_c = \frac{\delta u_0}{L_0} u_c'$
$v_c = \frac{\delta u_0}{L_0} v_c'$	$\bar{w}_c = u_0 w_c'$	$u_p = \frac{\delta u_0}{L_0} u_p'$	$v_p = \frac{\delta u_0}{L_0} v_p'$	$w_p = u_0 w_p'$
$P_c = \frac{u_0 L_0 \mu_p}{R_0^2} P_c'$	$P_p = \frac{u_0 L_0 \mu_p}{R_0^2} P_p'$	$\alpha = \frac{R_0}{L_0}$	$T_c' = \frac{T_c - T_0}{T_w - T_0}$	$T_p' = \frac{T_p - T_0}{T_w - T_0}$
$\delta^* = \frac{\delta}{R_0}$	$N = \frac{4R_0^2 \alpha_p^2}{K_p}$	$\alpha_0 = \frac{\alpha_p^2}{\alpha_c^2}$	$M = \frac{\sigma B^2 R_0^2}{\mu_p}$	$\rho_0 = \frac{\rho_p}{\rho_c}$
$Re = \frac{\rho_p R_0 u_0}{\mu_p}$	$Gr = \frac{g \rho_p \gamma_T R_0^2 (T_w - T_0)}{u_0 \mu_p}$	$\varepsilon = \frac{R_0}{b}$	$K_0 = \frac{K_p}{K_c}$	$Ec = \frac{u_0^2}{\bar{C}_p (T_w - T_0)}$
$Pr = \frac{\bar{C}_p \mu_p}{K_p}$	$Br = EcPr$			

The table mentioned above 5.1 has been utilized to transform governing equations into dimensionless forms. Then after fully developed flow, mild stenosis ($\delta^* << 1$), low Reynold number ($Re <<< 1$), and $O(1) = \alpha = \frac{R_0}{L_0}$ conditions have been employed to simplify dimensionless governing equations. The simplified form of the governing equations are written as

Core region

$$\frac{\partial P_c'}{\partial r'} = 0, \tag{5.20}$$

$$\frac{\partial P_c'}{\partial \theta'} = 0, \tag{5.21}$$

$$\frac{1}{\bar{D}} \frac{\partial P_c'}{\partial z'} = \frac{\Omega_c^*}{\mu_0} \left(\frac{\partial^2 w_c'}{\partial r'^2} + \frac{1}{r'} \frac{\partial w_c'}{\partial r'} + \frac{1}{r'^2} \frac{\partial^2 w_c'}{\partial \theta'^2} - \frac{\varepsilon^2 w_c'}{\bar{D}^2} + \frac{\varepsilon}{\bar{D}} \left[\cos\theta' \frac{\partial w_c'}{\partial r'} - \frac{\sin\theta'}{r'} \frac{\partial w_c'}{\partial \theta'} \right] \right) + \frac{1}{\mu_0} \left(\frac{\partial w_c'}{\partial r'} - \frac{\varepsilon w_c' \cos\theta'}{\bar{D}} \right) \frac{\partial \Omega_c^*}{\partial r'} + \frac{1}{\mu_0} \left(\frac{1}{r'^2} \frac{\partial w_c'}{\partial \theta'} + \frac{\varepsilon w_c \sin\theta'}{r' \bar{D}} \right) \frac{\partial \Omega_c^*}{\partial \theta'} - \frac{M m_a w_c}{1 + m_a^2} + \frac{G r T_c'}{\rho_0}, \tag{5.22}$$

$$\frac{\partial^2 T_c'}{\partial r'^2} + \frac{1}{r'} \frac{\partial T_c'}{\partial r'} + \frac{\varepsilon \cos\theta'}{\bar{D}} \frac{\partial T_c'}{\partial r'} - \frac{\varepsilon \sin\theta'}{r' \bar{D}} \frac{\partial T_c'}{\partial \theta'} + \frac{1}{r'^2} \frac{\partial^2 T_c'}{\partial \theta'^2} - \frac{k_0}{\alpha_0} N T_c' + Br k_0 \left(\frac{m_a M w_c'^2}{1 + m_a^2} + F_c' \right) = 0, \tag{5.23}$$

where

$$\bar{D} = 1 + \varepsilon r' \cos\theta',$$

$$\Omega_c^* = 2^{\frac{q-1}{2}} \left[\left(- \frac{\varepsilon w_c' \cos\theta'}{\bar{D}} + \frac{\partial w_c'}{\partial r'} \right)^2 + \left(\frac{\varepsilon w_c' \sin\theta'}{\bar{D}} + \frac{1}{r'} \frac{\partial w_c'}{\partial \theta'} \right)^2 \right]^{\frac{q-1}{2}},$$

$$F_c' = 2^{q-1} \left[\left(- \frac{\varepsilon w_c' \cos\theta'}{\bar{D}} + \frac{\partial w_c'}{\partial r'} \right)^2 + \left(\frac{\varepsilon w_c' \sin\theta'}{\bar{D}} + \frac{1}{r'} \frac{\partial w_c'}{\partial \theta'} \right)^2 \right]^q,$$

Plasma region

$$\frac{\partial P'_p}{\partial r'} = 0, \tag{5.24}$$

$$\frac{\partial P'_p}{\partial \theta'} = 0, \tag{5.25}$$

$$\frac{1}{\bar{D}}\frac{\partial P'_p}{\partial z'} = \left(\frac{\partial^2 w'_p}{\partial r'^2} + \frac{1}{r'}\frac{\partial w'_p}{\partial r'} + \frac{1}{r'^2}\frac{\partial^2 w'_p}{\partial \theta'^2} - \frac{\varepsilon^2 w'_p}{\bar{D}^2} + \frac{\varepsilon}{\bar{D}}\left[\cos\theta'\frac{\partial w'_p}{\partial r'} - \frac{\sin\theta'}{r'}\frac{\partial w'_p}{\partial \theta'}\right]\right) - \frac{M m_a w'_p}{1+m_a^2} + GrT'_p, \tag{5.26}$$

$$\frac{\partial^2 T'_p}{\partial r'^2} + \frac{1}{r'}\frac{\partial T'_p}{\partial r'} + \frac{\varepsilon\cos\theta'}{\bar{D}}\frac{\partial T'_p}{\partial r'} - \frac{\varepsilon\sin\theta'}{r'\bar{D}}\frac{\partial T'_p}{\partial \theta'} + \frac{1}{r'^2}\frac{\partial^2 T'_p}{\partial \theta'^2} + \left(\frac{m_a w'^2_p M}{1+m_a^2} + F'_p\right)Br - NT'_p = 0, \tag{5.27}$$

where

$$F'_p = 2\left[\left(-\frac{\varepsilon w'_p\cos\theta'}{\bar{D}} + \frac{\partial w'_p}{\partial r'}\right)^2 + \left(\frac{\varepsilon w'_p\sin\theta'}{\bar{D}} + \frac{1}{r'}\frac{\partial w'_p}{\partial \theta'}\right)^2\right].$$

Mathematical formulation of dimensionless boundary condition is mentioned in equation 5.28

$$\begin{cases} \frac{\partial w'_c}{\partial r'} = 0, \quad \frac{\partial T'_c}{\partial r'} = 0, & \text{at} \quad r' = 0, \\ w'_c = w'_p, \quad T'_c = T'_p, & \text{at} \quad r' = R'_1(z',t'), \\ \tau'_c = \tau'_p, \quad \frac{\partial T'_c}{\partial r'} = \frac{\partial T'_p}{\partial r'}, & \text{at} \quad r' = R'_1(z',t'), \\ w'_p = 0, \quad T'_p = 1, & \text{at} \quad r' = R'(z',t'), \\ \frac{\partial w'_c}{\partial \theta'} = 0, \quad \frac{\partial T'_c}{\partial \theta'} = 0, & \text{at} \quad \theta' = 0 \quad \& \quad \theta' = \pi, \\ \frac{\partial w'_p}{\partial \theta'} = 0, \quad \frac{\partial T'_p}{\partial \theta'} = 0, & \text{at} \quad \theta' = 0 \quad \& \quad \theta' = \pi. \end{cases} \tag{5.28}$$

5.3 Procedure of solution

With the use of the aforementioned non-dimensional boundary conditions, a computational process to obtain a solution of highly nonlinear PDEs (5.20)-(5.27) (dimensionless governing equations) has been performed using the Finite difference method [130].

The central difference formula of the second order has been employed to discretize the spatial derivatives in the uniform mesh size for the domain $[0 \;\; R'(z',t')] \times [o \;\; \pi]$. Discritization

of derivatives can be performed using given process in equation 5.29.-

$$\begin{cases} \frac{\partial G_s}{\partial r'} = \frac{(G_s)_{x+1,y}-(G_s)_{x-1,y}}{2\Delta r}, \\ \\ \frac{\partial G_s}{\partial \theta'} = \frac{(G_s)_{x,y+1}-(G_s)_{x,y-1}}{2\Delta \theta}, \\ \\ \frac{\partial^2 G_s}{\partial r'^2} = \frac{(G_s)_{x+1,y}-2(G_s)_{x,y}+(G_s)_{x-1,y}}{(\Delta r)^2}, \\ \\ \frac{\partial^2 G_s}{\partial \theta^2} = \frac{(G_s)_{x,y+1}-2(G_s)_{x,y}+(G_s)_{x,y-1}}{(\Delta \theta)^2}, \end{cases} \tag{5.29}$$

when blood flows in core region , then s will be consider for core region and if blood flows in plasma region , then s will be consider for plasma region.

In the present mathematical study Δr and $\Delta\theta$ represents the uniform mesh size in r' and θ' direction, respectively. The mathematical expression for Δr and $\Delta\theta$ are as follows- $\Delta r = \frac{R'(z',t')}{L_1-1}$ and $\Delta\theta = \frac{\pi}{L_2-1}$, where L_1 and L_2 denotes the total number of mesh points in r' & θ' directions. The step size in both directions is assumed $\Delta r = \Delta\theta = 0.001$. The error tolerance for both inner and outer iterations is setup 10^{-6}.

The discretization of these governing equations will be-

$$\begin{aligned} &\frac{1}{\bar{D}_{x,y}}\left(\frac{\partial P'_c}{\partial z'}\right)_{x,y} = \frac{(\Omega^*_c)_{x,y}}{\mu_0}\left(\frac{(w'_c)_{x+1,y}-2(w'_c)_{x,y}+(w'_c)_{x-1,y}}{(\Delta r)^2}+\frac{1}{r'_x}\frac{(w'_c)_{x+1,y}-(w'_c)_{x-1,y}}{2\Delta r}\right. \\ &+\frac{1}{r'^2_x}\frac{(w'_c)_{x,y+1}-2(w'_c)_{x,y}+(w'_c)_{x,y-1}}{(\Delta\theta)^2}-\frac{\varepsilon^2(w'_c)_{x,y}}{\bar{D}^2_{x,y}}+\frac{\varepsilon}{\bar{D}_{x,y}}\left[\cos\theta'_y\frac{(w'_c)_{x+1,y}-(w'_c)_{x-1,y}}{2\Delta r}\right. \\ &\left.\left.-\frac{\sin\theta'_y}{r'_x}\frac{(w'_c)_{x,y+1}-(w'_c)_{x,y-1}}{2\Delta\theta}\right]\right)+\frac{1}{\mu_0}\left(\frac{(w'_c)_{x+1,y}-(w'_c)_{x-1,y}}{2\Delta r}-\frac{\varepsilon(w'_c)_{x,y}\cos\theta'_y}{\bar{D}_{x,y}}\right) \\ &\frac{(\Omega^*_c)_{x+1,y}-(\Omega^*_c)_{x-1,y}}{2\Delta r}+\frac{1}{\mu_0}\left(\frac{1}{r'^2_x}\frac{(w'_c)_{x,y+1}-(w'_c)_{x,y-1}}{2\Delta\theta}+\frac{\varepsilon(w'_c)_{x,y}\sin\theta'_y}{r'_x\bar{D}_{x,y}}\right) \\ &\frac{(\Omega^*_c)_{x,y+1}-(\Omega^*_c)_{x,y-1}}{2\Delta\theta}-\frac{Mm(\tilde{W}_c)_{x,y}}{1+m^2}+\frac{Gr(T'_c)_{x,y}}{\rho_0}, \end{aligned} \tag{5.30}$$

$$\begin{aligned} &\frac{(T'_c)_{x+1,y}-2(T'_c)_{x,y}+(T'_c)_{x-1,y}}{(\Delta r)^2}+\frac{1}{r'_x}\frac{(T'_c)_{x+1,y}-(T'_c)_{x-1,y}}{2\Delta r}+\frac{\varepsilon\cos\theta'_y}{\bar{D}_{x,y}}\frac{(T'_c)_{x+1,y}-(T'_c)_{x-1,y}}{2\Delta r} \\ &-\frac{\varepsilon\sin\theta'_y}{\tilde{r}_x\bar{D}_{x,y}}\frac{(T'_c)_{x,y+1}-(T'_c)_{x,y-1}}{2\Delta\theta}+\frac{1}{r'^2_x}\frac{(T'_c)_{x,y+1}-2(T'_c)_{x,y}+(T'_c)_{x,y-1}}{(\Delta\theta)^2}-\frac{k_0}{\alpha_0}N(T'_c)_{x,y} \\ &=-\frac{m_a}{1+m_a^2}M\,Br\,k_0\,(w'^2_c)_{x,y}-Br\,k_0\,(F'_c)_{x,y}, \end{aligned} \tag{5.31}$$

$$\frac{1}{\bar{D}_{x,y}}\left(\frac{\partial P'_p}{\partial z'}\right)_{x,y} = \left(\frac{(w'_p)_{x+1,y}-2(w'_p)_{x,y}+(w'_p)_{x-1,y}}{(\Delta r)^2}+\frac{1}{r'_x}\frac{(w'_p)_{x+1,y}-(w'_p)_{x-1,y}}{2\Delta r}\right.$$
$$+\frac{1}{r'^2_x}\frac{(w'_p)_{x,y+1}-2(w'_p)_{x,y}+(w'_p)_{x,y-1}}{(\Delta\theta)^2}-\frac{\varepsilon^2(w'_p)_{x,y}}{\bar{D}^2_{x,y}}+\frac{\varepsilon}{\bar{D}_{x,y}}\left[\cos\theta'_y\frac{(w'_p)_{x+1,y}-(w'_c)_{x-1,y}}{2\Delta r}\right.$$
$$\left.\left.-\frac{\sin\theta'_y}{r'_x}\frac{(w'_p)_{x,y+1}-(w'_p)_{x,y-1}}{2\Delta\theta}\right]\right)-\frac{Mm_a(w'_p)_{x,y}}{1+m_a^2}+Gr(T'_p)_{x,y}, \tag{5.32}$$

$$\frac{(T'_p)_{x+1,y}-2(T'_p)_{x,y}+(T'_p)_{x-1,y}}{(\Delta r)^2}+\frac{1}{r'_x}\frac{(T'_p)_{x+1,y}-(T'_p)_{x-1,y}}{2\Delta r}+\frac{\varepsilon\cos\theta'_y}{\bar{D}_{x,y}}\frac{(T'_p)_{x+1,y}-(T'_p)_{x-1,y}}{2\Delta r}$$
$$-\frac{\varepsilon\sin\theta'_y}{r'_x\bar{D}_{x,y}}\frac{(T'_p)_{x,y+1}-(T'_p)_{x,y-1}}{2\Delta\theta}+\frac{1}{r'^2_x}\frac{(T'_p)_{x,y+1}-2(T'_p)_{x,y}+(T'_p)_{x,y-1}}{(\Delta\theta)^2}-N(T'_p)_{x,y}$$
$$=-\frac{m_a}{1+m_a^2}M\,Br\,(w'^2_p)_{x,y}-Br\,(F'_p)_{x,y}, \tag{5.33}$$

where $\bar{D}_{x,y}=1+\varepsilon r'_x\cos\theta'_y$,

$$(\Omega^*_c)_{x,y}=2^{\frac{q-1}{2}}\left[\left(-\frac{\varepsilon(w'_c)_{x,y}\cos\theta'_y}{\bar{D}_{x,y}}+\frac{(w'_c)_{x+1,y}-(w'_c)_{x-1,y}}{2\Delta r}\right)^2+\left(\frac{\varepsilon(w'_c)_{x,y}\sin\theta'_y}{\bar{D}_{x,y}}\right.\right.$$
$$\left.\left.+\frac{1}{r'_x}\frac{(w'_c)_{x,y+1}-(w'_c)_{x,y-1}}{2\Delta\theta}\right)^2\right]^{\frac{q-1}{2}},$$
$$(F'_c)_{x,y}=2^{q-1}\left[\left(-\frac{\varepsilon(w'_c)_{x,y}\cos\theta'_y}{\bar{D}_{x,y}}+\frac{(w'_c)_{x+1,y}-(w'_c)_{x-1,y}}{2\Delta r}\right)^2+\left(\frac{\varepsilon(w'_c)_{x,y}\sin\theta'_y}{\bar{D}_{x,y}}\right.\right.$$
$$\left.\left.+\frac{1}{r'_x}\frac{(w'_c)_{x,y+1}-(w'_c)_{x,y-1}}{2\Delta\theta}\right)^2\right]^q,$$
$$(F'_p)_{x,y}=2\left[\left(-\frac{\varepsilon(w'_p)_{x,y}\cos\theta'_y}{\bar{D}_{x,y}}+\frac{(w'_p)_{x+1,y}-(w'_p)_{x-1,y}}{2\Delta r}\right)^2+\left(\frac{\varepsilon(w'_p)_{x,y}\sin\theta'_y}{\bar{D}_{x,y}}\right.\right.$$
$$\left.\left.+\frac{1}{r'_x}\frac{(w'_p)_{x,y+1}-(w'_p)_{x,y-1}}{2\Delta\theta}\right)^2\right].$$

According to published research work [135, 136] on blood flow, pressure gradient may be taken constant in mathematical formulation, hence it is also assumed constant in this investigation.

$$\frac{\partial P'_c}{\partial z'}=\frac{\partial P'_p}{\partial z'}=P_0. \tag{5.34}$$

Since, from the above-published literature, the pressure gradient is constant. Therefore these non-dimensional governing equations can be reduced into 2D nonlinear PDEs. With the discretization of these PDEs, a five-band system of nonlinear algebraic equations have been obtained.

$$AX = bb,$$

where A is coefficient matrix.

The system is highly nonlinear; therefore, solving it using the Gaussian elimination method is not feasible.

Stone's strongly implicit method [131] has been employed to solve the system of nonlinear equations. A global nodal index k has been assigned for every mesh point.

$$k = (y-1) * L_1 + x.$$

Further, we will re-frame the discretized non-dimensional governing equations by assigning a unique nodel index $k = (y-1) * L_1 + x$.

$$\frac{1}{\bar{D}_k}\left(\frac{\partial P_c'}{\partial z'}\right)_k = \frac{(\Omega_c^*)_k}{\mu_0}\left(\frac{(w_c')_{k+1} - 2(w_c')_k + (w_c')_{k-1}}{(\Delta r)^2} + \frac{1}{r_k'}\frac{(w_c')_{k+1} - (w_c')_{k-1}}{2\Delta r}\right.$$
$$+ \frac{1}{r_k'^2}\frac{(w_c')_{k+L_1} - 2(w_c')_k + (w_c')_{k-L_1}}{(\Delta\theta)^2} - \frac{\varepsilon^2 (w_c')_k}{\bar{D}_k^2} + \frac{\varepsilon}{\bar{D}_k}\left[\cos\theta_k' \frac{(w_c')_{k+1} - (w_c')_{k-1}}{2\Delta r}\right.$$
$$\left.\left. - \frac{\sin\theta_k'}{r_k'}\frac{(w_c')_{k+L_1} - (w_c')_{k-L_1}}{2\Delta\theta}\right]\right) + \frac{1}{\mu_0}\left(\frac{(w_c')_{k+1} - (w_c')_{k-1}}{2\Delta r} - \frac{\varepsilon (w_c')_k \cos\theta_k'}{\bar{D}_k}\right)$$
$$\frac{(\Omega_c^*)_{k+1} - (\Omega_c^*)_{k-1}}{2\Delta r} + \frac{1}{\mu_0}\left(\frac{1}{r_k'^2}\frac{(w_c')_{k+L_1} - (w_c')_{k-L_1}}{2\Delta\theta} + \frac{\varepsilon (w_c')_k \sin\theta_k'}{r_k' \bar{D}_k}\right)\frac{(\Omega_c^*)_{k+L_1} - (\Omega_c^*)_{k-L_1}}{2\Delta\theta}$$
$$- \frac{Mm_a (w_c')_k}{1+m_a^2} + \frac{Gr (T_c')_k}{\rho_0}, \tag{5.35}$$

$$\frac{(T_c')_{k+1} - 2(T_c')_k + (T_c')_{k-1}}{(\Delta r)^2} + \frac{1}{r_k'}\frac{(T_c')_{k+1} - (T_c')_{k-1}}{2\Delta r} + \frac{\varepsilon\cos\theta_k'}{\bar{D}_k}\frac{(T_c')_{k+1} - (T_c')_{k-1}}{2\Delta r} - \frac{\varepsilon\sin\theta_k'}{r_k'\bar{D}_k}$$
$$\frac{(T_c')_{k+L_1} - (T_c')_{k-L_1}}{2\Delta\theta} + \frac{1}{r_k'^2}\frac{(T_c')_{k+L_1} - 2(T_c')_k + (T_c')_{k-L_1}}{(\Delta\theta)^2} - \frac{k_0}{\alpha_0} N(T_c')_k = -\frac{m_a}{1+m_a^2} M\, Br\, k_0\, (w_c'^2)_k$$
$$- Br\, k_0\, (F_c')_k, \tag{5.36}$$

$$\frac{1}{\bar{D}_k}\left(\frac{\partial P'_p}{\partial z'}\right)_k = \left(\frac{(w'_p)_{k+1}-2(w'_p)_k+(w'_p)_{k-1}}{(\Delta r)^2}+\frac{1}{r'_k}\frac{(w'_p)_{k+1}-(w'_p)_{k-1}}{2\Delta r}\right.$$
$$+\frac{1}{r'^2_k}\frac{(w'_p)_{k+L_1}-2(w'_p)_k+(w'_p)_{k-L_1}}{(\Delta\theta)^2}-\frac{\varepsilon^2(w'_p)_k}{\bar{D}_k^2}+\frac{\varepsilon}{\bar{D}_k}\left[\cos\theta'_k\frac{(w'_p)_{k+1}-(w'_c)_{k-1}}{2\Delta r}\right.$$
$$\left.\left.-\frac{\sin\theta'_k}{r'_k}\frac{(w'_p)_{k+L_1}-(w'_p)_{k-L_1}}{2\Delta\theta}\right]\right)-\frac{Mm_a(w'_p)_k}{1+m_a^2}+Gr(T'_p)_k, \tag{5.37}$$

$$\frac{(T'_p)_{k+1}-2(T'_p)_k+(T'_p)_{k-1}}{(\Delta r)^2}+\frac{1}{r'_k}\frac{(T'_p)_{k+1}-(T'_p)_{k-1}}{2\Delta r}+\frac{\varepsilon\cos\theta'_k}{\bar{D}_k}\frac{(T'_p)_{k+1}-(T'_p)_{k-1}}{2\Delta r}-\frac{\varepsilon\sin\theta'_k}{r'_k\bar{D}_k}$$
$$\frac{(T'_p)_{k+L_1}-(T'_p)_{k-L_1}}{2\Delta\theta}+\frac{1}{r'^2_k}\frac{(T'_p)_{k+L_1}-2(T'_p)_k+(T'_p)_{k-L_1}}{(\Delta\theta)^2}-N(T'_p)_k=-\frac{m_a}{1+m_a^2}M\,Br\,(w'^2_p)_k$$
$$-Br\,(F'_p)_k, \tag{5.38}$$

After allocating the global nodal index, the coefficient matrix [A] will be factorized into lower and upper triangular matrices. After factorized matrix [A], the residual will be computed. Further, backward and forward substitution will be employed to find a solution. This iterative process is repeated until the residual becomes lesser than the desirable error tolerance. Stone's method is used for inner iteration, then Newton's scheme is applied for outer iteration. For each inner and outer iteration, the absolute error tolerance of 10^{-6} is taken into account.

$$[A]X=[L][U]X=bb.$$

After numerically computed the velocity and temperature in core and plasma regions some important physical phenomena such as wall shear stress, Nusselt number, flow rate profiles can be calculated using numerical velocity and temperature profile data.

The Flow rate Q, frictional impedance λ and wall shear stress τ_w can be calculated as follows-

$$Q=\int_0^{R'(z',t')}\int_0^{\pi} r'w'dr'd\theta',$$

$$Q=\int_0^{R'_1(z',t')}\int_0^{\pi} r'w'_c(r',\theta',z')dr'd\theta'+\int_{R'_1(z',t')}^{R'(z',t')}\int_0^{\pi} r'w'_p(r',\theta',z')dr'd\theta', \tag{5.39}$$

$$\lambda=\frac{\int_0^L(-\frac{\partial P'}{\partial z'})dz'}{Q}, \tag{5.40}$$

$$\tau_w=-\left[\frac{\partial w'_p}{\partial r'}\right]_{r'=R'(z',t')}, \tag{5.41}$$

The Mathematical calculation of Nusselt number can performed as -

$$Nu = -\left[\frac{\partial T_p'}{\partial r'}\right]_{r'=R'(z',t')}. \tag{5.42}$$

5.4 Entropy Generation and irreversibility

Entropy generation is critical for understanding biological thermodynamics in blood flow through constricted regions. By considering above mentioned conditions, the general form of entropy generation can be written as follows-

$$E^{gen} = \underbrace{\frac{k(\nabla T)^2}{T_w^2}}_{\text{Thermal irreversibility}} + \underbrace{\frac{\mu}{T_w}F}_{\text{Fluid friction irrversibility}} + \underbrace{\frac{m_a}{1+m_a^2}\frac{\sigma B^2}{T_w}u^2}_{\text{Joule heating irrversibility}}, \tag{5.43}$$

The following are the mathematical formulae to estimate the amount of entropy generation in both regions:

$$E_c^{gen} = \underbrace{\frac{K_c}{T_w^2}\left[\left(\frac{\partial T_c}{\partial r}\right)^2 + \left(\frac{1}{r}\frac{\partial T_c}{\partial \theta}\right)^2 + \left(\frac{b}{D}\frac{\partial T_c}{\partial z}\right)^2\right]}_{\text{Thermal irreversibility}} + \underbrace{\frac{F_c}{T_w}}_{\text{Fluid friction irrversibility}} + \underbrace{\frac{m_a}{1+m_a^2}\frac{\sigma B^2}{T_w}w_c^2}_{\text{Joule heating irrversibility}}, \tag{5.44}$$

$$E_p^{gen} = \underbrace{\frac{K_p}{T_w^2}\left[\left(\frac{\partial T_p}{\partial r}\right)^2 + \left(\frac{1}{r}\frac{\partial T_p}{\partial \theta}\right)^2 + \left(\frac{b}{D}\frac{\partial T_p}{\partial z}\right)^2\right]}_{\text{Thermal irreversibility}} + \underbrace{\frac{F_p}{T_p}}_{\text{Fluid friction irrversibility}} + \underbrace{\frac{m_a}{1+m_a^2}\frac{\sigma B^2}{T_w}w_p^2}_{\text{Joule heating irrversibility}}, \tag{5.45}$$

where E_c^{gen} and E_p^{gen} denotes the entropy generation in core and plasma region, respectively. The equations 5.44 & 5.45, will be converted in their dimensionless form by using table 5.1 and considering above mentioned flow conditions-

$$E_c'^{gen} = \frac{E_c^{gen}}{E},$$

$$E_p'^{gen} = \frac{E_p^{gen}}{E},$$

$$E_c'^{gen} = \frac{1}{k_0}\left[\left(\frac{\partial T_c'}{\partial r'}\right)^2 + \left(\frac{1}{r'}\frac{\partial T_c'}{\partial \theta'}\right)^2\right] + \frac{Br}{A}F_c' + \frac{m_a}{1+m_a^2}\frac{BrMw_c'^2}{A}, \tag{5.46}$$

$$E_p'^{gen} = \left[\left(\frac{\partial T_p'}{\partial r}\right)^2 + \left(\frac{1}{r}\frac{\partial T_p'}{\partial \theta'}\right)^2\right] + \frac{Br}{A}F_p' + \frac{m_a}{1+m_a^2}\frac{BrMw_p'^2}{A}, \tag{5.47}$$

where $E = \frac{K_p(T_w-T_0)^2}{T_w^2 R_0^2}$, $A = \frac{T_w-T_0}{T_0}$.

5.5 Grid Independence test

For numerical simulation, the truncation error can be disregarded if the results of the calculations are stable regardless of the grid density or sparsity. As a result, the truncation error and even the reasonableness of numerical outputs are directly affected by whether or not the grid is independent. The outcomes of an unstable numerical simulation can be drastically altered by changing the grid resolution. Although in theory a dense grid could prevent this issue when dealing with a grid-independent problem, doing so could result in unnecessary use of computational resources. Thus, it is necessary to find the optimal grid size.

The optimal grid system for the current investigation is determined by running a "grid-independence test ", which provides a means of choosing a mesh density that is both computationally accurate and economically viable. The optimal grid size, (800×800), is listed in table (5.2); further refining the mesh size does not improve the accuracy. In order to solve the governing equations, we have adopt the central finite difference method to discretized the governing equations. The resultant governing system is second order convergent in space.

Table 5.2: Grid Independence Test

Grid	Nusselt number	Wall shear stress
100×100	0.948	1.120
200×200	0.914	1.0821
400×400	0.9058	1.0728
800×800	0.9035	1.0702
1000×1000	0.9031	1.070

5.6 Results and Discussion

A computational investigation has been introduced to visualize the impact of several parameters, including power-law fluid, Magnetic field, Hall parameter, radiation parameter etc., on the two-phase blood flow behaviour and its temperature profile in a curved artery. The calculation of entropy generation in diseases section of artery has been performed by considering

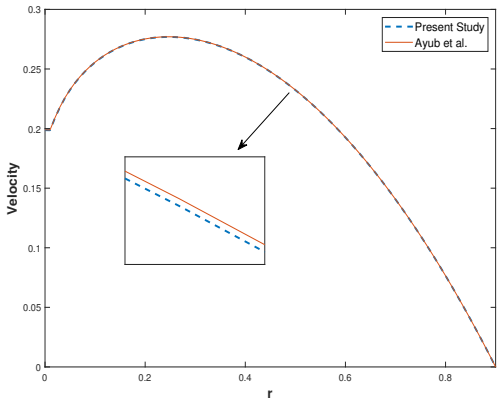

Figure 5.2: Validation of present investigation

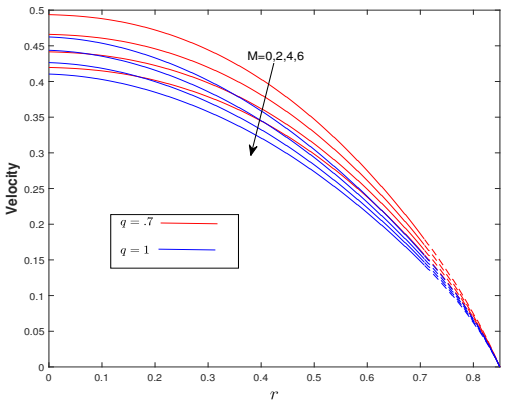

Figure 5.3: Velocity profile for M and q

the two-phase fluid approach. Present investigation considered the blood as non-Newtonian fluid (Power-law fluid) in the core region while showing the Newtonian fluid nature with constant viscosity in the plasma region. The plasma region is considered the $15-20\%$ of the whole artery region. A central difference scheme of second-order has been applied for the discretization of spatial derivatives, and Stone's strongly implicit method is used for solving a system of non-linear equations. The flow domain is discretized uniformly for both $(\tilde{r})$ & $(\tilde{\theta})$ directions. The step size in both directions is assumed $\Delta r = \Delta\theta = 0.001$. The error tolerance for both inner and outer iterations is setup 10^{-6}. The MATLAB codes for Stones scheme have been developed to demonstrate the graphical behaviour of various physical quantities such as velocity, temperature, WSS, frictional impedance, heat transfer rate and entropy generation etc. The table 1 provides the default values for different physical parameters and their source of references.

In this validation process, some assumptions in the present study have been neglected, such as magnetic field, Hall effect, blood is considered to single-phase fluid, and the consideration of nanofluid and catheter is ignored in the [80] observation. This validation process has been performed by considering the perturbation technique for [80] work and Stone's method for the present work. Figure 5.2 replicate the fair agreement between the present study and [80] observations.

The Blood behave a like biomagnetic fluid due to the existence of cell membrane, a complex interaction of proteins and haemoglobin in it. The main protein present in RBCs is haemoglobin, which contains iron oxide particles and it has the ability to bind oxygen atoms. The molecular structure system of haemoglobin is significantly influenced by the amount of iron oxide available in RBC. Therefore, being motivated by the blood's magnetic properties, a comparative computational study has been performed to illustrate the significance of magnetic field on stenosed curved artery. The variation in two-phase blood flow velocity

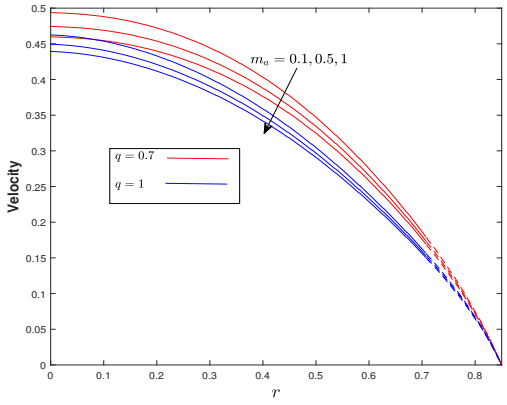

Figure 5.4: Variation in velocity for Hall parameter (m_a)

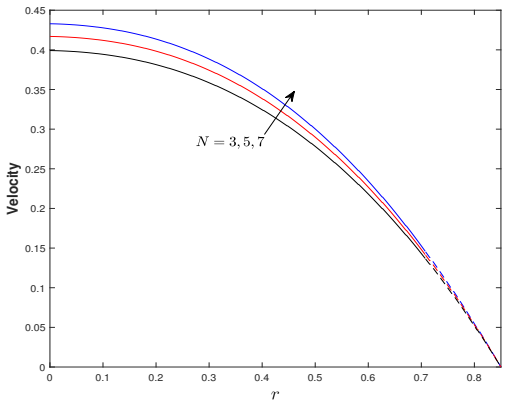

Figure 5.5: Velocity profile for thermal radiation

has been depicted in the figure 5.3. This study demonstrates that a strong electromotive field arises from applying an external magnetic field, perpendicular to the direction of blood flow. As a result, a force known as Lorentz force appears in the flow and lowers the flow speed. It can also be noticed that in the absence of a magnetic field, blood flow velocity remains higher. Clinical researchers can use these results during magnetic therapies and surgeries to reduce blood loss and also controlled magnetic field may be useful in treatment process of atherosclerosis, killing cancer cells and fractures etc. Figure 5.4 illustrates the fluctuation in flow velocity for the various values of the Hall parameter (m_a). The figure demonstrates that as the intensity of the Hall parameter increases, the velocity profile rises. Additionally, it has been found that when the strength of the hall parameter increases, the difference between velocity profiles for various values of m tends to decrease. A comparison between treating the blood in the core region as Newtonian and pseudoplastic (Power-law fluid) has also been performed using the aforementioned two figures. According to this study, the pseudoplastic fluid has a higher flow velocity ($q < 1$) than the Newtonian fluid ($q = 1$).

The influence of radiation parameter on the two-phase blood flow velocity has been formulated numerically and discussed with the help of figure 5.5. In this discussion, the nature of core region blood flow is considered pseudoplastic. The results of this research indicate that an increase in the intensity of thermal radiation that is applied to the arterial wall results in a greater production of heating energy in the blood flow, which in turn causes an increase in the temperature of the blood flow. As a result of this increase in the flow temperature, the blood flow becomes less viscous and flows with a greater degree of ease. Because of this, there is a discernible increase in blood flow velocity in response to an increase in the intensity of thermal radiation. Biologists and clinical researchers can adopt present study results of thermal radiation in the therapeutic process like killing cancer and damaged cells,

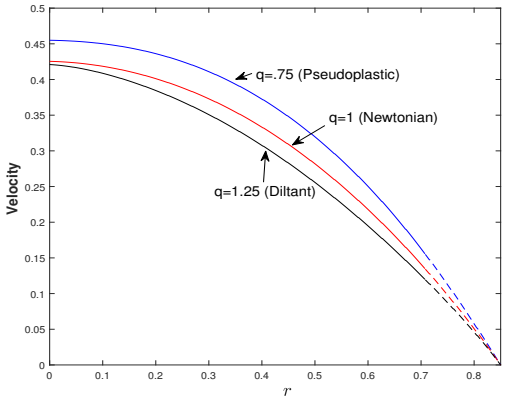

Figure 5.6: Velocity profile with q

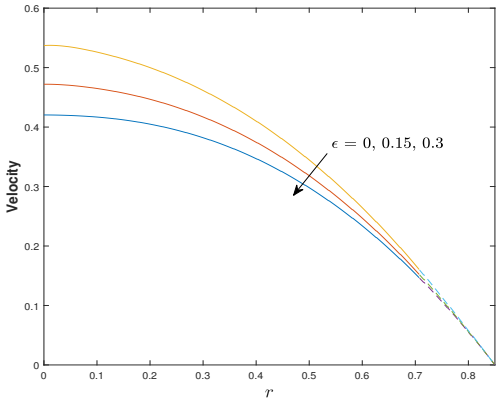

Figure 5.7: Velocity profile with ε

tumors, atherosclerosis, muscle pain etc. Sometimes, during thermal treatment of various diseases, blood flow velocity rises rapidly, which might be harmful; therefore, performing these therapies under the tool using the magnetic field concept will be helpful [137] to control flow velocity.

A comparative study for blood has been performed by assuming core region blood as Newtonian and non-Newtonian. This study is conducted in the form of a flow behaviour index (q) and depicted in figure 5.6. Here $q < 1$ represents the behaviour of blood as Pseudoplastic (shear-thinning), $q = 1$ Newtonian and $q > 1$ exhibits the Diltant (shear-thickening) behaviour. The figure reveals that, as the value of the flow behaviour increases, the blood flow velocity decreases in the whole artery. Therefore, for a realistic situation assuming blood as pseudoplastic nature will be good for the mathematical model to get an accurate result to predict disease conditions. According to the published literature [26] and from the obtained fruitful results for flow velocity, the authors decided to consider the Pseudoplastic ($q < 1$) behaviour of blood whenever blood is assumed non-Newtonian in this computational research work. The blood flow velocity for various values of arterial curvature has been computed numerically, and findings are shown in figure 5.7 to make the current study more realistic from the perspective of the human body. This study suggested that blood flow velocity decreases significantly with the value of arterial curvature (ε). Therefore, it can be concluded that lipid deposition chances are higher in the arteries which have high curvature due to slow fluid motion. The obtained results for the arterial curvature are in good agreement with the published work of [16].

A motivation to investigate the thermal radiation significance is taken from the above-mentioned thermal radiation applications in thermal therapies to cure serious diseases such as synovial bursa, muscle pain, cancer tumor and bones hilling, etc. Therefore, the change

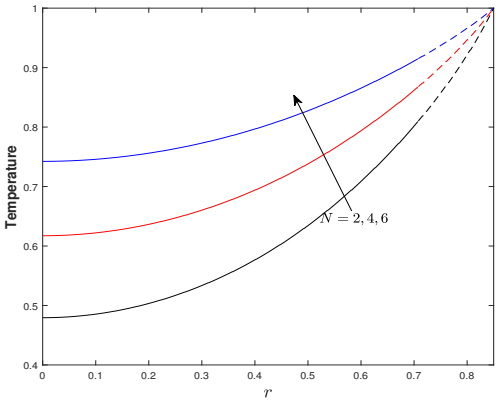

Figure 5.8: Temperature profile with N

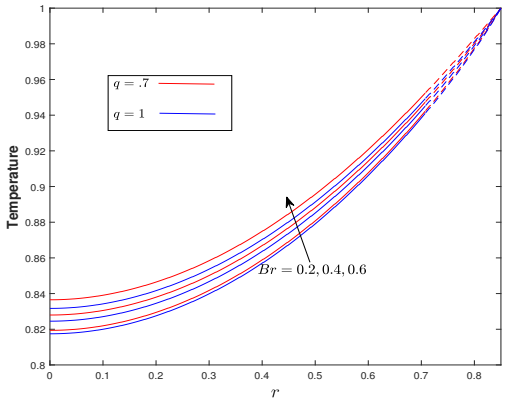

Figure 5.9: Temperature profile for Br and q

in blood temperature for the different thermal radiation intensities has been calculated numerically and discussed in the figure 5.8. This study reveals that, with the increase in value of the radiation parameter (N), the blood heated up, resultant blood temperature rises in the whole artery. Due to a significant boost in blood temperature with implication of radiation on the body, it can be used during surgery to kill cancer cells and atherosclerosis with minimum damage to organs and tissues.

The investigation of the Brinkman number (Br) is a fascinating topic because it differentiates the dominance of viscous heat generation and heat conduction due to external heating. Brinkman number is the ratio of heat generation by viscous heating and external heating .Therefore, figure 5.9 has been developed to analyze the impact of the Brinkman number on the blood flow through a stenosed curved artery. This study suggested that, for a fixed external surrounding heating source and applied thermal radiation, the heat conduction rate, which is generated by viscous dissipation between blood cells, decreases with the increase in value of the Brinkman number. This decrease in the rate of heat conduction reflects the significant effect of an increase in blood flow velocity for both the core and plasma regions. Therefore, a noticeable rise in blood flow temperature arises with the increase in value of Br. It can also be observed from the above figure that blood temperature is higher when blood is assumed pseudoplastic than Newtonian. This is just another argument in favour of using blood as a pseudoplastic fluid in mathematical modeling to achieve precise results.

Figures 5.10, is developed to illustrate the contributions of Hall parameter (m_a) on the wall shear stress profile for the curved artery throughout the entire stenotic region. In this study, the stenotic region has been considered to span $\tilde{z} = .75$ to $\tilde{z} = 1.75$. The study of the Hall parameter suggested that a significant decay in wall shear stress profile happens with the enhancement in Hall parameter value. Additionally, for a more accurate estimate of the wall shear stress profile, Figure 5.10, compares the Hall parameter's presence conditions

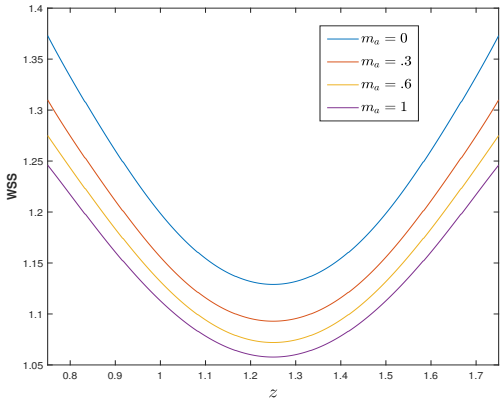

Figure 5.10: WSS profile for Hall parameter m_a

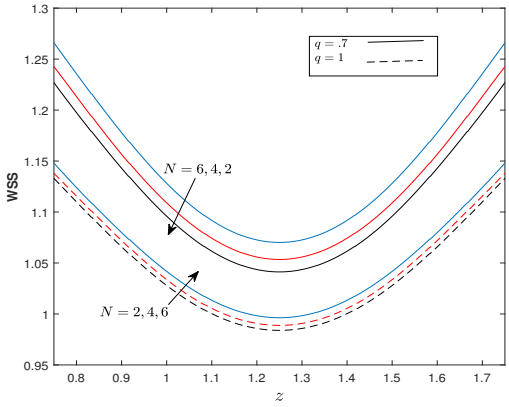

Figure 5.11: WSS profile for q and N

(presence $m_a \neq 0$ and absence $m_a = 0$). The WSS is higher in the absence of Hall parameter (also without magnetic field, $m_a = 0$) in comparison with the applied Hall parameter in the flow. Also, a drop in variation of WSS profile has been observed with a positive increase in the value of m_a.

The variation in the WSS profile for the different intensities of thermal radiation and flow index behaviour has been calculated numerically using Stone's scheme and discussed through the figure 5.11. The figure indicates that for all numeric values of radiation intensities (N) and flow nature index (q), firstly WSS profile diminishes in the stenotic region from $\tilde{z} = .75$ to $\tilde{z} = 1.25$; after that, WSS profile improves in the remaining diseased area. This study state that, with the positive enhancement in thermal radiation intensity, the blood flow velocity increases, which leads to an increment in the WSS profile in the entire stenotic region. A comparison has also been made between assuming core region blood as pseudoplastic fluid ($q < 1$) and Newtonian fluid ($q = 1$). The comparison concluded that WSS is higher when blood is assumed pseudoplastic fluid in mathematical modeling than Newtonian fluid. The results of the current computational work agree with [93], which claims that vascular segments and arteries with lower WSS are more likely to have lipid accumulation and stenosis. The biologist and researchers can adopt the finding relation of the present study between WSS and thermal radiation to reduce the risk of stenosis formation by implication of radiation in the blood flow.

The fluctuation in the WSS profile for various power of magnetic field (M) along with the curved arterial stenotic height ($\tilde{\delta}$) has been discussed in the figure 5.12. A linearly decay in WSS profile has been observed with the increase in stenosis height, which reveals fair agreement with the results of [132, 16]. This investigation has also undertaken a comparison between curved artery ($\varepsilon \neq 0$) and straight ($\varepsilon = 0$) conditions. It is concluded that with the increase in the value of arterial curvature, the blood experiences lower shear stress

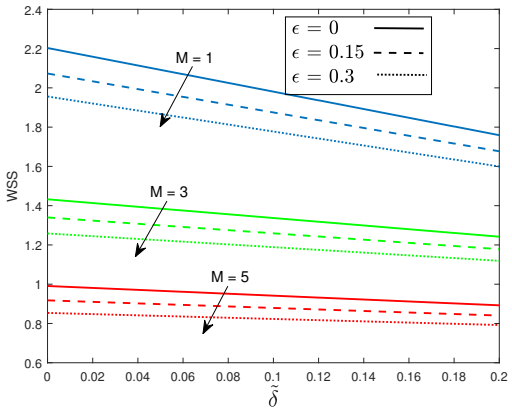

Figure 5.12: WSS profile for M and ε

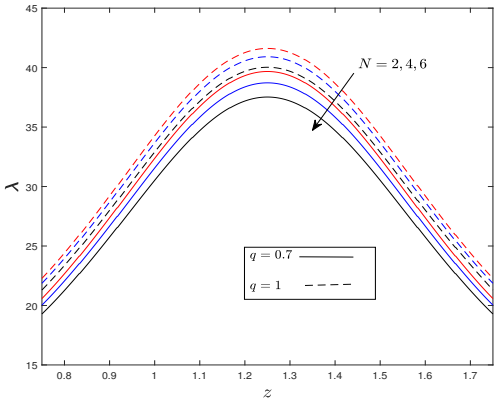

Figure 5.13: Frictional Impedance for q and N

at the wall. Therefore, straight arteries face heavy shear stress. The figure also describes the impact of the magnetic field on the WSS profile. A drop in the WSS profile has been observed with the increase in magnetic field intensity. This is happening because, with implification of the magnetic field, a retardation force known as the Lorentz force arises perpendicular to the flow, which affects the flow velocity by making it slow. Sometimes, high wall shear stress can damage endothelial walls [94]; therefore, performing radiation therapy under tools(machines) that use the magnetic field concept is essential to control the shear stress to prevent such severe damage.

The variance in the blood flow frictional impedance for the various values of the physical parameters thermal radiation (N) and Hall parameter (m_a), respectively, have shown in Figures 5.13 – 5.14. This mathematical study is performed in the whole stenotic. From the figures mentioned above, it can be concluded that the frictional impedance increases as stenosis height grow (from the z=.75 to z=1.25 region), and after that, it begins to decay in the remaining stenotic zone as stenosis height decreases. The increase in radiation intensity leads to a boost in both blood flow temperature and velocity. Therefore, the resistance between blood particles decreases with an increase in the value N. This study also reveals that frictional impedance between blood particles is lower when blood is considered a pseudoplastic fluid than Newtonian fluid.

It is also noted that for both pseudoplastic and Newtonian fluid conditions, the decrement rate of frictional impedance increases rapidly with enhancement in the value of N. A comparative study of the Hall parameter (m_a) to calculate frictional resistance of two-phase blood flow by considering blood as pseudoplastic is depicted in figure 5.14. The blood experiences the resistive Lorentz force when the magnetic field is applied perpendicular to the flow. As a result, the Lorentz force is also observed by Hall effect when the Hall parameter is introduced under a magnetic field. The positive add-in value of m_a leads to rise in blood's

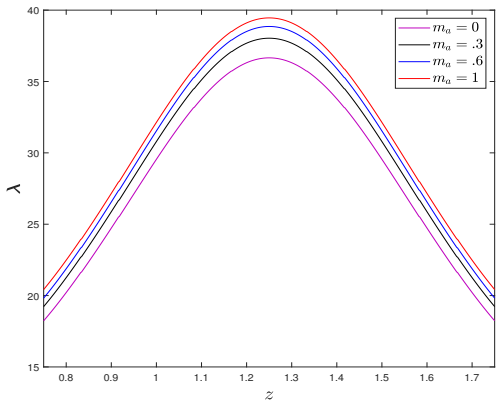

Figure 5.14: Frictional Impedance for m_a

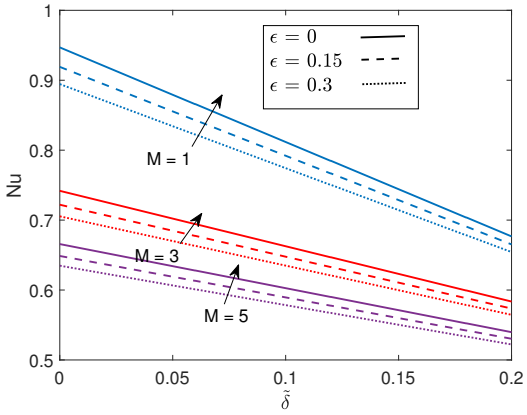

Figure 5.15: Nusselt number for M and ε

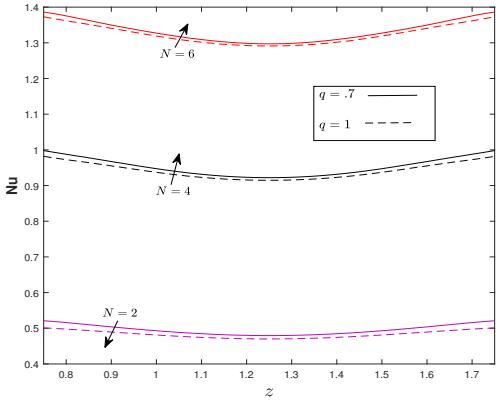

Figure 5.16: Nusselt number for N and q

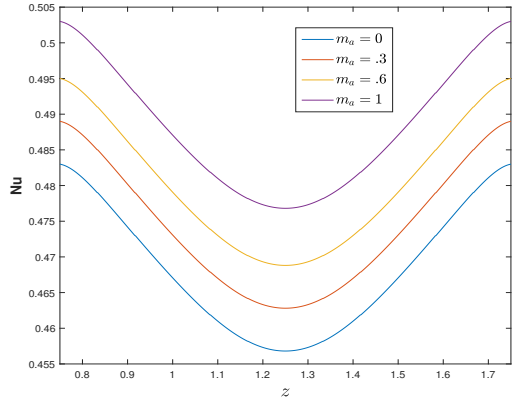

Figure 5.17: Nusselt number for m_a

friction resistance.

The importance of the magnetic field strength (M) and arterial curvature (ε) on the heat transfer rate at the interface of the wall have been simulated using Stone's method and illustrated with the help of the figure 5.15. The discussion of heat transfer has been performed for the maximum stenosis height ($\tilde{\delta}$), and observed that as the size (height) of stenosis increases, heat transfer rate diminishes at the arterial wall. This investigation also noticed that the heat transfer through the arterial wall is higher for the straight (circular,$\varepsilon = 0$) artery. Therefore, as the arterial curvature increases, the heat transfer across the wall diminishes significantly. The increase in magnetic field intensity leads to decay in blood flow velocity, and due to this, viscous heating also decreases. As a result, the heat transfer rate at the arterial wall also reflects the diminishing profile with the increase in magnetic field intensity.

Figures 5.16-5.17 explain the variation in heat transfer rate for various values of thermal radiation and the Hall parameter. These graphs showed the heat transfer rate throughout the stenotic area, defined as the area between $\tilde{z} = .75$ and $\tilde{z} = 1.25$. A comparative study

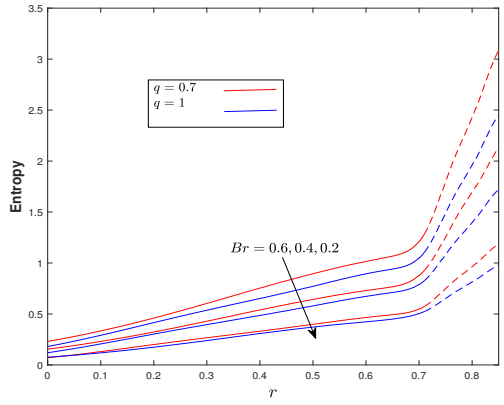

Figure 5.18: Entropy generation for q and Br

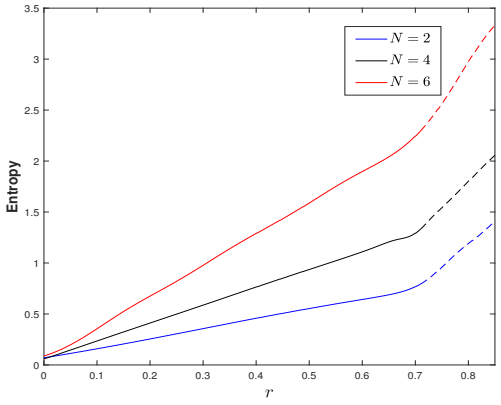

Figure 5.19: Entropy generation for N

has been made to elucidate the importance of choosing pseudoplastic fluid as blood in the modelling. It is found that the heat transfer rate is higher when blood is considered the pseudoplastic fluid than Newtonian fluid. The heat transport phenomenon at the artery wall is significantly influenced by thermal radiation. Figure 5.16 reveals that the heat transfer across the wall enhances with the increase in radiation intensity. Figure 5.17, reported that as the value of the Hall parameter (m_a)increases, the heat transfer rate across the arterial wall increases in the entire stenotic region.

Entropy generation is critical for understanding biological thermodynamics in blood flow through constricted regions because entropy generation indicates the reduction in quality energy which further can not use in work. The variation of entropy generation profile in a stenosed curved artery with the help of different values of Brinkman number (Br) has been discussed in the figure 5.18. The above figure shows that the heat conduction process, which is generated by viscous heating, is reduced by increasing Br value (i.e., heat transfer from the artery blood flow to the environment decreases). Therefore, blood cells produce more heat, which shows up as an increase in the blood flow temperature profile. As a result, blood generates more energy due to a rise in viscous heating with Br, but due to a sudden hike in quality energy, most of the energy is not available for work. It can be concluded that entropy production increases with the rise in frictional heating. Figure 5.18, also deliberate the comparative study for the flow behaviour index (q). This study that energy loss rises into blood flow becomes higher when core region blood is considered pseudoplastic fluid than Newtonian.

The figures 5.19-5.20 are developed to elucidate the impact of thermal radiation (N) and magnetic field (M) on the entropy generation profile for the stenosed curved artery. In this investigation, the core region of blood's properties is considered as of pseudoplastic fluid. The above-mentioned figures reflect that the amount of unusable energy (entropy) increases

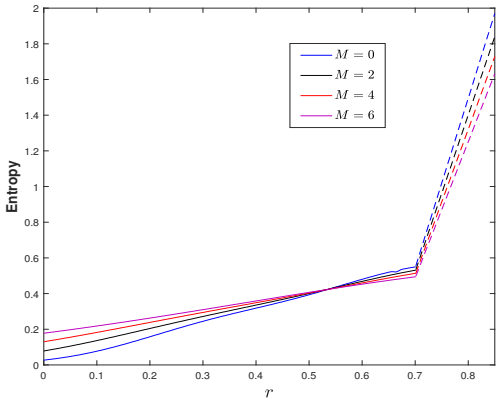

Figure 5.20: Entropy generation for M

rapidly in the plasma region and near the arterial wall. This occurs due to the presence of nutrients, ions, sugar, fat, and essential proteins like albumin and fibrinolytic protein in the plasma region, as well as the significant heat transfer that occurs across the arterial wall. Therefore it generates more energy in the plasma region, most of which is not usable for work. As a result, the plasma region experiences a sudden surge in entropy creation compared to the core region.

Figure 5.19 reveals that, as the strength of thermal radiation increases, it genrates more energy due to a rise in flow temperature. Resultant, entropy production also increases in blood flow. It can also be seen that there is a negligible hike in entropy at the center of the artery with the increase in the value of N because radiation is an external energy generation source, which mostly affects the arterial wall. The importance of the external applied magnetic field on the entropy generation profile has been discussed in figure 5.20. From the figure, it is observed that, with the increased magnetic field intensity, initially, entropy production increases in the core region, but as blood flow approaches the artery wall, it shows a negative effect.

Blood flow trapping in a stenosed curved artery by considering blood as pseudoplastic fluid is an exciting phenomenon to describe flow patterns. The figures 5.21-5.23 illustrate the comparative study of fluid flowing patterns for various values of physical parameters such as magnetic field (M), thermal radiation (N) and arterial curvature (ε). The streamlined patterns are obtained smooth due to considering the constant pressure gradient and low Reynold number in this numerical calculation. Figure 5.21, discussed the flow trapping pattern for different magnetic field values and stated that the area of maximum velocity difference is reduced with increased magnetic field intensity. This happens due to arising Lorentz force in blood flow, which retard the flow velocity. Applying thermal radiation to blood flow boosts the flow temperature, as a result, flow velocity also increases. Therefore,

difference between velocity rises, which can be seen in figure 5.22, that the area of maximum velocity increases with the rise in radiation strength. This investigation deals with the curved artery, therefore a comparative study between circular (straigth, $\varepsilon = 0$) and curved ($\varepsilon \neq 0$) to discuss the blood trapping phenomenon has been presented in the figure 5.23. Figure concluded that, the maximum blood flow velocity region decreases with the rise in the value of curvature parameter (ε), this is happen due to a drop in flow velocity for higher curvature of artery.

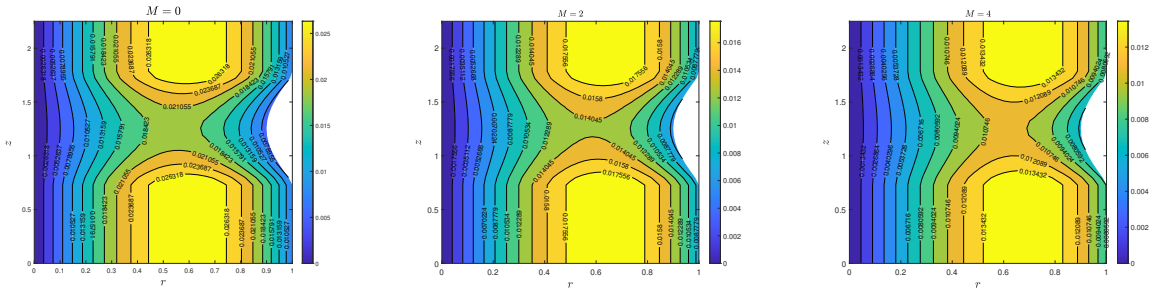

(a) (b) (c)

Figure 5.21: Blood flow pattern for magnetic field, (a) $M = 0$, (b) $M = 2$, (c) $M = 4$.

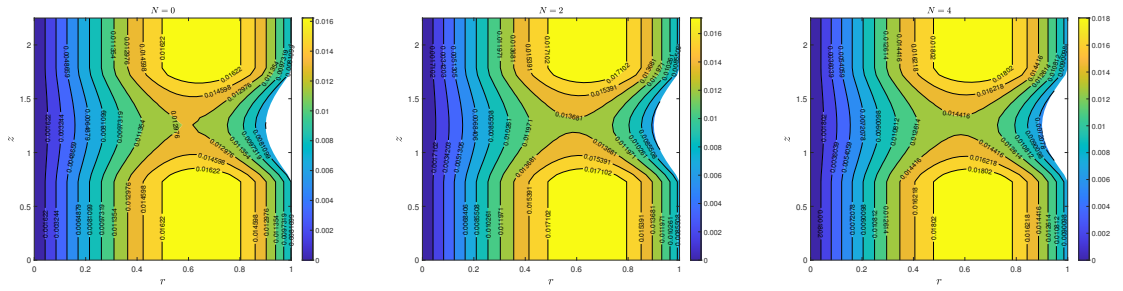

(a) (b) (c)

Figure 5.22: Blood flow pattern for thermal radiation, (a) $N = 0$, (b) $N = 2$, (c) $N = 4$.

5.7 Conclusion

A mathematical model of two-phase blood flow has been developed to perform a computational investigation of entropy analysis and blood phenomena in a curved arterial flow under the consequences of the Hall effect and magnetic field presence. To make this study more realistic, a model of patient specific elliptic shape stenosis at the arterial wall has been

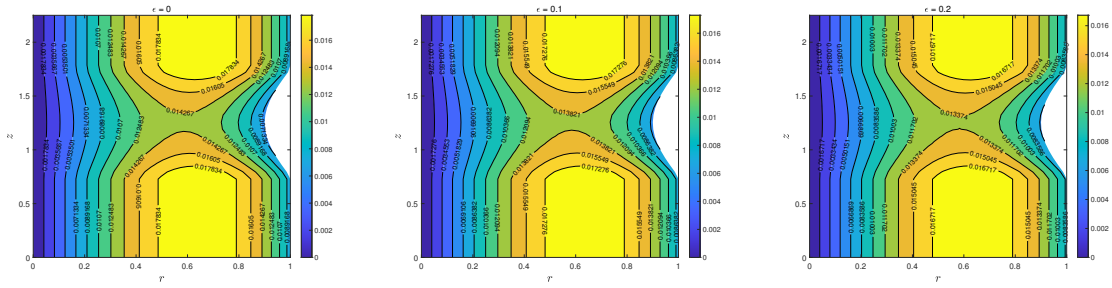

(a) (b) (c)

Figure 5.23: Blood flow pattern for arterial curvature, (a) $\varepsilon = 0$, (b) $\varepsilon = 0.1$, (c) $\varepsilon = 0.2$.

considered. The pseudoplastic fluid properties instead of Newtonian fluid have been considered for the core region blood flow to make the current investigation more realistic. The governing equations are written in a toroidal coordinate system, and it is discretized using a second-order central difference scheme. Stone's strongly implicit method is used for solving a system of non-linear equations in "MATLAB" software with tolerance of 10^{-6} in each iteration. The influence of several physical parameters such as q,N,m_a,Br,δ,M have been discussed graphically for the blood velocity, temperature, WSS, frictional impedance, heat transfer rate and entropy production. Clinical researchers and biologists can utilize finding of this computational investigation to predict endothelial cell damage and deposition of plaque in curved arteries with WSS profiles and can cure timely to reduce these severe situations. The use of radiation in thermal therapies will be helpful in the treatment of cancer cells, muscle pain and stiffness etc. Some significant outcomes of present mathematical investigation are listed below-

- A positive increase in the Hall parameter value is preferable for an increase in heat transfer rate, whereas flow velocity and the wall shear stress profile reduce with it.
- The blood flow produces more entropy with the increase in both viscous heating and thermal radiation intensity.
- Arteries with high curvature have a higher possibility for lipid and stenosis deposition due to decay in both the wall shear stress profile and heat transfer at the arterial wall.
- If pseudoplastic properties instead of Newtonian fluid properties are considered for blood, in mathematical modelling will give accurate results in understanding blood flow phenomena.

- The use of thermal radiation in therapies can lower arteriosclerosis deposition and increase heat transfer and flow velocity.
- The frictional impedance between blood cells rises significantly with the increase in values of both thermal radiation and Hall parameter.
- Using the magnetic field in thermal therapies will help to control flow velocity.
- The blood flow temperature is high for the pseudoplastic fluids than the Newtonian and diltant fluids.

Chapter 6

Computational analysis of electrokinetic energy conversion for power law gold nano fluid flow through curved artery: Entropy generation optimization [1]

6.1 Introduction

The study of microfluidics in micro-electromechanical systems (MEMS) is fascinating topic because of its important applications in both physical and biological processes. The presence of salt and minerals, such as sodium, potassium, magnesium and chloride etc., in the blood, makes it an electrolyte solution. Therefore, when blood (electrolyte) in come touch with arterial wall, it forms a thin electric double layer (EDL) at the wall. The study of electrokinetic force on the flow, which has power law fluid properties, has been performed by Chakraborty et al. [138, 139]. In this study, they analyzed blood flow velocity for the different hematocrit levels and electric field strength. A theoretical study to describe the effect of EDL thickness and flow behaviour index on the flow through a slit microchannel has been proposed by Zhao et al. [140]. The numerical discussion of high zeta potential effects on the flow through a curved microchannel by adopting the SIMPLE algorithm to solve momentum equations has been performed by Nekoubin [141]. This study considers power-law fluid properties and states that the axial velocity and flow rate enhances with a positive add-in zeta potential. Recently, an analytical study using the perturbation technique to discuss electrokinetic flow and energy conversion in curved tubes has been published by Ding et al. [142]. This study concluded that electrokinetic energy conversion efficiency is higher in curved tubes in comparison with straight tubes. Also, EDL potential is higher at the outer side bend of a curved tube than the inner side.

The study of streaming potential and electrokinetics energy conversion (EKEC) is a very fascinating topic for researchers when fluid flows in microchannels. The conversion process

[1] A considerable part of this chapter is Accepted in *Numerical Heat transfer, Part A: Applications*

of mechanical energy produced by pressure-driven flow and chemical energy of EDL into electric energy is called EKEC. Badopadhyaay et al. [143], performed a numerical investigation to determine the energy transfer efficiency in the narrow channel for power-law fluid and stated that mechanical energy conversion has been improved for the shear-thinning fluids in comparison with the Newtonian fluids with the no-slip boundary condition.The limitation of wall surface potential (zeta potential $\tilde{\phi}$) limit on the streaming potential and hydroelectric energy conversion efficiency for Phan-Thein-Tanner (PTT) fluid has been discussed by Sarkar [144]. They found that streaming potential and EKEC enhances for the $\tilde{\phi} \leq 6$ and for $6 < \tilde{\phi} \leq 10$ they shows reverse effect. Jian et al. [145, 146], discussed the EKEC efficiency in the cylindrical flow in presence of nanoparticle and concluded that for a certain limit of Debye length, both EKEC efficiency and streaming potential decreases with the increment in nanoparticle volume fraction.

In the last few decades, discovering the application of nanotechnology has been a curious topic for researchers in the field of medicine, thermal engineering, industry, etc. Nanoparticles are very small in size with a diameter range between 1-100 um and it enhances the thermal properties of the fluid. Wilczewska et al. [49] state that due to small dimension size, nanoparticles reflect their unique biological property to penetrate the tissue and cell membranes, which helps in the direct interaction of nanoparticles with the proteins and smaller cells. At present time there are so many nanoparticles with different nanostructures that have been used for diagnosing several diseases such as Caelyx® (Liposomes nanostructure with doxorubicin to cure ovarian and breast cancer), Tricor® (Nanocrystalline drugs with Fenofibrate in Hypercholesterolemia treatment), Amphotec® (Lipid colloidal dispersion nanostructure with Amphotericin B in cure of Fungal infections), etc [147]. Due to biocompatibility and magnetic properties, ultra superparamagnetic iron oxide (USPIO) nanoparticles are used in magnetic resonance imaging (MRI) and computed tomography (CT) to identify the situation of plaque deposition in arteries to prevent myocardial infarction [148]. Duivendvoorden et al. [149], performed an experimental study and explained that the use of a high dose of rHDL nanoparticle in statins therapy can reduce atherosclerosis deposition. Weinstein et al. [150] describe the importance of superparamagnetic iron oxide nanoparticles in the healing process of the nervous system and also obtained significantly good diagnosis results on the low tesla magnet. Recently, Poonam et al. [151] adopted the Crank-Nicolson method to computationally investigate the effect of (Au-Al_2O_3/ blood) hybrid-nanofluid in a curved artery. This investigation considered both stenosis and aneurysm arterial conditions to make this study more realistic. They suggested that adding the quantity of Al_2O_3 nanoparticles into Au-blood nanofluid helps boost the flow temperature, which may be beneficial during thermal therapies to kill cancer and tumour cells.

All the cited research papers in the literature survey provide information about fluid behaviour phenomena and heat transport for fluid flow in curved and straight tubes. As per the author's best knowledge, the power-law fluid model for blood flow with electric potential (for EDL potential) and the EKEC concept have not been studied earlier. Therefore, the prime objective of this article is to investigate the fluid phenomena (velocity, temperature, concentration, wall shear stress, Nusselt number), entropy generation, and EKEC efficiency for the blood flow (power-law fluid) through an overlapped stenosed curved artery. In the mathematical modelling, the effects of gold nanoparticles and their size have also been considered to describe their impact on blood flow. In curved tubes, it is very difficult to compute the analytical solution of a system of non-linear partial differential equations (Navier-Stokes and Poission-Boltzmann). Therefore, in this research work, a second-order finite difference scheme [130] has been adopted to discretize these system of nonlinear PDE's, after which these equations are solved using Stone's strongly implicit method [152] by considering the tolerance of 10^{-6}. The results for fluid physical phenomenas such as velocity, temperature, concentration, EKEC, entropy generation, WSS and nusselt number have been computed numerically by using "MATLAB" software and explained using graphs.
The novelty of present investigation includes-

- The effect of gold nanoparticles on the non-Newtonian blood flow (power-law fluid) through overlapped stenosed curved artery has been examined.
- The effect of nanoparticle size on the physical fluid phenomena has been investigated.
- The electric potential and EKEC efficiency profile for blood flow has been obtained.
- The entropy generation profile for blood flow for various physcial parameters has been figure out.

6.2 Problem formulation

In this study, investigation of laminar, incompressible blood flow through an overlapped stenosed curved artery has been performed. In this study, blood is considered a non-Newtonian fluid; therefore, properties of the power-law fluid have been taken into account for governing equation formation. In this investigation, blood flows through the curved artery, and the toroidal coordinate system (r, θ, z) have been employed to describe the arterial geometry. The z-axis represent the curved artery axis, r is taken along the radial direction and θ represent the angular direction .

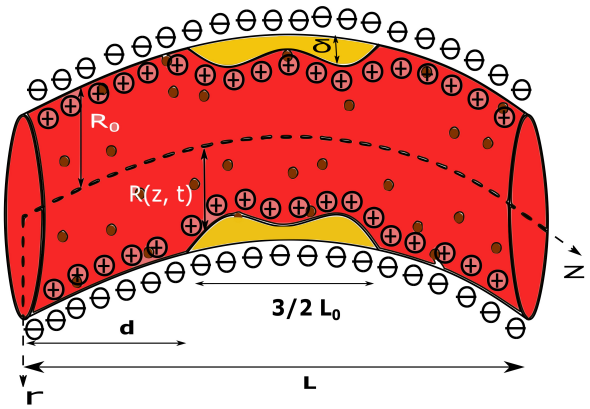

Figure 6.1: Graphical representation of curved artery

6.2.1 Mathematical formulation of stenosis

The time-dependent overlapped diseased artery section (stenosis) condition has been assumed for modeling of the curved arterial flow. $R(z,t)$ represent the artery radius in the stenotic region. The arteial wall has been considered negatively charged. Figure 6.1 presents the geometry of a stenosed curved artery. Numerically formulation of diseases section (stenosis) written as preceding [108]:
Mathematical formulation of overlapped stenosis:

$$R(z,t) = \begin{cases} \left[R_0 - \frac{\delta(z-d)}{L_0}\left(11 - \frac{94}{3L_0}(z-d) + \frac{32}{L_0^2}(z-d)^2 - \frac{32}{3L_0^3}(z-d)^3\right)\right]\Omega(t), & d \le z \le d + \frac{3}{2}L_0, \\ R_0\Omega(t) & \text{Rest region.} \end{cases} \tag{6.1}$$

$$\Omega(t) = 1 - \eta(\cos(\omega t) - 1)e^{-\eta\omega t}. \tag{6.2}$$

where $\frac{3}{2}L_0$ & L represents the length of overlapped diseases section of artery, respectively. δ and d indicate the stenosis maximum height and starting stenosis location, respectively.

6.2.2 Electrostatic potential

The presence of salt and minerals, such as sodium, potassium, magnesium and chloride etc., in the blood makes it an electrolyte solution. Therefore, when blood with a uniform dielectric constant (Ξ) flows into a curved artery, it induces interfacial charges on the arterial wall. The induced charges allow the moving free ions into blood to establish a thin electric double layer (EDL) at the arterial wall. In this EDL, an electric potential field (ψ_i) is generated with the net zero-charge density. Whereas a streaming(external) potential (ψ_a) occurs in the blood flow due to an externally applied electric field, which produces a net flow charge. The total electric potential (Ψ) is the combination of both induced (ψ_i) and streaming potential (ψ_a), i.e. $\Psi = \psi_i + \psi_a$. For a uniformly charged curved artery, electric potential can be written in form of the Poisson equation-

$$\nabla^2 \Psi = -\frac{\rho_{el}}{\Xi}, \tag{6.3}$$

where ρ_{el} represent the net electric charge density.
This study considered the flow through the curved artery; therefore, induced electric potential (ψ_i) also varies in the angular direction (θ) along with the radial direction (r), i.e. $\psi_i = \psi_i(r,\theta)$, and streaming potential have only axial dependence i.e. $\psi_a = \psi_a(z)$ [153, 142]. By substituting these assumptions into equation 6.3, we get-

$$\nabla^2 \psi_i(r,\theta) = -\frac{\rho_{el}}{\Xi}, \tag{6.4}$$

$$\nabla^2 \psi_a(z) = 0, \tag{6.5}$$

i.e.

$$\frac{\partial^2 \psi_a}{\partial z^2} = 0,$$

This indicates that $\frac{\partial \psi_a}{\partial z}$ is constant, so it can be written as-

$$E_s = -\frac{\partial \psi_a}{\partial z}, \tag{6.6}$$

The condition of symmetric electrolyte condition ($\Upsilon_+ = -\Upsilon_- = \Upsilon_v$) has been considered, therefore the mathematical formulation of net electric charge density can be specified as-

$$\rho_{el} = e(\Upsilon_+ n_+ + \Upsilon_- n_-) = e\Upsilon_v(n_- - n_-), \tag{6.7}$$

where e and Υ_v represent the electron charge and valence respectively, whereas n_+, n_- describe the cation and anion density quantity, respectively. The density of these charged ions

can be determined using Boltzmann distribution-

$$n_{\pm} = n_0 \exp\left(\mp \frac{\Upsilon_v e \psi_i}{K_B T_{la}} \right), \tag{6.8}$$

where n_0 denotes the ion density of bulk fluid, K_B and T_{la} symbolize the Boltzmann constant and local absolute temperature.
With the substituting the mathematical expression of ρ_{el} and $n_{\pm}$ from equations 6.7-6.8 into the equation 6.3, we get-

$$\nabla^2 \psi_i = \kappa^2 \psi_i, \tag{6.9}$$

where κ denotes the electro-kinetic width (Inverse of Debye length).
Debye length $\lambda = \sqrt{\frac{\Xi K_B T_{la}}{2 n_0 e^2 \Upsilon_v^2}}$.

The applied body force on the blood flow through the curved artery is the combination of both electric and magnetic field force. Therefore, the mathematical expression of electromagnetic body force can be formulated as-

$$\vec{F}_{em} = \rho_{el}\vec{E} + \vec{J} \times \vec{B}, \tag{6.10}$$

The generalized Ohm's law is written as [24]

$$\vec{J} = \sigma\left(\vec{E} + \vec{V} \times \vec{B} \right), \tag{6.11}$$

$$\vec{E} = -\nabla\Psi,$$

where $\vec{E}$, $\vec{J}$ and $\vec{B}$ denotes the electric field, electric current density and magnetic field, respectively. $\vec{V}$ indicates the flow velocity and $\vec{V} = (u, v, w)$ are the velocity components in the r, θ, z directions, respectively.

6.2.3 Nanoparticle

The injection of gold (Au) nanoparticles in the blood flow are beneficial in diagnosing several serious diseases. The nanoparticle volume fraction, as well as its particle size, also reflects the critical role in flow physiology. Therefore this study considers the particle size effect on the nanofluid viscosity and thermal conductivity.
The thermal conductivity and viscosity of the nanofluid using Corcione's model [51]-

$$\frac{K^{nf}}{K^b} = 1 + 4.4 Re_p^{0.4} Pr^{0.66} \left(\frac{T_b}{T_{fr}} \right)^{10} \left(\frac{K^p}{K^b} \right)^{.03} m^{0.66}, \tag{6.12}$$

$$\frac{\mu^{nf}}{\mu^{b}} = \frac{1}{1-34.87\left(\frac{dp}{db}\right)^{-0.3} m^{1.03}}, \tag{6.13}$$

where,

$$Re_p = \frac{2\rho^b \bar{k}_b T_b}{\pi(\mu^b)^2 d_p},$$

$$db = 0.1\frac{6M_a}{N_a \pi \rho^b}.$$

where, K^{nf}, μ^{nf} represents the thermal conductivity and viscosity of nanofluid (Au+blood), respectively.

K^b, μ^b, T_b, db denotes the blood thermal conductivity, viscosity, temperature and blood cells diameter, respectively. m is the volume fraction of nanoparticle.

Re_p is the particle Reynold number, T_{fr} blood freezing temperature, dp is nanoparticle diameter.

$\bar{k}_b$ is Boltzmann constant (1.38064×10^{-23}), M_a is molecular weight of base fluid (Blood) , N is Avogadro number.

The remaining thermal properties of nanofluid are considered according to Brinkman model are written as [50, 124]-

$$\begin{cases} \frac{\rho^{nf}}{\rho^b} = (1-m) + m\left(\frac{\rho^p}{\rho^b}\right), \\ \frac{\sigma^{nf}}{\sigma^b} = \frac{\sigma^p + (m-1)\sigma^b - (m-1)m(\sigma^b - \sigma^p)}{\sigma^p + (m-1)\sigma^b + m(\sigma^b - \sigma^p)}, \\ \frac{Dp^{nf}}{Dp^b} = \frac{1-m}{1+m/2}. \end{cases} \tag{6.14}$$

where, ρ^{nf}, σ^{nf}, Dp^{nf} are the density, electrical conductivity, and mass diffusivity of nanofluid, respectively.

ρ^b, σ^b, Dp^b are the density, electrical conductivity, and mass diffusivity of blood, respectively and ρ^p, σ^p are the density, electrical conductivity of nanoparticle (gold), respectively.

6.2.4 Governing equations

The Power-law fluid has been considered for the arterial blood flow and stress component for the this fluid is written as follows [25]-

$$(\tau)_{ij} = -PI + K\mu^{nf}\Omega_f(\phi)_{ij}, \tag{6.15}$$

where

$$\Omega_f = \left[(\phi)^2_{rr} + (\phi)^2_{\theta\theta} + (\phi)^2_{zz} + 2\left((\phi)^2_{r\theta} + (\phi)^2_{\theta z} + (\phi)^2_{zr}\right)\right]^{\frac{q-1}{2}}.$$

where, τ and ϕ represents the stress and strain tensors, respectively. K and q, represent the flow consistency and flow behaviour index, respectively. μ^{nf} state the nanofluid viscosity. The governing equations for curved artery can be written as follows [80, 154]-

$$\frac{b}{D}\frac{\partial w}{\partial z}+\frac{\partial u}{\partial r}+\frac{1}{r}\frac{\partial v}{\partial \theta}+\frac{u}{r}+\frac{u\cos\theta-v\sin\theta}{D}=0, \tag{6.16}$$

where, h denotes the radius of curvature.

$$D=b+r\cos\theta,$$

Momentum equations
r-direction:

$$\rho^{nf}\left(\frac{\partial u}{\partial t}+\frac{bw}{D}\frac{\partial u}{\partial z}+u\frac{\partial u}{\partial r}+\frac{v}{r}\frac{\partial u}{\partial \theta}-\frac{v^2}{r}-\frac{w^2\cos\theta}{D}\right)=\frac{b}{rD}\left(\frac{\partial}{\partial z}\left(r(\tau)_{rz}\right)+\frac{\partial}{\partial r}\left(\frac{Dr(\tau)_{rr}}{b}\right)\right.$$
$$\left.+\frac{\partial}{\partial \theta}\left(\frac{D(\tau)_{r\theta}}{b}\right)\right)-\frac{(\tau)_{\theta\theta}}{r}-\frac{\cos\theta(\tau)_{zz}}{D}+\rho_{el}\vec{E}_r+(\vec{J}\times\vec{B})_r, \tag{6.17}$$

θ direction :

$$\rho^{nf}\left(\frac{\partial v}{\partial t}+\frac{wb}{D}\frac{\partial v}{\partial z}+u\frac{\partial v}{\partial r}+\frac{v}{r}\frac{\partial v}{\partial \theta}+\frac{uv}{r}+\frac{w^2\sin\theta}{D}\right)=\frac{b}{rD}\left(\frac{\partial}{\partial z}\left(r(\tau)_{\theta z}\right)+\frac{\partial}{\partial r}\left(\frac{Dr(\tau)_{r\theta}}{b}\right)\right.$$
$$\left.+\frac{\partial}{\partial \theta}\left(\frac{D(\tau)_{\theta\theta}}{b}\right)\right)+\frac{(\tau)_{r\theta}}{r}+\frac{\sin\theta(\tau)_{zz}}{D}+\rho_{el}\vec{E}_\theta+(\vec{J}\times\vec{B})_\theta, \tag{6.18}$$

$\bar{z}$ direction :

$$\rho^{nf}\left(\frac{\partial w}{\partial t}+\frac{uw\cos\theta}{D}+\frac{wb}{D}\frac{\partial w}{\partial z}+u\frac{\partial w}{\partial r}-\frac{vw\sin\theta}{D}+\frac{v}{r}\frac{\partial w}{\partial \theta}\right)=\frac{b}{rD}\left(\frac{\partial}{\partial z}\left(r(\tau)_{zz}\right)\right.$$
$$\left.+\frac{\partial}{\partial r}\left(\frac{Dr(\tau)_{rz}}{b}\right)+\frac{\partial}{\partial \theta}\left(\frac{D(\tau)_{\theta z}}{b}\right)\right)+\frac{\cos\theta\ (\tau)_{rz}}{D}-\frac{\sin\theta(\tau)_{z\theta}}{D}+\rho_{el}\vec{E}_z+(\vec{J}\times\vec{B})_z, \tag{6.19}$$

Energy equation :

$$\rho^{nf}\bar{C}^{nf}\left(\frac{\partial T}{\partial t}+u\frac{\partial T}{\partial r}+\frac{v}{r}\frac{\partial T}{\partial \theta}+\frac{wb}{D}\frac{\partial T}{\partial z}\right)=K^{nf}\left(\frac{\partial^2 T}{\partial r^2}+\frac{1}{r}\frac{\partial T}{\partial r}+\frac{b^2}{D^2}\frac{\partial^2 T}{\partial z^2}+\frac{\cos\theta}{D}\frac{\partial T}{\partial r}\right.$$
$$\left.-\frac{\sin\theta}{rD}\frac{\partial T}{\partial \theta}+\frac{1}{r^2}\frac{\partial^2 T}{\partial \theta^2}\right)+Q+F+\frac{\vec{J}\cdot\vec{J}}{\sigma^{nf}}, \tag{6.20}$$

Concentration equation :

$$\left(\frac{\partial C}{\partial t}+u\frac{\partial C}{\partial r}+\frac{v}{r}\frac{\partial C}{\partial \theta}+\frac{wb}{D}\frac{\partial C}{\partial z}\right)=Dp^{nf}\left(\frac{\partial^2 C}{\partial r^2}+\frac{1}{r}\frac{\partial C}{\partial r}+\frac{b^2}{D^2}\frac{\partial^2 C}{\partial z^2}+\frac{\cos\theta}{D}\frac{\partial C}{\partial r}-\frac{\sin\theta}{rD}\frac{\partial C}{\partial \theta}\right.$$
$$\left.+\frac{1}{r^2}\frac{\partial^2 C}{\partial \theta^2}\right)+Rc(C-C_0), \tag{6.21}$$

Electric potential equation :

$$\left(\frac{\partial^2 \psi_i}{\partial r^2}+\frac{1}{r}\frac{\partial \psi_i}{\partial r}+\frac{b^2}{D^2}\frac{\partial^2 \psi_i}{\partial z^2}+\frac{\cos\theta}{D}\frac{\partial \psi_i}{\partial r}-\frac{\sin\theta}{rD}\frac{\partial \psi_i}{\partial \theta}+\frac{1}{r^2}\frac{\partial^2 \psi_i}{\partial \theta^2}\right)=\kappa^2\psi_i, \tag{6.22}$$

Here, F denotes the viscous dissipation and its mathematical expression for blood flow of core region is given in equation 6.23-

$$F=2^{\frac{q-1}{2}}\mu^{nf}K\left[(\phi)^2_{rr}+(\phi)^2_{\theta\theta}+(\phi)^2_{zz}+2\left((\phi)^2_{r\theta}+(\phi)^2_{\theta z}+(\phi)^2_{zr}\right)\right]^q. \tag{6.23}$$

Where, u,v,w represents the dimensional form of velocity components for blood flow in r,θ,z directions, respectively. Here, T, Q, C, Rc indicates the dimensional form of blood flow temperature, applied heating source, Concentration and chemical reaction parameter, respectively.

The above-mentioned dimensional form of governing and stenosis geometry equations will be transformed into the non-dimensional form using the following non-dimensional parameters mentioned in the table 6.1.

Table 6.1: Dimensionless parameter

$r=R_0r'$	$z=L_0z'$	$\theta=\theta'$	$\omega=\frac{u_0}{L_0}\omega'$	$L=L_0L'$
$d=L_0d'$	$t=\frac{L_0}{u_0}t'$	$R=R_0R'$	$P=\frac{u_0L_0\mu^b}{R_0^2}P'$	$u=\frac{\delta u_0}{L_0}u'$
$v=\frac{\delta u_0}{L_0}v'$	$w=u_0w'$	$\delta^*=\frac{\delta}{R_0}$	$\varepsilon=\frac{R_0}{b}$	$T'=\frac{T-T_w}{T_o-T_w}$
$\alpha=\frac{R_0}{L_0}$	$H=\frac{QR_0^2}{(\bar{T}_0-T_w)K^b}$	$M=\frac{\sigma B_0^2R_0^2}{u_0^2}$	$Re=\frac{\rho^bR_0u_0}{\mu^b}$	$Ec=\frac{u_0^2}{\bar{C}_p(\bar{T}_0-T_w)}$
$Pr=\frac{C_p\mu}{K^b}$	$Br=EcPr$	$C'=\frac{C-C_0}{C_w-C_0}$	$Sc=\frac{\mu^b}{\rho^bDp^b}$	$\xi=\frac{R_0^2\rho^bRc}{\mu^b}$
$\psi'_i=\frac{\Upsilon_ve\psi_i}{K_BT_{la}}$	$\rho_{el}=\frac{\Upsilon_veR_0^2}{K_BT_{la}}\rho'_{el}$	$E'_s=\frac{E_s}{E_0}$	$u_e=\frac{\Xi K_BT_{la}E_0}{\Upsilon_ve\mu^b}$	$u_r=\frac{u_e}{u_0}$

The dimensionless form of stenosis is considered as [134].

The table mentioned above 6.1 has been utilized to transform governing equations into dimensionless forms. Then after fully developed flow, mild stenosis ($\delta^* << 1$), and $O(1)=\alpha=\frac{R_0}{L_0}$ [31] conditions have been employed to simplify dimensionless governing equations.

The simplified form of the governing equations are written as-

$$\frac{\partial P'}{\partial r'} = 0, \tag{6.24}$$

$$\frac{\partial P'}{\partial \theta'} = 0, \tag{6.25}$$

$$\frac{1}{\bar{D}}\frac{\partial P'}{\partial z'} = \frac{\mu^{nf}}{\mu^{f}}\Omega_c^*\left(\frac{\partial^2 w'}{\partial r'^2}+\frac{1}{r'}\frac{\partial w'}{\partial r'}+\frac{1}{r'^2}\frac{\partial^2 w'}{\partial \theta'^2}-\frac{\varepsilon^2 w'}{\bar{D}^2}+\frac{\varepsilon}{\bar{D}}\left[\cos\theta'\frac{\partial w'}{\partial r'}-\frac{\sin\theta'}{r'}\frac{\partial w'}{\partial \theta'}\right]\right)+\frac{\mu^{nf}}{\mu^{f}}$$
$$\left(\frac{\partial w'}{\partial r'}-\frac{\varepsilon w'\cos\theta'}{\bar{D}}\right)\frac{\partial \Omega^*}{\partial r'}+\frac{\mu^{nf}}{\mu^{f}}\left(\frac{1}{r'^2}\frac{\partial w'}{\partial \theta'}+\frac{\varepsilon w'\sin\theta'}{r'\bar{D}}\right)\frac{\partial \Omega^*}{\partial \theta'}+\frac{\bar{\kappa}^2 u_r E_s'\varepsilon}{D}{\psi'}_i - Mw'\frac{\sigma^{nf}}{\sigma^{f}}, \tag{6.26}$$

$$\frac{\partial^2 T'}{\partial r'^2}+\frac{1}{r'}\frac{\partial T'}{\partial r'}+\frac{\varepsilon\cos\theta'}{\bar{D}}\frac{\partial T'}{\partial r'}-\frac{\varepsilon\sin\theta'}{r'\bar{D}}\frac{\partial T'}{\partial \theta'}+\frac{1}{r'^2}\frac{\partial^2 T'}{\partial \theta'^2}+\frac{K^b}{K^{nf}}\left(H+Br\,F'\right)+$$
$$\frac{K^f}{K^{nf}}\frac{\sigma^{nf}}{\sigma^{f}}\left(S_z E_s'^2+MBrw'^2\right)=0, \tag{6.27}$$

$$\frac{\partial^2 C'}{\partial r'^2}+\frac{1}{r'}\frac{\partial C'}{\partial r'}+\frac{\varepsilon\cos\theta'}{\bar{D}}\frac{\partial C'}{\partial r'}-\frac{\varepsilon\sin\theta'}{r'\bar{D}}\frac{\partial C'}{\partial \theta'}+\frac{1}{r'^2}\frac{\partial^2 C'}{\partial \theta'^2}-\frac{Dp^f}{Dp^{nf}}Sc\xi C'=0, \tag{6.28}$$

$$\frac{\partial^2 \psi_i'}{\partial r'^2}+\frac{1}{r'}\frac{\partial \psi_i'}{\partial r'}+\frac{\varepsilon\cos\theta'}{\bar{D}}\frac{\partial \psi_i'}{\partial r'}-\frac{\varepsilon\sin\theta'}{r'\bar{D}}\frac{\partial \psi_i'}{\partial \theta'}+\frac{1}{r'^2}\frac{\partial^2 \psi_i'}{\partial \theta'^2}-\bar{\kappa}^2\psi_i'=0, \tag{6.29}$$

where

$$\bar{D}=1+\varepsilon r'\cos\theta',$$

$$\Omega^*=2^{\frac{q-1}{2}}\left[\left(-\frac{\varepsilon w'\cos\theta'}{\bar{D}}+\frac{\partial w'}{\partial r'}\right)^2+\left(\frac{\varepsilon w'\sin\theta'}{\bar{D}}+\frac{1}{r'}\frac{\partial w'}{\partial \theta'}\right)^2\right]^{\frac{q-1}{2}},$$

$$F'=\frac{2^{q-1}}{(1-m)^{2.5}}\left[\left(-\frac{\varepsilon w'\cos\theta'}{\bar{D}}+\frac{\partial w'}{\partial r'}\right)^2+\left(\frac{\varepsilon w'\sin\theta'}{\bar{D}}+\frac{1}{r'}\frac{\partial w'}{\partial \theta'}\right)^2\right]^{q},$$

where, M, E_s', S_z are the non-dimensional form of magnetic field, streaming potential and heat generation due to joule heating. Mathematical formulation of dimensionless boundary

condition is mentioned in equation 6.30

$$\begin{cases} \frac{\partial w'}{\partial r'}=0, & \frac{\partial T'}{\partial r'}=0, & \frac{\partial C'}{\partial r'}=0, & \frac{\partial \psi_i'}{\partial r'}=0, & \text{at} \quad r'=0, \\ w'=0, & T'=0, & C'=1, & \psi_i'=\psi_w, & \text{at} \quad r'=R(z',t'), \\ \frac{\partial w'}{\partial \theta'}=0, & \frac{\partial T'}{\partial \theta'}=0, & \frac{\partial C'}{\partial \theta'}=0, & \frac{\partial \psi_i'}{\partial \theta'}=0, & \text{at} \quad \theta'=0 \quad \& \quad \theta'=\pi. \end{cases} \tag{6.30}$$

6.2.5 Streaming potential and EKEC

Ding et al. [142] calculated the streaming potential for the cured microtube using perturbation technique. In order to calculate streaming potential, firstly they introduced ionic current and its expression is-

$$I_{ion}=I_s+I_c=-2n_0e\Upsilon_v R_0^2u_0\left(\int_0^{\pi}\int_0^{R'(z',t')}\psi_i'w'r'dr'd\theta'+M_pu_rE_s'\int_0^{\pi}\int_0^{R'(z',t')}\frac{r'}{\bar{D}}dr'd\theta'\right), \tag{6.31}$$

where, M_p represents the dimensional conduction current (inverse of ionic Peclet number) The analytical form of the streaming potential is-

$$E_s=-\frac{\int_0^{\pi}\int_0^{R'(z',t')}\psi_i'w'r'dr'd\theta'}{M_pu_rE_s'\int_0^{\pi}\int_0^{R'(z',t')}\frac{r'}{\bar{D}}dr'd\theta'}, \tag{6.32}$$

Under the pressure-driven flow assumption, the conversion of mechanical and chemical energy produced by streaming potential and EDL, into the electric energy is called EKEC. The energy conversion efficiency have vital roles in fluid flow through micro-tubes, therefore EKEC efficiency in curved artery is follows as [155, 146]-

$$\bar{\chi}=\frac{\bar{P}_o}{\bar{P}_i}, \tag{6.33}$$

where, $\bar{P}_o$ and $\bar{P}_i$ are called the output and input power of the curved artery and defined as-

$$\bar{P}_i=\left|-\frac{b}{D}\frac{\partial P'}{\partial z'}Q\right|, \tag{6.34}$$

$$\bar{P}_o=\frac{1}{4}\left|I_sE_s\right|. \tag{6.35}$$

where Q known as volumetric flow rate.

6.3 Procedure of solution

With the use of the aforementioned non-dimensional boundary conditions, a computational process to obtain a solution of highly nonlinear PDEs (6.24)-(6.29) (dimensionless governing equations) has been performed using the Finite difference method [130].
The central difference formula of the second order has been employed to discretized the spatial derivatives in the uniform mesh size for the domain $[0 \;\; R'(z',t')] \times [o \;\; \pi]$. Discretization of derivatives can be performed using given process in equation 6.36.-

$$\begin{cases} \frac{\partial G_s}{\partial r'} = \frac{(G_s)_{x+1,y}-(G_s)_{x-1,y}}{2\Delta r}, \\ \\ \frac{\partial G_s}{\partial \theta'} = \frac{(G_s)_{x,y+1}-(G_s)_{x,y-1}}{2\Delta \theta}, \\ \\ \frac{\partial^2 G_s}{\partial r'^2} = \frac{(G_s)_{x+1,y}-2(G_s)_{x,y}+(G_s)_{x-1,y}}{(\Delta r)^2}, \\ \\ \frac{\partial^2 G_s}{\partial \theta'^2} = \frac{(G_s)_{x,y+1}-2(G_s)_{x,y}+(G_s)_{x,y-1}}{(\Delta \theta)^2}. \end{cases} \tag{6.36}$$

Here, G_s represents the velocity, temperature, concentration and potential term for blood flow.
In the present mathematical study Δr and $\Delta\theta$ represents the uniform mesh size in r' and θ' direction, respectively. The mathematical expression for Δr and $\Delta\theta$ are as follows- $\Delta r = \frac{R'(z',t')}{L_1-1}$ and $\Delta\theta = \frac{\pi}{L_2-1}$
where L_1 and L_2 denote the total number of mesh points in r' and θ' directions.
According to published research work [135, 136], due to pumping of heart, blood flow reflect the its pulsatile nature of flow. Therefore, the mathematical formulation of pressure gradient can be written as

$$\frac{\partial P'}{\partial z'} = P_0 e^{-\eta\omega t}. \tag{6.37}$$

Since, the above-mentioned non-dimensional governing equations non-dimensional governing equations can be reduced into 2D nonlinear PDEs. With the discretization of these PDEs, a five-band system of nonlinear algebraic equations have been obtained.

$$AX = bb.$$

where A is coefficient matrix.
The system is highly nonlinear; therefore, solving it using the Gaussian elimination method is not feasible.
Stone's strongly implicit method [152] has been employed to solve the system of nonlinear equations. A global nodal index k has been assigned for every mesh point.

$$k = (y-1) * L_1 + x.$$

After allocating the global nodal index, the coefficient matrix [A] will be factorized into lower and upper triangular matrices. After factorized matrix [A], the residual will be computed. Further, backward and forward substitution will be employed to find a solution. This iterative process is repeated until the residual becomes lesser than the desirable error tolerance. Stone's method is used for inner iteration, then Newton's scheme is applied for outer iteration. For each inner and outer iteration, the absolute error tolerance of 10^{-6} is taken into account.

$$[A]X = [L][U]X = bb.$$

After numerically computed the velocity and temperature, some important physical phenomena such as wall shear stress, Nusselt number, flow rate profiles can be calculated using numerical velocity and temperature profile data.
The Flow rate Q, frictional impedance λ and wall shear stress τ_w can be calculated as follows-

$$Q = \int_0^{R'(z',t')} \int_0^{\pi} r' w'(r', \theta', z') dr' d\theta', \tag{6.38}$$

$$\lambda = \frac{\int_0^L (-\frac{\partial P'}{\partial z'}) dz'}{Q}, \tag{6.39}$$

$$\tau_w = -\frac{\mu^{nf}}{\mu^b} 2^{\frac{q-1}{2}} \left(\frac{\partial w'}{\partial r'} \right)^q_{r=R'(z',t')}, \tag{6.40}$$

The Mathematical calculation of Nusselt number can performed as -

$$Nu = -\frac{K^{nf}}{K^b} \left(\frac{\partial T'}{\partial r'} \right)_{r=R'(z',t')}. \tag{6.41}$$

6.4 Entropy Generation and irreversibility

Entropy generation is critical for understanding biological thermodynamics in blood flow through constricted regions. By considering above mentioned conditions, the general form

of entropy generation can be written as follows-

$$E^{gen} = \underbrace{\frac{K^{nf}(\nabla T)^2}{T_w^2}}_{\text{Thermal irreversibility}} + \underbrace{\frac{F}{T_w}}_{\text{Fluid friction irrversibility}} + \underbrace{\frac{\vec{J}\cdot\vec{J}}{T_w\sigma^{nf}}}_{\text{Joule heating irrversibility}} + \underbrace{\frac{Dp^{nf}(\nabla C)^2}{C_w}}_{\text{Solute irrversibility}}, \tag{6.42}$$

The following are the mathematical formulae to estimate the amount of entropy generation in both regions:

$$\bar{E}^{gen} = \underbrace{\frac{K^{nf}}{\bar{T}_w^2}\left[\left(\frac{\partial T}{\partial r}\right)^2 + \left(\frac{1}{r}\frac{\partial T}{\partial \theta}\right)^2 + \left(\frac{b}{D}\frac{\partial T}{\partial z}\right)^2\right]}_{\text{Thermal irreversibility}} + \underbrace{\frac{F}{T_w}}_{\text{Fluid friction irrversibility}} + \underbrace{\frac{\vec{J}\cdot\vec{J}}{T_w\sigma^{nf}}}_{\text{Joule heating irrversibility}}$$
$$+ \underbrace{\frac{Dp^{nf}}{C_w^2}\left[\left(\frac{\partial C}{\partial r}\right)^2 + \left(\frac{1}{r}\frac{\partial C}{\partial \theta}\right)^2 + \left(\frac{b}{D}\frac{\partial C}{\partial z}\right)^2\right]}_{\text{Solute irreversibility}}, \tag{6.43}$$

The equations 6.43, will be converted in the dimensionless form by using table 6.1 and considering above mentioned flow conditions-

$$E'^{gen} = \frac{E^{gen}}{E},$$

$$E'^{gen} = \frac{K^{nf}}{K^b}\left[\left(\frac{\partial T'}{\partial r'}\right)^2 + \left(\frac{1}{\tilde{r}}\frac{\partial T'}{\partial \theta'}\right)^2\right] + \frac{Br}{A}F' + \frac{\sigma^{nf}}{\sigma^b}\frac{1}{A}\left[S_z E_s'^2 + MBrw'^2\right] + \frac{Dp^{nf}}{Dp^b}\frac{\Gamma\Lambda}{A}\left[\left(\frac{\partial C'}{\partial r'}\right)^2 + \left(\frac{1}{r'}\frac{\partial C'}{\partial \theta'}\right)^2\right], \tag{6.44}$$

where $E = \frac{K_p(T_0-T_w)^2}{T_w^2 R_0^2}$, $A = \frac{T_0-T_w}{T_w}$.

6.5 Results and Discusion

A numerical research study of blood flow through an overlapped stenosed curved artery has been carried out to investigate the influence of various physical parameters such as a magnetic field, inverse Debye length (inverse EDL thickness), heat source, flow behaviour index (power-law fluid), and so on. The thermal properties of gold nanoparticles have been taken into account in this study. Therefore, nanoparticle volume fraction and their size effects

have also been examined for various important physical phenomena. The study of entropy generation, energy conversion, and streaming potential (electric potential) have also been performed to make this study more realistic and impactful. The properties of power-law fluid have been considered for blood flow. The second-order finite difference method has been introduced to discretized non-dimensional governing equations. The flow domain is discretized uniformly for both (r') & (θ') directions. The step size in both directions is assumed $\Delta r = \Delta\theta = 0.001$. After discretization, to obtain flow velocity, temperature, concentration, and electric potential profiles, these systems of non-linear governing equations are computed using Stone's strongly implicit method. The error tolerance for both inner and outer iterations is set up 10^{-6}. The MATLAB codes for Stones scheme have been developed to demonstrate the graphical behaviour of various physical quantities such as velocity, temperature, concentration, WSS, electric potential, heat transfer rate, entropy generation and EKEC efficiency etc. Table 1 provides the default values for different physical parameters and their source of references. The thermophysical properties of blood and nanoparticle (Fe_3O_4) has been written in the table 6.2.

Figure 6.2 illustrates the validation of the current research work's mathematical model formulation and the adopted computational method's accuracy. This validation is made with the published work [156] under some assumptions. Under this assumption, the effects of the magnetic field, electric potential, and nanoparticle size effect have been ignored in our model, and the consideration of a catheter has been neglected in [156] observation. This validation process has been performed by considering the perturbation technique for [156] work and Stone's method for the present work. Figure 1 replicate the fair agreement between the present study and [156] observations.

Table 6.2: Thermophysical properties of blood and gold nanoparticle (Au) [157, 158]

Thermophysical parameter	Blood	Au
Density	1063	19300
Heat Capacity	3594	129
Thermal Conductivity	.492	318
Electrical Conductivity	.667	4.52×10^7
Thermal Expansion Coefficient	1.8×10^{-6}	1.42×10^{-5}

The presence of haemoglobin, cell membranes, and complex structural interactions between proteins in the blood make it a biomagnetic fluid. The main protein in RBCs is haemoglobin, which contains iron particles and transports oxygen from the lungs to other body parts such as the brain, muscles, etc. The haemoglobin structure is more sensitive to

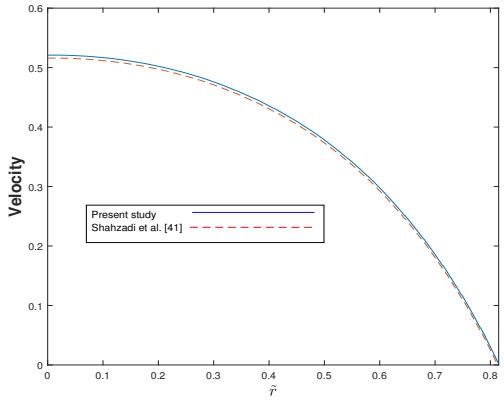

Figure 6.2: Validation of present investigation

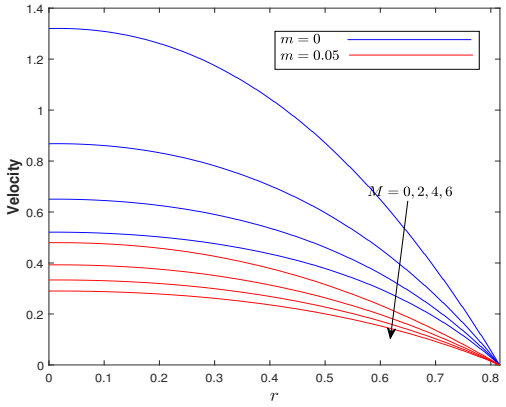

Figure 6.3: Velocity profile for M and m

its oxygen-carrying situation and shows a significant structural variation in both oxygen-carrying and non-carrying conditions. Therefore, motivated by the blood's magnetic properties, a comparative computational study has been performed to illustrate the significance of a magnetic field applied to a stenosed curved artery. Figure 6.3 depicts the effect of different magnetic field intensities on the blood flow velocity. This study states that, when an external magnetic field is applied perpendicular to its axial (flow) direction, it generates a strong electromotive force known as the Lorentz force, which leads to enhanced blood flow viscosity. Consequently, a notable drop in blood flow velocity has been noticed whenever magnetic field intensity increases. It is also worth noting that the flow velocity reduction rate decreases as the value of M increases. A comparison study to describe the significance of nanoparticles (gold Au) on the stenosed artery has also been conducted using the above-mentioned figure. The properties of nanoparticles state that they are more thermally conductive than blood, but they are also highly viscous. As a result, when nanoparticles are added to the base fluid (blood), the viscosity of the nanofluid (blood-Au) increases proportionally to the amount of Au volume fraction added to the blood. This increased viscosity leads to a decay in flow velocity. Since nanoparticles can traverse through the stenosis and mend artery walls, which blood cells are unable to do, these characteristics of nanoparticles are exploited in the treatment of arteriosclerosis. Also, nanoparticles are used to diagnose various severe diseases such as cancer cells, fungal infections, hypercholesterolemia, etc. [147].

The investigation of the effects of nanoparticle size and volume fraction on fluid phenomena has become a very interesting research topic in the field of bionanotechnology. Therefore, in this discussion we used the Corcione model [51], which discusses the nanoparticle diameter effects on the flow. Figure 6.4 depicts the effect of gold nanoparticle diameter on blood velocity through a curved artery. According to this study, for a fixed amount

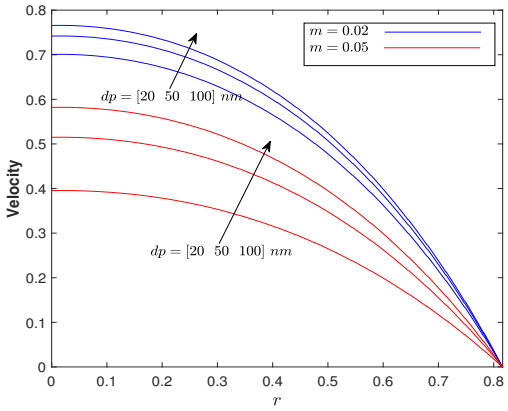

Figure 6.4: Velocity profile for dp and m

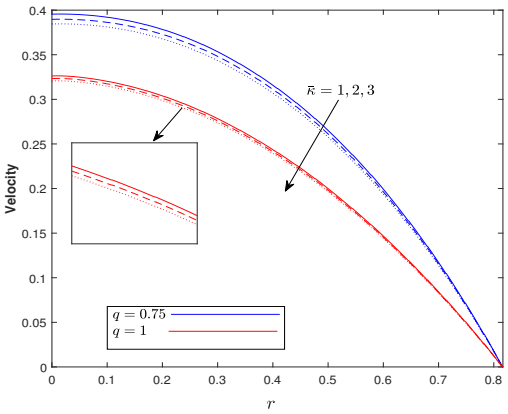

Figure 6.5: Velocity profile for $\bar{\kappa}$ and q

of nanoparticle concentration, blood flow velocity increases as particle diameter increases. This is happening because the number of nanoparticles is higher when they are small in size, so they can easily bind up with blood cells and travel everywhere in artery, resultant blood cells become more viscous. If we increase the size of nanoparticle, there is a reduction in viscosity and increment in the velocity as observed by [51]. It is also noted that the variation in flow velocity increases with increasing nanoparticle concentration for different nanoparticle sizes.

In the electro-kinetic field, the debye length plays an important role in electric potential distribution and flow velocity under the external eletric field condition. Figure 6.5 depicts the effect of electro-kinetic width (inverse Debye length) on flow velocity. An increase in Debye length leads to an increase in ions quantity, which is far from the charged surface and that is used to counter the surface-charged ions. As a result, electric potential decreases. Therefore, with the increase in electro-kinetic width (inverse Debye length), the flow velcoity also decreases. This paper also compares Newtonian and non-Newtonian fluid properties in terms of a flow behaviour index for blood flow velocity. In this case, $q < 1$ represents blood behaviour as pseudoplastic (shear-thinning), $q = 1$, and Newtonian. The figure reveals that, as the value of the flow behaviour index increases, the blood flow velocity decreases in the whole artery. Therefore, in a realistic situation, assuming that blood has a pseudoplastic nature will be good for the mathematical model to get an accurate result to predict disease conditions. The authors decided to consider the pseudoplastic ($q < 1$) behaviour of blood whenever blood is assumed to be non-Newtonian in this computational research work based on the published literature [26] and the fruitful obtained results for flow velocity.

From the point of view of a clinical researcher, figuring out how much heat is conducted from the artery is a very important area of study. Therefore, this work distinguishes

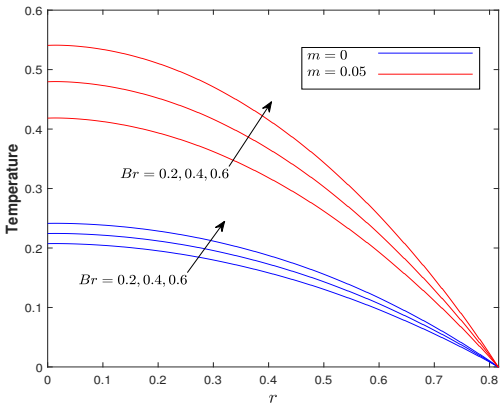

Figure 6.6: Temperature profile for Br and m

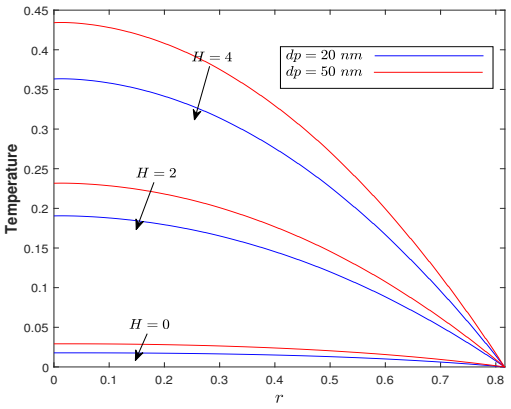

Figure 6.7: Temperature profile for H and dp

the dominance between viscous dissipation and external heating for how much heat is conducted from the artery in terms of the Brinkmann number Br. For fixed external heating, a positive increment in the value of the Brinkmann number leads to a decay in heat conduction from the arterial wall to the environment. In other words, it can also be said that, for fixed external heat, the generation of thermal energy by viscous dissipation is the same, but its conduction from arterial fluid to the environment is reduced. As a result, as the value of the Brinkmann number increases, the temperature of the arterial flow rises significantly, as illustrated in figure 6.6. This study also describes the role of gold nanoparticles on blood flow temperature. It is well known from the literature that gold nanoparticles are approximately 650 times more thermally conductive than blood. Therefore, when a small amount of gold nanoparticles is added to the blood flow, it increases its thermal conductivity significantly. As a result, the temperature of the blood flow rises. From the figure, it can also be observed that the variation in the flow temperature profile for different Brinkmann number values becomes high when nanoparticles are added to it. This is happening because small-sized nanoparticles easily bind with blood cells and generate more thermal energy in the form of viscous dissipation.

In thermal therapies, external heating is very helpful for healing serious diseases like synovial bursitis, muscle pain, killing cancer cells, osteoporosis, and so on. Therefore, the effects of external heating on the overlapped stenotic arterial flow in the presence of nanoparticles have been numerically analysed, and the results are shown in figure 6.7. This study reveals that, for a fixed Brinkmann number (i.e., fixed heat generation by viscous dissipation), the heat conduction rate from the environment to arterial blood flow increases with the increase in the heat source value. As a result, a significant boost in blood temperature is observed with the increase in value of H. This study also suggests that for a fixed amount of

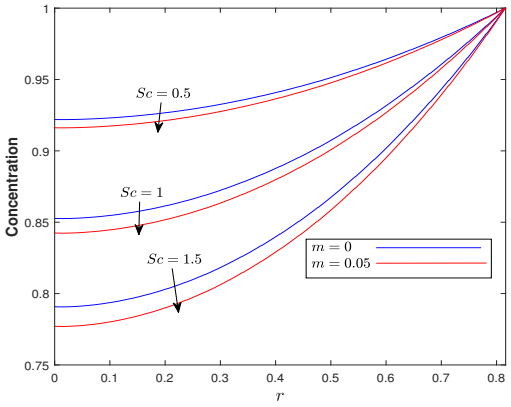

Figure 6.8: Concentration profile for *Sc* and *m*

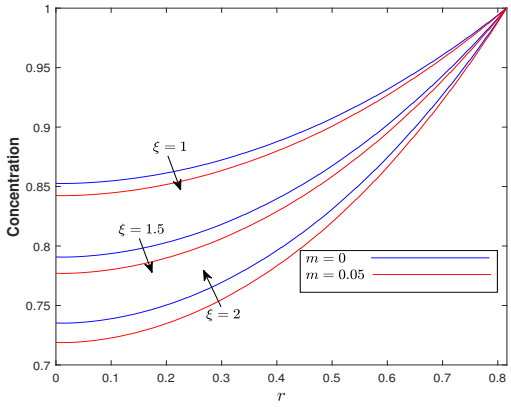

Figure 6.9: Concentration profile for ξ and *m*

nanoparticle volume fraction, a larger-sized nanoparticle is very suitable for flow temperature. Therefore, blood flow temperature can be increased by having large sized nanoparticles in the flow. The findings of this comparative study for nanoparticle size can be adopted by clinical researchers to kill cancer cells and plaque deposition during thermal therapies by inserting large-sized nanoparticles in the artery.

Figures 6.8-6.9 have been developed to analyse the variation in the blood flow concentration profile for various values of the Schmidt number (*Sc*) and chemical reaction parameter (ξ) in the radial direction, respectively. In this investigation, the effect of gold nanoparticles on the fluid concentration has also been examined. The addition of nanoparticles to blood flow reduces the fluid mass diffusion process, as can be seen from equation 6.14. As a result, a decrease in the blood flow concentration profile results from an increase in the volume fraction of nanoparticles. From both, it is also concluded that, the blood flow concentration profile shows a reverse trend with the increase in the values of both the Schmidt number and chemical reaction parameter. This is happening due to a reduction in molecular diffusivity with an increase in values of *Sc* and ξ; therefore, the concentration boundary layer becomes thinner.

According to the above-mentioned significance of nanoparticles in various diseases. Therefore, it is also very important to determine the nanoparticle effects on the wall shear stress (WSS) profile due to the ability of nanoparticles to move across the stenosis. Figure 6.10 shows the results of a numerical computation of the effect of nanoparticle volume fractions and their various sizes on the WSS profile. In this investigation, the WSS profile has been computed only for the stenotic region ($z' = .75$ to $z' = 2.25$). This study reveals that enhancement in the volume percentage of nanoparticles in blood flow shows a significant change in the WSS profile and increases significantly with a change in the volumetric concentration of nanoparticles in the blood. This is owing due to the capability of nanoparticles

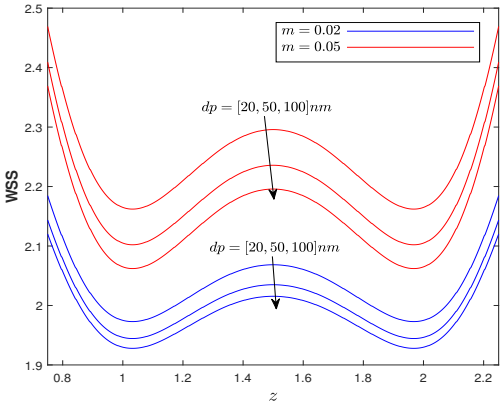

Figure 6.10: WSS profile for m and dp

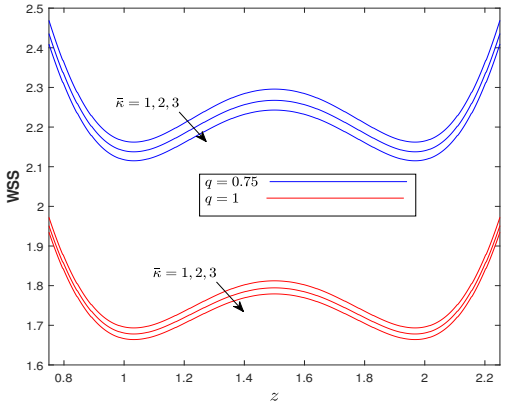

Figure 6.11: WSS profile for $\bar{\kappa}$ and q

to traverse across deposited plaque because, in the absence of nanoparticles, blood cells are not able to penetrate through stenosis. Therefore, when nanoparticles are added to blood, they make a path in the deposited plaque for blood cells; therefore, the flow gets smoother at the arterial wall. This happens because, for a small-sized nanoparticle, it is a little bit easy to cross every deposited stenosis, but sometimes large-sized particles get stuck in stenosis; therefore, they can't make a sufficient path from the stenosis for the blood cells. Thus, this study suggests that the use of small-sized nanoparticles is good for achieving good results for the wall shear stress profile in a stenosed curved arterial flow.

The comparative study of a fluid's Newtonian and non-Newtonian properties on the WSS profile has been presented in the figure 6.11. For that, power-law fluid has been considered, and this computation examination has been performed in terms of flow behaviour index (q). Here, $q < 1$ represents the fluid's shear-thinning (pseudoplastic) property, and $q = 1$ represents the fluid's Newtonian property. It is observed that as the value of flow index behaviour increases, the wall shear stress profile decreases rapidly. In other words, it can be said that assuming pseudoplastic properties of blood in the mathematical modelling will be better for attaining fruitful results for the WSS profile than assuming Newtonian properties of blood. This study also analysed the effect of electro-kinetic width (inverse debye length) on the WSS profile for the stenotic region. A decline in WSS profile is observed with the increase in electro-kinetic width. The obtained results for electro-kinetic width $\bar{\kappa}$ for WSS are in good agreement with the published work of [27].

The comparative fluctuation in the WSS profile for both conditions of the magnetic field, presence ($M \neq 0$) and absence ($M = 0$), along with the curved arterial stenotic height ($\tilde{\delta}$) has been discussed in figure 6.12. A linear decay in the WSS profile has been observed with the increase in stenosis height, which reveals fair agreement with the results of [132, 16]. This investigation has also undertaken a comparison between curved artery ($\varepsilon \neq 0$) and

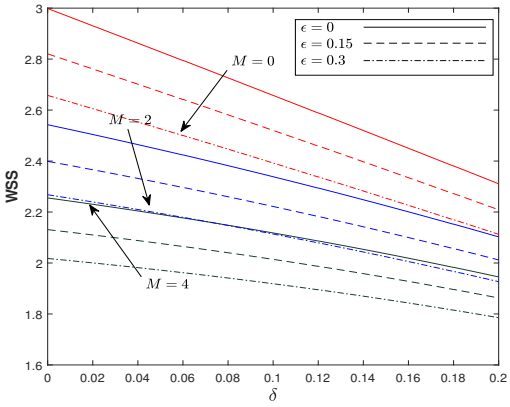

Figure 6.12: WSS profile for M and ε

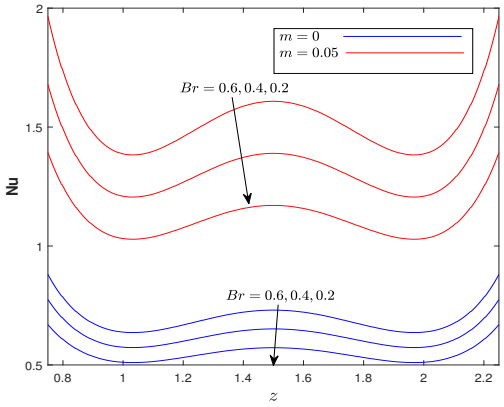

Figure 6.13: Nusselt number for Br and m

straight ($\varepsilon = 0$) conditions. It is concluded that with the increase in the value of arterial curvature, the blood experiences lower shear stress at the wall. Therefore, straight arteries face heavy shear stress due to higher flow velocity compared with curved arteries. The figure also describes that, with the positive improvement in magnetic field intensity, leads to increase Lorentz force power, which retards the flow speed at arterial wall. Therefore, shear stress between fluid layers decreases at arterial wall. According to the results of the curvature analysis, lipid deposition is highly likely to occur in arteries with high curvature.

The importance of the nanoparticle's presence on the heat transfer rate at the arterial wall has been computed numerically for the overlapped stenotic region using the Stones Scheme, and the results are discussed in figure 6.13. From the previous results, it is well known that with the addition of nanoparticles, the blood flow temperature increases. Therefore, in comparison with the absence of gold nanoparticles in blood, the heat transfer rate at the arterial wall increases significantly with the presence of nanoparticles in the flow. The impact of the Brinkmann number on the arterial heat transfer rate has also been discussed. The positive add in the Br value leads to increases in flow temperature due to a significant decay in the heat conduction rate, which was generated by viscous dissipation. Therefore, the blood heat transfer rate increases in the artery as well as its wall due to the boost in blood flow temperature with an increase in Br. Due to the significant increase in arterial wall heat transfer with the addition of nanoparticles, it will be helpful in the development of thermal therapies for clinical researchers to cure stenosis, kill cancer cells, etc. Figure 6.14 shows how important the size of the nanoparticles is for heat transfer at the arterial wall. This study suggests that using large-sized nanoparticles will be useful to increase arterial heat transfer in the clinical healing process. As a result, it is possible to conclude that as nanoparticle size increases, so does heat transfer at the arterial wall enhances.

Figure 6.15 depicts the variation in heat transfer rate for various values of arterial cur-

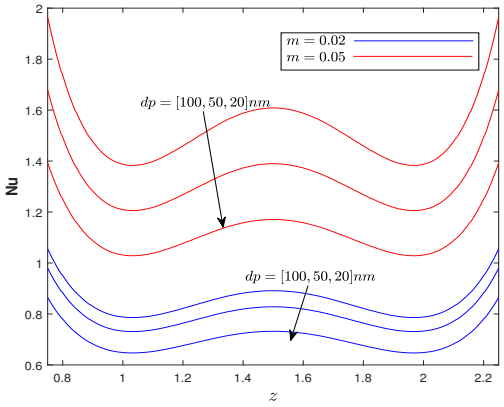

Figure 6.14: Nusselt number for dp and m

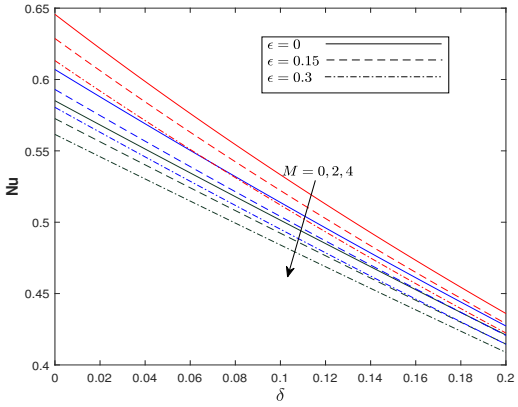

Figure 6.15: Nusselt number for M and ε

vature and magnetic field intensities. This discussion has been conducted with respect to stenosis height. A linear decay in the heat transfer rate profile is observed as stenosis height increases. In other words, it can be concluded that the formation of stenosis (lipid deposition) is responsible for the decay in heat transfer rate at the arterial wall. From the figure, it can be seen that the heat transfer rate decreases by approximately 33% for the artery with a 20% stenosis deposition compared with a healthy artery. A significant decline in arterial wall heat transfer rate has been observed for the increase in values of both arterial curvature and magnetic field intensities. This is because blood flows faster in a straight tube ($\varepsilon = 0$) than in a curved tube ($\varepsilon \neq 0$). Therefore, in curved tubes, the heat transfer rate at the arterial wall diminishes.

Entropy generation is essential to comprehending biological thermodynamics in blood flow in constricted regions of curved arteries because it represents the decrease in quality energy that can't be further utilised to do essential work. Figure 6.16 depicts the variation in unused energy production (entropy) in the radial direction for the different values of Brinkman number (Br). The preceding figures show that the blood flow temperature profile improves with an increase in the value of Br, resulting in greater energy in the flow. With a spike in Br values, a considerable increase in entropy formation is noticed due to the inability of the blood flow to convert the increased energy into useful work. This figure also provides a comparative analysis of the effects of using nanoparticles in blood flow or not using them in terms of entropy production. From the figure, it is noticed that in the absence of nanoparticles, flow generates more entropy in the centre region of the artery due to the high speed of flow there, and that afterward, entropy decreases as blood reaches the wall. Entropy also increases near the arterial wall due to the presence of useful nutrients, proteins, sugars, fats, etc. It is also observed that in the presence of nanoparticles, the entropy production is lower at the centre of the artery than in the rest of the arterial flow region. This

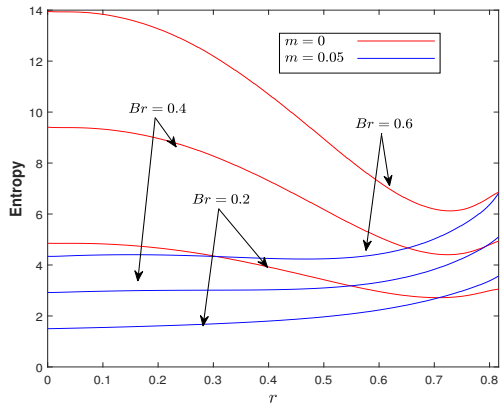

Figure 6.16: Entropy generation for Br and m

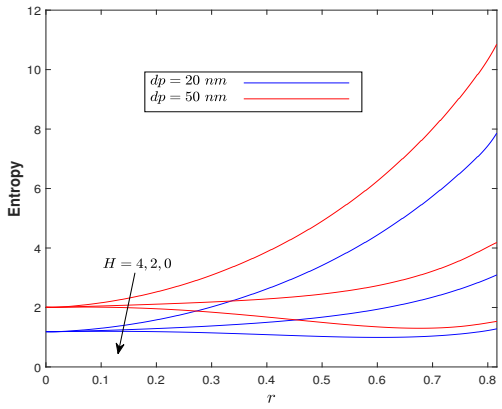

Figure 6.17: Entropy generation for H and dp

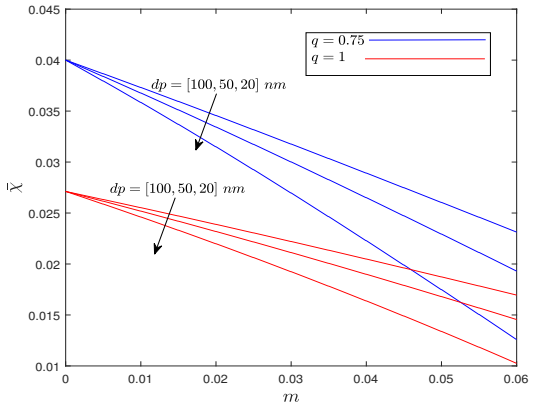

Figure 6.18: Energy conversion efficiency for dp and q

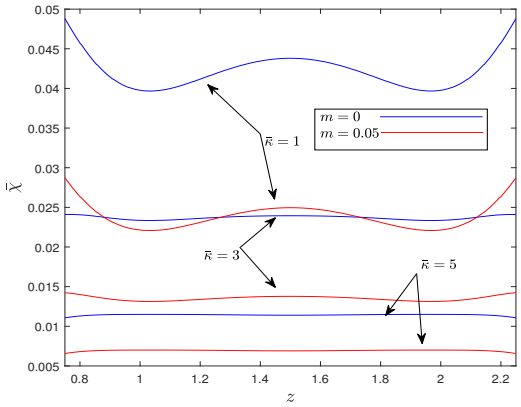

Figure 6.19: Energy conversion efficiency for $\bar{\kappa}$ and m

happens because, with the addition of nanoparticles, the flow velocity decreases; therefore, it generates less energy in the centre region of the artery due to less fluid friction. It is also notable that the flow is smooth near the stenosis in the presence of nanoparticles; therefore, at the near arterial wall, a sudden spike in entropy generation can be easily visualised.

The present comparative study is analysing the importance of nanoparticle size on blood flow, therefore, figure 6.17 illustrates the significance of gold nanoparticle size on the flow efficiency of entropy generation. This figure states that for a fixed volume fraction of nanoparticles, the entropy generation rate increases rapidly with the mixing of large-diameter nanoparticles. This is happen due to an increase in blood flow temperature for the larger-sized nanoparticle, therefore it produces more energy in blood flow. This figure also shows that the flow produced more entropy with the increase in external heating intensity.

The analysis of the conversion efficiency of blood flow mechanical energy into electro-kinetic energy with the different volume fractions of gold nanoparticles has been simulated

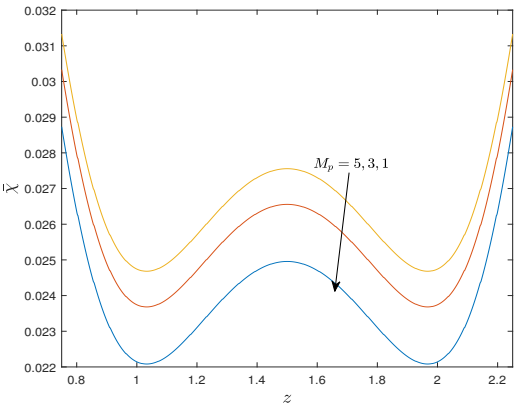

Figure 6.20: Energy conversion efficiency for M_p

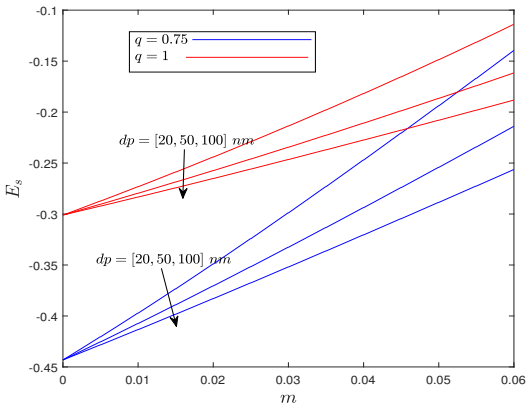

Figure 6.21: Streaming potential for dp and q

numerically and explained in figure 6.18. The figure shows that when a nanoparticle is added to the flow, it reduces the flow's conversion efficiency for converting mechanical and chemical energy into electrokinetic energy. Therefore, the increase in gold nanoparticle volume fraction reflects the sharp decline in the EKEC ($\bar{\chi}$) profile. The obtained relationship between the nanoparticle volume fraction and EKEC is in fairly good agreement with the findings of [145]. This figure also reveals that adding large-sized gold nanoparticles is important for blood flow to enhance its electrokinetic energy conversion efficiency. As a result, it can be concluded that EKEC ($\bar{\chi}$) efficiency increases with an increase in nanoparticle size. It should also be noted that for a higher amount of gold nanoparticles, the decay rate of the EKEC profile is faster for the small sized nanoparticles than for the larger sized nanoparticles.

The fluctuation in EKEC efficiency profile for the whole stenotic region ($0.75 \leq z \leq 2.25$) has been presented in the figures 6.19-6.20. Both figures reveal that EKEC efficiency decreases with an increase in stenosis depth at the arterial wall. Therefore, it can be concluded that the conversion rate of mechanical and chemical energy into electrokinetic energy is higher for the healthy artery than the diseased artery. Figure 6.19, replicates that as the value of $\bar{\kappa}$ increases i.e decrease in EDL thickness, the EKEC efficiency decreases. This is happening because the quantity of charged ions increases with the significant distance from the arterial wall for a large EDL thickness (small $\bar{\kappa}$), which used to counter the surface-charged ions. Therefore, this hike in charged ions increases the flow EKEC efficiency for the small value of $\bar{\kappa}$. The reverse effect on the EKEC efficiency profile has been observed for conduction current (inverse ionic Peclet number). The significant increment in the $\bar{\chi}$ profile with the increases in M_p has been observed, and this variation is depicted in the figure 6.20.

Figure 6.21 illustrates the variation in the streaming potential profile as a function

of gold nanoparticle volume fraction for the various values of nanoparticle size. It is well known that gold nanoparticles have a higher electrical conductivity than blood. When added to the blood, they completely bind up the blood cells and increase their electrical conductivity. Therefore, it can be noted that with the increase in nanoparticle quantity, the electric potential of the fluidic system enhances. As a result, the streaming potential for blood flow increases as the number of nanoparticles increases. On the other hand, this study suggests that the streaming potential profile reflects the reverse effects with the increase in nanoparticle size. In other words, it can be said that the blood electric potential efficiency can be amplified by using small-sized gold nanoparticles. The comparative analysis between assuming blood as pseudoplastic nature or a Newtonian nature has also been presented. It is obtained that when blood's Newtonian properties are considered, the streaming potential is higher than when considering the pseudoplastic fluid properties.

A fascinating phenomenon is to describe blood-trapping flow patterns in an overlapped stenosed curved artery by treating blood as a non-Newtonian fluid (Power-law). This phenomenon is highly important for researching blood flow mechanics in the complex arterial geometries usually associated with stenoses. Understanding these flow traps could help researchers create better treatments for cardiovascular disorders. Under certain circumstances, streamlines in the wave frame separate to catch a bolus that travels at the same pace as the wave. The complete flow trapping pattern for blood in a curved artery for various physical parameters such as gold nanoparticle volume fraction (m), nanoparticle diameter size (dp), arterial curvature (ε), magnetic field intensity (M) and inverse Deybe length (κ) have been described using figures 6.22-6.26. These figures also provide a comparative analysis for various values of these physical parameters. Figure 6.22, which provides the influence of nanoparticle presence in blood flow. From the figure, it can be seen that the size of the bolus reduces when gold nanoparticles are added to the blood flow. This is happening because gold nanoparticles are more viscous than blood; therefore, these particles form bonds with fluid cells and slow the flow speed. Figure 6.23 discusses the importance of nanoparticle size on the flow trapping pattern for a fixed quantity of nanoparticles in blood. The figure concluded that, when large-size nanoparticles are used for any therapy process, they smooth the flow pattern due to an increase in blood flow velocity with an increase in nanoparticle diameter. The main influence of large-sized nanoparticles is seen near the arterial wall rather than in the centre area of the artery. Figures 6.24-6.25, illustrate the comparative effect of arterial curvature and magnetic field intensity on the flow trapping pattern. From the both figures, it is observed that the size of the bolus formation and smoothness in flow trapping decrease with the increase in values of arterial curvature and magnetic field intensity. From these, it can be concluded that, in realistic situations, most of the arteries have a high curvature;

therefore, they have a higher chance for lipid/stenosis deposition due to less smoothness in blood flow. The blood flow trapping pattern for various values of inverse Debye length ($\bar{\kappa}$) has been depicted in figure 6.26. This figure illustrates that to counter the surface charged ions, the quantity of charged ions increases with the increase in EDL thickness. Therefore, flow becomes smoother with the increase in EDL thickness.

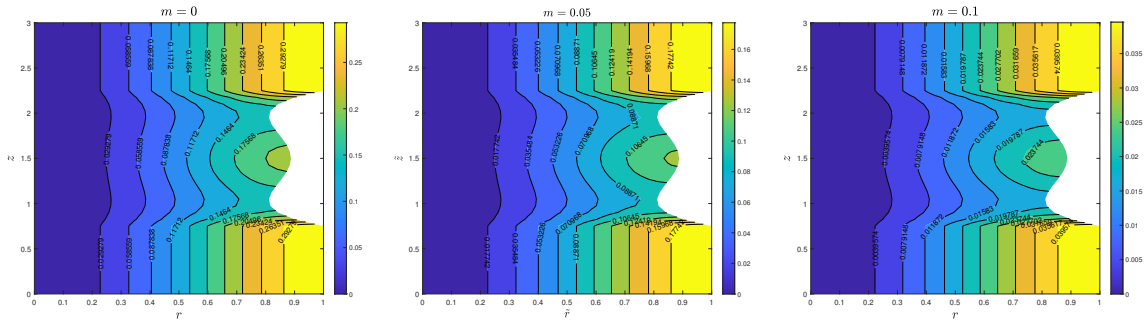

(a) (b) (c)

Figure 6.22: Stream function plot for nanoparticle volume fraction, (a) $m = 0$, (b) $m = .05$, (c) $m = .1$.

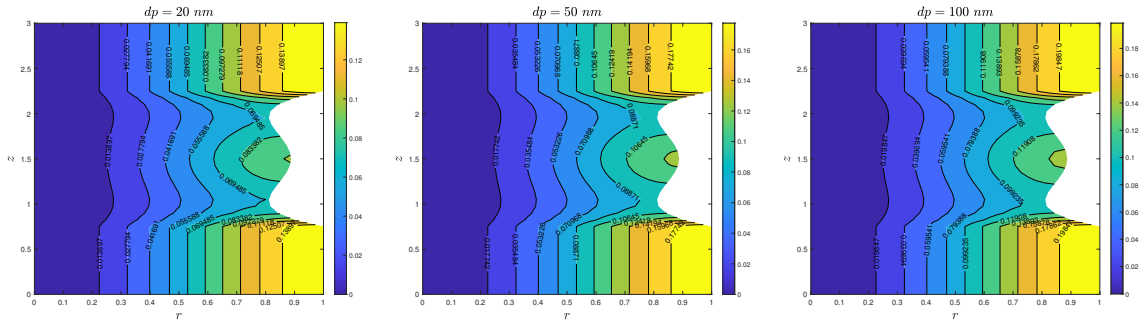

(a) (b) (c)

Figure 6.23: Stream function plot for nanoparticle size, (a) $dp = 20nm$, (b) $dp = 50nm$, (c) $dp = 100nm$.

6.6 Conclusion

A computational examination of blood flow through an overlapped stenotic curved artery has been performed in the presence of gold nanoparticles in the blood flow. To make

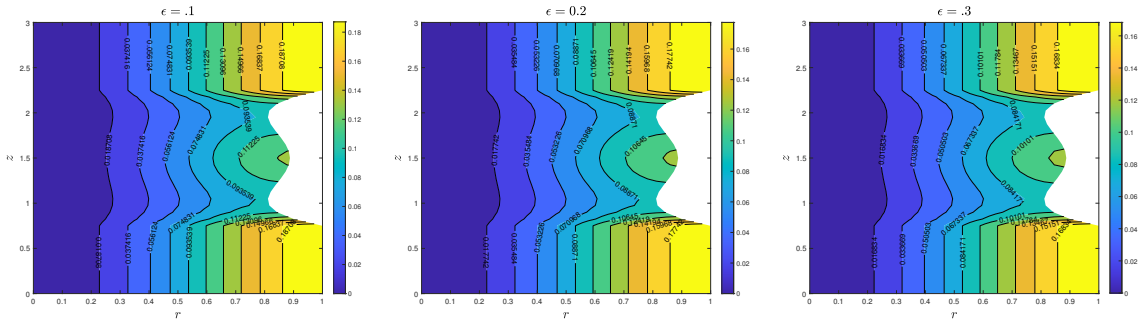

(a) (b) (c)

Figure 6.24: Stream function plot for arterial curvature, (a) $\varepsilon = 0.1$, (b)$\varepsilon = 0.2$, (c) $\varepsilon = 0.3$.

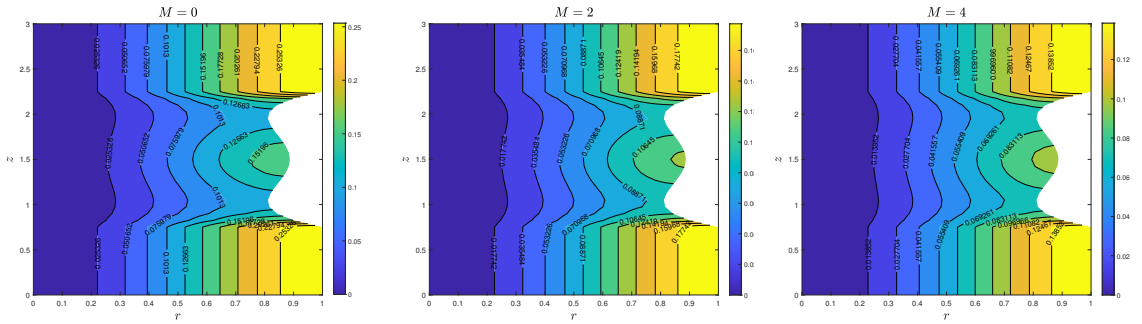

(a) (b) (c)

Figure 6.25: Stream function plot for Magnetic field intensity, (a) $M = 0$, (b)$M = 2$, (c) $M = 4$.

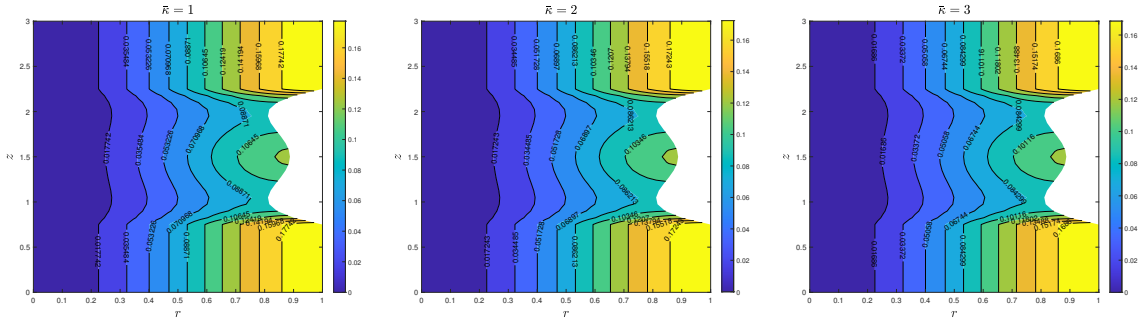

(a) (b) (c)

Figure 6.26: Stream function plot for Inverse of Debye length, (a) $\bar{\kappa} = 1$, (b)$\bar{\kappa} = 2$, (c) $\bar{\kappa} = 3$.

this investigation more plausible, a patient-specific stenosed arterial model and the non-Newtonian fluid (power-law fluid) properties of blood have been taken into account. The effect of nanoparticle size has also been analyzed. The study of electric potential (Poission-Boltzamann equation) is performed, therefore the arterial wall is considered negatively charged. The second-order centeral difference method has been adopted to discretized governing equations, and Stone's strongly implicit approach is used to solve these non-linear discretized equations. The effects of various physical parameters within their feasible range on the fluid velocity, temperature, concentration, EKEC, entropy, WSS, and nusselt number have been studied using "MATLAB" software. Clinical researchers and biologists may use the results of this computational study to forecast endothelial cell damage and plaque deposition in curved arteries with WSS profiles, by which the severity of these conditions can be reduced. In treating stenosis, cancer cells, muscular discomfort and stiffness, etc., employing nanoparticles and external heating sources in blood flow would be advantageous. The following are some noteworthy findings from the current mathematical investigation:

- The blood flows velocity decreases with the addition of gold nanoparticles and reflects a reverse trend with the increase in nanoparticle size.
- The flow velocity becomes high for the thin size of the electric double layer (EDL).
- Adding gold nanoparticles and lipid deposition in blood flow reduces the efficiency of electrokinetic energy conversion (EKEC).
- The electrokinetic energy conversion (EKEC) efficiency increases more quickly with increasing EDL thickness and nanoparticle size.
- The considerable increase in blood entropy production arises whenever viscous heating is boosted, and large-sized nanoparticles are introduced into the flow.
- Arteries with high curvature have a higher possibility for lipid and stenosis deposition due to decay in the wall shear stress and heat transfer rate profile.
- The gold nanoparticles increase the blood temperature and heat transfer across arterial walls; therefore, its use can reduce lipid deposition in CVD treatments.
- The presence of gold nanoparticles reduces the blood mass diffusion process; therefore blood flow concentration profile diminishes.

Chapter 7

Entropy generation analysis for two-phase power-law blood flow through a curved overlapping stenosed artery with induced magnetic field

7.1 Introduction

In western countries, the mortality rate due to cardiovascular diseases (CVD) has grown significantly faster among men and women. The main reason behind this is the deposition of plaque and atherosclerosis inside the artery, which narrows the artery flow diameter, by which a sufficient quantity of blood can't reach organs and tissues. Among doctors, Anigeography is the most common and effective diagnosis approach for CVD. In this treatment process, a small-diameter catheter is inserted into the artery, which removes cholesterol and lipid from inside the artery. Harding et al. [159] performed an experimental study of renal artery stenosis and developed a model, which can differentiate the patient with renal artery narrowing according to their risk. They state that patients with hypertension and congestive heart failure are at the highest risk of renal artery narrowing and angiography is the best and safest option to diagnose these types of disesases. A study to describe the correlation between catheter and artery diameter ratio to avoid the deposition of thrombosis on the catheter wall has been done by Nifong et al. [160]. They found that, if a big-size catheter is inserted into small diameter/length arteries, it may cause deposition of thrombosis and endothelial damage. Jayaraman et al. [161] performed a mathematical investigation of catheter size in the curved artery and stated that keeping the small ratio of catheter and artery radius may increase the success rate of balloon angioplasty. Mekheimer et al. [16] used a catheter at the artery's center to computationally observe the blood flow behavior in overlapped stenosed curved arteries. They discovered numerically that wall shear stress profile and flow velocity both considerably decrease as the catheter radius increases. Further, this study was carried

forward by Ahmed et al. [108], and they studied the blood flow nature in presence of Cu-nanoparticle and ballon-shaped thrombosis (at catheter wall).

Entropy generation is critical for understanding biological thermodynamics in blood flow through constricted regions. It can be quantified as the measure of the chaos in the system. Its application can be seen in various fields related to thermodynamics, such as electronic and information systems, cryogenics, power collection systems, geothermal systems etc. The human physiological system exhibits unpredictable and chaotic behaviour by convective heat into the environment. Bejan [162] investigated entropy generation in heat transfer phenomena and discovered that thermal irreversibility and fluid friction are significant sources of entropy generation. Barnoon et al. [163] considered the two-phase model to simulate the nanofluid flow in the square lid-driven cavity. Zidan et al. [164] explicated the mathematical model to illustrate the entropy generation inside the catheter artery with multiple stenoses and blood thrombus at the centre. Recently, Kumawat et al. [134] deliberate the computational study to determine the amount of entropy generation in curved artery by considering a two-phase flow approach. They reported that plasma creates more energy and entropy than the core region due to availability of beneficial proteins and fat in plasma region.

In the last few decades, the study of the magnetic field effect in biological fluids has attracted the attention of researchers as the human body experience different intensities of the magnetic field in their day-to-day life. There are numerous applications of the magnetic field that can be seen in medical field, such as using magnetic devices for cell separation [165], lowering the bleeding during surgery and cancer therapy [166], nanomagnetic particles in targeting drug delivery [71] and magnetic tracer development etc [167]. Firstly, Issacci et al. [37], numerically discussed the induced magnetic field concept in the curved pipe by considering a toroidal coordinate system. They found the solution in the power series form for both low and intermediate Hartmaan numbers and explained that with enhancing magnetic field intensity, the fluid compression improves near the tube wall in velocity contours. To demonstrate the effect of induced magnetic voltage on arterial and tissue blood flow, a numerical study is investigated by Kinouchi et al. [168]. They stated that magnetic-induced voltage in the aorta can produce electric signals in the heart and its surrounding tissues whenever an arterial wall is supposed to be non-electric in mathematical models. This study also describes that, after a significant limit of magnetic field intensity (10 T), the reduction in blood flow rate becomes significantly small.

Mekheimer et al. [29] conducted an analytical study of an induced magnetic field using a catheter in a tapered overlapped stenosed artery and the results show that axial magnetic

field induction enhances the increase in magnetic field strength and exhibits the reverse nature with magnetic Reynold number. The influence of the Joule effect on the tapered arterial flow in the presence of magnetic nanoparticles has been studied analytically by Bhatti et al. [169]. In this study, the Sutterby fluid model (non-Newtonian) has been considered, and the authors conclude that blood flow temperature enhances with the Joule effect becoming more dominant and that temperature is higher for a diverging arterial wall than the converging arterial wall condition. Recently, Sharma et al. [170] performed a numerical study to understand the effect of magnetic field on the two-phase blood flow through curved stenosed artery for the toroidal coordinate system and revealed that the risk of lipid deposition increases with the rise in curvature and magnetic field strength.

All the above computational and theoretical research work mentioned in the literature documented the flow and heat transport phenomena for blood flow. To the best knowledge of the authors, the power-law fluid model for blood with an induced magnetic field theory in a stenosed curved artery (two-phase blood flow) has not been discussed previously. Therefore, the prime objective of this article is to discuss induced magnetic field, heat and flow phenomena for power-law fluid through the stenosed curved artery (toroidal coordinate system). The nanoparticles (Fe_3O_4) and catheter influences have been utilized. The present investigation considered the blood as non-Newtonian fluid (Power-law fluid) in the core region while showing the Newtonian fluid nature with constant viscosity in the plasma region. The effect of various parameters such as flow behaviour index (q), magnetic field, magnetic Reynold number, Heat source, nanoparticle volume fraction and Brinkman number etc. have been illustrated with the help of graphs. The present investigation discussed the entropy generation concept, which occurs in the blood flow due to heat flux, viscous and Ohmic heating. A central difference scheme of second order [130] has been applied for the discretization of spatial derivatives, and Stone's strongly implicit method [131] is used for solving a system of non-linear equations. Clinical researchers and biologists may use the results of this computational study to forecast endothelial cell damage and plaque deposition in curved arteries with WSS profiles, by which the severity of these conditions can be reduced. In treating stenosis, cancer cells, muscular discomfort and stiffness, etc., employing nanoparticles and external heating sources in blood flow would be advantageous.

7.2 Problem formulation

An unsteady, incompressible flow of blood passing through a finite-length curved artery with elliptic shape stenosis is examined in this study. The two-phase blood flow assumption has been taken into account to make the study more feasible, as considered by [88, 132]. In

the core region, blood is considered non-Newtonian (Power law fluid), while, in the plasma region, blood is considered Newtonian fluid with constant viscosity. In this investigation, blood flow through the curved artery, and the toroidal coordinate system (r,θ,z) have been employed to describe the arterial geometry. The z-axis represent the curved artery axis, and r is taken along the radial direction.

7.2.1 Mathematical formulation of stenosis

The time-dependent overlapped diseased artery section (stenosis) condition has been assumed for both the core and plasma region. $R_1(z,t)$ and $R(z,t)$, represent the radius of the stenotic region for both the core and plasma region, respectively. At center of artery, a small diameter catheter has been introduced and it refers with the notation of $h(z)$. Figure 7.1 present geometry of stenosed curved artery. Numerically formulation of diseases section (stenosis) written as preceding [108]:
Mathematical formulation of plasma region stenosis:

$$R(z,t)=\begin{cases}\left[R_0-\frac{\delta(z-d)}{L_0}\left(11-\frac{94}{3L_0}(z-d)+\frac{32}{L_0^2}(z-d)^2-\frac{32}{3L_0^3}(z-d)^3\right)\right]\Omega(t), & d\le z\le d+\frac{3}{2}L_0\\ R_0\Omega(t) & \text{Rest region,}\end{cases} \tag{7.1}$$

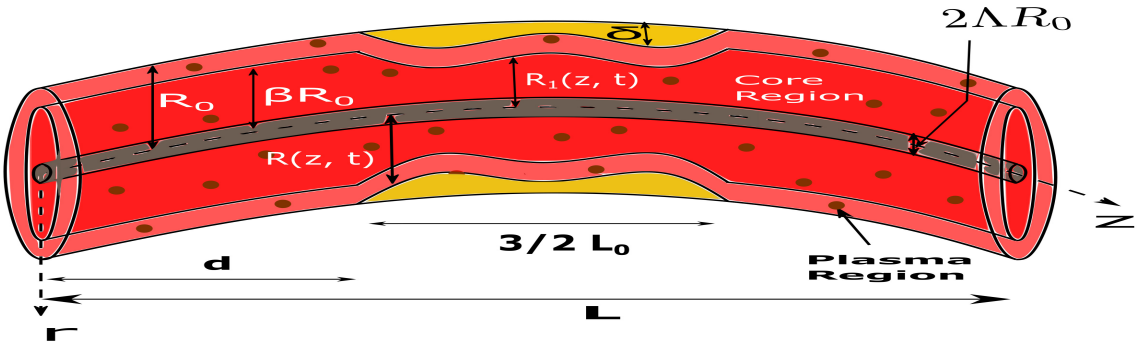

Figure 7.1: Graphical representation of curved artery

Mathematical formulation of core region stenosis:

$$R_1(z,t) = \begin{cases} \left[\beta R_0 - \frac{\delta(z-d)}{L_0}\left(11 - \frac{94}{3L_0}(z-d) + \frac{32}{L_0^2}(z-d)^2 - \frac{32}{3L_0^3}(z-d)^3\right)\right]\Omega(t), & d \le z \le d + \frac{3}{2}L_0 \\ \beta R_0 \Omega(t), & \text{Rest region.} \end{cases} \tag{7.2}$$

$$\Omega(t) = 1 - \eta(\cos(\omega t) - 1)e^{-\eta\omega t}. \tag{7.3}$$

The mathematical formulation of catheter into a curved artery is follows as-

$$h(z) = \Lambda R_0, \qquad \text{at} \qquad 0 \le z \le L. \tag{7.4}$$

where $\frac{3}{2}L_0$ & L represents the length of overlapped diseases section of artery, respectively. δ and d indicate the stenosis maximum height and starting stenosis location, respectively. Λ, represents the radius of catheter.
R_0 radius of healthy curved artery β expresses the ratio in the healthy artery section between core and complete artery radius. η is constant.

7.2.2 Magnetization

The blood in curved artery is considered MHD electrical conducting fluid with the applied uniform external magnetic field $\vec{B}_{ext}$ in the r and θ directions, respectively.
The solenoidal relation represents is

$$\nabla \cdot \vec{B} = 0, \tag{7.5}$$

The equation of conservation of electric charge density is written as-

$$\nabla \cdot \vec{J} = 0, \tag{7.6}$$

The Generalized Ampere's law:

$$\vec{J} = \frac{1}{\mu_e}(\nabla \times \vec{B}), \tag{7.7}$$

where $\vec{J}$, represents the electric current density and components of its are $(\vec{J}_r, \vec{J}_\theta, \vec{J}_z)$, in the (r,θ,z) directions, respectively. μ_e describe the magnetic permeability and B indicates the total magnetic field.
The Ohm's law is written as [24]-

$$\vec{J} = \sigma\left(\vec{E} + \vec{V} \times \vec{B}\right), \tag{7.8}$$

In this study the effect of polarization effect also neglected, therefore $\vec{E} = 0$, is taken zero into whole calculation.
The total magnetic field is the sum of uniform external and induced magnetic field and mathematical formulation of this written as follows-

$$\vec{B} = \vec{B}_{ext} + \vec{B}_i, \tag{7.9}$$

where $\vec{B}$ and $\vec{B}_i$ indicates the total magnetic field and induced magnetic field terms. The (B_r, B_θ, B_z) represents the magnetic field components in the (r, θ, z) directions, respectively.

$$\begin{cases} \vec{B}_{ext} = (B_0 \sin\theta, B_0 \sin\theta, 0), \\ \vec{B}_i = (B_r^i, B_\theta^i, B_z^i). \end{cases}$$

Since intensity of the applied magnetic field is higher than the induced magnetic field, therefore contribution of induced magnetic field terms can be neglected in the r & θ directions respectively.
With the using of above assumptions, the components of the total magnetic field is-

$$\vec{B} = (B_0 \sin\theta, B_0 \sin\theta, B_z^i). \tag{7.10}$$

7.2.3 Governing equations

The Power-law fluid has been considered in the core region and stress component for the this fluid is written as follows [25]-

$$(\tau_c)_{ij} = -P_c I + K\mu_c^{nf} \Omega_f (\phi_c)_{ij}, \tag{7.11}$$

where

$$\Omega_c = \left[(\phi_c)_{rr}^2 + (\phi_c)_{\theta\theta}^2 + (\phi_c)_{zz}^2 + 2\left((\phi_c)_{r\theta}^2 + (\phi_c)_{\theta z}^2 + (\phi_c)_{zr}^2 \right) \right]^{\frac{q-1}{2}},$$

Plasma region blood adopt the Newtonian fluid properties, therefore stress component in this region is written as-

$$(\tau_p)_{ij} = -P_p I + \mu_p^{nf} (\phi_p)_{ij}, \tag{7.12}$$

where, τ_c and τ_p represents the stress tensor for both core and plasma region, while, ϕ_c and ϕ_p, depicts the strain tensor profile in core and plasma region, respectively. K and q, represent the flow consistency and flow behaviour index, respectively. μ_c & μ_p, state the viscosity in core and plasma region.

The governing equations for curved artery can be written as follows [80, 154]-

$$\frac{b}{D}\frac{\partial w}{\partial z}+\frac{\partial u}{\partial r}+\frac{1}{r}\frac{\partial v}{\partial \theta}+\frac{u}{r}+\frac{u\cos\theta-v\sin\theta}{D}=0, \tag{7.13}$$

where, h denotes the radius of curvature.

$$D=b+r\cos\theta$$

Core region ($0<r<R_1(z,t)$**)**
Momentum equations
r-direction:

$$\rho_c^{nf}\left(\frac{\partial u_c}{\partial t}+\frac{bw_c}{D}\frac{\partial u_c}{\partial z}+u_c\frac{\partial u_c}{\partial r}+\frac{v_c}{r}\frac{\partial u_c}{\partial \theta}-\frac{v_c^2}{r}-\frac{w_c^2\cos\theta}{D}\right)=\frac{b}{rD}\left(\frac{\partial}{\partial z}\left(r(\tau_c)_{rz}\right)-\frac{(\tau_c)_{\theta\theta}}{r}\right.$$
$$\left.+\frac{\partial}{\partial r}\left(\frac{Dr(\tau_c)_{rr}}{b}\right)+\frac{\partial}{\partial \theta}\left(\frac{D(\tau_c)_{r\theta}}{b}\right)\right)-\frac{\cos\theta(\tau_c)_{zz}}{D}+\mu_e B_\theta\left(\frac{1}{r}\frac{\partial B_r}{\partial \theta}-\frac{\partial B_\theta}{\partial r}\right)$$
$$+\mu_e B_z\left(\frac{b}{D}\frac{\partial B_r}{\partial z}-\frac{\partial B_z}{\partial r}\right), \tag{7.14}$$

θ direction :

$$\rho_c^{nf}\left(\frac{\partial v_c}{\partial t}+\frac{w_c b}{D}\frac{\partial v_c}{\partial z}+u_c\frac{\partial v_c}{\partial r}+\frac{v_c}{r}\frac{\partial v_c}{\partial \theta}+\frac{u_c v_c}{r}+\frac{w_c^2\sin\theta}{D}\right)=\frac{b}{rD}\left(\frac{\partial}{\partial z}\left(r(\tau_c)_{\theta z}\right)+\frac{(\tau_c)_{r\theta}}{r}\right.$$
$$\left.+\frac{\partial}{\partial r}\left(\frac{Dr(\tau_c)_{r\theta}}{b}\right)+\frac{\partial}{\partial \theta}\left(\frac{D(\tau_c)_{\theta\theta}}{b}\right)\right)+\frac{\sin\theta(\tau_c)_{zz}}{D}+\mu_e B_r\left(\frac{\partial B_\theta}{\partial r}-\frac{1}{r}\frac{\partial B_r}{\partial \theta}\right)$$
$$+\mu_e B_z\left(\frac{b}{D}\frac{\partial B_\theta}{\partial z}-\frac{1}{r}\frac{\partial B_z}{\partial \theta}\right), \tag{7.15}$$

z direction :

$$\rho_c^{nf}\left(\frac{\partial w_c}{\partial t}+\frac{u_c w_c\cos\theta}{D}+\frac{w_c b}{D}\frac{\partial w_c}{\partial z}+u_c\frac{\partial w_c}{\partial r}-\frac{v_c w_c\sin\theta}{D}+\frac{v_c}{r}\frac{\partial w_c}{\partial \theta}\right)=\frac{b}{rD}\left(\frac{\partial}{\partial z}\left(r(\tau_c)_{zz}\right)\right.$$
$$\left.+\frac{\partial}{\partial r}\left(\frac{Dr(\tau_c)_{rz}}{b}\right)+\frac{\partial}{\partial \theta}\left(\frac{D(\tau_c)_{\theta z}}{b}\right)\right)+\frac{\cos\theta\ (\tau_c)_{rz}}{D}-\frac{\sin\theta(\tau_c)_{z\theta}}{D}+\mu_e B_r\left(\frac{\partial B_z}{\partial r}-\frac{b}{D}\frac{\partial B_r}{\partial z}\right)$$
$$+\mu_e B_\theta\left(\frac{1}{r}\frac{\partial B_z}{\partial \theta}-\frac{b}{D}\frac{\partial B_\theta}{\partial z}\right), \tag{7.16}$$

Energy equation :

$$\rho_c^{nf}\bar{C}_c^{nf}\left(\frac{\partial T_c}{\partial t}+u_c\frac{\partial T_c}{\partial r}+\frac{v_c}{r}\frac{\partial T_c}{\partial \theta}+\frac{w_c b}{D}\frac{\partial T_c}{\partial z}\right)=K_c^{nf}\left(\frac{\partial^2 T_c}{\partial r^2}+\frac{1}{r}\frac{\partial T_c}{\partial r}+\frac{b^2}{D^2}\frac{\partial^2 T_c}{\partial z^2}+\frac{\cos\theta}{D}\frac{\partial T_c}{\partial r}\right.$$
$$\left.-\frac{\sin\theta}{rD}\frac{\partial T_c}{\partial \theta}+\frac{1}{r^2}\frac{\partial^2 T_c}{\partial \theta^2}\right)+Q_c+F_c+\frac{\vec{J}\cdot\vec{J}}{\sigma^{nf}}, \tag{7.17}$$

Axial-induced magnetic field

$$\left(\frac{\partial B_z}{\partial t}+u_c\frac{\partial B_z}{\partial r}+\frac{v_c}{r}\frac{\partial B_z}{\partial \theta}+\frac{w_c b}{D}\frac{\partial B_z}{\partial z}\right)=\frac{1}{\sigma^{nf}\mu_e}\left(\frac{\partial^2 B_z}{\partial r^2}+\frac{1}{r}\frac{\partial B_z}{\partial r}+\frac{b^2}{D^2}\frac{\partial^2 B_z}{\partial z^2}+\frac{\cos\theta}{D}\frac{\partial B_z}{\partial r}\right.$$
$$\left.-\frac{\sin\theta}{rD}\frac{\partial B_z}{\partial \theta}+\frac{1}{r^2}\frac{\partial^2 B_z}{\partial \theta^2}\right)+B_r\frac{\partial w_c}{\partial r}+\frac{B_\theta}{r}\frac{\partial w_c}{\partial \theta}+\frac{bB_z}{D}\frac{\partial w_c}{\partial z}, \tag{7.18}$$

Here, F_c denotes the viscous dissipation and its mathematical expression for blood flow of core region is given in equation 7.19-

$$F_c=2^{\frac{q-1}{2}}\mu_c^{nf}K\left[(\phi_c)_{rr}^2+(\phi_c)_{\theta\theta}^2+(\phi_c)_{zz}^2+2\left((\phi_c)_{r\theta}^2+(\phi_c)_{\theta z}^2+(\phi_c)_{zr}^2\right)\right]^q. \tag{7.19}$$

Where, u_c, v_c, w_c represents the dimensional form of velocity components for core region in r,θ,z directions, respectively. Here, T_c, Q_c indicates the dimensional form of blood flow temperature, applied heating source for the core region blood flow. The superscript $(^{nf})$ indicates the properties of nanofluid.

Plasma region i.e. $R_1(z,t) < r < R(z,t)$

Momentum equations-

r-direction :

$$\rho_p^{nf}\left(\frac{\partial u_p}{\partial t}+\frac{bw_p}{D}\frac{\partial u_p}{\partial z}+u_p\frac{\partial u_p}{\partial r}+\frac{v_p}{r}\frac{\partial u_p}{\partial \theta}-\frac{v_p^2}{r}-\frac{w_p^2\cos\theta}{D}\right)=\frac{b}{rD}\left(\frac{\partial}{\partial z}\left(r(\tau_p)_{rz}\right)\frac{(\tau_p)_{\theta\theta}}{r}\right.$$
$$\left.+\frac{\partial}{\partial r}\left(\frac{Dr(\tau_p)_{rr}}{b}\right)+\frac{\partial}{\partial \theta}\left(\frac{D(\tau_p)_{r\theta}}{b}\right)\right)--\frac{\cos\theta(\tau_p)_{zz}}{D}+\mu_e B_\theta\left(\frac{1}{r}\frac{\partial B_r}{\partial \theta}-\frac{\partial B_\theta}{\partial r}\right)$$
$$+\mu_e B_z\left(\frac{b}{D}\frac{\partial B_r}{\partial z}-\frac{\partial B_z}{\partial r}\right), \tag{7.20}$$

θ- direction :

$$\rho_p^{nf}\left(\frac{\partial v_p}{\partial t}+\frac{w_p b}{D}\frac{\partial v_p}{\partial z}+u_p\frac{\partial v_p}{\partial r}+\frac{v_p}{r}\frac{\partial v_p}{\partial \theta}+\frac{u_p v_p}{r}+\frac{w_p^2\sin\theta}{D}\right)=\frac{b}{rD}\left(\frac{\partial}{\partial z}\left(r(\tau_p)_{\theta z}\right)+\frac{(\tau_p)_{r\theta}}{r}\right.$$
$$\left.+\frac{\partial}{\partial r}\left(\frac{Dr(\tau_p)_{r\theta}}{b}\right)+\frac{\partial}{\partial \theta}\left(\frac{D(\tau_p)_{\theta\theta}}{b}\right)\right)+\frac{\sin\theta(\tau_p)_{zz}}{D}+\mu_e B_r\left(\frac{\partial B_\theta}{\partial r}-\frac{1}{r}\frac{\partial B_r}{\partial \theta}\right)$$
$$+\mu_e B_z\left(\frac{b}{D}\frac{\partial B_\theta}{\partial z}-\frac{1}{r}\frac{\partial B_z}{\partial \theta}\right), \tag{7.21}$$

$\bar{z}$- direction :

$$\rho_p^{nf}\left(\frac{\partial w_p}{\partial t}+\frac{u_p w_p\cos\theta}{D}+\frac{w_p b}{D}\frac{\partial w_p}{\partial z}+u_p\frac{\partial w_p}{\partial r}-\frac{v_p w_p\sin\theta}{D}+\frac{v_p}{r}\frac{\partial w_p}{\partial \theta}\right)=\frac{b}{rD}\left(\frac{\partial}{\partial z}\left(r(\tau_p)_{zz}\right)\right.$$
$$\left.+\frac{\partial}{\partial r}\left(\frac{Dr(\tau_p)_{rz}}{b}\right)+\frac{\partial}{\partial \theta}\left(\frac{D(\tau_p)_{\theta z}}{b}\right)\right)+\frac{\cos\theta\ (\tau_p)_{rz}}{D}-\frac{\sin\theta(\tau_p)_{z\theta}}{D}+\mu_e B_r\left(\frac{\partial B_z}{\partial r}-\frac{b}{D}\frac{\partial B_r}{\partial z}\right)$$
$$+\mu_e B_\theta\left(\frac{1}{r}\frac{\partial B_z}{\partial \theta}-\frac{b}{D}\frac{\partial B_\theta}{\partial z}\right), \tag{7.22}$$

Energy equation :

$$\rho_p^{nf}\bar{C}_p^{nf}\left(\frac{\partial T_p}{\partial t}+u_p\frac{\partial T_p}{\partial r}+\frac{v_p}{r}\frac{\partial T_p}{\partial \theta}+\frac{w_p b}{D}\frac{\partial T_p}{\partial z}\right)=K_p^{nf}\left(\frac{\partial^2 T_p}{\partial r^2}+\frac{1}{r}\frac{\partial T_p}{\partial r}+\frac{b^2}{D^2}\frac{\partial^2 T_p}{\partial z^2}+\frac{\cos\theta}{D}\frac{\partial T_p}{\partial r}\right.$$
$$\left.-\frac{\sin\theta}{rD}\frac{\partial T_p}{\partial \theta}+\frac{1}{r^2}\frac{\partial^2 T_p}{\partial \theta^2}\right)+Q_p+F_p+\frac{\vec{J}\cdot\vec{J}}{\sigma^{nf}}, \tag{7.23}$$

Axial-induced magnetic field

$$\left(\frac{\partial B_z}{\partial t}+u_p\frac{\partial B_z}{\partial r}+\frac{v_p}{r}\frac{\partial B_z}{\partial \theta}+\frac{w_p b}{D}\frac{\partial B_z}{\partial z}\right)=\frac{1}{\sigma^{nf}\mu_e}\left(\frac{\partial^2 B_z}{\partial r^2}+\frac{1}{r}\frac{\partial B_z}{\partial r}+\frac{b^2}{D^2}\frac{\partial^2 B_z}{\partial z^2}+\frac{\cos\theta}{D}\frac{\partial B_z}{\partial r}\right.$$
$$\left.-\frac{\sin\theta}{rD}\frac{\partial B_z}{\partial \theta}+\frac{1}{r^2}\frac{\partial^2 B_z}{\partial \theta^2}\right)+B_r\frac{\partial w_p}{\partial r}+\frac{B_\theta}{r}\frac{\partial w_p}{\partial \theta}+\frac{bB_z}{D}\frac{\partial w_p}{\partial z}, \tag{7.24}$$

Here, F_p denotes the viscous dissipation and its mathematical expression for blood flow of plasma region is given in equation 7.25-

$$F_p=2\mu_p^{nf}\left[(\phi_p)_{rr}^2+(\phi_p)_{\theta\theta}^2+(\phi_p)_{zz}^2+2\left((\phi_p)_{r\theta}^2+(\phi_p)_{\theta z}^2+(\phi_p)_{zr}^2\right)\right]. \tag{7.25}$$

Where, u_p, v_p, w_p represents the dimensional form of velocity components for plasma region in r, θ, z directions, respectively. T_p, Q_p demonstrate the dimensional form of plasma region temperature and external heating source, respectively.

The above-mentioned dimensional form of governing and stenosis geometry equations will

be transformed into the non-dimensional form using the following non-dimensional parameters mentioned in the table 7.1.

Table 7.1: Dimensionless parameter

$r = R_0 r'$	$z = L_0 z'$	$\theta = \theta'$	$\omega = \frac{u_0}{L_0}\omega'$	$L = L_0 L'$
$d = L_0 d'$	$t = \frac{L_0}{u_0} t'$	$R = R_0 R'$	$R_1 = R_0 R_1'$	$u_c = \frac{\delta u_0}{L_0} u_c'$
$v_c = \frac{\delta u_0}{L_0} v_c'$	$\bar{w}_c = u_0 w_c'$	$u_p = \frac{\delta u_0}{L_0} u_p'$	$v_p = \frac{\delta u_0}{L_0} v_p'$	$w_p = u_0 w_p'$
$P_c = \frac{u_0 L_0 \mu_p}{R_0^2} P_c'$	$P_p = \frac{u_0 L_0 \mu_p}{R_0^2} P_p'$	$\alpha = \frac{R_0}{L_0}$	$T_c' = \frac{T_c - T_0}{T_w - T_0}$	$T_p' = \frac{T_p - T_0}{T_w - T_0}$
$\delta^* = \frac{\delta}{R_0}$	$Rm = \frac{1}{\sigma_p \mu_e R_0 u_0}$	$H = \frac{Q_p R_0^2}{(\bar{T}_0 - T_w) K_p}$	$M = \frac{\sigma B_0^2 \mu_e}{\rho_p u_0^2}$	$\rho_0 = \frac{\rho_p}{\rho_c}$
$Re = \frac{\rho_p R_0 u_0}{\mu_p}$	$Q_0 = \frac{Q_p}{Q_c}$	$\varepsilon = \frac{R_0}{b}$	$K_0 = \frac{K_p}{K_c}$	$Ec = \frac{u_0^2}{\bar{C}_p (T_0 - T_w)}$
$Pr = \frac{\bar{C}_p \mu_p}{K_p}$	$Br = EcPr$			

The dimensionless form of stenosis is considered as [134].
The table mentioned above 7.1 has been utilized to transform governing equations into dimensionless forms. Then after fully developed flow, mild stenosis ($\delta^* << 1$), and $O(1) = \alpha = \frac{R_0}{L_0}$ [31] conditions have been employed to simplify dimensionless governing equations. The simplified form of the governing equations are written as

Core region

$$\frac{\partial P_c'}{\partial r'} = 0, \tag{7.26}$$

$$\frac{\partial P_c'}{\partial \theta'} = 0, \tag{7.27}$$

$$\begin{aligned}\frac{1}{\bar{D}}\frac{\partial P_c'}{\partial z'} &= \frac{\Omega_c^*}{\mu_0 (1-m)^{2.5}}\left(\frac{\partial^2 w_c'}{\partial r'^2} + \frac{1}{r'}\frac{\partial w_c'}{\partial r'} + \frac{1}{r'^2}\frac{\partial^2 w_c'}{\partial \theta'^2} - \frac{\varepsilon^2 w_c'}{\bar{D}^2} + \frac{\varepsilon}{\bar{D}}\left[\cos\theta' \frac{\partial w_c'}{\partial r'} - \frac{\sin\theta'}{r'}\frac{\partial w_c'}{\partial \theta'}\right]\right) \\ &+ \frac{1}{\mu_0 (1-m)^{2.5}}\left(\frac{\partial w_c'}{\partial r'} - \frac{\varepsilon w_c' \cos\theta'}{\bar{D}}\right)\frac{\partial \Omega_c^*}{\partial r} + \frac{1}{\mu_0 (1-m)^{2.5}}\left(\frac{1}{r'^2}\frac{\partial w_c'}{\partial \theta'} + \frac{\varepsilon w_c' \sin\theta'}{r' \bar{D}}\right)\frac{\partial \Omega_c^*}{\partial \theta'} \\ &+ ReM\left(B_{r'}' \frac{\partial B_{z'}'}{\partial r'} + \frac{B_{\theta'}'}{r'}\frac{\partial B_{z'}'}{\partial \theta'}\right)\end{aligned} \tag{7.28}$$

$$\begin{aligned}&\frac{\partial^2 T_c'}{\partial r'^2} + \frac{1}{r'}\frac{\partial T_c'}{\partial r'} + \frac{\varepsilon \cos\theta'}{\bar{D}}\frac{\partial T_c'}{\partial r'} - \frac{\varepsilon \sin\theta'}{r' \bar{D}}\frac{\partial T_c'}{\partial \theta'} + \frac{1}{r'^2}\frac{\partial^2 T_c'}{\partial \theta'^2} + k_0 \frac{K^b}{K^{nf}}\left(\frac{H}{Q_0} + Br\, F_c'\right) \\ &+ k_0 \frac{K^b}{K^{nf}}\frac{\sigma^b}{\sigma^{nf}}\frac{M\, Re\, Br}{R_m}\left(\left(\frac{1}{r'}\frac{\partial B_{z'}'}{\partial \theta'}\right)^2 + \left(\frac{\partial B_{z'}'}{\partial r'}\right)^2 + \left(\frac{1}{r'}\frac{\partial B_{r'}'}{\partial \theta'}\right)^2\right) = 0,\end{aligned} \tag{7.29}$$

$$\frac{\partial^2 B'_{z'}}{\partial r'^2}+\frac{1}{r'}\frac{\partial B'_{z'}}{\partial r'}+\frac{\varepsilon\cos\theta'}{\bar{D}}\frac{\partial B'_{z'}}{\partial r'}-\frac{\varepsilon\sin\theta'}{r'\bar{D}}\frac{\partial B'_{z'}}{\partial \theta'}+\frac{1}{r'^2}\frac{\partial^2 B'_{z'}}{\partial \theta'^2}+\frac{1}{R_m}\frac{\sigma^b}{\sigma^{nf}}\left(B'_{r'}\frac{\partial w'_c}{\partial r'}+\frac{B'_{\theta'}}{r'}\frac{\partial w'_c}{\partial \theta'}\right)=0, \tag{7.30}$$

where

$$\bar{D}=1+\varepsilon r'\cos\theta',$$

$$\Omega_c^*=2^{\frac{q-1}{2}}\left[\left(-\frac{\varepsilon w'_c\cos\theta'}{\bar{D}}+\frac{\partial w'_c}{\partial r'}\right)^2+\left(\frac{\varepsilon w'_c\sin\theta'}{\bar{D}}+\frac{1}{r'}\frac{\partial w'_c}{\partial \theta'}\right)^2\right]^{\frac{q-1}{2}},$$

$$F'_c=\frac{2^{q-1}}{(1-m)^{2.5}}\left[\left(-\frac{\varepsilon w'_c\cos\theta'}{\bar{D}}+\frac{\partial w'_c}{\partial r'}\right)^2+\left(\frac{\varepsilon w'_c\sin\theta'}{\bar{D}}+\frac{1}{r'}\frac{\partial w'_c}{\partial \theta'}\right)^2\right]^{q},$$

Plasma region

$$\frac{\partial P'_p}{\partial r'}=0, \tag{7.31}$$

$$\frac{\partial P'_p}{\partial \theta'}=0, \tag{7.32}$$

$$\frac{1}{\bar{D}}\frac{\partial P'_p}{\partial z'}=\frac{1}{(1-m)^{2.5}}\left(\frac{\partial^2 w'_p}{\partial r'^2}+\frac{1}{r'}\frac{\partial w'_p}{\partial r'}+\frac{1}{r'^2}\frac{\partial^2 w'_p}{\partial \theta'^2}-\frac{\varepsilon^2 w'_p}{\bar{D}^2}+\frac{\varepsilon}{\bar{D}}\left[\cos\theta'\frac{\partial w'_p}{\partial r'}-\frac{\sin\theta'}{r'}\frac{\partial w'_p}{\partial \theta'}\right]\right)$$
$$+ReM\left(B'_{r'}\frac{\partial B'_{z'}}{\partial r'}+\frac{B'_{\theta'}}{r'}\frac{\partial B'_{z'}}{\partial \theta'}\right), \tag{7.33}$$

$$\frac{\partial^2 T'_p}{\partial r'^2}+\frac{1}{r'}\frac{\partial T'_p}{\partial r'}+\frac{\varepsilon\cos\theta'}{\bar{D}}\frac{\partial T'_p}{\partial r'}-\frac{\varepsilon\sin\theta'}{r'\bar{D}}\frac{\partial T'_p}{\partial \theta'}+\frac{1}{r'^2}\frac{\partial^2 T'_p}{\partial \theta'^2}+\frac{K^b}{K^{nf}}\left(F'_pBr+H\right)+\frac{K^b}{K^{nf}}\frac{\sigma^b}{\sigma^{nf}}$$
$$\frac{M\ Re\ Br}{R_m}\left(\left(\frac{1}{r'}\frac{\partial B'_{z'}}{\partial \theta'}\right)^2+\left(\frac{\partial B'_{z'}}{\partial r'}\right)^2+\left(\frac{1}{r'}\frac{\partial B'_{r'}}{\partial \theta'}\right)^2\right)=0, \tag{7.34}$$

$$\frac{\partial^2 B'_{z'}}{\partial r'^2}+\frac{1}{r'}\frac{\partial B'_{z'}}{\partial r'}+\frac{\varepsilon\cos\theta'}{\bar{D}}\frac{\partial B'_{z'}}{\partial r'}-\frac{\varepsilon\sin\theta'}{r'\bar{D}}\frac{\partial B'_{z'}}{\partial \theta'}+\frac{1}{r'^2}\frac{\partial^2 B'_{z'}}{\partial \theta'^2}+\frac{1}{R_m}\frac{\sigma^b}{\sigma^{nf}}\left(B'_{r'}\frac{\partial w'_p}{\partial r'}+\frac{B'_{\theta'}}{r'}\frac{\partial w'_p}{\partial \theta'}\right)=0, \tag{7.35}$$

where

$$F'_p=\frac{2}{(1-m)^{2.5}}\left[\left(-\frac{\varepsilon w'_c\cos\theta'}{\bar{D}}+\frac{\partial w'_c}{\partial r'}\right)^2+\left(\frac{\varepsilon w'_c\sin\theta'}{\bar{D}}+\frac{1}{r'}\frac{\partial w'_c}{\partial \theta'}\right)^2\right].$$

Mathematical formulation of dimensionless boundary condition is mentioned in equation 7.36

$$\begin{cases} w'_c = 0, \quad T'_c = 1, \quad B'_{z'} = 0, & \text{at} \quad r' = h'(z'), \\ w'_c = w'_p, \quad T'_c = T'_p, & \text{at} \quad r' = R'_1(z',t'), \\ \tau'_c = \tau'_p, \quad \frac{\partial T'_c}{\partial r'} = \frac{\partial T'_p}{\partial r'}, & \text{at} \quad r' = R'_1(z',t'), \\ w'_p = 0, \quad T'_p = 0, \quad B'_{z'} = 0, & \text{at} \quad r' = R'(z',t'), \\ \frac{\partial w'_c}{\partial \theta'} = 0, \quad \frac{\partial T'_c}{\partial \theta'} = 0, \quad \frac{\partial B'_{z'}}{\partial \theta'} = 0, & \text{at} \quad \theta' = 0 \quad \& \quad \theta' = \pi, \\ \frac{\partial w'_p}{\partial \theta'} = 0, \quad \frac{\partial T'_p}{\partial \theta'} = 0, & \text{at} \quad \theta' = 0 \quad \& \quad \theta' = \pi. \end{cases} \tag{7.36}$$

7.3 Procedure of solution

With the use of the aforementioned non-dimensional boundary conditions, a computational process to obtain a solution of highly nonlinear PDEs (7.26)-(7.35) (dimensionless governing equations) has been performed using the Finite difference method [130].
The central difference formula of the second order has been employed to discretize the spatial derivatives in the uniform mesh size for the domain $[0 \;\; R'(z',t')] \times [o \;\; \pi]$. Discritization of derivatives can be performed using given process in equation 7.37.-

$$\begin{cases} \frac{\partial G_s}{\partial \tilde{r}} = \frac{(G_s)_{x+1,y} - (G_s)_{x-1,y}}{2\Delta r}, \\ \\ \frac{\partial G_s}{\partial \tilde{\Theta}} = \frac{(G_s)_{x,y+1} - (G_s)_{x,y-1}}{2\Delta \Theta}, \\ \\ \frac{\partial^2 G_s}{\partial \tilde{r}^2} = \frac{(G_s)_{x+1,y} - 2(G_s)_{x,y} + (G_s)_{x-1,y}}{(\Delta r)^2}, \\ \\ \frac{\partial^2 G_s}{\partial \tilde{\Theta}^2} = \frac{(G_s)_{x,y+1} - 2(G_s)_{x,y} + (G_s)_{x,y-1}}{(\Delta \Theta)^2}. \end{cases} \tag{7.37}$$

when blood flows in core region , then s will be consider for core region and if blood flows in plasma region , then s will be consider for plasma region.
In the present mathematical study Δr and $\Delta\theta$ represents the uniform mesh size in r and θ direction, respectively. The mathematical expression for Δr and $\Delta\theta$ are as follows- $\Delta r = \frac{R'(z',t')}{L_1 - 1}$ and $\Delta\theta = \frac{\pi}{L_2 - 1}$.
where L_1 and L_2 denotes the total number of mesh points in r & θ directions.

According to published research work [135, 136], due to pumping of heart, blood flow reflect the its pulsatile nature of flow. Therefore, the mathematical formulation of pressure gradient can be written as

$$\frac{\partial P_c'}{\partial z'} = \frac{\partial P_p'}{\partial z'} = P_0 e^{-\eta \omega t'}. \tag{7.38}$$

Since, the above-mentioned non-dimensional governing equations non-dimensional governing equations can be reduced into 2D nonlinear PDEs. With the discretization of these PDEs, a five-band system of nonlinear algebraic equations have been obtained.

$$AX = bb.$$

where A is coefficient matrix.
The system is highly nonlinear; therefore, solving it using the Gaussian elimination method is not feasible.
Stone's strongly implicit method [131] has been employed to solve the system of nonlinear equations. A global nodal index k has been assigned for every mesh point.

$$k = (y-1) * L_1 + x.$$

After allocating the global nodal index, the coefficient matrix [A] will be factorized into lower and upper triangular matrices. After factorized matrix [A], the residual will be computed. Further, backward and forward substitution will be employed to find a solution. This iterative process is repeated until the residual becomes lesser than the desirable error tolerance. Stone's method is used for inner iteration, then Newton's scheme is applied for outer iteration. For each inner and outer iteration, the absolute error tolerance of 10^{-6} is taken into account.

$$[A]X = [L][U]X = bb.$$

After numerically computed the velocity and temperature in core and plasma regions some important physical phenomena such as wall shear stress, Nusselt number, flow rate profiles can be calculated using numerical velocity and temperature profile data.
The Flow rate Q, frictional impedance λ and wall shear stress τ_w can be calculated as follows-

$$Q = \int_0^{R'(z',t')} \int_0^{\pi} r' w' dr' d\theta',$$

$$Q = \int_0^{R_1'(z',t')} \int_0^{\pi} r' w_c'(r', \theta', z') dr' d\theta' + \int_{R_1'(z',t')}^{R'(z',t')} \int_0^{\pi} r' w_p'(r', \theta', z') dr' d\theta', \tag{7.39}$$

$$\lambda = \frac{\int_0^L (-\frac{\partial P'}{\partial z'}) dz'}{Q}, \tag{7.40}$$

$$\tau_w = -\frac{\mu^{nf}}{\mu^b} 2^{\frac{q-1}{2}} \left[\frac{\partial w'_p}{\partial r'}\right]_{r'=R'(z',t')}, \tag{7.41}$$

The Mathematical calculation of Nusselt number can performed as -

$$Nu = -\frac{K^{nf}}{K^b} \left[\frac{\partial T'_p}{\partial r'}\right]_{r'=R'(z',t')}. \tag{7.42}$$

7.4 Entropy Generation and irreversibility

Entropy generation is critical for understanding biological thermodynamics in blood flow through constricted regions. By considering above mentioned conditions, the general form of entropy generation can be written as follows-

$$E^{gen} = \underbrace{\frac{K^{nf}(\nabla T)^2}{T_w^2}}_{\text{Thermal irreversibility}} + \underbrace{\frac{F}{T_w}}_{\text{Fluid friction irrversibility}} + \underbrace{\frac{\vec{J}\cdot\vec{J}}{T_w \sigma^{nf}}}_{\text{Joule heating irrversibility}}, \tag{7.43}$$

The following are the mathematical formulae to estimate the amount of entropy generation in both regions:

$$\bar{E}_c^{gen} = \frac{K_c^{nf}}{T_w^2}\left[\left(\frac{\partial T_c}{\partial r}\right)^2 + \left(\frac{1}{r}\frac{\partial T_c}{\partial \theta}\right)^2 + \left(\frac{b}{D}\frac{\partial T_c}{\partial z}\right)^2\right] + \frac{F_c}{T_w} + \frac{\vec{J}\cdot\vec{J}}{T_w\sigma^{nf}}, \tag{7.44}$$

$$\bar{E}_p^{gen} = \frac{K_p^{nf}}{T_w^2}\left[\left(\frac{\partial T_p}{\partial r}\right)^2 + \left(\frac{1}{r}\frac{\partial T_p}{\partial \theta}\right)^2 + \left(\frac{b}{D}\frac{\partial T_p}{\partial z}\right)^2\right] + \frac{F_p}{T_p} + \frac{\vec{J}\cdot\vec{J}}{T_w\sigma^{nf}}, \tag{7.45}$$

where, E_c^{gen} and E_p^{gen} denotes the entropy generation in core and plasma region, respectively. The equations 7.44 & 7.45, will be converted in their dimensionless form by using table 7.1 and considering above mentioned flow conditions-

$$E_c'^{gen} = \frac{E_c^{gen}}{E},$$

$$E_p'^{gen} = \frac{E_p^{gen}}{E},$$

$$E_c'^{gen} = \frac{K^{nf}}{K^b k_0}\left[\left(\frac{\partial T_c'}{\partial r'}\right)^2 + \left(\frac{1}{r'}\frac{\partial T_c'}{\partial \theta'}\right)^2\right] + \frac{Br}{A\mu_0}F_c' + \frac{\sigma^b}{\sigma^{nf}}\frac{BrMRe}{AR_m}\left[\left(\frac{1}{r'}\frac{\partial B_{z'}'}{\partial \theta'}\right)^2 + \left(\frac{\partial B_{z'}'}{\partial r'}\right)^2 + \frac{\cos^2\theta'}{r'^2}\right], \tag{7.46}$$

$$E_p{}^{gen} = \frac{K^{nf}}{K^b}\left[\left(\frac{\partial T_p'}{\partial r'}\right)^2 + \left(\frac{1}{r'}\frac{\partial T_p'}{\partial \theta'}\right)^2\right] + \frac{Br}{A}F_p' + \frac{\sigma^b}{\sigma^{nf}}\frac{BrMRe}{AR_m}\left[\left(\frac{1}{r'}\frac{\partial B_{z'}'}{\partial \theta'}\right)^2 + \left(\frac{\partial B_{z'}'}{\partial r'}\right)^2 + \frac{\cos^2\theta'}{r'^2}\right], \tag{7.47}$$

where $E = \frac{K_p(T_0-T_w)^2}{T_w^2 R_0^2}$, $A = \frac{T_0-T_w}{T_w}$.

7.5 Results and Discussion

A computational investigation has been introduced to visualize the impact of several parameters, including power-law fluid, Magnetic field, heat source parameter etc., on the two-phase blood flow behaviour and its temperature profile in a curved artery. The impact of nanoparticles (Fe_3O_4) has been considered in the blood flow. The calculation of entropy generation and axial-induced magnetic field in the overlapped diseases section of the artery has been performed by considering the two-phase fluid approach. The present investigation considered the blood as non-Newtonian fluid (Power-law fluid) in the core region while showing the Newtonian fluid nature with constant viscosity in the plasma region. The plasma region is considered the $10-15\%$ of the whole artery region. In this analysis, the assumption of a cylinder shape catheter in the middle of a curved artery has been made to make this investigation more realistic. A central difference scheme of second-order has been applied for the discretization of spatial derivatives, and Stone's strongly implicit method is used for solving a system of non-linear equations. The flow domain is discretized uniformly for both (r') & (θ') directions.. The step size in both directions is assumed $\Delta r = \Delta\theta = 0.001$. The error tolerance for both inner and outer iterations is set up 10^{-6}. The MATLAB codes for Stones scheme have been developed to demonstrate the graphical behaviour of various physical quantities such as velocity, temperature, WSS, induced magnetic field, heat transfer rate and entropy generation etc. Table 1 provides the default values for different physical parameters

and their source of references. Table 7.2 represents the nanoparticles thermo-physical properties and their formulations.

The validation of the present investigation has been performed to validate utilized a mathematical model and applied numerical method consistency. This validation is made with the published work of [80], and it is discussed in figure 7.2. In this validation process, some assumptions in the present study have been neglected, such as magnetic field, induced magnetic field, blood is considered to single-phase fluid, and the consideration of catheter's ballon shape is ignored in the [80] observation. This validation process has been performed by considering the perturbation technique for [80] work and Stone's method for the present work. Figure 7.2 replicate the fair agreement between the present study and [80] observations. The thermophysical properties of blood and nanoparticle (Fe_3O_4) has been written in the table 7.3.

Table 7.2: Thermophysical parameters of nanofluid [158, 171]

Properties	Mathematical expression for nanofluid
Viscosity	$\mu^{nf} = \frac{\mu^b}{(1-m)^{2.5}}$
Density	$\rho^{nf} = (1-m)\rho^b + m\rho^s$
Heat Capacity	$(\rho C_p)^{nf} = (1-m)(\rho C_p)^b + m(\rho C_p)^s$
Thermal Conductivity	$\frac{K^{nf}}{K^b} = \frac{K^s+(m-1)K^b-(m-1)m(K^b-K^s)}{K^s+(m-1)K^b+m(K^b-K^s)}$
Electrical Conductivity	$\frac{\sigma^{nf}}{\sigma^b} = \frac{\sigma^s+(m-1)\sigma^b-(m-1)m(\sigma^b-\sigma^s)}{\sigma^s+(m-1)\sigma^b+m(\sigma^b-\sigma^s)}$
Thermal Expansion Coefficient	$\gamma^{nf} = (1-m)\gamma^b + m\gamma^s$

Table 7.3: Thermophysical properties of blood and nanoparticle (Fe_3O_4) [172, 171]

Thermophysical parameter	Blood	Fe_3O_4
Density	1063	5200
Heat Capacity	3594	670
Thermal Conductivity	0.492	6
Electrical Conductivity	0.667	2.5×10^4
Thermal Expansion Coefficient	1.8×10^{-6}	1.3×10^{-5}

The Blood behave a like biomagnetic fluid due to the existence of cell membrane, a complex interaction of proteins and hemoglobin in it. The main protein present in RBCs is hemoglobin, which contains iron oxide particles and it has the ability to bind oxygen atoms. The molecular structure system of hemoglobin is significantly influenced by the amount of

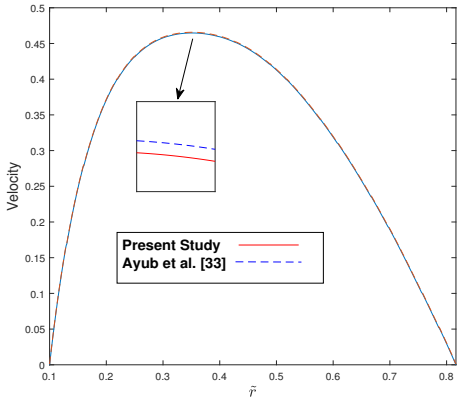

Figure 7.2: Validation of present investigation

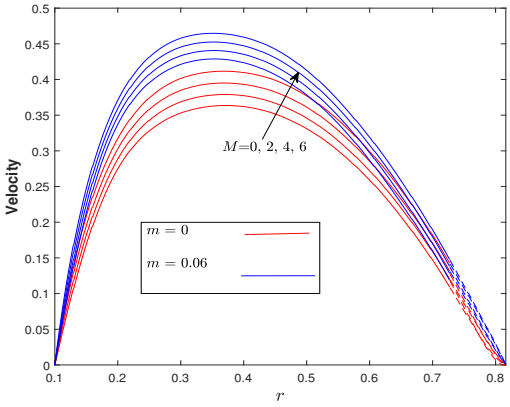

Figure 7.3: Velocity profile for M and m

iron oxide available in RBC. Therefore, being motivated by the blood's magnetic properties, a comparative computational study has been performed to illustrate the significance of magnetic field on stenosed curved artery. The variation in two-phase blood flow velocity has been depicted in the figure 7.3. This study demonstrates that a strong electromotive field arises from applying an external magnetic field, perpendicular to the direction of blood flow. As a result, a force known as Lorentz force appears in the flow and lowers the flow speed. It can also be noticed that in the absence of a magnetic field, blood flow velocity remains higher. Clinical researchers can adopt the present study's magnetic field theory findings and reduce blood loss during surgeries by enhancing magnetic field intensity. A comparison research to describe the significance of nanoparticle (Iron oxide Fe_3O_4) on the stenosed artery has also been conducted using the above-mentioned figure. This figures demonstrate that the blood's thermal characteristics and temperature are improved when nanoparticles are injected into the flow. As a result, stenosed arteries experience a considerable increase in blood flow velocity. Since nanoparticles can traverse through the stenosis and mend artery walls, which blood cells are unable to do, these characteristics of nanoparticles are exploited in the treatment of arteriosclerosis. Also, nanoparticles are used to diagnose various severe diseases such as cancer cells, fungal infections, hypercholesterolemia, etc. [147]

A comparative study for blood has been performed by assuming core region blood as Newtonian and non-Newtonian. This study is conducted in the form of a flow behaviour index (q) and depicted in figure 7.4. Here $q < 1$ represents the behaviour of blood as Pseudoplastic (shear-thinning), $q = 1$ Newtonian and $q > 1$ exhibits the Diltant (shear-thickening) behaviour. The figure reveals that, as the value of the flow behaviour increases, the blood flow velocity decreases in the whole artery. Therefore, for a realistic situation assuming blood as pseudoplastic nature will be good for the mathematical model to get an accurate result to predict disease conditions. According to the published literature [26] and from the

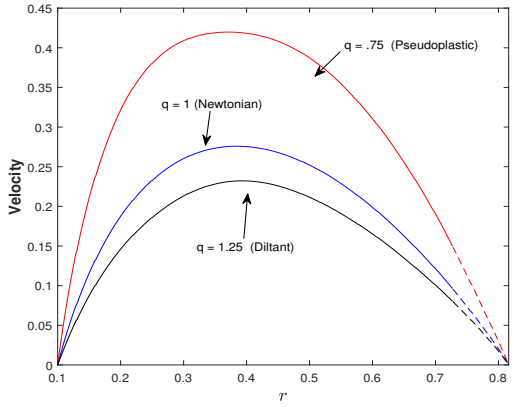

Figure 7.4: Velocity profile with q

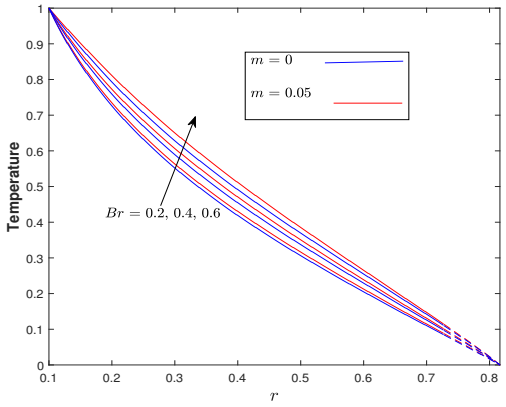

Figure 7.5: Temperature profile with Br and m

obtained fruitful results for flow velocity, the authors decided to consider the Pseudoplastic ($q < 1$) behaviour of blood whenever blood is assumed non-Newtonian in this computational research work.

The investigation of the Brinkman number (Br) is a fascinating topic because it differentiates the dominance between viscous heating and external heating in terms of the generation of heat conduction in the flow. Brinkman number is the heat conduction ratio by viscous heating and external heating. Therefore, figure 7.5 has been developed to analyze the impact of the Brinkman number on the blood flow through a stenosed curved artery. This study is also suggested that at a fixed external heating source, a positive increment in the value of Br, reflects the decrease in heat conduction rate due to internal viscous heating; therefore, the blood temperature in the artery rises significantly. It is also noted that at the catheter wall, the flow generates more heat due to high friction between the catheter wall and blood molecules; as a result, at the catheter wall, the temperature difference is very high in comparison with the flow in the rest arterial area. The ability of the nanoparticle to travel across the stenosis, based on the literature review, makes the nanoparticle particularly useful in diagnosing atherosclerosis. Therefore, this study also presents a comparative study to demonstrate the impact of nanoparticles (Iron oxide Fe_3O_4) on the temperature profile. The findings for nanoparticle state that the blood flow temperature enhances with the addition of nanoparticles in flow. The temperature differential between the absence and presence of nanoparticles in the flow grows with an increase in Br values, as seen in the picture.

A motivation to investigate the external heating source significance is taken from the above-mentioned thermal heating applications in thermal therapies to cure serious diseases such as synovial bursa, muscle pain, cancer tumor and bones hilling, etc. Therefore, the change in blood temperature for the different heating source intensities in nanoparticles presence has been calculated numerically and discussed in figure 7.6. This study reveals

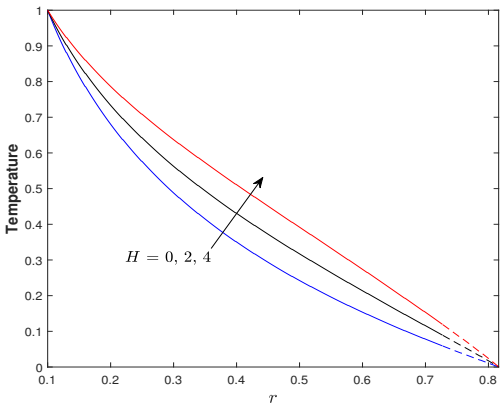

Figure 7.6: Temperature profile with H

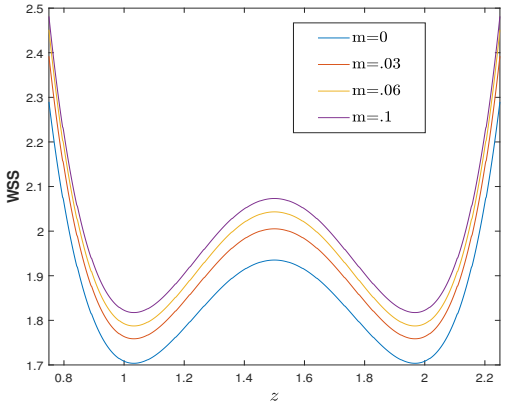

Figure 7.7: WSS profile for nanoparticle volume fraction m

that, with the increase in value of the external heat source (H), the heat conduction between arterial blood and environmental heating increases, and resultant blood temperature rises in the whole artery. Biologists and clinical researchers can adopt present study results of heat source in the therapeutic process like killing cancer and damaged cells, tumors, atherosclerosis, muscle pain etc. Sometimes, insertion of nanoparticles during thermal treatment of various diseases causes in rises rapid of blood flow velocity , which might be harmful; therefore, performing these therapies under the tool using the magnetic field concept will be helpful [137] to control flow velocity.

In the biomechanics field, analysis of the wall shear stress profile is crucial to understand the flow behavior in the diseases (stenosis) segment. Therefore, figure 7.7, illustrates the variation in the wall shear stress profile of blood flow in the entire overlapped stenotic region for curved artery. This figure also described the importance of nanoparticles in terms of volume fraction (m) on the arterial wall stress profile. In this study, the stenotic region has been considered to span $\tilde{z} = .75$ to $\tilde{z} = 2.25$. As per the previous results of nanoparticle fraction on velocity profile in the present study that with the increase of nanoparticle concentration in blood, the flow gets smoother, therefore at the arterial wall, the WSS profile also enhances. Hence it can be concluded that flow disturbance reduces in the stenosis region with the injection of nanoparticles in blood flow. Additionally, for a more accurate estimate of the WSS profile, Figure 7.7 also compares the nanoparticle's presence conditions (presence $m \neq 0$ and absence $m = 0$). This study also suggested that a certain amount of nanoparticle concentration is helpful for reducing flow disturbance after it does not affect so much flow, which can be seen from the results for $m = 0.06$ and $m = .1$.

The variation in the WSS profile for the different intensities of magnetic Reynold number (Rm) and flow index behaviour (q) has been calculated numerically using Stone's scheme

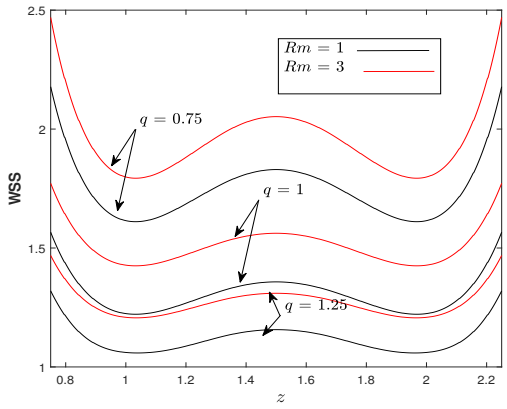

Figure 7.8: WSS profile for q and Rm

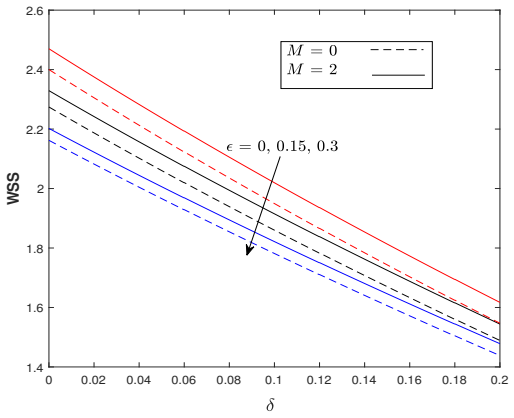

Figure 7.9: WSS profile for M and ε

and discussed through the figure 7.8. The figure indicates that for all numeric values of magnetic Reynold number (Rm) and flow nature index (q), the WSS profile reflects both diminishing and increasing behaviour according to stenosis height nature. The present study performed a comparative analysis among all three flow nature conditions (Pseudoplastic ($q < 1$), Newtonian ($q = 1$) and Diltant ($q > 1$)) to make this research more realistic. The comparison concluded that WSS is higher when blood is assumed pseudoplastic fluid in mathematical modelling than Newtonian and Diltant fluid. This study also asserts that, with the positive enhancement in magnetic Reynold number, the blood flow gets smoother at the arterial wall, which leads to an increment in the WSS profile in the entire stenotic region. The results of the current computational work agree with [93], which claims that vascular segments and arteries with lower WSS are more likely to have lipid accumulation and stenosis.

The comparative fluctuation in the WSS profile for both conditions of the magnetic field, presence ($M \neq 0$) and absence ($M = 0$), along with the curved arterial stenotic height ($\tilde{\delta}$) has been discussed in figure 7.9. A linear decay in the WSS profile has been observed with the increase in stenosis height, which reveals fair agreement with the results of [132, 16]. This investigation has also undertaken a comparison between curved artery ($\varepsilon \neq 0$) and straight ($\varepsilon = 0$) conditions. It is concluded that with the increase in the value of arterial curvature, the blood experiences lower shear stress at the wall. Therefore, straight arteries face heavy shear stress due to higher flow velocity compared with curved arteries. The figure also describes that, with the positive improvement in magnetic field intensity, the shear stress profile increases due to an enhancement in the blood flow temperature with Joule heating.

The influence of superparamagnetic iron oxide nanoparticles (Fe_3O_4) on the heat transfer rate (Nu) across the arterial wall in terms of volume fraction (m) has been obtained

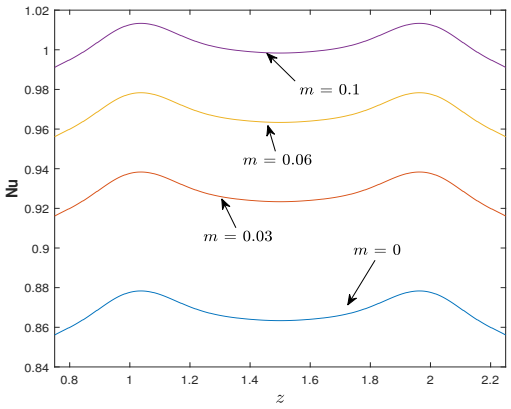

Figure 7.10: Nusselt number for m

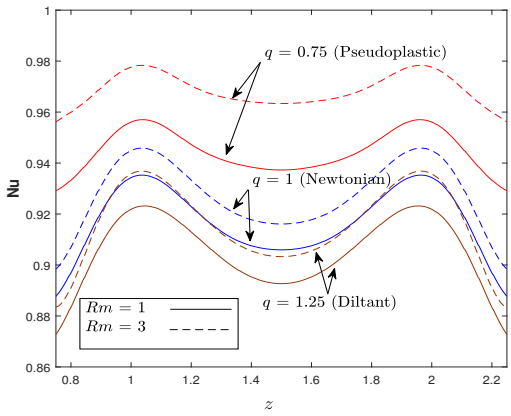

Figure 7.11: Nusselt number for q and Rm

numerically using Stone's scheme, and conclusions are discussed in figure 7.10. The heat transfer rate is assessed in the entire overlapped stenosed region. This study state that the flow temperature hikes with the addition of nanoparticles; therefore, a positive rise in the heat transfer across the arterial wall happens with an increase in nanoparticle volume fraction (m). In this investigation, pure blood condition (i.e. nanoparticle absence $m = 0$) has also been considered, and a notable rise in heat transfer has been observed. It is also identified that as the amount of nanoparticles in the blood increases, the variation in Nu profile decreases. A comparative study has been made to elucidate the importance of choosing pseudoplastic fluid as blood in the modelling. Therefore figure 7.11 has been developed to explain to analyze the flow behaviour index (q) effect on the heat transfer profile at the arterial wall. The figure reveals that the heat transfer rate decays with the positive add in the value of q, i.e. the heat transfer rate is higher when blood is considered the pseudoplastic fluid ($q < 1$) than Newtonian ($q = 1$) and Dilatnt ($q > 1$) fluid. This investigation also discusses the magnetic Reynold number (Rm) effect, which is arisen due to the magnetic induction equation in blood flow and states that heat transfer at arterial wall enhances with the positive increase in value of Rm.

The importance of the magnetic field strength (M) and arterial curvature (ε) on the heat transfer rate at the interface of the wall have been simulated using Stone's method and illustrated with the help of the figure 7.12. The discussion of heat transfer has been performed for the maximum stenosis height (δ^*), and observed that as the size (height) of stenosis increases, the heat transfer rate also enhances at the arterial wall. This investigation also noticed that the heat transfer through the arterial wall is higher for the straight (circular,$\varepsilon = 0$) artery. Therefore, as the arterial curvature increases, the heat transfer across the wall diminishes significantly. The increase in magnetic field intensity leads to an increase in the blood flow temperature, and due to this, viscous heating also increases. As a result, the heat

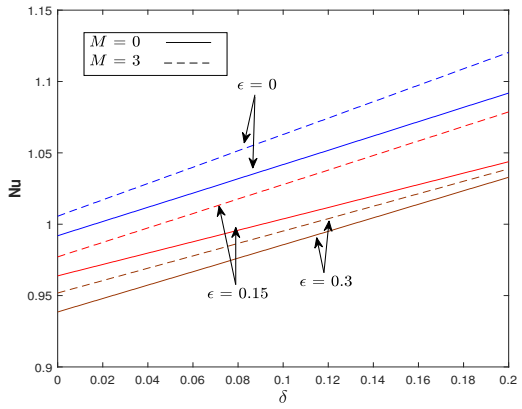

Figure 7.12: Nusselt number for ε and M

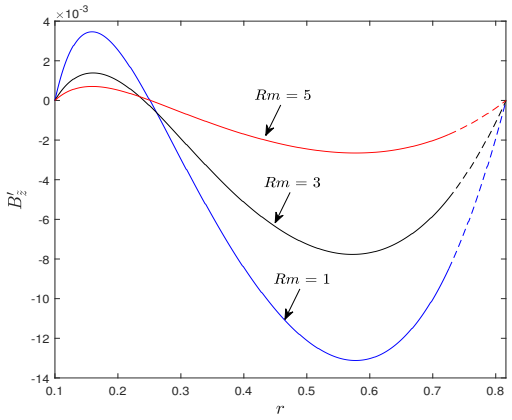

Figure 7.13: Induced magnetic field for Rm

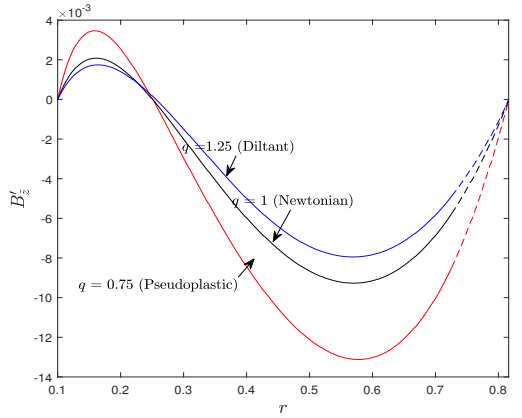

Figure 7.14: Induced magnetic field for q

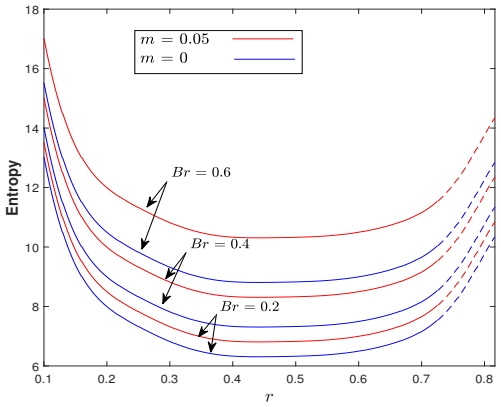

Figure 7.15: Entropy generation for Br and m

transfer rate at the arterial wall also reflects the rising profile with the increased magnetic field intensity. The obtained relation between Nusselt number and stenosis height reflects fair agreement with the published research [173]. They state that higher heat transfer can disturb the flow and its temperature profile.

The variation in the axial-induced magnetic field for the various values of physical parameters magnetic Reynold number (Rm) and flow behaviour index (q) in the radial direction have been discussed graphically and depicted in the figures 7.13-7.14. From both figures, it can be seen that, near the catheter wall, firstly axial-induced magnetic field ($B'_{z'}$) increases; after that, as blood flows towards the arterial wall, it shows the opposite behaviour. The obtained profile ($B'_{z'}$) behaviour is in fair agreement with the published work [29] of blood flow in the presence of the catheter in the middle of artery. The parabolic profile for the axial-induced magnetic field is obtained in both upper (positive) and lower (negative) regions. Figure 7.13-7.14 states that, at the catheter wall, with the increase in value of magnetic Reynold number (Rm), the ($B'_{z'}$) profile increases and reflects the opposite behaviour with enhance in

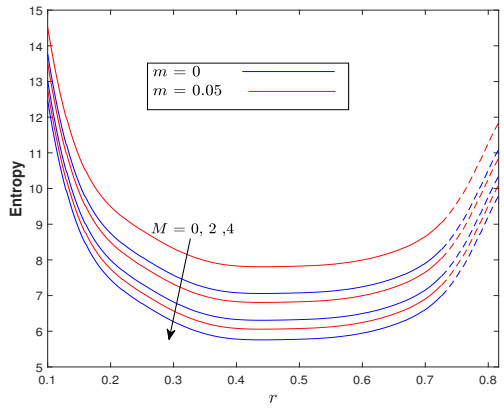

Figure 7.16: Entropy generation for M and m

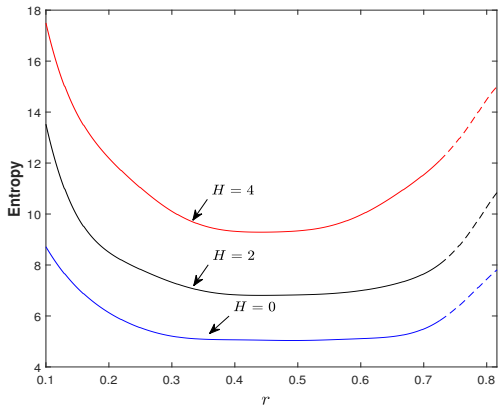

Figure 7.17: Entropy generation for H

the value of flow behaviour index (q) after that shows opposite behaviour as flow reaches toward the arterial wall.

Entropy generation is critical for understanding biological thermodynamics in blood flow through constricted regions because entropy generation indicates the reduction in quality energy which further can not use in work. The variation of entropy generation profile in an overlapped stenosed curved artery with the help of different values of Brinkman number (Br) has been discussed in figure 7.15. The above figure shows that the viscous heating between blood molecules increases significantly with the positive add in the value of Br. This happens because, at fixed external heating, the heat conduction rate due to viscous dissipation decreases significantly; therefore, arterial blood flow temperature rises when it flows in a curved artery. As a result, blood generates more energy due to a rise in viscous heating with Br, but due to a sudden hike in quality energy, most energy is unavailable for work. It can also be seen that due to high surface friction at the catheter wall, flow produces more entropy, and as blood flows away from the catheter, the bulk of generated energy is used for work; therefore, entropy production decreases at mid-region between the catheter and arterial wall. It can be concluded that entropy production increases with the rise in frictional heating. Figure 7.15, also presents the comparative analysis for the use of nanoparticles in blood flow. This study state that with the addition of nanoparticles in blood flow, the flow temperature rise; therefore, entropy also increases in the blood flow.

The figures 7.16-7.17 are developed to elucidate the impact of the magnetic field (M) and external heating source (H) on the entropy generation profile for the overlapped stenosed curved artery. In this investigation, the core region of blood's properties is considered as pseudoplastic fluid. The above-mentioned figures reflect that the amount of unusable energy (entropy) increases rapidly in the plasma region and near the arterial wall. This occurs due to the presence of nutrients, ions, sugar, fat, and essential proteins like albumin and

fibrinolytic protein in the plasma region, as well as the significant heat transfer that occurs across the arterial wall. Therefore it generates more energy in the plasma region, most of which is not usable for work. As a result, the plasma region experiences a sudden surge in entropy creation compared to the core region. The importance of the external applied magnetic field on the entropy generation profile has been discussed in figure 7.16. From the figure, it is observed that, with the increased magnetic field intensity, the retarding force known as Lorentz force acts perpendicular to the flow direction; therefore, flow velocity as well as energy generation reduces. As a result, entropy production decays with the enhancing magnetic field intensity. A decrement in entropy generation variation is observed between the nanoparticle's presence ($m \neq 0$) and absence conditions ($m = 0$) with a positive addition in the value of M. Figure 7.17 reveals that as value of the external heating source (H) increases, it generates more energy due to a rise in flow temperature. Resultant, entropy production also increases in blood flow. Due to becoming flow smoother at the mid-region ($.35 < \tilde{r} < .58$) of one side of the artery, it can also be seen that in this region, the entropy production becomes almost stable.

Blood flow trapping in a stenosed curved artery by considering blood as pseudoplastic fluid is an exciting phenomenon to describe flow patterns. Under certain situations, streamlines in the wave frame separate to catch a bolus that travels at the same pace as the wave. Trapping is the production of an internally circulating bolus of fluid by a closed streamline. The wave transports a bolus, which is defined as a volume of fluid bordered by closed streamlines in the wave frame. The figures 7.18-7.20 illustrate the comparative study of fluid flowing patterns for various values of physical parameters such as Fe_3O_4 nanoparticle volume fraction (m), arterial curvature (ε) and magnetic field intensity (M). In this analysis, the assumption of a cylinder shape catheter in the middle of a curved artery has been made to make this investigation more realistic. Figure 7.18 discussed a comparative analysis of nanoparticle presence in blood flow. According to this figure, a rise in the bolus size of maximum velocity in the overlapping stenosis zone increases with the increase in nanoparticle volume. This is due to the fact that nanoparticles (Fe_3O_4) are more thermally conductive than blood. When nanoparticles are injected into the bloodstream to treat critical illnesses such as stenosis deposition, cancer, muscular discomfort, and so on, they improve blood thermal conductivity by combining with the blood. As a consequence, the temperature of the blood flow increases dramatically. Therefore blood velocity and bolus size, which use for trapping flow situations, also enhance significantly. Figures 7.19-7.20, indicate the importance of various values of arterial curvature (ε) and magnetic field intensity (M) on the blood flow trapping phenomena. From both figures, it is observed that the bolus size, which describes the flow trapping, decays with the increase in value of both parameters ε and M.

By making the artery more curved, we can conclude that flow velocity decreases, and the fear of stenosis deposition rises significantly.

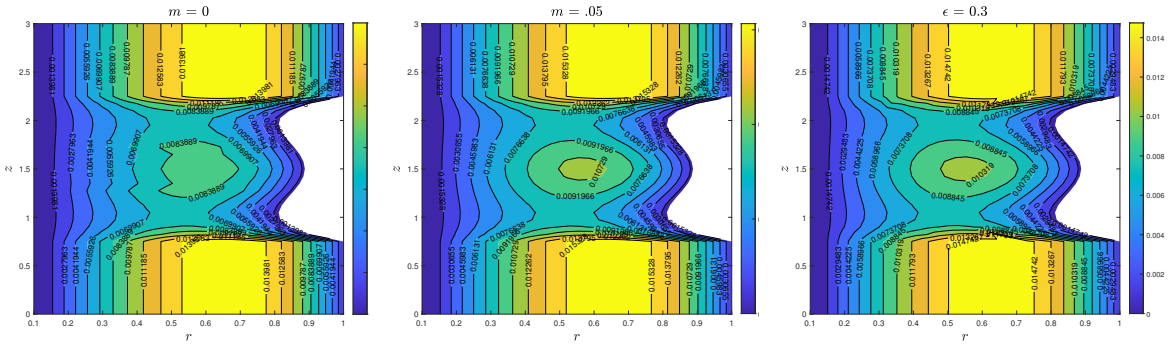

(a) (b) (c)

Figure 7.18: Blood flow pattern for nanoparticle volume fraction, (a) $m = 0$, (b) $m = .05$, (c) $m = .1$.

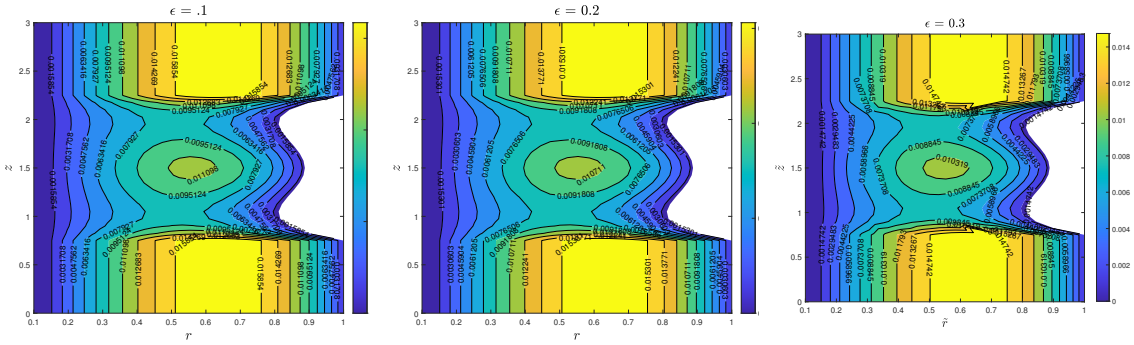

(a) (b) (c)

Figure 7.19: Blood flow pattern for arterial curvature, (a) $\varepsilon = 0.1$, (b) $\varepsilon = 0.2$, (c) $\varepsilon = 0.3$.

7.6 Conclusion

Using a two-phase blood flow model, a mathematical examination of the stenosed curved artery has been carried out. A patient-specific stenosed arterial model has been taken. To make the current investigation more plausible, the pseudoplastic fluid characteristics rather than Newtonian fluid have been taken into account for the core region blood flow. The effect of Fe_3O_4 nanoparticle and cylinder shape catheter has been also observed. The governing equations are expressed in a toroidal coordinate system, and it's discretization process

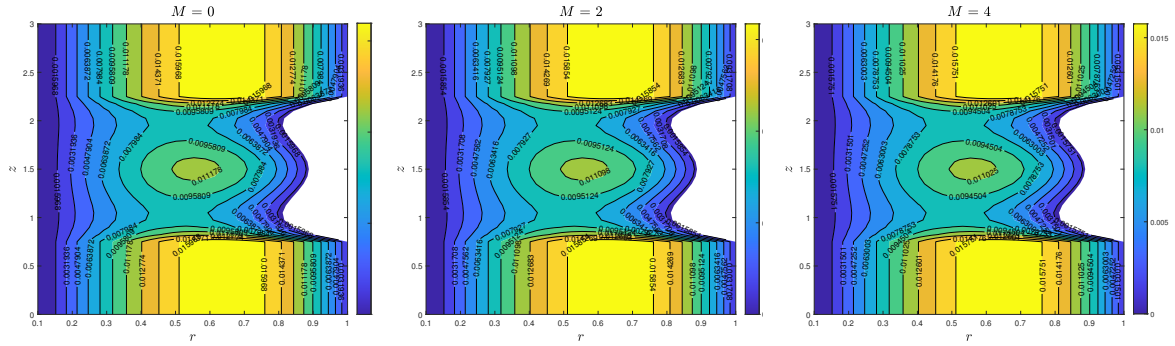

(a) (b) (c)

Figure 7.20: Blood flow pattern for magnetic field, (a) $M = 0$, (b) $M = 2$, (c) $M = 4$.

is implemented using a second-order central difference scheme. In "MATLAB" software, a system of non-linear equations is computed with a tolerance of 10^{-6} each iteration by adopting Stone's highly implicit methodology. The influence of several physical parameters such as q,H,m,Br,Rm,M, ε have been discussed graphically for the blood velocity, temperature, WSS, heat transfer rate, axial induced magnetic field and entropy production. Clinical researchers and biologists may use the results of this computational study to forecast endothelial cell damage and plaque deposition in curved arteries with WSS profiles, by which the severity of these conditions can be reduced. In treating stenosis, cancer cells, muscular discomfort and stiffness, etc., employing nanoparticles and external heating sources in blood flow would be advantageous. The following are some noteworthy findings from the current mathematical investigation:

- Arteries with high curvature have a higher possibility for lipid and stenosis deposition due to decay in the wall shear stress and heat transfer rate profile.
- If pseudoplastic properties instead of Newtonian fluid properties are considered for blood, in mathematical modelling will give accurate results in understanding blood flow phenomena.
- The Fe_3O_4 nanoparticles increase the blood temperature and heat transfer across arterial walls; therefore, its use can reduce lipid deposition in CVD treatments.
- The increment in magnetic Reynold number (Rm) leads to rising in the wall shear stress profile while showing reverse effects for axial induced magnetic field profile. These outcomes are in fairly agreement with [29, 174].

- The use of external heating source thermal therapies can increase both blood temperature and entropy production in flow.
- With the increase in viscous heating, flow generates more energy as well as entropy.
- Using the magnetic field in thermal therapies will help to control flow velocity.

Chapter 8

Conclusions and Future work

This chapter discuss the main outcome of this thesis work in conclusion section and further the possibilities for extending this work has been given in future work section.

8.1 Conclusions

The main motivation of this thesis work is to analyse the blood transport phenomena in a stenosed curved artery. Chapter 1 briefly introduces bio-fluid mechanics, the cardiovascular system, physical parameters, and methodology. Chapter 2 explains the two-phase blood flow model in curved arteries with variable viscosity and uniform magnetic field. The hematocrit-dependent viscosity for core region flow and the temperature-dependent viscosity model for plasma region have been considered. The temperature profile is obtained using the perturbation technique, while the velocity profile is calculated using the finite difference method. Results show that an increment in hematocrit level replicates RBC dominance in blood; therefore, the blood becomes thicker due to increased viscosity. The blood velocity increases with the flow temperature increase, while it shows the reverse effect with magnetic field intensity. Chapter 3 explained the heat and mass transport for the two-phase blood flow through a stenosed curved artery. In this, temperature-dependent viscosity for the core region, whereas plasma region viscosity is considered constant. This chapter provides a descriptive comparison between the conditions of assuming the arterial wall is permeable or impermeable (no-slip) and concludes that flow velocity is higher for a permeable arterial wall. The temperature profile is higher for the straight arteries ($\varepsilon = 0$) compared to curved arteries ($\varepsilon \neq 0$), while blood concentration reflects the reverse effect with arterial curvature. This chapter also states that using an external heat source (H) in hyperthermia and laser therapies can reduce the deposition of plaque and clot at a time of healing process, which happens due to a hike in flow temperature with an increase in H. Further, this work is extended into Chapter 4 by estimating the entropy generation profile for curved arterial

flow under the Joule heating and viscous dissipation. This chapter results that due to the presence of protein, nutrients, and significant heat transfer in the plasma region, blood produces a large amount of energy in the plasma region, although the majority of this energy is not employed for work. A significant rise in the entropy generation profile is observed with an increase in the Brinkman number (Br). This chapter also marked a notable growth in fear of deposition of plaque (lipid) appears with the rise in both arterial curvature and permeability wall condition, which happen due to a reduction in the wall shear stress profile. Chapter 5 provides a descriptive analysis of blood phenomena and entropy generation for the non-Newtonian blood flow model under the consequences of the Hall effect. The non-Newtonian fluid (power-law fluid) properties for the core region, while Newtonian fluid properties for plasma region flow, have been considered. This chapter explains that if pseudoplastic properties are considered for blood instead of Newtonian fluid properties in mathematical modelling, it will give accurate results in understanding blood flow phenomena. The blood's heat transfer properties reflect the good response in the Hall effect presence, and at the arterial wall, heat transfer rate enhances with the increase in Hall parameter value. But both blood flow velocity and wall shear stress profile decrease with the Hall parameter value increase. This chapter also states that using thermal radiation in therapies can lower arteriosclerosis deposition and increase heat transfer and flow velocity. The conversion process of mechanical energy produced by pressure-driven flow and chemical energy of EDL into electric energy is called electrokinetic energy conversion (EKEC). Therefore, considering the overlapped stenosis condition, chapter 6 provides the study of electrokinetic energy conversion (EKEC) efficiency and entropy for the power-law blood flow model. In this chapter thermal properties of gold nanoparticles are also considered, and the effect of nanoparticle volume fraction and their size on the EKEC efficiency, entropy and heat transfer are also observed. Results of the present study conclude that when gold nanoparticles are added to the blood flow, it reduces the flow's conversion efficiency for converting mechanical and chemical energy into electrokinetic energy, while this conversion efficiency is higher for large-size nanoparticles. The flow velocity and EKEC efficiency are higher for the thin size of electric double layer (EDL) thickness. The gold nanoparticle reduces the blood mass diffusion process, while the presence of gold nanoparticles enhances the heat transfer process; therefore, it can be used to minimise lipid deposition in CVD treatments. Chapter 7 presents the study of two-phase blood flow having non-Newtonian fluid (power-law fluid) for the core region and Newtonian fluid for the plasma region flow through an overlapped stenosed curved artery. The effect of induced magnetic field and iron oxide nanoparticles on heat and entropy analysis is also studied. Stone's strongly implicit method is adopted to solve a highly non-linear coupled system of partial differential equations. This study

concludes that the increased magnetic Reynold number enhances wall shear stress and heat transfer at the arterial wall. The thermal properties of blood flow enhance with the addition of iron oxide nanoparticles; therefore, blood temperature and heat transfer across arterial walls significantly improve with this mixture.

8.2 Future Scope

The mathematical models examined in this thesis describe single and two phase model of blood flow in curved artery. We have considered both Newtonian and non-Newtonian fluid properties for core region blood flow. In the clinical point of view, the following aspects of research work we would like to explore in future course:

- The electrokinetic energy conversion for single fluid model has been analyzed in the thesis, further this work can be extended for the two-phase blood flow through curved artery.
- In this thesis the only presence of single nanoparticle has been analyzed, further this work can be extended for presence of two or more nanoparticles in terms of hybrid and modified nanofluids.
- Modeling of optimal targeted drug delivery (magnetic nanoparticles) under the controlled magnetic field can be explored for the both single and two-phase blood flow models in curved artery.
- The analysis of solute dispersion for the two-phase blood flow through curved artery can be explored.

Bibliography

1. Jaiswal, S. & Yadav, P. K. A micropolar-Newtonian blood flow model through a porous layered artery in the presence of a magnetic field. *Physics of Fluids* **31,** 071901 (2019).
2. Sharma, B. K., Sharma, M. & Gaur, R. *Thermal radiation effect on inclined arterial blood flow through a non-Darcian porous medium with magnetic field* in *Proceeding: First Thermal and Fluids Engineering Summer Conference, ASTFE Digital Library* **17** (2015), 2159–2168.
3. Tripathi, B & Sharma, B. Effect of variable viscosity on MHD inclined arterial blood flow with chemical reaction. *International Journal of Applied Mechanics and Engineering* **23** (2018).
4. Késmárky, G., Kenyeres, P., Rábai, M. & Tóth, K. Plasma viscosity: a forgotten variable. *Clinical hemorheology and microcirculation* **39,** 243–246 (2008).
5. Shah, P. D., Tiwari, A. & Chauhan, S. S. Solute dispersion in micropolar-Newtonian fluid flowing through porous layered tubes with absorbing walls. *International Communications in Heat and Mass Transfer* **119,** 104724 (2020).
6. Ponalagusamy, R & Selvi, R. T. Influence of magnetic field and heat transfer on two-phase fluid model for oscillatory blood flow in an arterial stenosis. *Meccanica* **50,** 927–943 (2015).
7. Ogulu, A & Abbey, T. M. Simulation of heat transfer on an oscillatory blood flow in an indented porous artery. *International communications in heat and mass transfer* **32,** 983–989 (2005).
8. Tripathi, B. & Sharma, B. K. *Influence of heat and mass transfer on MHD two-phase blood flow with radiation* in *AIP Conference Proceedings* **1975** (2018), 030009.
9. Medvedev, A. & Fomin, V. *Two-phase blood-flow model in large and small vessels* in *Doklady Physics* **56** (2011), 610–613.
10. Tripathi, B. & Sharma, B. K. MHD blood flow and heat transfer through an inclined porous stenosed artery with variable viscosity. *arXiv preprint arXiv:1610.03470* (2016).

11. Nadeem, S, Akbar, N. S. & Hameed, M. Peristaltic transport and heat transfer of a MHD Newtonian fluid with variable viscosity. *International journal for numerical methods in fluids* **63,** 1375–1393 (2010).

12. Tripathi, B. & Sharma, B. K. Two-phase analysis of blood flow through a stenosed artery with the effects of chemical reaction and radiation. *Ricerche di Matematica,* 1–27 (2021).

13. Tripathi, B., Sharma, B. K. & Sharma, M. Modeling and analysis of MHD two-phase blood flow through a stenosed artery having temperature-dependent viscosity. *The European Physical Journal Plus* **134,** 466 (2019).

14. Sankar, D. & Hemalatha, K. A non-Newtonian fluid flow model for blood flow through a catheterized artery—steady flow. *Applied mathematical modelling* **31,** 1847–1864 (2007).

15. Sharma, B. D. & Yadav, P. K. A two-layer mathematical model of blood flow in porous constricted blood vessels. *Transport in Porous Media* **120,** 239–254 (2017).

16. Mekheimer, K. S. & El Kot, M. Suspension model for blood flow through catheterized curved artery with time-variant overlapping stenosis. *Engineering Science and Technology, an International Journal* **18,** 452–462 (2015).

17. Ponalagusamy, R & Selvi, R. T. Blood flow in stenosed arteries with radially variable viscosity, peripheral plasma layer thickness and magnetic field. *Meccanica* **48,** 2427–2438 (2013).

18. Sultan, F., Khan, N. A., Qasim, M. & Afridi, M. I. Numerical simulation of the flow of nano-Eyring-Powell fluid through a curved artery with time-variant stenosis and aneurysm. *Nihon Reoroji Gakkaishi* **47,** 75–85 (2019).

19. Sharma, B. K., Tailor, V. & Goyal, M. Heat source and soret effects on megneto-micropolar fluid flow with variable permeability and chemical reaction. *Global Journal of Pure and Applied Mathematics* **13,** 5195–5212 (2017).

20. Mamatha, S., Raju, C. S., Prasad, P. D., Ajmath, K., Makinde, O. D., *et al. Exponentially decaying heat source on MHD tangent hyperbolic two-phase flows over a flat surface with convective conditions* in *Defect and Diffusion Forum* **387** (2018), 286–295.

21. Ibrahim, S. M., Kumar, P. V. & Makinde, O. D. *Chemical reaction and radiation effects on non-Newtonian fluid flow over a stretching sheet with non-uniform thickness and heat source* in *Defect and Diffusion Forum* **387** (2018), 319–331.

22. Rashidi, M. M., Bhatti, M. M., Abbas, M. A. & Ali, M. E.-S. Entropy generation on MHD blood flow of nanofluid due to peristaltic waves. *Entropy* **18,** 117 (2016).

23. Mekheimer, K. S., Zaher, A. & Hasona, W. Entropy of AC electro-kinetics for blood mediated gold or copper nanoparticles as a drug agent for thermotherapy of oncology. *Chinese Journal of Physics* **65,** 123–138 (2020).

24. Sharma, B. K., Jha, A. K. & Chaudhary, R. Hall effect on MHD mixed convective flow of a viscous incompressible fluid past a vertical porous plate immersed in porous medium with heat source/sink. *Rom. Journal Phys* **52,** 487–503 (2007).

25. Agrawal, S., Jayaraman, G, Srivastava, V. & Nigam, K. Power law fluids in a circular curved tube. Part I. Laminar flow. *Polymer-Plastics Technology and Engineering* **32,** 595–614 (1993).

26. Gan, Y. *Continuum mechanics: progress in fundamentals and engineering applications* (BoD–Books on Demand, 2012).

27. Narla, V. & Tripathi, D. Electroosmosis modulated transient blood flow in curved microvessels: study of a mathematical model. *Microvascular research* **123,** 25–34 (2019).

28. Narla, V., Tripathi, D. & Bég, O. A. Electro-osmotic nanofluid flow in a curved microchannel. *Chinese Journal of Physics* **67,** 544–558 (2020).

29. Mekheimer, K. S., Haroun, M. H. & El Kot, M. Induced magnetic field influences on blood flow through an anisotropically tapered elastic artery with overlapping stenosis in an annulus. *Canadian Journal of Physics* **89,** 201–212 (2011).

30. Casson, N. Flow equation for pigment-oil suspensions of the printing ink-type. *Rheology of disperse systems,* 84–104 (1959).

31. Young, D. Effect of a time-dependent stenosis on flow through a tube. **90,** 248–245 (1968).

32. Young, D. Fluid mechanics of arterial stenoses. **101,** 157–175 (1979).

33. Padmanabhan, N & Jayaraman, G. Flow in a curved tube with constriction-an application to the arterial system. *Medical and Biological Engineering and Computing* **22,** 216–224 (1984).

34. Jayaraman, G & Dash, R. Numerical study of flow in a constricted curved annulus: An application to flow in a catheterised artery. *Journal of Engineering Mathematics* **40,** 355–375 (2001).

35. Sharma, B. K. & Kumawat, C. Impact of temperature dependent viscosity and thermal conductivity on MHD blood flow through a stretching surface with ohmic effect and chemical reaction. *Nonlinear Engineering* **10,** 255–271 (2021).

36. Siddiqa, S., Naqvi, S., Hossain, M., Massarotti, N & Mauro, A. Strong temperature dependent viscosity effects on bio-magnetic fluid flow under the action of localized magnetic field and viscous dissipation. *Journal of Molecular Liquids* **248,** 616–625 (2017).

37. Issacci, F, Ghoniem, N. & Catton, I. Magnetohydrodynamic flow in a curved pipe. *The Physics of fluids* **31,** 65–71 (1988).

38. Akar, S., Esfahani, J. A. & Shaegh, S. A. M. A numerical investigation of magnetic field effect on blood flow as biomagnetic fluid in a bend vessel. *Journal of Magnetism and Magnetic Materials* **482,** 336–349 (2019).

39. Datta, N. & Jana, R. N. Oscillatory magnetohydrodynamic flow past a flat plate with Hall effects. *Journal of the physical society of Japan* **40,** 1469–1474 (1976).

40. Szwast, M. & Piatkiewicz, W. Hall effect in electrolyte flow measurements: introduction to blood flow measurements. *Artificial Organs* **36,** 551–555 (2012).

41. El Kot, M. & Abd Elmaboud, Y. Unsteady pulsatile fractional Maxwell viscoelastic blood flow with Cattaneo heat flux through a vertical stenosed artery with body acceleration. *Journal of Thermal Analysis and Calorimetry,* 1–14 (2021).

42. Misra, J., Sinha, A & Shit, G. Flow of a biomagnetic viscoelastic fluid: application to estimation of blood flow in arteries during electromagnetic hyperthermia, a therapeutic procedure for cancer treatment. *Applied Mathematics and Mechanics* **31,** 1405–1420 (2010).

43. Misra, J. & Sinha, A. Effect of thermal radiation on MHD flow of blood and heat transfer in a permeable capillary in stretching motion. *Heat and Mass Transfer* **49,** 617–628 (2013).

44. Haynes, R. H. Physical basis of the dependence of blood viscosity on tube radius. *American Journal of Physiology-Legacy Content* **198,** 1193–1200 (1960).

45. Shukla, J., Parihar, R. & Gupta, S. Effects of peripheral layer viscosity on blood flow through the artery with mild stenosis. *Bulletin of Mathematical Biology* **42,** 797–805 (1980).

46. Bejan, A. Entropy generation minimization: The new thermodynamics of finite-size devices and finite-time processes. *Journal of Applied Physics* **79,** 1191–1218 (1996).

47. Rashidi, M., Abelman, S & Mehr, N. F. Entropy generation in steady MHD flow due to a rotating porous disk in a nanofluid. *International journal of Heat and Mass transfer* **62,** 515–525 (2013).

48. Ranjit, N., Shit, G. & Tripathi, D. Entropy generation and Joule heating of two layered electroosmotic flow in the peristaltically induced micro-channel. *International Journal of Mechanical Sciences* **153,** 430–444 (2019).

49. Wilczewska, A. Z., Niemirowicz, K., Markiewicz, K. H. & Car, H. Nanoparticles as drug delivery systems. *Pharmacological reports* **64,** 1020–1037 (2012).

50. Feng, X. & Johnson, D. W. Mass transfer in SiO2 nanofluids: a case against purported nanoparticle convection effects. *International Journal of Heat and Mass Transfer* **55,** 3447–3453 (2012).

51. Corcione, M. Empirical correlating equations for predicting the effective thermal conductivity and dynamic viscosity of nanofluids. *Energy conversion and management* **52,** 789–793 (2011).

52. Stone, H. L. Iterative solution of implicit approximations of multidimensional partial differential equations. *SIAM Journal on Numerical Analysis* **5,** 530–558 (1968).

53. Dean, W. R. XVI. Note on the motion of fluid in a curved pipe. *The London, Edinburgh, and Dublin Philosophical Magazine and Journal of Science* **4,** 208–223 (1927).

54. Dean, W. LXXII. The stream-line motion of fluid in a curved pipe (Second paper). *The London, Edinburgh, and Dublin Philosophical Magazine and Journal of Science* **5,** 673–695 (1928).

55. Berger, S., Talbot, L & Yao, L. Flow in curved pipes. *Annual review of fluid mechanics* **15,** 461–512 (1983).

56. Rand, P. W., Lacombe, E., Hunt, H. E. & Austin, W. H. Viscosity of normal human blood under normothermic and hypothermic conditions. *Journal of Applied Physiology* **19,** 117–122 (1964).

57. Snyder, G. K. Influence of temperature and hematocrit on blood viscosity. *American Journal of Physiology-Legacy Content* **220,** 1667–1672 (1971).

58. Guard, C. L. & Murrish, D. E. Effects of temperature on the viscous behavior of blood from antarctic birds and mammals. *Comparative Biochemistry and Physiology Part A: Physiology* **52,** 287–290 (1975).

59. Secomb, T. W. & Pries, A. R. Blood viscosity in microvessels: experiment and theory. *Comptes Rendus Physique* **14,** 470–478 (2013).

60. Çinar, Y., Şenyol, A. M. & Duman, K. Blood viscosity and blood pressure: role of temperature and hyperglycemia. *American journal of hypertension* **14,** 433–438 (2001).

61. Eckmann, D. M., Bowers, S., Stecker, M. & Cheung, A. T. Hematocrit, volume expander, temperature, and shear rate effects on blood viscosity. *Anesthesia & Analgesia* **91,** 539–545 (2000).

62. Mekheimer, K. S. & Abd Elmaboud, Y. Simultaneous effects of variable viscosity and thermal conductivity on peristaltic flow in a vertical asymmetric channel. *Canadian Journal of Physics* **92,** 1541–1555 (2014).

63. Tanveer, A, Hayat, T & Alsaedi, A. Variable viscosity in peristalsis of Sisko fluid. *Applied Mathematics and Mechanics* **39,** 501–512 (2018).

64. Ponalagusamy, R & Priyadharshini, S. Numerical investigation on two-fluid model (micropolar-Newtonian) for pulsatile flow of blood in a tapered arterial stenosis with radially variable magnetic field and core fluid viscosity. *Computational and Applied Mathematics* **37,** 719–743 (2018).

65. Tripathi, B., Sharma, B. K. & Sharma, M. MHD Pulsatile Two-Phase Blood Flow Through a Stenosed Artery with Heat and Mass Transfer. *arXiv preprint arXiv:1705.09794* (2017).

66. Tripathi, B. & Sharma, B. K. Influence of Heat and Mass Transfer on Two-Phase Blood Flow with Joule Heating and Variable Viscosity in the Presence of Variable Magnetic Field. *International Journal of Computational Methods* **17,** 1850139 (2020).

67. Rao, A. R. & Deshikachar, K. Physiological-type flow in a circular pipe in the presence of a transverse magnetic field. *Journal of the Indian Institute of Science* **68,** 247 (1988).

68. Pourmehran, O., Gorji, T. B. & Gorji-Bandpy, M. Magnetic drug targeting through a realistic model of human tracheobronchial airways using computational fluid and particle dynamics. *Biomechanics and modeling in mechanobiology* **15,** 1355–1374 (2016).

69. Larimi, M., Ghanaat, A, Ramiar, A & Ranjbar, A. Forced convection heat transfer in a channel under the influence of various non-uniform transverse magnetic field arrangements. *International Journal of Mechanical Sciences* **118,** 101–112 (2016).

70. Nguyen, N.-T. Micro-magnetofluidics: interactions between magnetism and fluid flow on the microscale. *Microfluidics and nanofluidics* **12,** 1–16 (2012).

71. Barnothy, M. F. *Biological effects of magnetic fields* (Springer, 2013).

72. Haik, Y., Pai, V. & Chen, C.-J. Apparent viscosity of human blood in a high static magnetic field. *Journal of Magnetism and Magnetic Materials* **225,** 180–186 (2001).

73. Bhatti, M. M. Biologically inspired intra-uterine nanofluid flow under the suspension of magnetized gold (Au) nanoparticles: applications in nanomedicine. *Inventions* **6,** 28 (2021).

74. Bhatti, M., Zeeshan, A, Bashir, F, Sait, S. M. & Ellahi, R. Sinusoidal motion of small particles through a Darcy-Brinkman-Forchheimer microchannel filled with non-Newtonian fluid under electro-osmotic forces. *Journal of Taibah University for Science* **15,** 514–529 (2021).

75. Gijsen, F., Allanic, E, Van De Vosse, F. & Janssen, J. The influence of the non-Newtonian properties of blood on the flow in large arteries: unsteady flow in a 90 curved tube. *Journal of biomechanics* **32,** 705–713 (1999).

76. Nadeem, S & Ijaz, S. Theoretical analysis of metallic nanoparticles on blood flow through stenosed artery with permeable walls. *Physics Letters A* **379,** 542–554 (2015).

77. Bit, A. *et al.* Three dimensional numerical analysis of hemodynamic of stenosed artery considering realistic outlet boundary conditions. *Computer methods and programs in biomedicine* **185,** 105163 (2020).

78. Biglarian, M. *et al.* Computational investigation of stenosis in curvature of coronary artery within both dynamic and static models. *Computer methods and programs in biomedicine* **185,** 105170 (2020).

79. Shahzadi, I. & Nadeem, S. Analysis of Ag/blood-mediated transport in curved annulus with exclusive nature of convective boundary. *Physica Scripta* **94,** 115011 (2019).

80. Ayub, M., Shahzadi, I. & Nadeem, S. A ballon model analysis with Cu-blood medicated nanoparticles as drug agent through overlapped curved stenotic artery having compliant walls. *Microsystem Technologies* **25,** 2949–2962 (2019).

81. Mori, Y. Study on forced convective heat transfer in curved pipes. *Int. J. Heat Mass Trans.* **8,** 67–82 (1965).

82. Mori, Y. & Nakayama, W. Study of forced convective heat transfer in curved pipes (2nd report, turbulent region). *International journal of heat and mass transfer* **10,** 37–59 (1967).

83. Patankar, S. V., Pratap, V. & Spalding, D. in *Numerical Prediction of Flow, Heat Transfer, Turbulence and Combustion* 117–129 (Elsevier, 1983).

84. Nobari, M. & Mehrabani, M. A numerical study of fluid flow and heat transfer in eccentric curved annuli. *International Journal of Thermal Sciences* **49,** 380–396 (2010).

85. Akbarinia, A & Laur, R. Investigating the diameter of solid particles effects on a laminar nanofluid flow in a curved tube using a two-phase approach. *International Journal of Heat and Fluid Flow* **30,** 706–714 (2009).

86. Ramanamurthy, J., Prasad, K. & Narla, V. Unsteady peristaltic transport in curved channels. *Physics of Fluids* **25,** 091903 (2013).

87. Bugliarello, G. & Hayden, J. W. Detailed characteristics of the flow of blood in vitro. *Transactions of the Society of Rheology* **7,** 209–230 (1963).

88. Bugliarello, G. & Sevilla, J. Velocity distribution and other characteristics of steady and pulsatile blood flow in fine glass tubes. *Biorheology* **7,** 85–107 (1970).

89. Shukla, J., Parihar, R. & Gupta, S. Biorheological aspects of blood flow through stenosed artery with mild stenosis: effects of peripherical layer. *Biorheological* **17,** 403–410 (1980).

90. Tiwari, A. & Chauhan, S. S. Effect of varying viscosity on two-fluid model of pulsatile blood flow through porous blood vessels: a comparative study. *Microvascular research* **123,** 99–110 (2019).

91. Patankar, S. V. & Spalding, D. B. A calculation procedure for heat, mass and momentum transfer in three-dimensional parabolic flows. *Internation journal of Heat Mass Transfer* **15,** 1787–1806 (1972).

92. Ahmed, A. & Nadeem, S. Effects of magnetohydrodynamics and hybrid nanoparticles on a micropolar fluid with 6-types of stenosis. *Results in physics* **7,** 4130–4139 (2017).

93. Katritsis, D. *et al.* Wall shear stress: theoretical considerations and methods of measurement. *Progress in cardiovascular diseases* **49,** 307–329 (2007).

94. FRY, D. L. Certain chemorheologic considerations regarding the blood vascular interface with particular reference to coronary artery disease. *Circulation* **40,** IV–38 (1969).

95. Asha, S. & Sunitha, G. Thermal radiation and Hall effects on peristaltic blood flow with double diffusion in the presence of nanoparticles. *Case Studies in Thermal Engineering* **17,** 100560 (2020).

96. Rahimi-Gorji, M. *et al.* Intraperitoneal aerosolized drug delivery: technology, recent developments, and future outlook. *Advanced Drug Delivery Reviews* (2020).

97. Gorji, M. R. *et al.* Electrostatic precipitation pressurized intraperitoneal aerosol chemotherapy (ePIPAC): Finding the optimal electrical potential. *European Journal of Surgical Oncology* **47,** e30 (2021).

98. Braet, H. *et al.* Exploring high pressure nebulization of Pluronic F127 hydrogels for intraperitoneal drug delivery. *European Journal of Pharmaceutics and Biopharmaceutics* **169,** 134–143 (2021).

99. Ali, A., Jana, R. & Das, S. Significance of entropy generation and heat source: the case of peristaltic blood flow through a ciliated tube conveying Cu-Ag nanoparticles using Phan-Thien-Tanner model. *Biomechanics and Modeling in Mechanobiology,* 1–20 (2021).

100. Beavers, G. S. & Joseph, D. D. Boundary conditions at a naturally permeable wall. *Journal of fluid mechanics* **30,** 197–207 (1967).

101. Sparrow, E., Beavers, G. S. & Masha, B. Laminar flow in a rectangular duct bounded by a porous wall. *The Physics of Fluids* **17,** 1465–1467 (1974).

102. Chakravarty, S. & Datta, A. Pulsatile blood flow in a porous stenotic artery. *Mathematical and computer modelling* **16,** 35–54 (1992).

103. Mishra, S., Siddiqui, S. & Medhavi, A. Blood flow through a composite stenosis in an artery with permeable wall. *Int. J. Appl. Math. Appl* **6,** 58–73 (2011).

104. Srivastav, R. K. & Srivastava, V. On two-fluid blood flow through stenosed artery with permeable wall. *Applied Bionics and Biomechanics* **11,** 39–45 (2014).

105. Kahshan, M., Lu, D., Rahimi-Gorji, M. & Do, H.-T. A mathematical model of blood flow in a permeable channel: application to flat plate dialyzer. *Physica Scripta* **95,** 045202 (2020).

106. Akbar, N. S., Rahman, S., Ellahi, R & Nadeem, S. Nano fluid flow in tapering stenosed arteries with permeable walls. *International Journal of Thermal Sciences* **85,** 54–61 (2014).

107. Ellahi, R, Rahman, S., Nadeem, S & Akbar, N. S. Blood flow of nanofluid through an artery with composite stenosis and permeable walls. *Applied Nanoscience* **4,** 919–926 (2014).

108. Ahmed, A. & Nadeem, S. Shape effect of Cu-nanoparticles in unsteady flow through curved artery with catheterized stenosis. *Results in physics* **7,** 677–689 (2017).

109. Zhang, B. *et al.* Correlation between quantitative analysis of wall shear stress and intima-media thickness in atherosclerosis development in carotid arteries. *Biomedical engineering online* **16,** 1–17 (2017).

110. Escuer, J. *et al.* Influence of vessel curvature and plaque composition on drug transport in the arterial wall following drug-eluting stent implantation. *Biomechanics and Modeling in Mechanobiology* **20,** 767–786 (2021).

111. Hasnain, J. & Abbas, Z. Entropy generation analysis on two-phase micropolar nanofluids flow in an inclined channel with convective heat transfer. *Thermal Science* **23,** 1765–1777 (2019).

112. Dutta, A., Chattopadhyay, H., Yasmin, H. & Rahimi-Gorji, M. Entropy generation in the human lung due to effect of psychrometric condition and friction in the respiratory tract. *Computer methods and programs in biomedicine* **180,** 105010 (2019).

113. Ganesh, N. V., Al-Mdallal, Q. M. & Chamkha, A. J. A numerical investigation of Newtonian fluid flow with buoyancy, thermal slip of order two and entropy generation. *Case Studies in Thermal Engineering* **13,** 100376 (2019).

114. Sohail, M. *et al.* Theoretical and numerical investigation of entropy for the variable thermophysical characteristics of couple stress material: Applications to optimization. *Alexandria Engineering Journal* **59,** 4365–4375 (2020).

115. Dadheech, P. K. *et al.* Entropy analysis for radiative inclined MHD slip flow with heat source in porous medium for two different fluids. *Case Studies in Thermal Engineering,* 101491 (2021).

116. Tiwari, A., Shah, P. D. & Chauhan, S. S. Solute dispersion in two-fluid flowing through tubes with a porous layer near the absorbing wall: Model for dispersion phenomenon in microvessels. *International Journal of Multiphase Flow* **131,** 103380 (2020).

117. Lowe, G. D. Blood viscosity and cardiovascular risk. *Current Opinion in Lipidology* **4,** 283–287 (1993).

118. Bhatti, M. & Rashidi, M. Study of heat and mass transfer with Joule heating on magnetohydrodynamic (MHD) peristaltic blood flow under the influence of Hall effect. *Propulsion and Power Research* **6,** 177–185 (2017).

119. Ranjit, N., Shit, G. & Tripathi, D. Joule heating and zeta potential effects on peristaltic blood flow through porous micro vessels altered by electrohydrodynamic. *Microvascular research* **117,** 74–89 (2018).

120. Farooq, A., Kahshan, M, Saleem, S, Rahimi-Gorji, M. & Al-Mubaddel, F. S. Entropy production rate in ciliary induced flows through cylindrical tubules under the consequences of Hall effect. *Journal of the Taiwan Institute of Chemical Engineers* **120,** 207–217 (2021).

121. Ellahi, R, Rahman, S., Nadeem, S & Akbar, N. S. Influence of heat and mass transfer on micropolar fluid of blood flow through a tapered stenosed arteries with permeable walls. *Journal of computational and theoretical Nanoscience* **11,** 1156–1163 (2014).

122. Abbasi, F., Hayat, T & Alsaedi, A. Numerical analysis for MHD peristaltic transport of Carreau-Yasuda fluid in a curved channel with Hall effects. *Journal of Magnetism and Magnetic Materials* **382,** 104–110 (2015).

123. Akram, J., Akbar, N. S. & Tripathi, D. Thermal analysis on MHD flow of ethylene glycol-based BNNTs nanofluids via peristaltically induced electroosmotic pumping in a curved microchannel. *Arabian Journal for Science and Engineering* **47,** 7487–7503 (2022).

124. Khanduri, U. & Sharma, B. K. Hall and ion slip effects on hybrid nanoparticles (Au-GO/blood) flow through a catheterized stenosed artery with thrombosis. *Proceedings of the Institution of Mechanical Engineers, Part C: Journal of Mechanical Engineering Science,* 09544062221136710 (2022).

125. Shehzad, S. A., Saba, S. & Abbasi, F. Influence of Curvature Dependent Channel walls on MHD Peristaltic Flow of Viscous Fluid with Hall Currents and Joule Dissipation. *ScientiaIranica* (2022).

126. Mekheimer, K. S. & El Kot, M. Influence of magnetic field and Hall currents on blood flow through a stenotic artery. *Applied Mathematics and Mechanics* **29,** 1093–1104 (2008).

127. Prakash, J & Makinde, O. D. Radiative heat transfer to blood flow through a stenotic artery in the presence of magnetic field. *Latin American applied research* **41,** 273–277 (2011).

128. Eid, M. R., Alsaedi, A., Muhammad, T. & Hayat, T. Comprehensive analysis of heat transfer of gold-blood nanofluid (Sisko-model) with thermal radiation. *Results in physics* **7,** 4388–4393 (2017).

129. Sharma, B., Khanduri, U., Mishra, N. K. & Mekheimer, K. S. Combined effect of thermophoresis and Brownian motion on MHD mixed convective flow over an inclined stretching surface with radiation and chemical reaction. *International Journal of Modern Physics B,* 2350095 (2022).

130. Patankar, S. V. & Spalding, D. B. in *Numerical prediction of flow, heat transfer, turbulence and combustion* 54–73 (Elsevier, 1983).

131. Dupont, T., Kendall, R. P. & Rachford Jr, H. An approximate factorization procedure for solving self-adjoint elliptic difference equations. *SIAM Journal on Numerical Analysis* **5,** 559–573 (1968).

132. Kumawat, C., Sharma, B. K. & Mekheimer, K. S. Mathematical analysis of two-phase blood flow through a stenosed curved artery with hematocrit and temperature dependent viscosity. *Physica Scripta* **96,** 125277 (2021).

133. Zaman, A., Khan, A. A., Mabood, F., Abbasi, A. & Badruddin, I. A. Thermal analysis of unsteady hybrid nanofluid magneto-hemodynamics flow via overlapped curved stenosed channel. *Proceedings of the Institution of Mechanical Engineers, Part C: Journal of Mechanical Engineering Science* **236,** 8754–8766 (2022).

134. Kumawat, C., Sharma, B., Al-Mdallal, Q. M. & Rahimi-Gorji, M. Entropy generation for MHD two phase blood flow through a curved permeable artery having variable viscosity with heat and mass transfer. *International Communications in Heat and Mass Transfer* **133,** 105954 (2022).

135. Tiwari, A. & Chauhan, S. S. Effect of varying viscosity on a two-layer model of the blood flow through porous blood vessels. *The European Physical Journal Plus* **134,** 41 (2019).

136. Sankar, D. & Hemalatha, K. A non-Newtonian fluid flow model for blood flow through a catheterized artery—steady flow. *Applied mathematical modelling* **31,** 1847–1864 (2007).

137. Chinyoka, T & Makinde, O. Computational dynamics of arterial blood flow in the presence of magnetic field and thermal radiation therapy. *Advances in Mathematical Physics* **2014** (2014).

138. Das, S. & Chakraborty, S. Analytical solutions for velocity, temperature and concentration distribution in electroosmotic microchannel flows of a non-Newtonian bio-fluid. *Analytica chimica acta* **559,** 15–24 (2006).

139. Chakraborty, S. Electroosmotically driven capillary transport of typical non-Newtonian biofluids in rectangular microchannels. *Analytica Chimica Acta* **605,** 175–184 (2007).

140. Zhao, C., Zholkovskij, E., Masliyah, J. H. & Yang, C. Analysis of electroosmotic flow of power-law fluids in a slit microchannel. *Journal of colloid and interface science* **326,** 503–510 (2008).

141. Nekoubin, N. Electroosmotic flow of power-law fluids in curved rectangular microchannel with high zeta potentials. *Journal of Non-Newtonian Fluid Mechanics* **260,** 54–68 (2018).

142. Ding, Z., Tian, K. & Jian, Y. Electrokinetic flow and energy conversion in a curved microtube. *Applied Mathematics and Mechanics* **43,** 1289–1306 (2022).

143. Bandopadhyay, A. & Chakraborty, S. Steric-effect induced alterations in streaming potential and energy transfer efficiency of non-Newtonian fluids in narrow confinements. *Langmuir* **27,** 12243–12252 (2011).

144. Sarkar, S. Streaming-potential-mediated pressure-driven transport of Phan-Thien–Tanner fluids in a microchannel. *Physical Review E* **101,** 053104 (2020).

145. Xie, Z. & Jian, Y. Electrokinetic energy conversion of nanofluids in MHD-based microtube. *Energy* **212,** 118711 (2020).

146. Li, N., Zhao, G., Gao, X., Zhang, Y. & Jian, Y. The Impacts of Viscoelastic Behavior on Electrokinetic Energy Conversion for Jeffreys Fluid in Microtubes. *Nanomaterials* **12,** 3355 (2022).

147. Bamrungsap, S. *et al.* Nanotechnology in therapeutics: a focus on nanoparticles as a drug delivery system. *Nanomedicine* **7,** 1253–1271 (2012).

148. Weissleder, R. *et al.* Ultrasmall superparamagnetic iron oxide: characterization of a new class of contrast agents for MR imaging. *Radiology* **175,** 489–493 (1990).

149. Duivenvoorden, R. *et al.* A statin-loaded reconstituted high-density lipoprotein nanoparticle inhibits atherosclerotic plaque inflammation. *Nature communications* **5,** 1–12 (2014).

150. Weinstein, J. S. *et al.* Superparamagnetic iron oxide nanoparticles: diagnostic magnetic resonance imaging and potential therapeutic applications in neurooncology and central nervous system inflammatory pathologies, a review. *Journal of Cerebral Blood Flow & Metabolism* **30,** 15–35 (2010).

151. Poonam, Sharma, B., Kumawat, C. & Vafai, K. Computational biomedical simulations of hybrid nanoparticles (Au-Al_2O_3/blood-mediated) transport in a stenosed and aneurysmal curved artery with heat and mass transfer: Hematocrit dependent viscosity approach. *Chemical Physics Letters,* 139666 (2022).

152. Dupont, T., Kendall, R. P. & Rachford Jr, H. An approximate factorization procedure for solving self-adjoint elliptic difference equations. *SIAM Journal on Numerical Analysis* **5,** 559–573 (1968).

153. Yun, J. H., Chun, M.-S. & Jung, H. W. The geometry effect on steady electrokinetic flows in curved rectangular microchannels. *Physics of Fluids* **22,** 052004 (2010).

154. Bakalis, P. A. & Hatzikonstantinou, P. M. Effect of curvature and magnetic field on MHD flow of a liquid metal in a curved annular duct. *International Journal of Numerical Methods for Heat & Fluid Flow* (2015).

155. Goswami, P. & Chakraborty, S. Energy transfer through streaming effects in time-periodic pressure-driven nanochannel flows with interfacial slip. *Langmuir* **26,** 581–590 (2010).

156. Shahzadi, I. & Ijaz, S. On model of hybrid Casson nanomaterial considering endoscopy in a curved annulas: a comparative study. *Physica Scripta* **94,** 125215 (2019).

157. Gandhi, R., Sharma, B., Kumawat, C. & Bég, O. A. Modeling and analysis of magnetic hybrid nanoparticle (Au-Al 2 O 3/blood) based drug delivery through a bell-shaped occluded artery with joule heating, viscous dissipation and variable viscosity effects. *Proceedings of the Institution of Mechanical Engineers, Part E: Journal of Process Mechanical Engineering,* 09544089221080273 (2022).

158. Sharma, B., Gandhi, R. & Bhatti, M. Entropy analysis of thermally radiating MHD slip flow of hybrid nanoparticles (Au-Al_2 O_3/Blood) through a tapered multi-stenosed artery. *Chemical Physics Letters* **790,** 139348 (2022).

159. Harding, M. B. *et al.* Renal artery stenosis: prevalence and associated risk factors in patients undergoing routine cardiac catheterization. *Journal of the American Society of Nephrology* **2,** 1608–1616 (1992).

160. Nifong, T. P. & McDevitt, T. J. The effect of catheter to vein ratio on blood flow rates in a simulated model of peripherally inserted central venous catheters. *Chest* **140,** 48–53 (2011).

161. Jayaraman, G & Tewari, K. Flow in catheterised curved artery. *Medical and Biological Engineering and Computing* **33,** 720–724 (1995).

162. Bejan, A. A study of entropy generation in fundamental convective heat transfer (1979).

163. Barnoon, P., Toghraie, D., Dehkordi, R. B. & Abed, H. MHD mixed convection and entropy generation in a lid-driven cavity with rotating cylinders filled by a nanofluid using two phase mixture model. *Journal of Magnetism and Magnetic Materials* **483,** 224–248 (2019).

164. Zidan, A. *et al.* Entropy generation for the blood flow in an artery with multiple stenosis having a catheter. *Alexandria Engineering Journal* **60,** 5741–5748 (2021).

165. Haik, Y., Pai, V. & Chen, C.-J. Development of magnetic device for cell separation. *Journal of Magnetism and Magnetic Materials* **194,** 254–261 (1999).

166. Voltairas, P., Fotiadis, D. & Michalis, L. Hydrodynamics of magnetic drug targeting. *Journal of biomechanics* **35,** 813–821 (2002).

167. Freeman, M., Arrott, A & Watson, J. Magnetism in medicine. *Journal of Applied Physics* **31,** S404–S405 (1960).

168. Kinouchi, Y, Yamaguchi, H & Tenforde, T. Theoretical analysis of magnetic field interactions with aortic blood flow. *Bioelectromagnetics: Journal of the Bioelectromagnetics Society, The Society for Physical Regulation in Biology and Medicine, The European Bioelectromagnetics Association* **17,** 21–32 (1996).

169. Bhatti, M. M., Sait, S. M. & Ellahi, R. Magnetic nanoparticles for drug delivery through tapered stenosed artery with blood based non-newtonian fluid. *Pharmaceuticals* **15,** 1352 (2022).

170. Sharma, B., Kumawat, C. & Makinde, O. Hemodynamical analysis of MHD two phase blood flow through a curved permeable artery having variable viscosity with heat and mass transfer. *Biomechanics and Modeling in Mechanobiology,* 1–29 (2022).

171. Poonam, Sharma, B., Kumawat, C. & Vafai, K. Computational biomedical simulations of hybrid nanoparticles (Au-Al2O3/blood-mediated) transport in a stenosed and aneurysmal curved artery with heat and mass transfer: Hematocrit dependent viscosity approach. *Chemical Physics Letters,* 139666 (2022).

172. Reddy, S., Raju, C., Gunakala, S. R., Basha, H. T. & Yook, S.-J. Bio-magnetic pulsatile CuO- Fe_3O_4 hybrid nanofluid flow in a vertical irregular channel in a suspension of body acceleration. *International Communications in Heat and Mass Transfer* **135,** 106151 (2022).

173. Liu, X. *et al.* The thermal behavior of blood flow in the arteries with various radii and various stenosis angles using non-Newtonian Sisko model. *Alexandria Engineering Journal* **61,** 7195–7201 (2022).

174. Mekheimer, K. S. Peristaltic flow of a magneto-micropolar fluid: effect of induced magnetic field. *Journal of Applied Mathematics* **2008** (2008).

List of Publications

The following works included in this thesis in chapter form have been published/ communicated in the following journals:

1. **C. Kumawat**, B. Sharma, and K. Mekheimer, Mathematical analysis of two-phase blood flow through a stenosed curved artery with hematocrit and temperature dependent viscosity, Physica Scripta, vol. 96, no. 12, p. 125277, 2021.

2. B. Sharma, **C. Kumawat**, and O. Makinde, Hemodynamical analysis of MHD two phase blood flow through a curved permeableartery having variable viscosity with heat and mass transfer," Biomechanics and Modeling in Mechanobiology, vol. 21, no. 3, pp. 797-825, 2022.

3. **C. Kumawat**, B. Sharma, Q. M. Al-Mdallal, and M. Rahimi-Gorji, Entropy generation for MHD two phase blood flow througha curved permeable artery having variable viscosity with heat and mass transfer, International Communications in Heat and Mass Transfer, vol. 133, p. 105954, 2022.

4. B. K. Sharma, **C. Kumawat**, U. Khanduri, K. Mekheimer, Numerical investigation of the entropy generation analysis for radiative MHD Power-law fluid flow of blood through a curved artery with Hall effect, Waves in Random and Complex Media, 2023.

5. B. K. Sharma, **C. Kumawat**, M M Bhatti, Optimizing Energy Generation in Power-law Nanofluid Flow Through Curved Arteries with gold nanoparticles, Numerical Heat Transfer, Part A: Applications, (Accepted).

6. **C. Kumawat**, B. K. Sharma, L Ali, T Muhammad, Computer simulation of two phase power-law nanofluid of blood flow through a curved overlapping stenosed artery with induced magnetic field: Entropy generation optimization, (Revision Submitted).

Conferences/ Workshop Attended

1. Entropy Generation and Heat transfer of Two-phase Blood flow through a curved permeable artery with Hematocrit dependent viscosity with Joule effect, **International Conference on Advances in Transport Phenomena (ICATP 2022)**- A Virtual Meet, VIT-AP, India, 16^{th}-18^{th} July 2022.

2. Workshop on **Machine learning for Data Science using Python**, Department of CSE, NIT Warangal, India, 16^{th}-30^{th} July 2022.

3. Workshop on **Recent Development in Numerical Methods for Partial Differential Equations, Department of Mathematics & Scientific Computing**, NIT Hamirpur, India, 30^{th} May-3^{rd} June 2022.

4. TEQIP Short term course **Mathematical tools for boundary value problems and applications" Department of Mathematics**, IIT KGP. India, 9^{th}-13^{th} March 2020.

5. Effects of temperature-dependent viscosity and thermal conductivity on MHD blood flow through a stretching surface with Joule effect and chemical reaction, **International Conference and 22^{nd} Annual Convection of VijnanaParishad of India on Advances in Operations Research, Statistics and Mathematics (AOSM 2019)**, BITS- Pilani, Rajasthan, India, 28^{th}-30^{th} Dec. 2019.

Brief Biography of the Candidate

Mr. Chandan Kumawat is a full time research scholar in the department of Mathematics, BITS Pilani, Pilani Campus, Rajasthan since January 2014. He received his Bachelor of Science (B.Sc.) in 2015 from Mehta College & Institute of Technology, Harmada, Jaipur, Rajasthan. He completed his Master's degree in Mathematics from Mehta College & Institute of Technology, Harmada, Jaipur, Rajasthan in 2017. Later on, he joined at Birla Institute of Technology and Sciences Pilani, Pilani Campus to pursue his Doctor of Philosophy (Ph.D.) in the area of Biomechanics under the guidance of Prof. Bhupendra Kumar Sharma. Till date, he has published 6 research papers in reputed international journals and presented 2 papers in international conferences.

Brief Biography of the Supervisor

Dr. Bhupendra Kumar Sharma is a Professor & former Head, Department of Mathematics, Birla Institute of Technology and Science, Pilani, (BITS Pilani) Pilani Campus, Rajasthan, India. His research interest includes Heat and Mass Transfer, Arterial Blood Flow, Magnetic Targeting Drug Delivery, Porous Medium, Boundary Layer Theory, Micro-polar Fluid, Differential Equations etc. He has published more than 85 international/national journals of repute, and authored two books on Engineering Mathematics. He is member of editorial board, advisory board of a number of journal of reputes. Prof Sharma is a member of various academic committees of many Institutes/ Universities such as advisory committee, selection committee etc. He has also participated in many conferences and workshops.